Macroscopic role of solid-liquid and liquid-gas interfaces on the water-rock interaction in porous media

Armin Mozhdehei

To cite this version:

Armin Mozhdehei. Macroscopic role of solid-liquid and liquid-gas interfaces on the water-rock interaction in porous media. Other. Université d'Orléans, 2023. English. NNT : 2023ORLE1011 . tel-04297631

HAL Id: tel-04297631
https://theses.hal.science/tel-04297631

Submitted on 21 Nov 2023

UNIVERSITÉ D'ORLÉANS

ÉCOLE DOCTORALE
Énergie - Matériaux - Sciences de la Terre et de l'Univers (EMSTU)
Institut des Sciences de la Terre d'Orléans (ISTO)

THÈSE présentée par :

Armin Mozhdehei

Soutenue le : **12 Mai 2023**

Pour obtenir le grade de : **Docteur de l'Université d'Orléans**
Discipline/ Spécialité : Sciences de l'univers

Macroscopic Role of Solid-Liquid and Liquid-Gas Interfaces on the Water-Rock Interaction in Porous Media

THÈSE dirigée par :

M. MERCURY Lionel	Professeur, Université d'Orléans, Directeur de thèse
Mme. SLODCZYK Aneta	Ingénieur de recherche, CNRS, Co-directrice de thèse

RAPPORTEURS :

Mme. LE CAER Sophie	Directrice de Recherche, CNRS
M. LUTZENKIRCHEN Johannes	Chercheur, Institut de technologie de Karlsruhe

---

JURY :

M. AZAROUAL Mohamed	Directeur de Recherche, BRGM, Président de jury
M. CREUX Patrice	Professeur, Université de Pau et des Pays de l'Adour
Mme. SULPIZI Marialore	Professeur, Université de la Ruhr à Bochum

Résumé étendu en français

Dans les sols et les formations géologiques souterraines, les gradients de potentiel chimique locaux entraînent ou résultent (d')un certain nombre de processus hydrogéochimiques, tels que la précipitation/dissolution de minéraux, le séchage, le transfert de masse advectif ou diffusif, contribuant à agrandir ou rétrécir l'espace poral. L'interaction des solutions aqueuses avec les solides se produisant par le biais de processus géochimiques est fortement impactée par les ajouts d'intrants et/ou la quantité d'eau disponible. Cela rend la réactivité fluide-roche d'une importance primordiale pour quantifier et prédire comment les hydrosystèmes naturels évoluent sous pression anthropique, en particulier dans les milieux non saturés. Dans ce contexte où la réactivité locale joue un rôle majeur, la surface des interfaces eau-roche est depuis longtemps l'objet d'une attention particulière de la part des géochimistes. En parallèle, de nombreuses applications d'ingénierie prennent en compte l'effet de la variation de réactivité pour la remédiation des eaux souterraines ou pour étudier l'étanchéité des barrières de confinement géologiques. Par exemple, dans les aquifères contaminés, les hydrocarbures et les solvants chlorés piégés par capillarité sont une source de composants toxiques et cancérigènes dans les eaux souterraines sur de très longues durées. Les gradients chimiques locaux générés par cette pollution pourraient être utilisés afin d'éliminer les contaminants colloïdaux stockés dans les pores qui ne sont pas accessibles par les gradients de pression. Enfin, les gradients de potentiel chimique local peuvent affecter l'efficacité des méthodes de récupération assistée du pétrole et la durée de vie opérationnelle des doublets géothermiques.

Les couplages hydro-géochimiques dans les systèmes aquifères poreux multi-échelles (du nanomètre au millimètres) et les roche de couverture affectent les performances des stockages souterrains, notamment en ce qui concerne l'équilibre du transfert de masse interphase (liquide-solide-gaz). Par exemple, il existe un intérêt croissant pour l'utilisation de formations géologiques profondes aux fins de stockage à long/court terme de dioxyde de carbone (CO_2), de vecteurs énergétiques comme le H_2 ou l'air comprimé, et de stockage de déchets radioactifs. Leur efficacité est assurée par la barrière de confinement constituée soit par la roche couverture limitant la formation (CO_2 et H_2), soit par la faible perméabilité de la roche hôte (déchets nucléaires). Pour illustrer les effets synergiques et coopératifs qui peuvent se produire, nous prenons comme exemple le cas du stockage du CO_2. Cette technique propose d'atténuer le changement climatique global et la transition écologique associée en injectant une partie du gaz excédentaire dans les aquifères profonds (formation saline). Avant l'injection de CO_2, l'eau de la formation saline interagit avec son solide hôte en raison de sa forte capacité de solvant. Après injection de CO_2, la flottabilité du CO_2 injecté, moins dense que la saumure, fait migrer le CO_2 vers le haut de la formation. Le CO_2 est empêché de remonter à la surface grâce à une couverture imperméable. Par conséquent, la roche de couverture est en contact physique avec le panache de CO_2 pendant la majeure partie de la durée de vie du stockage, et cette condition à l'interface aquifère-roche de couverture conduit à un état multiphasique (solide-liquide et liquide-gaz). Le contact direct du CO_2 et de la roche de couverture entraîne le dessèchement de l'interface de la roche de couverture par évaporation et à la fabrication de ponts capillaires à l'échelle nanométrique, en fonction de la distribution de la taille des pores. La capillarité est favorisée par des canaux nanométriques, apparaissant à l'interface liquide-gaz et se propageant dans la roche de couverture, qui peuvent modifier la réactivité de l'eau. Cette condition affecte l'ensemble du corps poreux (du pore à l'échelle macroscopique) quelle que soit la taille des pores, tant qu'ils sont hydrauliquement connectés au nano-pont. En conséquence, la mise en place de ponts capillaires très localisés peut modifier les propriétés de confinement (solubilité gaz/solide, écoulement préférentiel eau/gaz, etc.) de toute la formation sus-jacente (roche de couverture) au cours du temps, ce qui joue un rôle crucial pour éviter toute fuite significative de CO_2.

En ce qui concerne les contextes susmentionnés, cette étude s'est concentrée sur les gradients de potentiel chimique locaux le long des interfaces à deux échelles différentes, à savoir l'échelle de l'interface (nm-µm), à laquelle les phases interagissent ensemble, et l'échelle des pores, à laquelle les gradients interfaciaux se combinent en propriétés moyennées sur un grand volume de matière à travers un réseau de pores. Les géochimistes s'appuient souvent sur le modèle standard dans lequel les forces motrices macroscopiques et les bilans de masse résultants dans l'interaction eau-roche peuvent être décrits de manière adéquate par les propriétés globales des phases en interaction. Cette approche commune suppose que la surface solide est infiniment mince, ce qu’on appelle l'approximation capillaire, qui signifie un saut brusque et « immédiat » des propriétés d'une phase à une autre. Par conséquent, l'interface correspondant au domaine entre chaque phase est thermodynamiquement négligeable, sauf avec des solutions nano-confinées ou des cristaux de taille nanométrique (effet de taille finie). Cependant, de nombreuses études théoriques et observations directes sur le terrain ont contesté ce point de vue en démontrant que les propriétés de la solution dépendaient de la distance à une surface solide (c'est-à-dire le rayon des pores) ou de la présence d'une interface liquide-air incurvée. Il y a eu beaucoup de discussions et différentes conclusions concernant l’échelle sur laquelle les propriétés changent sont données, et des seuils variant de 1 à 1000 nm ont été rapportées dans différents articles.

L’échelle de l'interface est très souvent examinée du point de vue solide en essayant de déchiffrer si une couche superficielle lessivée peut ou non impacter le couplage de transport réactif local ou conserve encore une minéralogie variable due aux processus d'altération préférentielle. Des études récentes à haute résolution ont remis en question cet ancien scénario, démontrant que l'interface solide est très mince et conceptualisant les échanges de masse pour les réactions eau-silicate par dissolution-reprécipitation à l'échelle de l'interface. Pour donner un autre exemple bien connu mais très différent, la communauté s'interroge toujours sur l'écart entre les taux de réaction en laboratoire et sur le terrain des silicates. Notre travail part de l’hypothèse que le problème doit aussi être examiné du point de vue de l'eau, qui dépend du solide avec lequel elle interagit. Il pourrait donc contribuer à ces deux débats.

L'échelle des pores associe des problèmes de frontière solide-liquide, avec l'influence de l'état de surface des parois solides sur l'eau, et avec la capacité de la cavité à héberger des ponts capillaires liquide-air. La capillarité est ici regardée non pas sous le prisme habituel de la partition diphasique, mais comme une force motrice pour la réactivité à l'échelle des pores. La loi de Young-Laplace permet de se rendre compte que la pression de l'eau liquide devient négative en valeur absolue chaque fois que le liquide est piégé dans un pore inférieur à 1,5 μm. Ici, une certaine confusion peut survenir en conceptualisant le concept de pression uniquement en termes de théorie cinétique des gaz, où pression et densité sont directement proportionnelles, de sorte que la pression nulle correspond à une absence de matière. Mais les liquides et les solides n'ont pas cette proportionnalité pression-densité en raison de la cohésion de ces états condensés de la matière. C'est pourquoi une pression négative peut se mettre en place dans les liquides (tension de l'eau) comme dans les solides (force tensile, ou résistance à la traction). Dès lors qu'une pression interstitielle négative s’installe, le potentiel chimique de l’eau devenue capillaire change (via l'intégrale V.dP), en plus d’exercer une contrainte de traction sur les parois solides sur lesquelles s’ancre le pont. La physico-chimie et la mécanique de l’ensemble de la masse d’eau hydrauliquement connectée au pont capillaire sont ainsi modifiées et obéissent au comportement capillaire même si les interfaces courbes liquide-air ne prennent place que le long d'un nombre limité de pores.

Par conséquent, le gradient de potentiel chimique aux interfaces multiphasiques (solide-liquide et liquide-gaz) à différentes échelles (nm à macro) doit être examiné de façon mécaniste pour comprendre comment les processus hydro-géochimiques sont enracinés à la plus petite échelle phénoménologique possible. Cela doit améliorer notre conceptualisation du transport réactif, en combinant les mécanismes élémentaires pertinents avec la quantification appropriée pour établir des capacités de modélisation prédictive grâce aux lois physico-chimiques.

Ainsi, les principaux objectifs de cette étude sont de démêler l'effet des interfaces dans l'état multiphasique dans les milieux poreux géologiques en utilisant des modèles de pores synthétiques tels que les inclusions fluides (FI) et les puces nanofluidiques. L'hypothèse de départ est que la réactivité le long des interfaces obéit aux potentiels chimiques locaux des phases en contact, ce qui ne se limite pas aux propriétés massiques. Concernant ce concept, nous visons à quantifier la variation de réactivité à l'échelle des pores en fonction de la distance aux interfaces (point de vue interface) ou de la taille du pont capillaire liquide-air le plus fin (perspective à l'échelle des pores) pour répondre au transfert de masse et questions d'écoulement des fluides dans les structures poreuses souterraines. Les objectifs détaillés sont les suivants :

1) Explorer et quantifier la variation de potentiel chimique (réactivité) des phases, en particulier au niveau de la zone de contact entre ces phases. Étudier l'effet de la température/pression sur les signatures enregistrées pour déterminer les racines physiques des propriétés observées.
2) Évaluer les types de forces de surface et les caractéristiques de surface des parois solides (hydrophobicité/hydrophilie, double couche électrique) qui peuvent jouer un rôle dans un effet exprimé le long de l'interface.
3) Caractériser l'effet de la taille des nanopores sur le flux capillaire et la cinétique d'évaporation de l'eau par rapport à la loi de Kelvin.
4) Étudier la géochimie contrôlée par la taille des pores hôtes de ponts capillaires, en ce qui concerne les phénomènes de transition de phase et les états métastables se produisant dans les systèmes capillaires à double pores (taille des pores très contrastée).

La nature enfouie et opaque des formations géologiques empêche la visualisation directe des processus hydrogéochimiques dans le sous-sol. Cela nous conduit à des expériences en laboratoire utilisant des matériaux spécifiquement synthétisés pour simuler la physico-chimie d'interaction dans des structures poreuses souterraines (expériences à l'échelle des pores). Dans un premier temps, l'interface eau-roche (liquide-solide) a été méticuleusement étudiée par une méthode de micro-spectroscopie vibrationnelle en mode transmission et à différentes températures. En effet, la micro-spectroscopie FTIR à haute résolution est un outil approprié pour l'étude des propriétés de l'eau en sondant sa connectivité moléculaire en fonction des conditions. En utilisant des micro-faisceaux, cette méthode permet de suivre les variations des propriétés de l'eau dans un pore en fonction de la distance aux parois solides avec une résolution spatiale fixée par la taille du faisceau. La micro-spectroscopie FTIR sera donc notre sonde énergétique pour enregistrer comment l'énergie vibratoire de l'eau change en s'approchant de la surface solide et de la frontière vapeur d'eau.

En ce qui concerne la configuration expérimentale, nous avons utilisé quatre configurations différentes pour effectuer les mesures micro-FTIR à haute résolution. Nous avons découvert que deux paramètres principaux jouent un rôle majeur dans la micro-spectroscopie infrarouge moyen à haute résolution : la disposition optique du microscope et la source infrarouge. Compte tenu de la disposition optique des microscopes, le mode confocal avec une configuration à double ouverture et à voie unique connecté au détecteur à élément unique au tellurure de mercure et de cadmium (MCT) a une efficacité supérieure en termes de résolution spatiale au microscope sans ouverture connecté au détecteur matriciel à plan focal (FPA). De plus, en évaluant trois sources infrarouges différentes (Globar, laser supercontinuum et synchrotron), les données FTIR hyperspectrales ont révélé que le laser supercontinuum (avec une taille d'ouverture 5×5 µm) et le faisceau synchrotron (avec une taille d'ouverture 3×3 µm) peuvent seules être exploitées pour effectuer des mesures à haute résolution jusqu'à la limite de diffraction pour étudier le comportement de l'eau dans des cavités fermées à l'échelle micrométrique (inclusions fluides synthétiques et naturelles).

Les inclusions fluides sont totalement fermées, ont une géométrie interfaciale bien définie et ont un volume total constant, ce qui permet de suivre le diagramme P-T en changeant la température ou la pression. Nous avons montré que le comportement de l'eau et les spectres correspondants sont fortement affectés lorsque le faisceau s'approche de la surface solide et de la bulle de gaz. Cependant, ils sont en partie influencés par l'aberration optique, comme les franges d'interférence et la diffusion de Mie. Ces phénomènes peuvent se superposer à des caractéristiques spectrales chimiques et peuvent jeter un doute sur l'origine de telles signatures et leur signification dans l'interface eau-solide et liquide-gaz. Par conséquent, la conception expérimentale et le traitement des données sont cruciaux pour interpréter correctement les spectres acquis.

Après traitement des données, nous avons établi que les interfaces solide-liquide et liquide-gaz affichaient une signature spectrale dépendant de la distance pour l'eau sur une épaisseur de 1±0,5 µm à partir de la surface solide ou de la frontière avec l'air. Il s'agit de l'apparition d'une signature spectrale spécifique au sein de la bande d'élongation OH de l'eau près des interfaces solide-liquide et liquide-vapeur, appelée signature interfaciale. La bande d'élongation OH peut être attribuée au nombre moyen de liaisons H dans l'environnement local des molécules. A partir de ces considérations, il est courant de décrire cette bande d'étirement par des composantes gaussiennes, chacune attribuée à des molécules ayant un nombre de coordination donné. La bande d'élongation OH est généralement décomposée en trois sous-bandes gaussiennes. La gaussienne centrée autour de 3250 cm^{-1}, dite eau de réseau (NW), est attribuée à des molécules ayant un nombre de coordination de quatre et une structure localement tétraédrique. La composante gaussienne à nombre d'onde intermédiaire (c.a. 3450 cm^{-1}), eau dite intermédiaire (IW), représente les molécules dans le milieu non tétraédrique avec un nombre de coordination proche de 3. Enfin, la composante gaussienne à nombre d'onde élevé (entre 3650 et 3750 $cm^{- 1}$), l'eau multimère (MW), est attribuée aux molécules d'eau moins connectées avec un nombre de coordination de 2 à 0.

Près de l'interface eau-solide, la signature spectrale montre un pic supplémentaire sur un côté mais au sein de la bande d'élongation OH de l'eau, vers 3700 cm^{-1}, ce qui correspond à des molécules d'eau moins connectées. Cette bande détectée entre 3650 et 3750 cm^{-1} est visible lorsque le minéral-hôte est le quartz ou la fluorite mais est absente dans de la calcite. Dans ce dernier cas, on observe au contraire un enrichissement des molécules d'eau bien connectées (faible nombre d'ondes) en lien avec la nature hydrophile de la surface de ce solide. Cela signifie que cet effet interfacial est contrôlé par la nature hydrophobe/hydrophile de la surface des murs solides du pore, donc tire son origine de l'énergie de surface solide-liquide.

Pour ce qui est de l'interface eau-air, un pic de type hydrophobe (pic vers 3700 cm^{-1}) apparaît ce qui est en lien avec la nature hydrophobe bien connue de cette interface. Cependant le pic est au-delà de la bande d'élongation OH, bien distinct d'elle, correspondant au mode OH libre mesuré dans la littérature à partie de mesures avec des méthodes non linéaires à portée nanométrique (spectroscopie infrarouge SFG et SHG).

Par comparaison, les bandes d'élongation OH de l'eau normale (l'eau en-dehors d'un milieu fermé) et de l'eau piégée volumique (l'eau située dans une cavité fermée, mais loin de toute interface solide-liquide ou liquide-gaz) montrent les caractéristiques habituelles de l'eau : prédominance de la composante à faible nombre d'onde (environ 3250 et 3450 cm^{-1}), et pas d'épaulement ni d'enrichissement aux nombres d'onde plus élevés (environ 3700 cm^{-1}).

Nous avons également mené une étude en température, pour observer que l'eau interfaciale près de la surface de quartz est moins tétra-coordonnée que l'eau piégée volumique (33 % moins de molécules d'eau bien connectées à température ambiante et 35% à 155°C). De plus, le pic vers 3700 cm^{-1} devient plus intense à des températures élevées (jusqu'à 155°C), ce qui signifie que l'augmentation de la température a un effet de désorganisation (chaotrope) sur le réseau moléculaire de l'eau, qui vient s'ajouter à celui de la frontière solide, diminuant le nombre de coordination moyen. Dans l'ensemble, le réseau moléculaire de l'eau interfaciale est dominé par les IW (molécules 3-connectées), un fait promu par la température, remarquablement différent de l'eau piégée volumique dominée par les molécules NW (molécules 4-connectées) même à haute température.

Notre résultat suivant a été de trouver un moyen d'interpréter les signatures basées sur l'IR dans les environnements naturels en créant un lien entre les propriétés microscopiques et macroscopiques. Pour ce faire, une fonction de partition spécifique développée précédemment a été utilisée pour convertir les propriétés vibrationnelles de l'eau (échelle microscopique) en ses propriétés thermodynamiques (échelle macroscopique). La conversion de la signature spectrale près de la frontière du quartz en énergie libre de Gibbs conduit à une empreinte de surface de 600 J/mol à température ambiante (22°C) à 1000 J/mol à haute température (155°C). Cette augmentation de l'énergie libre de Gibbs augmente le potentiel chimique et modifie la réactivité de l'eau, c'est-à-dire modifie les solubilités d'équilibre le long de l'interface solide-liquide.

Ce changement de réactivité intervient sur une épaisseur de 1±0,5 µm, ce qui conduit à définir plutôt un domaine "d'interphase" entre la région interfaciale et la zone de volume qu'une "interface" géométriquement nette liée à la variation de phase. De plus, ce changement significatif de la réactivité chimique de l'eau liquide se produit en raison d'une augmentation de l'énergie libre de Gibbs, avec un écart accru par la température. En conséquence, l'eau interfaciale est moins stable que l'eau volumique, donc plus réactive et plus susceptible de dissoudre la matrice solide. En général, la géochimie de l’interaction eau-roche pourrait être impactée par ces résultats. Par exemple, la sursaturation à long terme dans les grands bassins sédimentaires ou l'amélioration de la solubilité couramment observée dans les petits pores (inférieurs à 1 µm), qui sont justifiées par les termes "solubilité contrôlée à la taille des pores" ou "effet de confinement," pourraient s'expliquer par la plus grande réactivité de l'eau (ou de la solution) dans le domaine d'interphase des pores. Et on peut supposer que ces conséquences pratiques soient maximisées au cours des processus diagénétiques ou hydrothermaux en raison de la sensibilité thermique de cet effet d'interface.

L'étude des origines possibles de l'effet d'interface près de l'interface solide-liquide, comme la forme/taille du pore, la composition de la solution occluse avec une salinité/pH variée et différents minéraux hôtes, démontre que seule la propriété de surface solide (hydrophilie/hydrophobicité) joue un rôle dans le contrôle du comportement interfacial et de l'effet d'interface. Nous avons observé que les propriétés volumiques sont retrouvées à environ 1±0,5 µm du solide ; cependant, l'étendue de l'effet d'interface enregistré ici n'a jamais été envisagée sur une telle distance. En termes de physique de l’eau pure, des mesures neutrons ont montré que la portée de la liaison H n’excédait pas 3 couches moléculaires (presque 1 nm), donc qu’un effet plus lointain ne pouvait être dû à la dynamique de la liaison hydrogène. L'insensibilité du domaine d'interphase aux géométries des parois, aux compositions des solutions occluses, voire des minéraux hôtes tant qu’ils restent hydrophobes, de même que la très longue portée d’1 µm, signifient que nous avons affaire à un champ de force systématique à longue portée, tel que la combinaison d'une interaction hydrophobe avec un champ électrostatique.

À l’échelle microscopique, le manque d'affinité entre l’eau et le solide (hydrophobicité), la très forte affinité de l’eau pour elle-même, peut conduire le liquide à se refermer sur lui-même. Cette tendance à l'interface donne lieu à une couche de faible densité le long du domaine eau-hydrophobe. Une fois que cette couche à faible densité est en place, macroscopiquement, deux principaux champs à longue portée peuvent propager davantage l'effet d'interface, en fonction de la conceptualisation. La première possibilité est un modèle en pression de disjonction, où le système solide-air-liquide rassemble les trois diélectriques à l'intérieur desquels la pression de disjonction peut s'installer. La deuxième option est une analogie capillaire, considérant la faible densité produite par un alignement de nano-ponts (liquide concave vers la vapeur). Dans les deux modèles, on peut envisager le rôle de l'électrification à l'interface qui ajoute une contribution électrostatique à la pression de disjonction ou capillaire.

Dans la deuxième partie de cette étude, l'interface eau-air (liquide-gaz) et leur effet de ponts capillaires sur les propriétés de l'eau ont été étudiés par des puces nanofluidiques. Ces dispositifs ont montré un énorme potentiel pour résoudre les problèmes d'écoulement souterrain et de transport réactif au cours des dernières décennies. Ils permettent un contrôle précis et une visualisation directe et en temps réel, des flux, des réactions et des mécanismes de transport de l'échelle micrométrique à l'échelle nanométrique. Dans notre approche, nous avons utilisé un jeu de puces nanofluidique avec une géométrie de bouteille d'encre (c'est-à-dire un assemblage de nano-ponts et de macro-réservoir), permettant de modifier le potentiel chimique de l'ensemble de la masse d'eau hydrauliquement connectée à des interfaces capillaires.

La capillarité dans des nano-canaux de 5 nm a été contrôlée en ajustant l'humidité relative (HR) de l'air dans un macro-réservoir (78%). Nous avons pu observer que l'eau ne s'évaporait pas des nano-canaux, mais cavitait dans les grands réservoirs loin derrière les nanocanaux. Nous avons également étudié le processus de séchage lorsque l'humidité relative devient inférieure à sa valeur d'équilibre. Dans ce cas, le macro-réservoir s'évapore au travers des nano-canaux à une vitesse contrôlée par la taille du nano-canal et par sa géométrie. Avec nos canaux rectangulaires, nous avons pu observer le rôle des films de coin dans la cinétique d'évaporation.

Ces résultats illustrent que la pression capillaire se propage dans toute la masse d'eau connectée au pont capillaire, conduisant tout le système à obéir à la géochimie capillaire. Dans l'environnement naturel, cet effet capillaire se produit dans une interface entre une roche de couverture et une bulle de CO_2. A ce niveau, la mise en place de ponts capillaires modifie la réactivité de toute l'eau présente dans la roche de couverture peu perméable. En conséquence, l'état et la réactivité de l'eau dans les barrières de confinement des stockages souterrains peuvent être interrogés, au-delà même du cas de stockage de CO_2. Avec le stockage de déchets nucléaires, la formation-hôte elle-même est saturée en eau, et les tunnels ventilés constituent les zones asséchantes qui permettent la mise en place de l’effet capillaire. Il peut ainsi déclencher les processus capillaires dans l'ensemble du réservoir d'eau relié hydrauliquement.

Depuis l'interface jusqu’au point de vue à l'échelle du pore il reste encore de nombreuses questions auxquelles il faut répondre. Pour approfondir l'effet de surface solide sur l’eau d’interphase, nous proposons de concevoir une série de nouvelles inclusions fluides, toutes synthétiques mais avec une variété d'hôtes minéraux allant d'hydrophile à hydrophobe. En outre, ils doivent être remplis de diverses solutions aqueuses pour mieux comprendre le rôle des solutés dissous cosmotropes et chaotropes dans l'organisation de l'interface (ou non). Un autre aspect lié à ces nouvelles fabrications serait le contrôle de l'épaisseur des inclusions. Nous avons rencontré de nombreux problèmes pratiques lié à la saturation du signal (de nombreuses inclusions ont été rejetées), conduisant à rejeter des échantillons ou à pénaliser le rapport signal sur bruit.

L’échelle des pores offre quant à elle des voies prometteuses pour mieux comprendre comment les gradients géochimiques s'accumulent à certaines interfaces critiques et propagent leurs propriétés spécifiques et locales aux réservoirs d'eau. Les ponts capillaires collés à une couche nanoporeuse alors qu'ils sont en contact avec une phase gazeuse de séchage sont un acteur thermodynamique inconnu pour contrôler la réactivité et la distribution diphasique à travers l'ensemble d'une roche couverture et/ou d’une barrière de confinement. Nos résultats préliminaires encourageants avec les puces nanofluidiques ouvrent la voie à des perspectives évidentes. Deux types d'expériences peuvent être facilement proposées, avec des solutions saturées soumises à une évaporation capillaire, force motrice pour faire précipiter de cristaux et observer le rôle de la taille de pores et de la nature des interfaces, ou bien avec un flux de nanoparticules pour inséminer les modèles nanofluidiques avec des solutions sursaturées et observer là aussi ce qui se passera. Une approche alternative peut être proposée avec une puce à base de silicium. En effet, le silicium est transparent à l'infrarouge moyen et peut être facilement silanisé pour contrôler l'hydrophilie/hydrophobicité. De cette manière, nous pourrions quantifier et observer les transitions de phase avec des états de surface solide contrôlés. Mais l'enjeu sera de remplir de manière contrôlée les canaux hydrophobes et, au-delà, d'avoir suffisamment d'eau piégée dans les canaux pour capter un signal. Un dernier scénario prospectif peut être d'utiliser de l'alumine/silicium poreux obtenu par anodisation et ensuite fonctionnalisé en paroi, toutes technologies déjà existantes. Dans ce cas, le micro-faisceau ne serait pas nécessaire et différentes échelles de longueur pourraient être testées. L'utilisation de ces types d'échantillons pourrait donner lieu à une étude systématique d'un couplage interface/confinement. D'après notre lecture, il semble que le comportement interfacial ne soit pas considéré dans l'interprétation des études actuelles tournées vers le confinement.

Abstract

In water-rock interaction, the surface area of interfaces has received long-term attention from geochemists, but local reactivity along interfaces also plays a significant role. The standard approach uses the bulk properties of interacting phases to describe the macroscopic driving forces and the resulting mass balances. However, direct field observations challenged classicism, demonstrating that the pore radius, the distance to the solid boundary, or the presence of a curved liquid-air interface can drive the phase transitions along unexpected reactional pathways. This study has targeted two types of experiments to probe what can be the additional parameters to be involved in the reasoning, one at the interface-scale, mainly focused on the water-solid boundary, and one at the pore-scale, turned to the influence of capillary bridges on the in-pore geochemistry. First, the interface-based infrared micro-spectroscopy measurements, using micro-beam (laser and synchrotron source) and a confocal microscope, were performed on a micrometric closed cavity (fluid inclusion) to explore the variation of the vibrational energy of water as a function of the distance to the solid boundary. The hyperspectral data displayed a distance-dependent signature for water over a 1 ± 0.5 μm thickness (called interphase domain) because of the solid surface property (hydrophobic effect) and the resulting surface energies. The conversion of the spectral signature near the quartz boundary into Gibbs free energy leads to a 600 J/mol surface-imprinting at room temperature (22°C) to 1000 J/mol at high temperature (155°C). Consequently, this increasing chemical potential changes the reactivity along such a solid-liquid interface, which affects a significant amount of water. It comes out that the surface chemistry of minerals and not only their composition, shape, or size play a crucial role in water-rock interactions in pores, channels, and cavities. Second, the reactivity variation in a pore network is closely linked to the presence (or not) of liquid-air capillary bridges and their capillary intensity. We exploited nanofluidic chipsets to establish capillarity in a controlled way by tuning the relative humidity, with which we explored the water-rock-gases equilibria at various capillary states leading to a phase transition. The water cavitation phenomenon and the kinetics of the evaporation show the effect of relative humidity on the capillary-driven effect, besides the prominent influence of the shape and size of the heterogeneities. These measurements question the systematic use of the bulk phases datasets to evaluate and predict how water-rock interactions occur and evolve with time in the porous media, especially in water-unsaturated aquifers.

Keywords: Reactivity variation, Thermodynamic, Vibrational spectroscopy, Interface/Interphase, Capillary bridge.

Acknowledgment

I would like to extend my heartfelt appreciation and acknowledge the following individuals and groups who have played a crucial role in the successful completion of my PhD research:

First and foremost, I am deeply grateful to my supervisors for their unwavering support, invaluable guidance, insightful advice, and boundless patience. Their expertise and mentorship have been instrumental in shaping my research and academic growth. After that I am deeply grateful to Sophie Le Caer and Johannes Lutzenkirchen as reporter of my thesis and also Mohamed Azaroual, Patrice Creux, and Marialore Sulpizi as member of jury for their time, dedication, and scholarly input. Their collective expertise and diverse perspectives have enriched the discussions and enhanced the overall quality of this manuscript. Also, I would like to express my sincere gratitude to the members of the ISTOpore and nanoμfluidic research groups, including the PhD students, postdocs, and researchers. Their collaboration, stimulating discussions, and contributions have significantly enriched my work and made this journey all the more fulfilling.

I am indebted to the researchers at the Synchrotron facility center of France (SOLEIL) for their kind assistance and providing access to their state-of-the-art facilities. Their support has been crucial in carrying out the experiments and obtaining valuable data for my research. Special appreciation goes to Ferederic Jamme, Christophe Sandt, and Ferenc Borondic for their insightful discussions, valuable suggestions, and contributions, which have greatly enhanced the quality and depth of my work. I would like to acknowledge the researchers at the CEMHTI, particularly Prof. Patrick Simon and Aurelien Canizares, for their collaboration and valuable insights, which have broadened my understanding and opened new avenues in my research.

I am grateful to Prof. Kohler and his research team for their fruitful collaboration, which has enriched my research experience and brought about innovative ideas and perspectives. A heartfelt thanks goes to Prof. Hines for her generous assistance in the data treatment. I would like to express my appreciation to Alexander Tarantola for providing us with new ideas and valuable samples, which have expanded the scope and possibilities of my research.

I am also grateful to all my colleagues in the workshop, IT department, and administrative staffs of ISTO. Their support, technical assistance, and administrative guidance have been invaluable throughout this journey. I would like to extend special thanks to Frederic Savoie, Rémi Champallier, Esteban Le Moing, Julien Catherine, Florian Duval, Marie-France Rouillier, and Olivier Gaudefroy for their continuous support and collaboration.

Also, I would like to express my deepest appreciation and gratitude to my family for their support and love throughout my PhD journey. Their constant encouragement, understanding, and sacrifices have been the foundation of my success. I am grateful for their belief in me, even during the most challenging times.

Finally, I’d like to thank all those who have contributed to my research in various ways and have not been specifically mentioned. Your collective support and encouragement have been essential in making this achievement possible.

Thank you all for your invaluable contributions and support.

Contents

List of table

List of figures

1. Introduction

1.1. Overview

In the soils and subsurface geological formations, **local chemical potential gradients** drive, or result from, a number of hydro-geochemical processes, such as precipitation/dissolution mechanism [1, 2], drying [3, 4], interphase mass transfer [5], and chemical reactions [6]. The **fluid-rock (solid-liquid) interaction** occurs **at the scale of "elementary" phases put in physical contact (nm-µm)** through geochemical processes and drives the chemical evolution of large hydrosystems over time and under anthropogenic activities. Many engineering applications have foreseen the effect of the reactivity variation for groundwater remediation or for sealing damaged geological confinement barriers [7, 8]. For example, in contaminated aquifers, hydrocarbons and chlorinated solvents trapped by capillary forces are a source of toxic and carcinogen components released in groundwater. The local chemical gradients generated by this pollution could be used for groundwater remediation to remove colloidal contaminants stored in pores that are not accessible by pressure gradients [9]. Moreover, the local chemical potential gradient may affect the efficiency of the enhanced oil recovery methods [10-12] and the operational lifetime of geothermal doublets [13, 14].

Furthermore, hydro-geochemical couplings in multiscale (nm to macro) porous aquifer/caprock systems play a major role in the performance of underground storages, especially concerning the balance of the interphase mass transfer (liquid-solid-gas). There is a growing interest in using deep geological formations as long/short-term storage of carbon dioxide (CO_2) [15-17], energetic vectors like H_2 or compressed air [18-20], and radioactive waste disposal [21-23]. Their efficiency is ensured by the containment barrier of either the caprock limiting the formation (CO_2 and H_2) or the low permeability of the host rock (nuclear wastes). To illustrate the synergistic and cooperative effects which can occur, we exemplify the case of CO_2 storage. This technique proposes mitigating global climate change and the associated ecological transition by injecting part of the excess gas into deep aquifers (saline formation). Before CO_2 injection, water in the saline formation interacts with its host solid due to its strong solvent capacity [24]. After CO_2 injection, the buoyancy of injected CO_2, which is less dense than brine, makes the CO_2 to migrate toward the top of the formation. CO_2 is prevented from flowing back to the surface by an impervious caprock, which is called structural trapping [25]. Consequently, the caprock is in physical contact with the CO_2 plume during most of the storage lifetime, and this condition at the aquifer-caprock interface leads to the **multiphasic state (solid-liquid and liquid-gas)**, as shown in Figure 1.1. The direct contact of CO_2 and the caprock results in drying the caprock interface by evaporation or fabricating nanoscale capillary bridges depending on the pore size distribution (PSD). Capillarity is promoted with nanometric channels, occurring at the liquid-gas interface and propagating in the caprock. This condition affects the **whole pore body (from pore to macro scale)** regardless of the pore sizes, as long as they are hydraulically connected to the nano-throat. As a consequence, it can modify the containment properties (gas/solid solubility, preferential pathway, etc.) of the overlying formation (caprock) through time, which plays a crucial role in avoiding any significant CO_2 leakage.

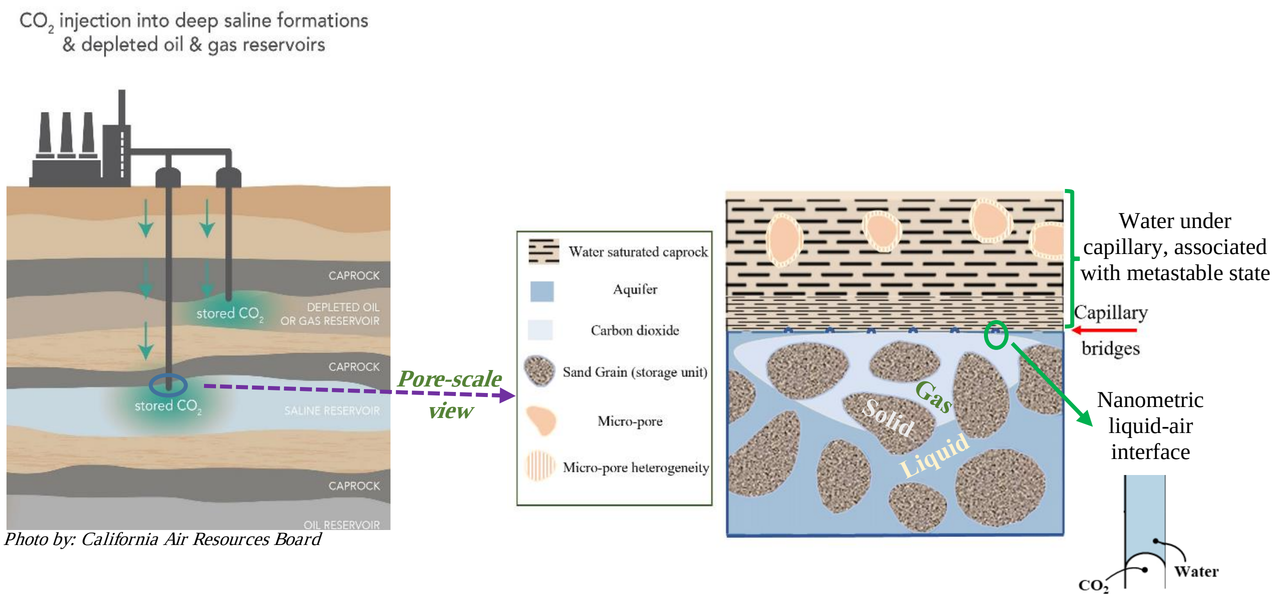

Photo by: California Air Resources Board

Figure 1.1. Schematic view of multiphasic (liquid-solid and liquid-gas) state in the subsurface during CO_2 storage in the deep aquifer.

Regarding the physical conceptualization, geological porous media are intrinsically complex systems because of the heterogeneities and the PSD throughout the pore network. At this scale, we are dealing with the combined effects of different factors from the pore throat to the pore body (from nm to millimeter scale), which provide specific physics as a result of the "ink-bottle" structure (Figure 1.2): Haines jumps, adsorption-desorption hysteresis, water metastability, etc. For instance, water drainage is stopped at the narrow pore throats until reaching the condition for the capillary bridges to be broken. Whereas during imbibition, water can invade the pore body (the largest portion of the network), according to the condition fixed by the size of this pore body, then jumping to the following narrow part. Consequently, the mechanical status of water bridging at the pore throat impacts water retention and even the hydrodynamics throughout the whole network [26, 27]. Nanopores are arguably the most critical part of many pore systems, consisting of almost 30% of the PSD in the sedimentary basins [28]. These pores may act as constrictions (i.e., pore throats), constraining overall flow, especially with the two-phase flow, which attracts a great deal of attention in fluid mechanics applied to natural media. What is more neglected is how the nanothroats may affect the fluid thermodynamics, the chemical rates, and the equilibrium conditions of local reaction processes [26].

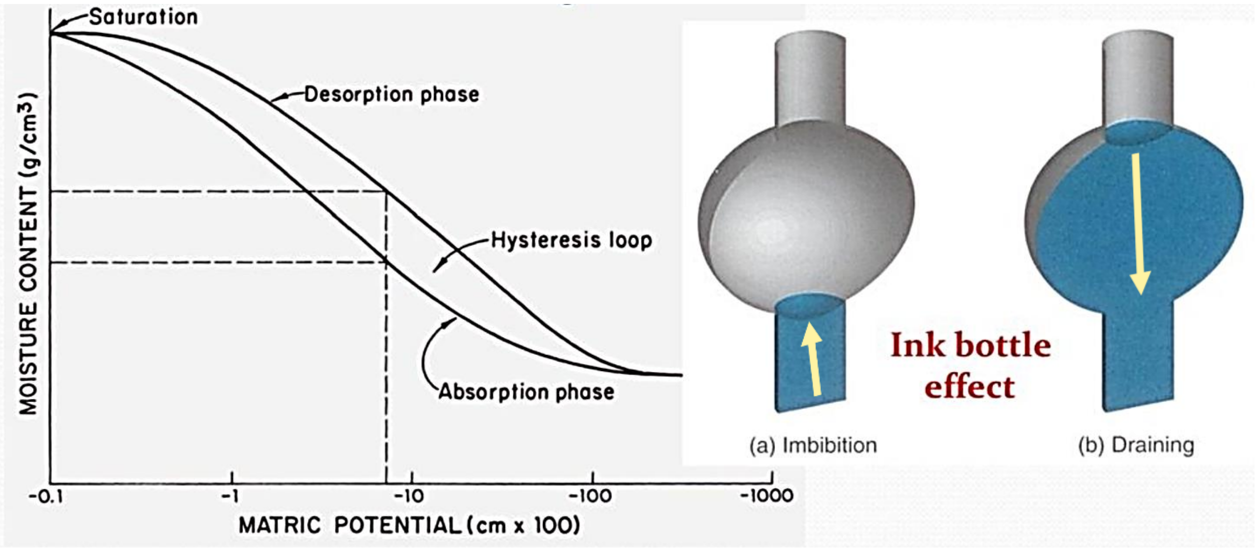

Figure 1.2. Hysteresis and ink bottle effect [27]. A small radius in discontinuous pore channels governs the water level during capillary draining (drying), while a large radius limits capillary rise (wetting).

The conceptualization of the ink-bottle effect shows how the liquid-solid-air relationship in real pore networks depends on both geometries and composition over scales ranging from the nanometer at which two different phases contact together, to the megascopic scale of aquifers and sedimentary basin, via the pore scale, which is the first level aggregating the coupling between structure and properties. Natural scientists often try to define an elementary volume in which all the critical properties are averaged to represent the general behavior. In this study, we are willing to enter inside the pore scale to clarify how the elementary mechanisms are coupled. We do believe it is an essential step to develop mechanistic-based predictive modelling in the environmental sciences.

1.2. Motivation and problem statement

The reactive transport phenomena within the geological porous media occur over broad spatial and temporal scales and play a role depending on, for instance, chemical microenvironments, coupled thermal–chemical processes, and mineral-fluid reaction rates [29]. The water-rock interaction studies have been developed for decades, according to the principles of equilibrium thermodynamics completed by many kinetic laws to involve specific reactional paths, especially at Earth surface conditions. However, porous media hosts paradoxical mechanisms about fluid-rock interaction and mass transfer processes, which are poorly understood though tackled with the classic approaches. Various observations revealed that the straightforward reasoning from bulk phases, irrespective of pore size and multiphasic configurations (except for the supposedly rare nanometer scale), does not entirely diagnose natural systems. Fluid-rock interactions are rooted in the reactive driving forces present along the interfaces between solid and liquid. Mass balances at the global scale average the diversity and complexity occurring at the local scale. But the up/down-scale coupling (upscale) or decoupling (downscale) processes are largely unknown, especially in terms of physical chemistry conceptualization.

The standard approach to quantify the driving forces uses chemical potentials of interacting phases by calculating the thermodynamically stable assemblages. This common approach assumes that the solid surface is infinitely thin, often called the capillary approximation meaning a sharp and ‘immediate’ jump from one phase to another. Consequently, the interface corresponding to the domain between each phase is thermodynamically negligible, except with nano-confined solutions or nano-sized crystals (finite size effect). These calculations are classically confronted with field observations before building coupled modeling intended for environmental diagnoses or predictivity.

Direct field observations of phase transition demonstrated that the pore radius with a threshold around some micrometers matters in the mass balance in a very different way than the one predicted by the standard model. Studying salt domes in Germany, Putnis et al. observed that the salt fills the larger intergranular pore space of the sandstone (10 to 40μm), whereas smaller pores (<1μm) are devoid of salt [30]. Baermann et al., by drilling the sedimentary basin of northern Germany, noted that anhydrite exists in large pores (tens of micron range) but not in pores smaller than 1 μm [31]. Indeed, the reactivity variation due to the surface area of the solid-liquid interface in the small pores (higher reactive surface area) is supposed to lead the solution to maintain higher supersaturation.

Likewise, the effect of pore radius and crystallite size has been involved in accounting for silica supersaturation commonly observed in large sedimentary basins, despite very slow advection (no driving forces) and very old (i.e., mature) sedimentary deposits [32-35]. In these cases, the driving forces for creating the silica supersaturation would relate to nanophases of silica [32-35]. However, they are not observed in situ and are unlikely to persist as a long-term component of sedimentary layers, at least up to a point becoming the controlling phase of the silica concentration at the aquifer scale.

The aquifer scale studies are often performed through reactive transport modelling (RTM) or at least completed with these approaches. It means the standard methods are employed to reconstruct the piezometric surfaces and the geochemical signatures through the relevant assumptions and descriptions of structure and compositions. Steefel and Lichtner, by modelling the reactive transport in a Jordan basin, were constrained to assume that the geochemical behavior was changing from large to small fractures due to changing surface area. That allowed them to make the model successful but implies that small fractures were kept open while the close large fractures were cementing [36].

Emmanuel remarked that the interfacial energy effect (surface energy) plays a crucial role when going towards the nano-world, with the role of curvature (capillary-elastic pressure) and the surface-to-volume ratio penalizing the Gibbs free energy of the smaller grains. A simple calculation made Emmanuel to predict that quartz precipitation was inhibited in pores smaller than 10 microns, although standard kinetic models predict that these pores should be sealed [37]. In this way of reasoning, Prieto et al. calculated within a Classical Nucleation Theory (CNT) framework that at a given supersaturation value, the precipitation occurs much faster in a large pore (100 µm, 4 seconds) than in a small pore (0.1 µm, nine orders of magnitude slower). He justified this behavior by considering the surface energies (interfacial tension) as the main fitting parameter in the small pores [38]. Also, Mürmann et al., by molecular dynamic (MD) simulations, showed that the threshold from which anhydrite precipitates in a pore is 69 microns and related this effect to the chemical composition in the electrical double layer (EDL) by considering that the surface charge on the pore walls will interact with the ions in the fluid and change their activity and hence the required supersaturation of the fluid to trigger nucleation [39].

Then, the solution properties regarding the precipitation and crystallization are primarily impacted by the dimensionality of the hosting solid pore especially related to the mean distance between solid surfaces (distance to the solid boundary), which can give rise to the “confinement effect” [40-46]. Confinement influences crystallization processes over a length scale ranging from the nanometer to tens of micrometers and originates from a wide range of mechanisms [47]. Indeed, chemical reactivity can be modulated in different ways by the confinement effect; however, the mechanism of how the confinement effect changes the reaction remains unclear [48]. Moreover, there has been much discussion and different conclusions regarding the length scale over which the properties change are observed [49-51].

A review article by Gardeniers emphasizes the variation of chemical reactions and protein dynamics by spectroscopic methods while the solution is confined in channels ranging from 50 nm to 1 µm [52]. Le Caër et al., by conducting the ATR-FTIR measurements, declared that the vibrational properties of water are disturbed for pore sizes up to 320 nm. Tsukahara et al., by an NMR study of water, detected that the molecular network of water was modified for channel sizes up to 1 µm [53]. Moreover, Zheng et al., by considering the effect of solid surface properties, showed that hydrophilic interfaces play a more significant role than is commonly believed [54]. Similar to liquid crystals, solutes in aqueous suspension are excluded from the vicinity of many interfaces. Zheng et al. declared that there is a long-range restriction of water molecules nucleating at the interface, and many aspects of surface and interfacial chemistry must be affected by such unexpectedly extensive zones of mobility-limited water [54]. As a result, hydrophilic/hydrophobic balance might be the track to follow in the hydrogeochemical processes.

In this way, Stack et al., using Small Angle X-ray Scattering (SAXS) measurements, observed that precipitation in nanopores may or may not be inhibited with respect to the pore radius depending on the surface chemistry between precipitate and substrate. In this research, they designed two pore size distributions (nano (8 nm) and macro pores (tens of microns)) with different surface functional groups leading to varied surface wettability at the water-solid interface [55]. The prominent role of the surface property of pore walls was also the direct conclusion of an FTIR-based study at the one-pore scale, which our team carried out before this project [56, 57]. First, Bergonzi reported the striking results about lateral variations of the spectral signatures of liquid water trapped in one closed micro-cavity created in quartz (synthetic fluid inclusion, SFI) [56]. The studied pore was formed synthetically in a mineral through a nature-mimicking hydrothermal process, so it was a “normal” pore apart from its closeness.

Nevertheless, all these ‘normal’ materials and methods resulted in measuring a thick interlayer all around the inclusion wherein liquid water shows a different infrared spectral profile (band shape, intensity, and peak position) than is usually known and very close to what nonlinear optical spectroscopy (2-3 nm sensitive) records when water is deposited onto hydrophobic solid boundaries. Bergonzi made an additional step forward by turning the spectroscopic signature into a thermodynamic difference, coming out with a 1 kJ/mol change over approximately 1 µm far from the solid [56, 57]. The group justified their results by considering the long-range surface energies like hydrophobic and osmotic forces and surface properties like wettability. These previous studies clearly show that the **interface scale phenomena** play a role in the **pore scale behavior**. Meanwhile, the reasoning behind this cooperative mechanism, exact components and forces, is unclear by now. However, it is interesting to note that the same research team already revealed this when employing the synchrotron-based FTIR micro-spectroscopy on (other) fluid inclusions to record the spectral signature of water under tensile state changing spectral profile as a function of the distance to boundary [58]. Identically, measurements performed by Guilhaumou et al. [59] and Nieuwoudt et al. [60] with the synchrotron radiation source recorded significant IR deformation of the OH-stretching band in their fluid inclusions.

The pore scale associates issues about the solid-liquid boundary, primarily concerned with the influence of the surface state of solid walls on water and the ability of the cavity to host capillary bridging, not under the usual prism of diphasic partition, but as a driver for pore-scale reactivity. The Young-Laplace law makes it straightforward to realize that the liquid water pressure becomes negative in absolute terms whenever the liquid is trapped in a pore smaller than 1.5 µm. Indeed, some confusion may arise conceptualizing the concept of pressure only in terms of the kinetic theory of gases, where pressure and density are directly proportional, so that vacuum means no matter at all, which puts an obvious limiting value. Yet, liquids and solids do not have this pressure-density proportionality due to the cohesion of these condensed states of matter. This is why negative pressure can occur in liquids (water tension) as in solids (tensile strength). What is, however, neglected is that a negative pore pressure provides reasons for the chemical potential to change (via the V.dP integral) and installs additional tensile stress from water on the solid matrix. Another useful remark is to state that the physical chemistry and the mechanics of one entire water body are thus modified and become capillary-controlled if capillary liquid-air interfaces take place only in one pore or along a limited number of them (remind the ink-bottle effect evoked above).

Consequently, the chemical potential gradient at the multiphasic interfaces (solid-liquid and liquid-gas) at different scales (nm to macro) must be mechanistically examined to understand how the hydro-geochemical processes are rooted at the smaller possible phenomenological scale. This must improve our upscaling conceptualization of reactive transport, combining the relevant elementary mechanisms with the proper quantification to secure through physical-chemistry laws predictive modeling capabilities.

1.3. Objectives and methodology

The primary objectives of this study are to unravel the effect of interfaces in the multiphasic condition in the geological porous media by employing synthesized pore models such as fluid inclusions (FIs) and nanofluidic chipsets. The starting hypothesis is that the reactivity along the interfaces obeys the local chemical potentials of the contacting phases, which does not restrict to the bulk properties. Regarding this concept, we aim to quantify the reactivity variation in the pore scale as a function of the distance to interfaces (interface viewpoint) or the size of the thinnest liquid-air capillary bridge (pore-scale perspective) for answering the mass transfer and fluid flow questions in subsurface porous structures. The detailed objectives are as follows:

1) Exploring and quantifying the chemical potential (reactivity) variation of phases, especially at the contact area between them. Studying the effect of temperature/pressure on the recorded signatures to determine the physical roots of the observed properties.
2) Evaluating the types of surface forces and surface features of solid walls (hydrophobicity/hydrophilicity, electrical double layer) that can play a role in a purposely interface-driven effect.
3) Comprehensive characterization of the nanopore size effect on the capillary-driven flow and kinetic of water evaporation with respect to Kelvin's law.
4) Investigating the pore-size controlled and capillary-controlled geochemistry with respect to phase transition phenomena and the metastable states occurring in the dual pore capillary systems (highly-contrasted pore size).

The deeply buried and opaque nature of geological formations precludes the direct visualization of hydro-geochemical processes in the subsurface. This leads us to laboratory experiments employing specifically synthesized materials to simulate subsurface porous structures flow and transport physics (pore-scale experiments). **First**, the water-rock (liquid-solid) interface was investigated meticulously by a vibrational micro-spectroscopy method. To do that, we followed the promising methodology (i.e., high-resolution FTIR and Raman micro-spectroscopy) applied in the previous studies by the Mercury research team [56-58]. FTIR micro-spectroscopy is a well-known tool in the study of the properties of water and its molecular connectivity through probing the dipole moments variation [61-69]. This method can monitor the variations in the properties of water in a pore or media close to solid surfaces compared to a reference state with a spatial resolution limited by the beam size [61, 70-74]. Besides the FTIR, Raman micro-spectroscopy was employed since it can offer complementary quantitative information.

To move into details, the interface-based measurements were performed similarly to the previous study [56] on a one closed cavity with constant composition, constant volume, and well-defined solid-liquid interfaces. As shown in Figure 1.3, the SFI is one closed pore (cavity) with a size commensurable to common field-type porosity, occluded in transparent (optically observable) crystals and clear-cut solid walls. Likewise, SFI was used to explore the variation of the water molecules vibrational energy as a function of the distance to the solid boundary (solid-liquid interface, yellow dash-line in Figure 1.3).

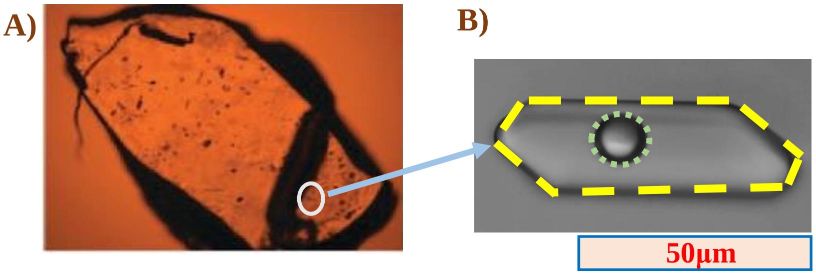

Figure 1.3. A) Quartz fragment containing the synthetic fluid inclusion. B) Micrographic image of the synthetic fluid inclusions, SFI-1, including water and a bubble of saturated water vapor. The yellow dash-line and green dot-line represent the solid-liquid and the liquid-gas interface, respectively.

To explore the particular behavior of liquid water near the interfaces, three terms will be used in this study: “normal water,” “bulk (in-pore) water,” and “interfacial water.” **Normal water** corresponds to water not located inside any closed media. **Bulk (in-pore) water** refers to the water located in a cavity, far away from any solid-liquid or liquid-gas interfaces. **Interfacial water** is defined as water within a layer along a solid boundary (solid-liquid interface) or along a water vapor boundary (liquid-gas interface).

The infrared micro-spectroscopy was harnessed as a thermodynamic probe using special micro-beams and a confocal microscope. This configuration allows a 3D IR tomography of the cavity that reveals distance-dependent vibrational energy (absorption signatures). IR micro-spectroscopy provides information on the microscopic properties of water. However, the implications in natural systems are macroscopic. As a result, it is necessary to pass from microscopic vibrational properties, which are acquired through measurements, to macroscopic properties. In this way, a partition function has been used to convert the infrared properties of water to thermodynamic ones, interpretable in natural environments [57].

Second, the water-air (liquid-gas) interface and their capillary bridges effect on the water properties were studied by nano/microfluidics devices. These devices have shown tremendous potential in solving subsurface flow and reactive transport questions in the past few decades.

They are sometimes referred to as Aquifer-on-a-Chip or Geological-Lab-on-Chip [75]. This model sample allows precise control and direct, real-time visualization of flows, reactions, and transport mechanisms from the microscale down to the nanoscale [76-81]. Meanwhile, it is worth outlining that exploiting nanofluidic chipsets remains restricted to understanding the physics/chemical conceptual schemes of functioning. In our approach, they are not intended to realize analogical models due to the discrepancies (2D topology, network structure, the composition of liquid and solids, simplicity of geometries, etc.) between the manufactured chipset and actual rock and soils.

As shown in Figure 1.4, nanofluidic chipsets are designed to control the inner flow and composition in macro-reservoirs or connected nanochannels, and allow an optical observation of phase transition in this pore model. This is intended to collect quantitative and conceptual information about pore-size controlled and capillary-controlled geochemistry in multiphasic porous media.

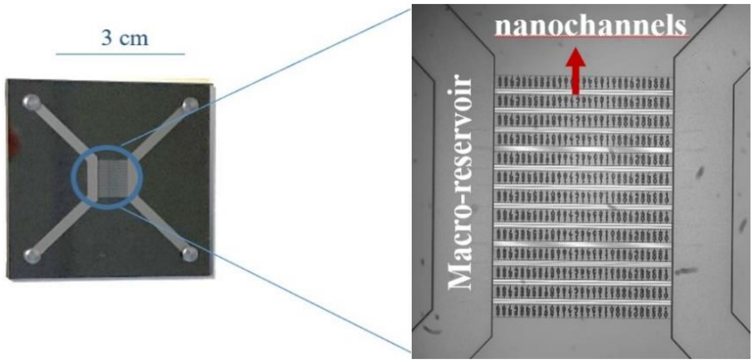

Figure 1.4. Schematic view of the nanofluidic chipset design with two macro-reservoirs connected by the series of nanochannels.

1.4. Outline

This dissertation is organized as follows:

Chapter 2 presents the research background of this study. First, the properties of water molecules and hydrogen bonds are presented. Then, the basis of vibrational spectroscopy methods (FTIR and Raman scattering) is introduced with specific attention to the water regarding their molecular connectivity. Normal modes of water are discussed by focusing on the OH stretching band. A bibliography overview of liquid-solid and liquid-gas interfaces and their respective curvature is given in the third part. Moreover, the propagation scope of the surface energies/forces and capillary effects on the water properties are discussed. Finally, the nucleation procedure in porous media is mentioned with respect to the classical and non-classical nucleation theory.

Chapter 3 is dedicated to the experimental methodology of this study regarding the interface scale (liquid-solid and liquid-air interfaces) problem. First, we introduce the samples (synthetic and natural fluid inclusions) and experimental methods (FTIR and Raman scattering). Since the FTIR micro-spectroscopy is the main technique used in this study, special attention will be paid to the characterization of micro-beam employed by different infrared setups (IR sources, detectors, microscopes, and their optical arrangement) to conduct the high-resolution FTIR measurements down to the diffraction limit. Finally, the procedure for converting the FTIR spectral signature to the thermodynamic properties is presented.

Chapter 4 will present the experimental results of water properties occluded in varied fluid inclusions (FIs) as a function of the distance to the solid boundary (liquid-solid interface) and water vapor boundary (liquid-gas interface). The post-treatment methods are detailed, interference fringe removal and Mie-scattering correction, for correcting the possible optical aberration issues that may create artificial deformations. Four different experimental setups were also tested with respect to their ability/efficiency for recording the interfacial signature of water. The core of this chapter relates to presenting all the acquired datasets as a function of the distances to the solid-liquid interface (in the three directions) and evaluating the effect of temperature, polarization of the incident radiation, fluid composition, and nature of the solid mineral host on it. The liquid-air interface is also briefly studied, that required to fix a quantitative way how correcting the strong Mie effect visible along that boundary.

Chapter 5 is devoted to developing the consequences of our IR-based findings regarding water-hydrophobe behavior and illustrating which type of reactivity variation can be expected from the FTIR features. In this chapter, we will investigate the macroscopic consequence of the IR-based micrometric properties in the geochemical reactivity. In this way, we provide an overview of how the reactivity of in-pore water changes by approaching the solid boundary with respect to the long-range forces field emanating from the solid surface.

Chapter 6 turns to the liquid-gas interface of a multiphasic hydrosystem, acting as a capillary bridge with a cooperative effect on the pore scale geochemistry. Drainage-imbibition processes, by which we started these experiments, already revealed important specificities of the capillary-driven flow, including the evaporation kinetics of a reservoir through nanochannels and the occurrence of water boiling (cavitation) at RT and far from any evaporating surface. This metastability-based process is important because it not only causes a specific phase transition (bubbling at a distance from capillary bridges) but is also responsible for a brutal change in the thermodynamic status of the liquid water and, therefore, its solvent properties.

Finally, chapter 7 will summarize the results of this thesis and conclude. Some perspectives and technical improvements in understanding and managing liquid-solid and liquid-gas interfaces will be finally proposed.

2. Research background

In this chapter, the research background of this study is introduced in four different sections. First, the general properties of water molecules are described with a focus on H-bond network. The basis of vibrational spectroscopy methods (FTIR and Raman), powerful tools for studying water behavior, is presented in the second part. Then, the characteristic features of different interfaces: solid-liquid, liquid-vapor, and solid-liquid-vapor are shown, and the effect of interfacial and surface energies is pronounced. Last but not least, the classical and non-classical nucleation theory is presented in order to clarify the crystallization processes in the porous media.

2.1. General properties of water molecules

2.1.1. Structure of water molecule

Water is a non-linear molecule consisting of one oxygen atom bonded to two hydrogen atoms (Figure 2.1A). Because of the higher electronegativity of the oxygen than the hydrogen atoms, the bonds are polar covalent (polar bonds called O-H vibrators). As a result, the oxygen atom acquires a partial negative charge (δ−), while each hydrogen atom acquires a partial positive charge (δ+) (Figure 2.1B). The molecule adopts a bent (V-shaped) structure because oxygen atom has two lone pairs of electrons.

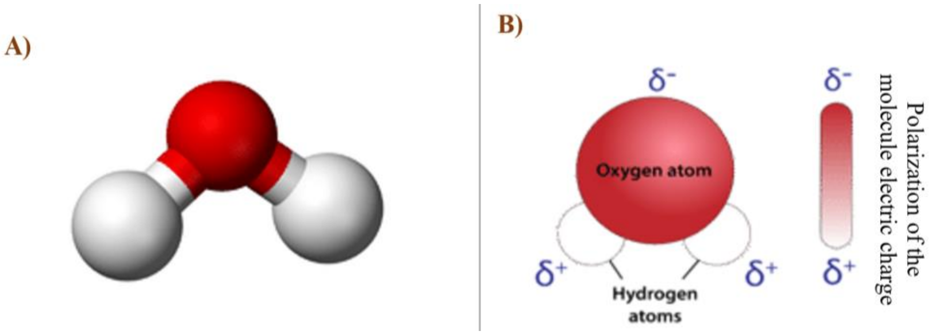

Figure 2.1. A) Visualized water molecule structure: ball-and-stick model. B) Water as a polar molecule with high electron density around the more electronegative oxygen atom.

2.1.2. Covalent bond vs. Hydrogen bond

Figure 2.2 shows two types of chemical bonds in liquid water: covalent and hydrogen bonds. The **covalent bond** is one of the chemical bonds formed when two valence electrons of two atoms are put in common, such as O – H bonding in water molecules. While the **hydrogen bond** is established between a hydrogen atom attached to a very electronegative atom like O. The hydrogen atoms in one water molecule are attracted to the non-bonding electron pairs of the oxygen atom on an adjacent water molecule (shown in Figure 2.2). Hydrogen bonds are strongly attracted to the lone-pair electrons on a nearby oxygen atom and are stronger than conventional dipole-dipole forces [82, 83].

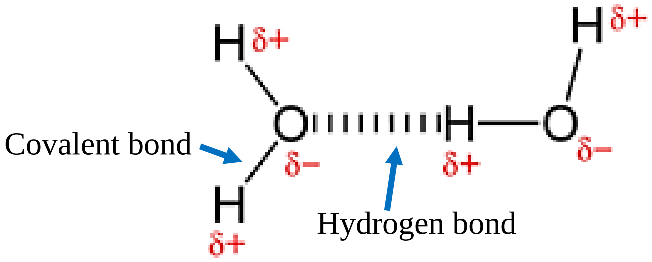

Figure 2.2. Two types of chemical bonds in the water molecule: covalent and Hydrogen bonds. The latter is an attraction between a lone pair of electrons on the oxygen atom of one molecule and the hydrogen atom of a nearby molecule.

Water's unique and anomalous properties due to hydrogen bonding and its complex structure have been discussed in several reviews [84, 85]. Establishing a hydrogen bond with another water molecule forms a dimer. The creation of the hydrogen bond brings the two molecules closer together. The distance between the donor hydrogen atom and the acceptor oxygen atom becomes 0.20 nm [86]. This distance is less than the sum of the van der Waals radii of the two atoms (0.26 nm). Also, the energy of the hydrogen bond between two water molecules is approximately 20 kJ.mol^{-1} [69].

The hydrogen bond is directional and imposes orientation constraints on the water molecules by aligning with the axis of the valence bond with which it is associated. In liquid water, when the three O – H ⋯ O atoms are aligned, the strength of the H bond is optimal. The directional character of the hydrogen bond limits to 4 number of neighboring molecules to which a water molecule can bind. Nevertheless, due to its low mass, the hydrogen atom is very mobile and can deviate from the O – O axis by rotation of the water molecule. Small deviations from linearity (about 20%) have little effect on hydrogen bonding [87].

Like in ice, each molecule in liquid water can establish up to four hydrogen bonds with its nearest adjacent molecules. This is because each oxygen atom has two lone pairs, which lead it to create hydrogen bonds with the hydrogen atoms of two other separate molecules. Figure 2.3 shows an approximately tetrahedral geometry (high connectivity) around each oxygen atom, consisting of two covalent and two hydrogen bonds.

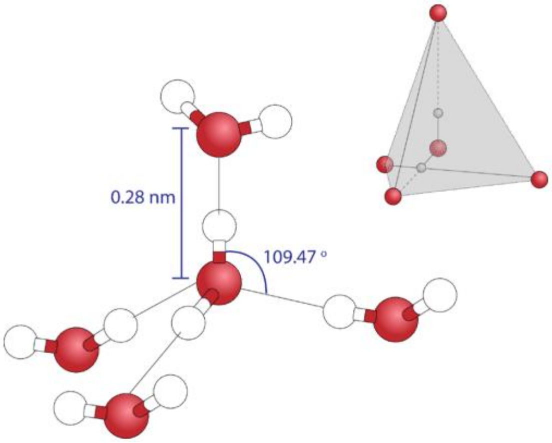

Figure 2.3. As a result of two covalent bonds and two hydrogen bonds, the geometry around each oxygen atom is approximately tetrahedral.

The average connectivity number of a water molecule (the number of hydrogen bonds per water molecule) is equal to 3.4 ± 0.1 at 25°C, according to the numerical [88-90] and experimental studies [91, 92]. The value of 3.8 is also reported for the average coordination number of H-bonds [93]. Then, liquid water can be considered a network of molecules randomly linked by H bonds. However, some parameters, such as ions activity in the solutions, temperature, pressure, and approaching the solid surface, might affect the H-bonding among the water molecules through their structure-making (kosmotropic) or structure-breaking (chaotropic) effect [94]. In the destructuring condition, like near specific solid-liquid interfaces, the OH groups without any hydrogen bond, called “free” or dangling OH groups, can be found. These free OH or dangling OH groups are similar to a free water molecule in the vapor state except for being hydrogen bonded to two other water molecules. This mode will be shown and discussed in section 2.3.2.

2.1.3. Dipole moment and polarizability

Even though the total charge of a water molecule is zero, the positive and negative charges do not completely overlap. The bent shape of the water molecule makes it polar with a strong dipole moment. The dipole moment, μ, for a molecule is a function of the magnitude of the atomic charges (e_i) and their positions (r_i).

$$\mu = \sum e_i r_i \qquad (2.1)$$

The asymmetry of the water molecule leads to a dipole moment in the symmetry plane pointed toward the more positive hydrogen atoms. The dipole moment is a vector quantity, and its value for the water is about 1.855 D [90]. The dipole moment of water is at the origin of its interaction with electromagnetic radiations; infrared spectroscopy is particularly sensitive to the dipole moment of the water molecule.

Apart from the permanent dipole moment, an external electric field can be at the origin of the so-called induced (or temporary) dipole moment. When water molecules are placed in an electric field ($\vec{E}$), they undergo deformation, and their electrons tend to move in the direction of the electric field and its nuclei in the opposite direction. As a consequence of this deformation, there is an induced dipole moment $\vec{p}$, which can be expressed in the following way:

$$\vec{p} = [\alpha]\vec{E} \qquad (2.2)$$

where $[\alpha]$ is the polarizability tensor:

$$\begin{bmatrix} p_x \\ p_y \\ p_z \end{bmatrix} = \begin{bmatrix} \alpha_{xx} & \alpha_{xy} & \alpha_{xz} \\ \alpha_{yx} & \alpha_{yy} & \alpha_{yz} \\ \alpha_{zx} & \alpha_{zy} & \alpha_{zz} \end{bmatrix} \begin{bmatrix} E_x \\ E_y \\ E_z \end{bmatrix} \qquad (2.3)$$

$\vec{p}$ is called polarization, and the magnitude of the induced dipole moment relates to the polarizability of the molecular species. At the molecular level, the polarizability varies according to the orientation of the field ($\vec{E}$) with respect to the molecular axis. Raman spectroscopy is particularly sensitive to the polarizability of the water molecule. It is worth noting that the water molecule polarizability is weak, around 1.68×10^{-24} cm^3 [95].

2.2. Vibrational spectroscopy

High-resolution vibrational micro-spectroscopy is particularly well suited to investigate the properties of water. FTIR and Raman spectroscopy provide characteristic fundamental vibrations employed for molecular structure identification. These two techniques are complementary. With respect to the center of molecular symmetry, some vibrations can be exclusively active in IR or Raman spectroscopy, or as in the case of water molecules, active in both techniques. The mutual exclusion rule is related to the distinct physical phenomena and, consequently, different selection rules that govern these two techniques.

Infrared and Raman spectroscopy result from the interaction of electromagnetic radiation with molecular vibrations but differ in the manner in which photon energy is transferred to the molecule by changing its vibrational state (Figure 2.4). According to the quantum theory, the energy exchanges between the molecule and radiation can be described by the following equation:

$$\Delta E = h\omega \qquad (2.4)$$

Where ΔE: energy change between upper state and lower state of energy, h: Planck constant, and ω: wavenumber unit (cm^{-1}). Molecular motion (vibrations) can have only discrete energy states, unique to a given molecule. Energy state change is accompanied by the gain or loss of one (in the case of FTIR) or two (Raman) quanta of energy.

Infrared spectroscopy (Figure 2.4) is based on the one-photon absorption process. MIR radiation (from a polychromatic source such as Globar or synchrotron) is absorbed in discrete wavenumbers called the "fingerprint region" of the chemical bond. After absorption of a photon, a molecule undergoes a transition from a ground state of vibrational energy to an excited vibrational state. The IR absorption is a resonance condition involving the electric dipole (μ) transition between vibrational energy levels [96-98]. The vibration will be IR active if the changes of dipole moment are not null during the molecular vibrations.

$$\left(\frac{\delta\mu}{\delta Q}\right)_0 \neq 0 \qquad (2.5)$$

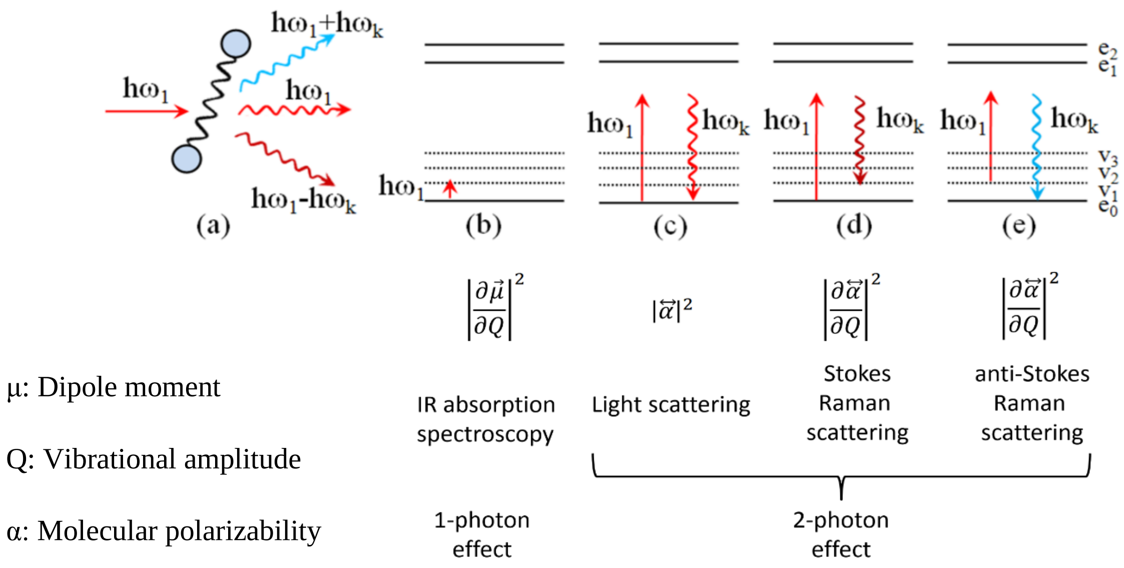

Figure 2.4. Basis of FTIR and Raman spectroscopy. a) matter-radiation interaction: photon interacting with a molecule. b) one photon IR absorption process. Two-photon light scattering: c) elastic Rayleigh scattering, d) Raman inelastic light-scattering, Stokes process, and e) Raman inelastic light-scattering, anti-Stokes process.

Raman spectroscopy (Figure 2.4) is a two-photon inelastic light-scattering phenomenon. Herein, the interaction between radiation (monochromatic source as a laser) and a molecule is an off-resonance condition involving the induced dipole moment. It occurs due to molecular polarizability (α), where polarizability is the deformation of the electron cloud around the molecule by an external electric field. In order to be Raman active, the molecular vibration must cause a change of polarizability during vibrations.

$$\left(\frac{\delta\alpha}{\delta Q}\right) \neq 0 \qquad (2.6)$$

As shown in Figure 2.4, the Raman scattering is always accompanied by the most probable elastic process, Rayleigh scattering (Figure 2.4c), where no energy is lost or gained [99]. There are two types of Raman scattering processes: Stokes (Figure 2.4d) and anti-Stokes (Figure 2.4e). In the case of Stokes process, the excited molecules relax back to a vibrationally excited state; hence the emitted photons have smaller energy than the exciting ones (Stokes lines, $h\ (\omega_1 - \omega_k)$). The reverse situation is also possible; molecules, which were originally in a vibrationally excited state, can after excitation, relax to the ground state emitting photons of higher energy than the exciting ones (anti-Stokes lines, $h\,(\omega_1 + \omega_k)$). Raman anti-Stokes is less probable at room temperature as most molecules are in the ground state [100-102].

In conclusion, the FTIR and Raman spectra can provide crucial information on molecular structure, dynamics, and environment [62, 103-105]. The vibrational bands are characterized by their peak position (wavenumber, cm^{-1}), spectral profile (band shape), and intensity. The wavenumber of these molecular vibrations depends on the masses of the atoms, their geometric arrangement, and the strength of their chemical bonds. Since the vibrational energy levels are unique for each molecule, the analysis of the bands provides a unique characterization of a particular molecule.

Finally, it is worth stressing that due to the strong dipole moment and very weak molecular polarizability, the IR technique is more sensitive to studying the water behavior than the Raman scattering method. In the next section, we will focus on the FTIR spectrum of water.

2.2.1. Vibrational spectroscopy of water

2.2.1.1. The FTIR spectrum of normal water at room temperature

Figure 2.5 shows the FTIR spectrum of normal water. The far-infrared region of the FTIR water spectrum shows a very broad band called libration (hindered-rotation), extending from 200 cm^{-1} to 1000 cm^{-1}, where it overlaps with the connectivity band (c.a. 200 cm^{-1}). Indeed, the connectivity band corresponds to the stretching vibration between two molecules linked by a hydrogen bond and shows a translational character. While the libration band illustrates the rotational movements of water molecules with respect to the neighboring water molecules. These two bands, called intermolecular bands, are governed by a force constant of hydrogen bonds among the molecules. The integrated intensity of the libration band indicates a greater amplitude of this mode. It clarifies that band broadening relates to weakening the force constant, not losing the order. The large amplitudes of the rapid libration give rise to the fluidity of liquid water and limit the rotational correlation between the intermolecular interaction of each H_2O molecule to its adjacent H_2O neighbors [69].

To deal with the complexity of the vibrational motion in polyatomic molecules, we need to utilize the spatial degree of freedom, which means an independent direction of motion leading to a change in the distance between atoms or the angle between bonds. For a polyatomic molecule of

N atoms, 3N-5 coordinate numbers are required to describe the vibrational movements of a linear molecule. In the case of a non-linear water molecule, 3 normal modes are expected (3N − 6 normal modes, where N is the number of atoms).

There are three normal modes of water molecular vibrations, namely one bending and two stretching modes. Two stretching modes, described as a continuous modification of interatomic distance between oxygen and hydrogen, are symmetric stretching (υ_1) and asymmetric stretching mode (υ_3), centered around 3250 and 3450 cm^{-1}, respectively. The bending mode (υ_2), changing an angle between two OH bonds, is centered around 1600 cm^{-1}. These modes are known as intramolecular bands in the water molecule modes since they correspond to the vibrational movements of individual molecules.

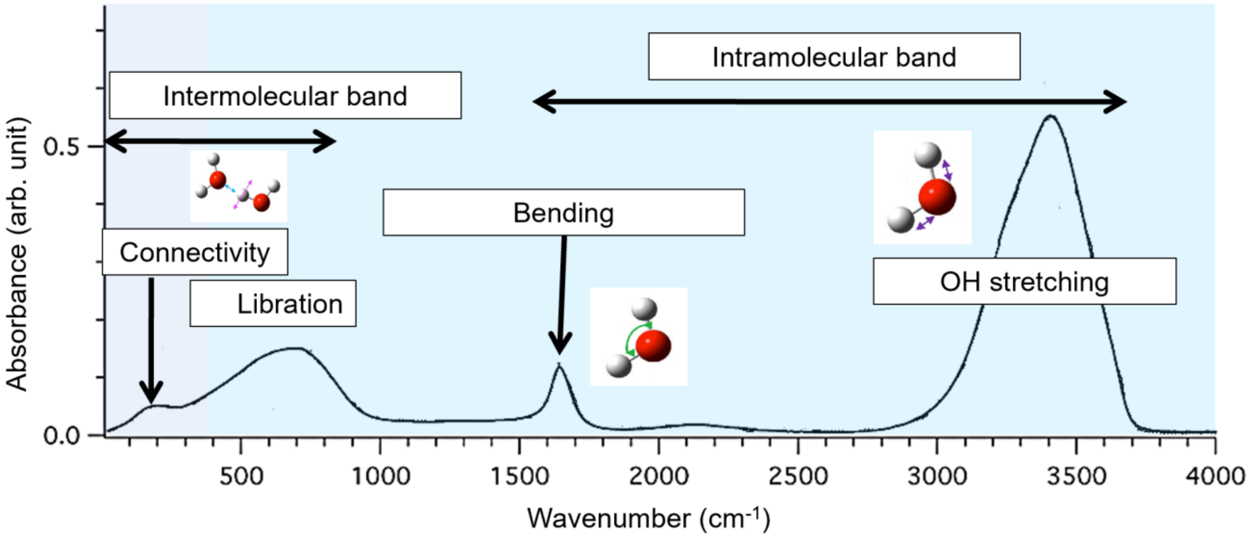

Figure 2.5. The FTIR spectrum of normal water, including connectivity, libration, bending, and stretching bands [57].

2.2.1.2. Thermal effect on the FTIR spectra of normal water

Figure 2.6 shows the libration, connectivity, bending, and stretching bands variation of normal water at different temperatures, from -10 to 90°C [57]. Bergonzi et al. declared no significant displacement of the bands with the temperature, except for the OH stretching band, where the peak position shifted toward the higher wavenumber (blue-shifted behavior), and its integrated area decreased. This observation illustrates the importance of the OH stretching band for investigating water behavior.

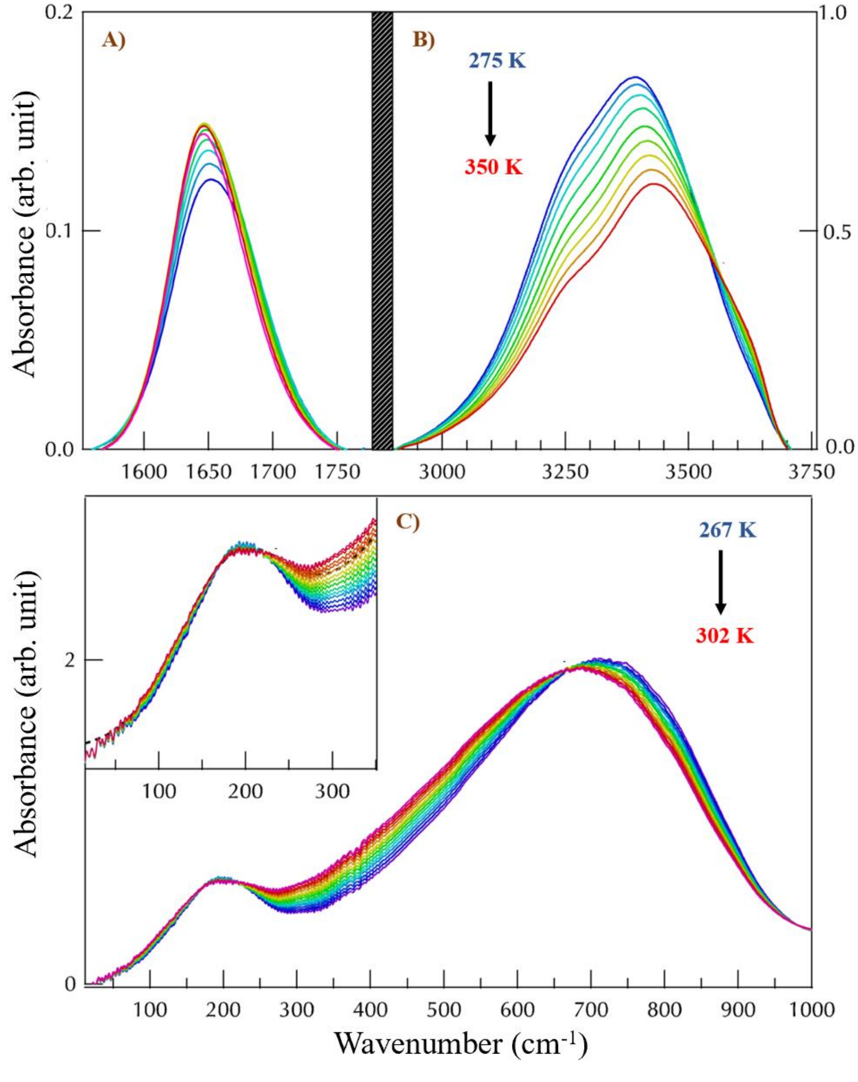

Figure 2.6. IR absorption of A) bending, B) OH stretching, and C) libration and connectivity bands of liquid water as a function of temperature [57].

2.2.1.3. Properties of OH stretching band (intramolecular band)

The OH stretching spectral region (from 3000 to 3800 cm^{-1}) is the most “useful” part of the water spectrum. This is because the OH stretching band is very sensitive to the molecular environment and represents the hydrogen bonds and molecular network connectivity [106]. Moreover, a detailed analysis of the ice and liquid water FTIR spectra led Marechal to conclude that this band is predominantly modulated by libration, which makes the OH stretching band a powerful tool to prospect how the H_2O molecule behaves with temperature [69]. Also, this spectral range is crucial for the objectives of this dissertation (Chapter 1) since it provides a possibility for studying other types of liquid water, such as confined water on a nanometric scale, water located near the solid-liquid interface, or water containing different ionic components [71, 107, 108].

Rundle and Parasol, and Nakamoto et al. have linked the wavenumber of vibration of the stretching mode to the distance between the two oxygen atoms of the O-H...O bond [109, 110]. As a result, they attributed an average length of the hydrogen bond to each vibrational wavenumber. Nakamoto et al. have demonstrated that the higher the vibration wavenumber, the greater the length of the bond [110], and Mikenda have proposed a specific exponential relation between the vibration wavenumber and the hydrogen bond length [111]. According to Mikenda’s equation and the data obtained with the X-ray and neutron methods, they attributed the main sub-band frequency of the stretching band (3400 cm^{-1}) to the $R_{O\text{-}O}$ equal to 2.85 Å.

2.2.1.4. Decomposition of OH stretching band

As summarized in a recent review [112], water and OH groups have been studied extensively by vibrational spectroscopy, but different interpretations of the FTIR water spectrum exist [113-116]. By combining in situ FTIR spectroscopy with multivariate data analysis, the spectral profile of water (band shape and intensity), which change with an electrochemical environment, could be extracted [117, 118]. In general, the OH stretch band can be assigned to the average number of H-bonding in the local environment of the molecules. From these considerations, it is common to describe the stretching band by several Gaussian components; each attributed to molecules having a given coordination number [71, 103-105, 107, 119, 120].

As shown in Figure 2.7, the OH stretching band is generally decomposed into three Gaussian sub-bands [103, 107]. The Gaussian centered around 3250 cm^{-1}, the so-called network water (NW), is attributed to molecules having a four coordination number and a locally tetrahedral structure since this component is close to the wavenumber of ice. The intermediate wavenumber Gaussian (c.a. 3450 cm^{-1}), intermediate water (IW), represents the molecules in the non-tetrahedral environment with a coordination number close to 3. Finally, the high-wavenumber Gaussian component (between 3650 and 3750 cm^{-1}), multimer water (MW), is attributed to less-connected water molecules with a coordination number from 2 to 0.

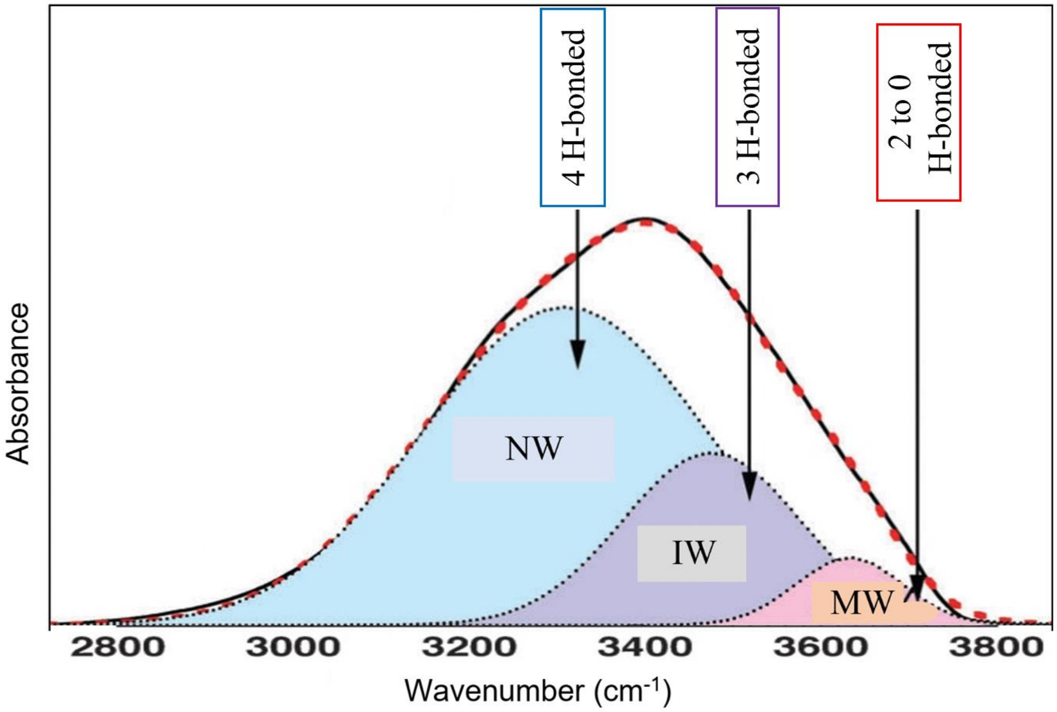

Figure 2.7. Three Gaussian sub-bands of OH stretching band, namely network water (NW, well-connected molecules with 4 H-bonds), intermediate water (IW, close to 3 H-bonded molecules), and multimer water (MW, less-connected molecules from two to zero H-bonds) [107].

2.3. Interfaces and curvature

The physical research domain can be roughly categorized into macroscopic phases, such as solids, liquids, and gases. When a liquid and a vapor phase coexist, each phase is described by a set of properties, such as pressure and density, and there is a region between these phases with a density that varies as a function of location. This region can be conceptualized as a two-dimensional mathematical entity separating the two phases — an interface — characterized by a surface area (but without thickness or volume) and a characteristic property called interfacial tension, a specific pressure tension that develops at the surface of separation between phases. Around two centuries ago, the significance of interfacial tension became apparent through the work of scientists such as Thomas Young [121], Agnes Pockels [122], and Josiah Willard Gibbs [123]. The importance of interfacial tension has grown, particularly in light of 1) emerging technologies that rely on, or are governed by, interfacial forces and 2) increased awareness of natural processes that are also dictated by interfacial tension.

2.3.1. Two-phase interface

One specific topic of interest within interfacial science is the effect of a curved interface on the behavior and properties of the phases which it separates. In many natural and industrial environments, the interface between two phases is flat; therefore, the pressure in one phase equals the pressure in the other. However, the pressure in each phase is no longer equal when a curved interface is present— such as for a bubble of vapor or a droplet of liquid. As described by the Young–Laplace equation, the difference in pressures is proportional to the interfacial tension and inversely proportional to the radius of curvature (i.e., the radius of a spherical bubble) as shown in the following equation:

$$P^L - P^V = \sigma_{LV}\left(\frac{1}{r_1}+\frac{1}{r_2}\right) \qquad (2.7)$$

Where P^L → the pressure in the liquid phase, P^V → the pressure in the vapor phase, σ_{LV} → surface tension between liquid water and water vapor in the air, and r_1 and r_2 → the two principal radii of curvature. In this equation, the radii of curvature are defined as positive when they are in the liquid (e.g., for a droplet).

The Laplace expression is: $\Delta P = \left(\frac{1}{r_1} + \frac{1}{r}\right)$, r_1 and r_2 are the two main radii of curvature of the curved meniscus. For a hemispheric meniscus, $r_1 = r_2$. A **cylindrical capillary** displays, in general, two different main radii of curvature so that $r' = r_1 + r_2$, and $\boldsymbol{\Delta P = \sigma_{LV}/r'}$. In a **slit formed** by plane-parallel solids, $r_1 = r$ and $r_2 \approx \infty$ (parallel to the slit axis), so that: $\boldsymbol{\Delta P = \sigma_{LV}/r}$.

For a pure liquid in equilibrium with its vapor, the Kelvin equation describes how a spherical vapor-liquid interface alters the vapor phase pressure [124]; Gibbs later corrected it to the following thermodynamically consistent form for a spherical interface via the equality of chemical potential in each phase combined with the Young–Laplace equation [123, 125]:

$$\frac{2\sigma_{LV}}{r} = \frac{RT}{v^L}\ln\left(\frac{P^V}{P^{sat}}\right) \text{ or } \Delta P = \frac{RT}{v^L}\ln\left(\frac{P^V}{P^{sat}}\right) \qquad (2.8)$$

where R: is gas constant, T: is temperature, v^L: is the molar volume of water ($1.805 \times 10^{-5}\ m^3/mol$), P^V is the pressure in the vapor phase for a given interfacial radius of curvature (r), and P^{sat} is the saturated vapor pressure for a flat interface. The Kelvin equation is valid when the vapor phase can be treated as an ideal gas, and the liquid phase is incompressible. This equation is written in the case of a drop of liquid in a bulk vapor phase (convex curvature), the radius is a positive value, and thus the vapor pressure is greater than the vapor pressure in equilibrium with a flat interface. In contrast, for a capillary bridge (concave curvature), the radius of curvature is negative, which means that the vapor pressure is lower than the flat-interface vapor pressure.

Besides the liquid-vapor (infinite elastic interface), interfacial phenomena at solid-liquid interfaces play important roles in various natural and industrial processes. At the microscopic level, it is well established that solids and liquids influence their respective structural and chemical properties. In many conditions and environments, ions and some specific functional groups are present at the interface and thus play critical roles in introducing perturbations to the near solid-water interface. Indeed, they are an essential component of physical chemistry solutions and the geochemical environment. Once at the interface, ions may bind to the solid surface, localize in the topmost adsorbed layer, or diffuse within the interface and up to the bulk water.

In this study, the leading scientific objective is to investigate the behavior of interfacial water. We call "interfacial" water because it is located within a layer along a solid boundary (solid-liquid interface) or along a water vapor boundary (liquid-gas interface) [56, 126]. When liquid water is in contact with the boundary, water molecules can interact with it. These interactions can influence the ability of water molecules to establish a network of hydrogen bonds [127-132]. The physical properties of interfacial water thus differ from bulk water. Experimental measurements and the two comprehensive reviews by Henderson [41] and Thiel and Madey [133] show that the number of molecular layers, which undergo disturbances of its properties via its network of hydrogen bonds, is 2-3 layers (≈1 nm) [42, 134-138].

Indeed, the variation in interfacial water properties depends on the chemistry of the solid surface with which the water is in contact (i.e., the interaction between fluids and solids is affected by interfacial curvature). For instance, an important question arises: will a liquid spread out on and completely wet a solid (well-connected surface), or will it adopt a spherical shape and not wet the surface (non-connected surface)? The wetting behavior of a liquid on a certain solid phase is characterized by a contact angle measured through the liquid at the location where the liquid interface touches the solid. A contact angle of 0° corresponds to a perfectly wetting liquid (hydrophilic), whereas a contact angle of 180° attributes to a perfectly non-wetting liquid for that solid (hydrophobic). Wettability is a matter of affinity. It means that in hydrophilic surfaces, an object attracts water molecules more strongly than they attract each other, and a surface can form strong hydrogen bonds with neighboring water molecules at the top first layer of a solid. On the contrary, we are dealing with the non-binding surface in hydrophobic surfaces, where the solid surface makes the solvent adopt a configuration, allowing it to “coexist” with this surface.

Vibrational spectroscopy methods are a powerful tool for probing the orientation, local environment (regarding molecular connectivity), and intermolecular strength of hydrogen bonds of water molecules at the interface. Among these techniques, there is a surface-specified method called sum-frequency generation vibrational spectroscopy (SFG-VS), which has been widely used for its ability to probe interfacial water molecular networking via its vibrational states. The comparison of the spectra acquired by this technique for the normal water and at the water near the different interfaces (solid, liquid, and gas) is presented in Figure 2.8 [139-142]. Figure 2.8A shows the spectrum of normal water, while Figure 2.8B&D represent the water spectrum near the air interface. As shown, we are dealing with two different spectral profiles (band shape, intensity, and peak position) in a way that the normal water (Figure 2.8A) does not have any peaks c.a. 3700 cm^{-1}, corresponding to the dangling OH mode, while the spectrum of the water-air interface (Figure 2.8B&D) shows a distinct peak at this wavenumber.

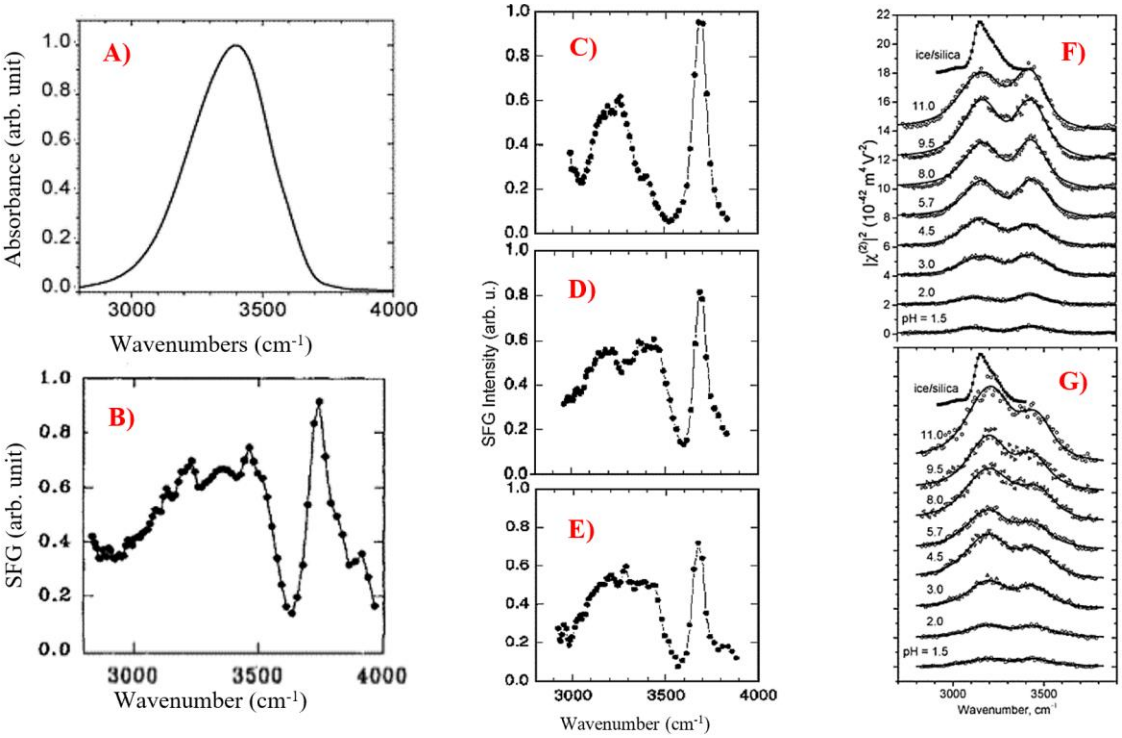

Figure 2.8. A) Sum-frequency generation (SFG) spectrum of normal water. B) SFG spectra of water at the interface with air [142]. SFG spectra of water near a hydrophobic interface C) Water/OTS, D) Water/vapor, and E) Water/hexane [141, 142]. SFG spectra of water at the interface with F) the (0001) plane of α-quartz and G) an amorphous silica surface as a function of pH [142].

Du et al. recorded the spectrum of water in contact with a silica surface covered with a monolayer of octadecyl trichlorosilane (OTS) by SFG measurements (Figure 2.8C) [141]. They observed the appearance of peak c.a. 3700 cm^{-1}. This peak in the water spectrum was observed as a result of the hydrophobic surface (OTS), revealing that water molecules do not form hydrogen bonds with OTS (dangling OH mode). However, there are still weak van der Waals interactions between free-OH and the CH_3 end groups of OTS, causing the peak shift. Furthermore, the spectrum also shows the two peaks at 3250 cm^{-1} and 3450 cm^{-1}. The peak at 3250 cm^{-1} is more significant than in the case of the water/air interface (Figure 2.8B&D). Shen and Ostroverkhov proposed that, unlike the water/air interface, the OTS silica surface is a rigid wall, forcing the interfacial water molecules to form a more ordered hydrogen bond network [142]. In the same way of hydrophobic solid surface, Du et al. observed the dangling OH mode of water molecules near the water-hexane interface (Figure 2.8E).

Moreover, Du et al. recorded the spectra of water in contact with a silica surface at different bulk pH values [140]. As shown in Figure 2.8F&G, the spectra do not display any peaks c.a. 3700 cm^{-1}. As can be seen in Figure 2.8G, the intensity of peak c.a. 3250 cm^{-1} rises more noticeably with pH, implying a more polar-ordered network near the quartz surface. In general, silica can form either a hydrophilic or hydrophobic surface with respect to the ratio of siloxane bridge ($Si - O - Si$) to silanol groups ($Si - O - H$). If the quartz surface is hydrophilic, it can establish hydrogen bonds with neighboring water molecules, leading to the elimination of free OH mode (no peak c.a. 3700 cm^{-1}, more intense peak c.a. 3250 cm^{-1}). In this way, SFG measurements have been performed on other hydrophilic surfaces [41, 142-145]. These studies revealed the presence of two peaks at 3250 cm^{-1} and 3450 cm^{-1} in the case of hydrophilic surface, generalizing the conclusions that the water network is locally ordered close to a hydrophilic solid surface. On the contrary, in the case of water near to hydrophobic surface (water-air, water-OTS layer, and water-hexane interfaces) additional peak centered between 3650 and 3750 cm^{-1}, attributed to free OH groups, was observed (Figure 2.8B-E) [41, 143, 146].

All the results presented above have shown that a solid surface causes a change in the hydrogen bond network of water. The surface vibrational spectroscopic method (like SFG) underlines that the molecular network of water can be ordered or disordered at the interface with a solid surface depending on the wettability (hydrophobic or hydrophilic).

2.3.2. Multiphasic situation inside the pore (solid-liquid-vapor)

While the previous sections discussed a two-phase interface (liquid-vapor and solid-liquid), we focus on the multiphasic system (three-phases: solid-liquid-vapor) in this section. As mentioned above, the wetting behavior of a liquid on a certain solid phase is characterized by a contact angle (θ) measured through the liquid at the location where the liquid-vapor interface interacts with the solid. When the solid surface is physically smooth and chemically homogeneous, and the liquid is in the shape of a spherical cap (in the absence of any external forces, including gravity), the contact angle is defined by the Young equation: $\cos\theta = \frac{\sigma^{SV} - \sigma^{SL}}{\sigma^{LV}}$ (2.9) where θ is the contact angle, and σ is the interfacial tension of the solid-vapor (SV), solid-liquid (SL), or liquid-vapor (LV) interfaces.

Equation 2.9 has been derived by balancing mechanical forces [121], minimizing free energy under a constraint of constant liquid volume [147], and maximizing entropy subject to physical and geometric constraints using Gibbsian composite-system thermodynamics [148]. Each approach concludes with this equation being the condition for mechanical equilibrium.

Generally, the chemical and physical properties of each phase influence the resultant contact angle, and by manipulating these properties, desired contact angles can be attained. Introducing roughness to the solid substrate is a common method of controlling wetting behavior. By doing so, the liquid may either rest on top of the rough surface with trapped pockets of air or completely fill the surface with no air entrapment. The level of roughness can be tuned to achieve the preferred state of wetting and the corresponding contact angle. Besides the wettability, the surface energies emanating from the solid surface play a significant role in the multiphasic situation.

2.3.2.1. Surface energy

Surface stress is generally defined as a reversible work per area to stretch a solid surface elastically, while liquid surface tension, which is often confused with surface free energy, is the reversible work per unit area to create a surface [149, 150]. Besides these two terms, the stability of a surface is described by its surface energy (γ), a measure of the excess energy of surface atoms due to various factors, such as the broken bonds yielding undercoordinated atoms. This fundamental quantity is important in understanding the surface structure, reconstruction, roughness, and crystal equilibrium shape [151]. For example, the Wulff shape is often the equilibrium or growth shape of the crystal and can be an essential contributor to determining the material physical properties [152]. According to Wulff's theorem: “The minimum surface energy for a given volume of a polyhedron will be achieved if the distances of its faces from one given point are proportional to their surface tension.”

Before introducing the surface forces, the capillarity state will be explained. Capillary pressure has been introduced as the leading parameter of the thermodynamic properties of in-pore water [153-155]. Indeed, capillarity is intrinsically a tensile phenomenon, wherein decreasing internal pressure allows water to ascend against gravity (capillary ascent, as for tree sap) and remain suspended, although surrendered by air (pendular water in fine porous aggregates of soils). The Young-Laplace equation can be written (in the different form as equation 2.7) as the relation between the radius of a depleted hemispheric water-air meniscus and as a function of the decreasing internal pressure of water:

$$\Delta P = \frac{2\sigma_{LV}}{r} cos\theta \qquad (2.10)$$

where, ΔP = $P^L - P^V$; σ_{LV} → the surface tension between capillary liquid water and water vapor in air; θ → the apparent (macroscopic) contact angle between the meniscus and the walls of the dry pore; r is the pore radius. The Radius of the meniscus (conventionally negative for capillary meniscus) is obtained by: $r_{menisc} = r_{pore}/cos\theta$. It seems that pores must have a specific size to support a capillary meniscus under a given tension: the Young-Laplace equation gives a mechanical condition to capillarity.

Indeed, the energy required to deplete the meniscus (i.e., the energy necessary to decrease the water pressure) is provided by water-vapor equilibrium: as long as the atmosphere contains saturated water vapor, no capillarity is possible; in the presence of an under-saturated atmosphere, water can either evaporate (Young-Laplace condition not satisfied) or be in the “capillarity” state (presence of suitably-sized capillary). Kelvin's equation quantifies the evaporation/capillarity condition (same as equation 2.8):

$$\frac{RT}{v^L} \ln\left(\frac{P^V}{P^{sat}}\right) = \frac{2\sigma_{LV}}{r} \cos\theta \qquad (2.11)$$

For the cylindrical tubes or the slit:

$$\frac{RT}{v^L} \ln\left(\frac{P^V}{P^{sat}}\right) = \frac{\sigma_{LV}}{r} \cos\theta \qquad (2.12)$$

Taking into account the change of water volume as a function of capillary pressure, equation (2.11) becomes:

$$RT \ln\left(\frac{P^V}{P^{sat}}\right) = \int_1^{P_{capwat}} v^L dp \qquad (2.13)$$

where P_{capwat} stands for the internal pressure of liquid water under a depleted meniscus.

As water pressure decreases, the equilibrium saturation of the atmosphere decreases, and the pore size is required to confine the capillary meniscus. At a relative humidity of 90% ($RH = \frac{P^V}{Psat} \times 100$), water confined in 10.2 nm cylindrical pores undergoes a tension of –143 bars (as shown in Table 2.1) [155]. However, in such a thin pore, the proximity of the solid walls must be considered based on a correct assessment of the **role of surface forces** on in-pore water properties. Churaev et al. declared that in 10 nm hydrophilic pores, 35% of the in-pore water is influenced by surface forces [156]. Surface forces are defined as the electric field and molecular forces in the transition zone between two phases, decreasing with distance into each contiguous phase.

Table 2.1. Physical chemistry of capillary and droplet water at 25°C [155].

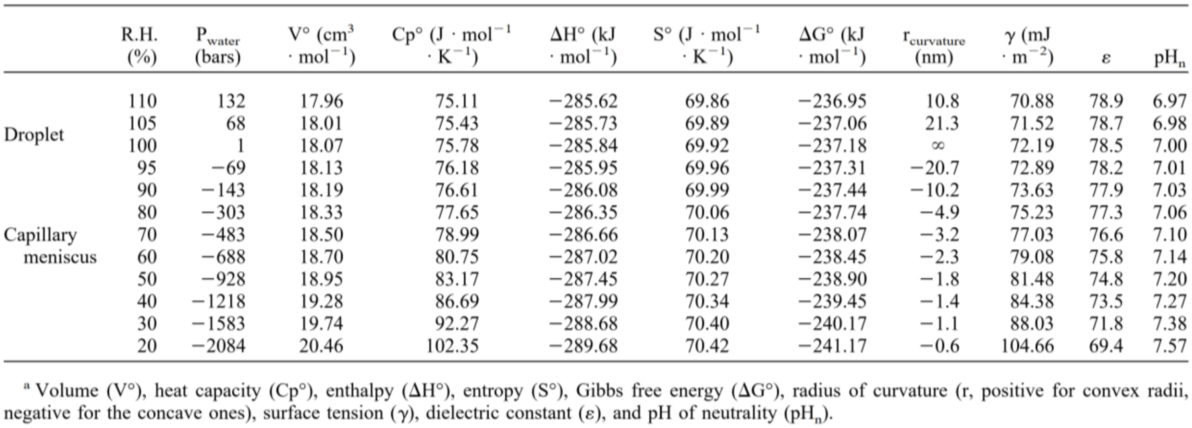

	R.H. (%)	P_{water} (bars)	V° ($cm^3 \cdot mol^{-1}$)	Cp° ($J \cdot mol^{-1} \cdot K^{-1}$)	ΔH° ($kJ \cdot mol^{-1}$)	S° ($J \cdot mol^{-1} \cdot K^{-1}$)	ΔG° ($kJ \cdot mol^{-1}$)	$r_{curvature}$ (nm)	γ ($mJ \cdot m^{-2}$)	ε	pH_n
Droplet	110	132	17.96	75.11	−285.62	69.86	−236.95	10.8	70.88	78.9	6.97
	105	68	18.01	75.43	−285.73	69.89	−237.06	21.3	71.52	78.7	6.98
	100	1	18.07	75.78	−285.84	69.92	−237.18	∞	72.19	78.5	7.00
Capillary meniscus	95	−69	18.13	76.18	−285.95	69.96	−237.31	−20.7	72.89	78.2	7.01
	90	−143	18.19	76.61	−286.08	69.99	−237.44	−10.2	73.63	77.9	7.03
	80	−303	18.33	77.65	−286.35	70.06	−237.74	−4.9	75.23	77.3	7.06
	70	−483	18.50	78.99	−286.66	70.13	−238.07	−3.2	77.03	76.6	7.10
	60	−688	18.70	80.75	−287.02	70.20	−238.45	−2.3	79.08	75.8	7.14
	50	−928	18.95	83.17	−287.45	70.27	−238.90	−1.8	81.48	74.8	7.20
	40	−1218	19.28	86.69	−287.99	70.34	−239.45	−1.4	84.38	73.5	7.27
	30	−1583	19.74	92.27	−288.68	70.40	−240.17	−1.1	88.03	71.8	7.38
	20	−2084	20.46	102.35	−289.68	70.42	−241.17	−0.6	104.66	69.4	7.57

[a] Volume (V°), heat capacity (Cp°), enthalpy (ΔH°), entropy (S°), Gibbs free energy (ΔG°), radius of curvature (r, positive for convex radii, negative for the concave ones), surface tension (γ), dielectric constant (ε), and pH of neutrality (pH_n).

Gibbs theory of capillarity is expressed by the interface excess properties. Despite the undefined localization of the geometrical boundary surface, this approach appeared very convenient and fruitful as long as the interlayer (at least part of it) retains the intensive properties of the bulk phase. This configuration gives rise to a first kind of surface forces, including (1) van der Waals molecular forces (range ≤ 10 nm) and (2) electric forces acting on ions near the interface (Figure 2.9). The latter is often described using electrical double layer (EDL) theories, with a dense angstrom-range domain, depending on the charge of the solid surface, and a diffuse part extending farther (> 50 nm, up to 1 µm for very dilute solutions) depending on the ionic concentration in the neighborhood of the interface. These forces are responsible for the magnitude of the interfacial tension and the potential jump from bulk to the interfacial domain. They are pronounced when the system loses its thermodynamic equilibrium in the electrokinetic phenomena (e.g., streaming potential or electro-osmotic effects).

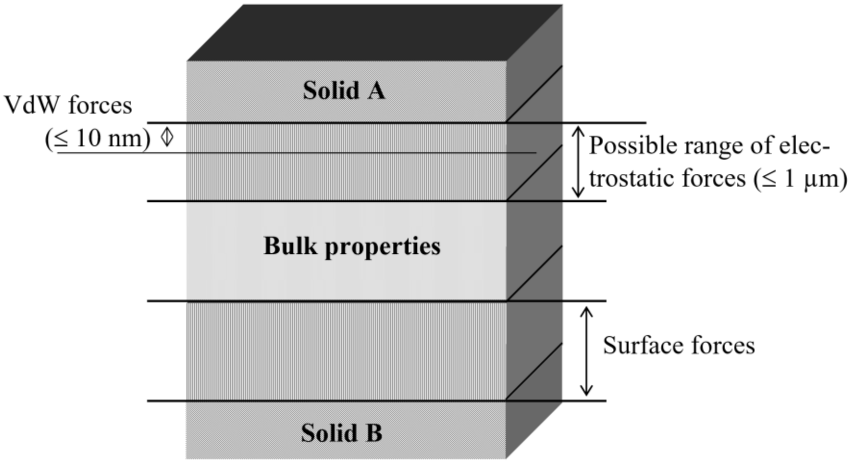

Figure 2.9. Thin Gibbs layer: wetting films on solids interlayered by bulk phase (vertical distances are neither proportional nor realistic).

A second class of long-range surface forces arises when two interfacial regions overlap. Up to the overlapping, decreasing the interfacial thickness only requires overcoming viscous and other passive forces. When the two fields overlap, the interlayer thickness can be changed only by doing positive (negative) work to overcome the repulsive (attractive) force appearing in the overlapping domain. Generally, overlapping occurs when interlayer space is less than the long-range action of surface forces, which is about 100 nm to 1 μm, depending on the nature of pore walls and the composition of the solution [157, 158]. It must be noted that such forces operate whatever the nature of the fluid phase exists in the interlayer, vacuum, gas, or liquid. Likewise, the pressure in the thin interlayer differs from the pressure in the bulk phase by the value of the disjoining pressure (Π).

2.3.2.2. Disjoining pressure

When two solid particles, which may have different natures, are separated by a distance (h) in a fluid phase (Figure 2.10), the chemical potential at point 1 differs from point 2 because of the overlapping of interfacial fields. As a consequence, particles should tend to join ($\mu_1 > \mu_2$, phase (c) moves from 1 to 2) or disjoin ($\mu_1 < \mu_2$, phase c moves from 2 to 1). Applying a pressure (positive or negative) on the particles is required to prevent phase c from moving and maintain the system in equilibrium with a separating distance (h). The sign of this pressure can be positive or negative, depending on the tendency of surface forces to increase or reduce the thickness of the interfacial layer. Van der Waals forces between two bodies are always attractive in a vacuum, whatever the fluid filling between two identical bodies. Then, the force can be attractive or repulsive between two bodies separated by fluid [159]. The attractive (repulsive) action of surface forces between two particles implies that a positive (negative) pressure must be exerted on the solids to prevent them from joining. This additional pressure is called “disjoining pressure.”

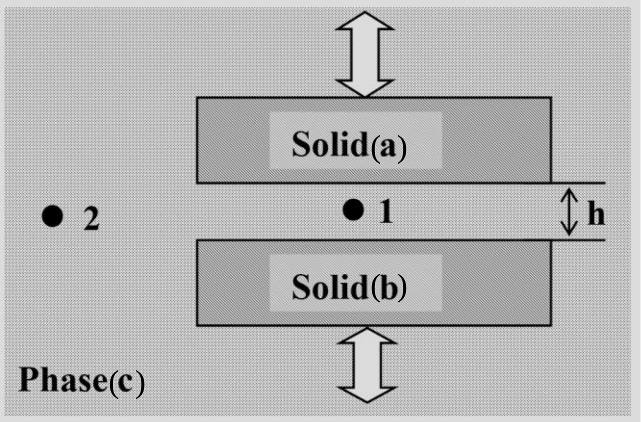

Figure 2.10. Two solid particles, (a) and (b), are maintained at a specific distance (h) from each other in a fluid phase (c) by compression (solid tending to disperse) or tension (solid tending to collapse) [160].

Thus, disjoining pressure measures the excess pressure within the interfacial layer required to maintain the two particles at a certain distance (h), owing to the additional fields relative to the total pressure in the adjacent bulk phase. When surface forces are repulsive, this film pressure is a tension; when they are attractive, film pressure is compressive on the facing solids. In other words, disjoining pressure measures either the excess pressure exerted by the surface forces from solids to film or the tension within the film required to maintain the particle at a certain distance (h) despite the overlap of the two interfacial fields. In this sense, the disjoining pressure can be written as the following pressure difference [157]:

$$\Pi = P_{EXT} - P_{Film} = P_1 - P_0 \qquad (2.14)$$

where Π: disjoining pressure, P_{EXT}: pressure transmitted to the thin layer from the adjoining solids, P_{Film}: pressure within the film, P_1: pressure on the interfacial layer surface; $P_1 = P_{EXT}$, and P_0: pressure in the bulk phase from which the interlayer extends; $P_0 = P_{Film}$. If the film is not in contact with the bulk phase, then P_0 should be interpreted as the pressure which the bulk would exert when being in equilibrium with the film [161].

Disjoining pressure results from the action of surface and electromagnetic forces. It divides into different parts. Three major components are included in disjoining pressure for polar solvents at the contact of pore walls, such as molecular $\Pi_m(h)$, structural $\Pi_s(h)$, and electrostatic $\Pi_e(h)$ part. The molecular component is related to the attracting forces (DLVO theory, which combines the effects of the van der Waals attraction and the electrostatic repulsion due to the electrical double layer (EDL)) acting between macroscopic condensed bodies. It is the only component that is always present and is much more important over film thickness lower than 50 nm. It accounts for the molecular attraction between solids through the inter-film gap under the action of dispersion forces [162-164].

The structural component (Π_s) is attributed to a structural rebuilding within the boundary layers overlapping zone [158, 165, 166]. Π_s is a non-DLVO component controlled by long-range surface forces such as van der Waals, dipole, quadrupole forces, and hydrogen bonds for water [158]. Nevertheless, the radius of action of these forces strongly depends on the wettability of the substrate (hydrophilic/phobic properties). Pashley and Kitchener demonstrated that on a hydrophobic surface, the characteristic range of these forces might reach several hundreds of nanometers [167]. One possible explanation of this effect is that boundary water layers formed at hydrophobic surfaces have a structure different from that at hydrophilic ones. Also, the role of hygroscopic surface groups, such as sodium chloride, calcium chloride, calcium oxide, etc., appears to be determinant by guiding an ordered layering of bound water molecules around charged surface groups [168] or more generally around surface-active sites, which is sites able to form hydrogen bonds with water molecules [158].

The electrostatic component (Π_e) arises from the overlapping of diffuse ionic layers. Electrostatic forces in colloids with identical particle surface potentials (ψ_1) are repulsive, increasing colloidal system stability. In wetting films, a solid substrate potential (ψ_1) differs from the liquid-air interface potential (ψ_2) in value and sometimes even in sign: they represent a non-symmetrical case. At ψ_1 ψ_2 negative, electrostatic forces are attractively stabilizing the wetting film. At positive ψ_1 ψ_2 condition, the forces are attractive for $h < h^0$, with $h^0 = (1/\kappa) \times \ln(\psi_1/\psi_2)$ [169, 170], where $1/\kappa$ (Debye radius) measures the thickness of the diffuse layer. The critical film thickness h^0 corresponds to the change in the sign of electrostatic forces. For instance, at $\psi_1/\psi_2 = 2$, h^0 is equal to about 60 nm for very dilute electrolyte solutions (< 10 μmol). For more concentrated solutions, h^0 may reduce to 1 nm (≈ 0.4 nm in seawater) [171]. As noted, the thickness of wetting films cannot be justified without considering the role of structural forces (structural component of disjoining pressure (i.e., wettability of the substrate)). DLVO components compensate each other at low Π, but the molecular component tends to predominate over the electrostatic one with increasing Π. Figure 2.11 shows the total disjoining pressure acting in a flat slit-shaped pore with 100 nm height, where the structural component is always dominated.

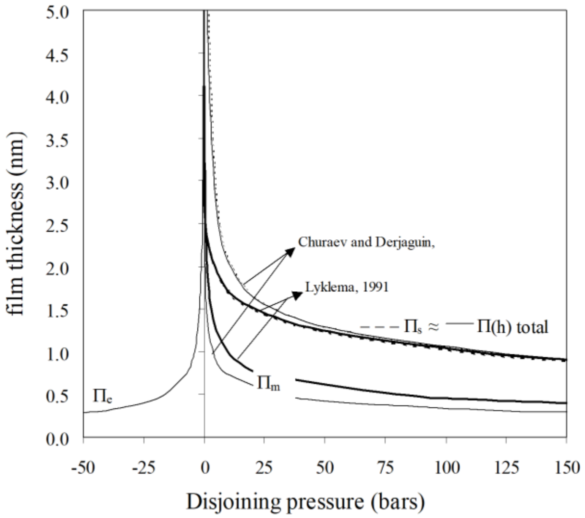

Figure 2.11. Disjoining pressure components (molecular Π_m, structural Π_s, electrostatic Π_e) as a function of film thickness in a 100 nm slit-shaped pore. Dotted and continuous lines highlight the difference between structural component (dotted line) and total (solid line) disjoining pressure [172].

2.4. Classical and non-classical nucleation theory

After mentioning the different interfaces and interfacial energies, we will discuss the nucleation procedure, which has gained attention in different science domains, from organic/inorganic matters to mineral crystallization. Nucleation corresponds to forming a new thermodynamic phase from an old phase with high free energy to an organized structure/pattern with low free energy [173]. The nucleation concept has general applicability in various phase transition systems, including crystallization, melting, cavitation, boiling, condensation, etc. [174-177]. To understand the nucleation mechanism, fundamental theories explain the nucleation pathways from the perspective of classical nucleation theory (CNT). Nowadays, different modified approaches for the CNT, such as density functional and diffuse interface theory, have been suggested to reach a more precise definition. However, the CNT, which was once considered to have general applicability to all nucleating systems, gradually gives way to a non-classical pathway. The non-classical approach is now a dominating mechanism in solution crystallization.

As mentioned, CNT is the most common theoretical model for understanding the nucleation of a new thermodynamic phase, such as a liquid or solid. It is an approximate theory that gives a reasonable prediction of nucleation rates. It is based on the condensation of vapor to a liquid which can be extended to other liquid–solid equilibrium systems, such as crystallization from melts and solutions. The change in the free energy of the system during homogeneous nucleation of a spherical nucleus of radius r is given by:

$$\Delta G = -\frac{4\pi r^3}{3\nu} KT \ln S + 4\pi r^2 \sigma \qquad (2.15)$$

where the first term represents the contribution made to ΔG by bulk free energy, $\frac{4\pi r^3}{3\nu}$ represents the number of molecules in a cluster of radius r with the volume of a single molecule as ν, $S = P/P^*$ is the vapor supersaturation ratio, and σ is the surface energy of the interface between the drop and the surrounding vapor. For the nucleus larger than r, the first term dominates, leading to the decrease in ΔG since it represents the energy decrease upon transition from vapor to liquid. When r is less, the second term dominates, describing the creation of a new surface leading to the increase in ΔG. Thus, the two terms in equation 2.15 depend differently on r, so the free energy (ΔG) of formation passes through a maximum = r_c, where r_c is the radius of a critical nucleus at which the probability of a nucleus formation goes through a minimum (Figure 2.12).

Differentiating this equation with respect to r for finding the r_c gives $r_c = 2\sigma / KT \ ln \ S$, and the barrier to nucleation is given by the equation:

$$\Delta G^* = \frac{16\pi\sigma^3 v^2}{3K^2T^2 \ln S^2} \qquad (2.16)$$

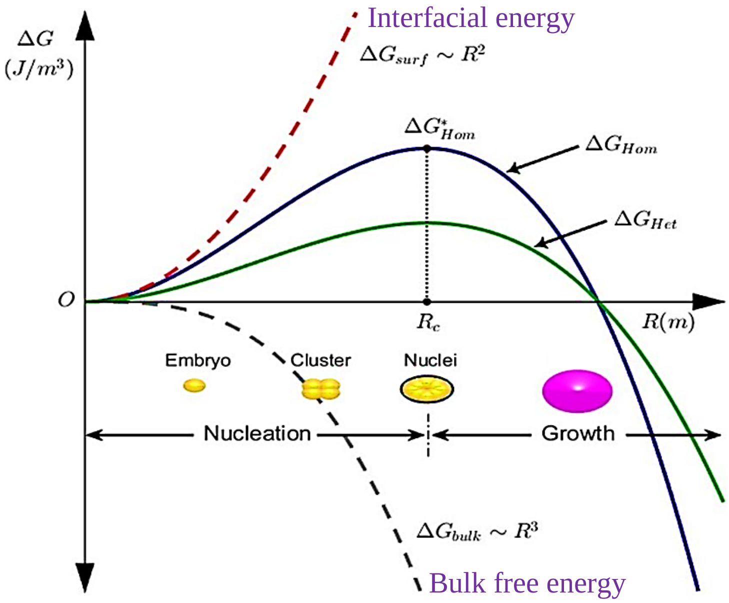

*Figure 2.12. the schematic representation of the dependence of nucleation barrier ΔG*on the radius (r)According to classical nucleation theory, [173].*

The critical nucleus is in metastable equilibrium with the vapor, and adding molecules decreases the free energy. The nucleation rate, J (number of nuclei per unit volume and per unit time), can be expressed in the form of the Arrhenius reaction velocity equation:

$$J = A \exp\left[-\frac{\Delta G^*}{KT}\right] \qquad (2.17)$$

where A is determined from kinetic considerations, K is the Boltzmann constant, and T is the temperature. Substituting the critical nucleation barrier ΔG^* at a given supersaturation in equation 2.17 gives the final expression for nucleation rate (J):

$$J = A \exp\left[-\frac{16\pi\sigma^3 v^2}{3K^3T^3(\ln S)^2}\right] \qquad (2.18)$$

Equation 2.18 generally is written differently in the geoscience papers [178]:

$$J = \Gamma \exp\left[-\frac{\delta\sigma^3 Y^2}{K^3 T^3 (\ln S)^2}\right] \qquad (2.19)$$

where δ is a shape-related factor, σ is the fluid–mineral interfacial energy of the nucleus, Y is the volume of a growth unit in the nucleus, and S is the supersaturation (more simply defined as the ratio of concentration in the solution to the concentration at equilibrium). The pre-exponential factor Γ is related to the rate at which the nucleus can grow to a supercritical size, and hence it involves the diffusion of growth units to the surface of the nucleus. Equation 2.19 shows that the value of the nucleation rate is a very sharp function of supersaturation value (Ω). Also, salts with a significant surface energy (σ) (and hence low solubility) and large molar volume (Y) require a higher value of supersaturation for nucleation to become measurable.

Figure 2.13 shows the shape of the nucleation rate as a function of a critical supersaturation (Ω_{crit}), at which nucleation becomes spontaneous. Equation 2.19 has been written with the assumption that the supersaturation value is constant, and the system reaches this value instantaneously. This equation takes no account of how the supersaturation is reached. In other words, it does not consider gradients in supersaturation either in space or time. However, the actual value of the supersaturation achieved in any given system depends on the rate of change of supersaturation [178, 179].

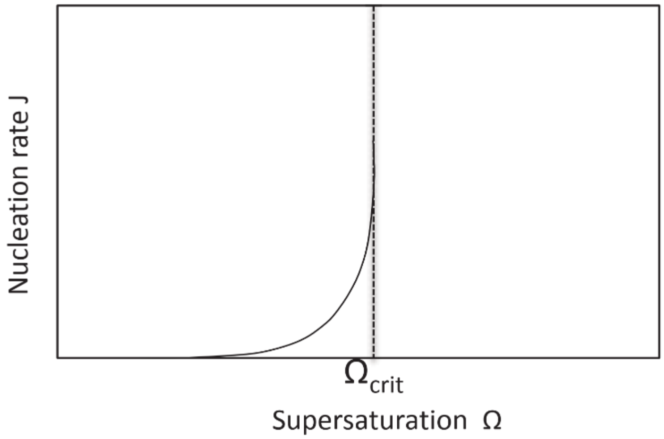

Figure 2.13. The nucleation rate as a function of the supersaturation value, showing a critical supersaturation value for nucleation [178].

Some of the simplifying assumptions of CNT are listed here: 1) the nucleus can be described with the same macroscopic properties (density, structure, composition) of the stable phase, 2) the nucleus is spherical, and the interface between the nucleus and the solution has a sharp boundary, and 3) vapor-liquid interface is approximated as planar, regardless of critical cluster size. The latter is known as a capillary approximation and may be reasonable for large clusters, but the surface is highly curved for small clusters, and the approximation leads to significant discrepancies [173, 180]. The assumption of spherical shape is also not valid as in the case of solution like NaCl producing cubic-shaped nucleus.

CNT reasonably estimates critical supersaturations and nucleation rates for some systems, such as water. Also, it can capture the underlying physics of the phenomena and provide a reasonable qualitative interpretation of nucleation data. However, reaching an accurate quantitative description in CNT for various systems is almost impossible. Another shortcoming of the theory is that it is unable to explain the vanishing nucleation barrier at high supersaturations. Despite different extensions and developments in theoretical approaches, CNT still serves as a platform to start more sophisticated models to capture the complexity of molecular-level procedures accompanying nucleation.

One of the successful modifications of CNT is the extended modified liquid drop (EMLD) model proposed by Reguera et al., which does not need any information on intermolecular potential like other molecular theories and accurately describes the properties of very small confined systems [181]. In the subsequent work, an alternate model for the nucleation based on EMLD and dynamic nucleation theory (DNT) was proposed, which incorporates the fluctuations relevant for small systems and is able to predict the spinodal. They suggested a new definition for a cluster based on the cluster volume that minimizes the pressure within the container [182].

Density functional theory (DFT) is another popular approach to studying the vapor−liquid equilibria based on microscopic molecular interaction, which avoids the capillary approximations of CNT. The DFT, sometimes referred to as non-classical theory, is a powerful tool to analyze various vapor−liquid, liquid−solid nucleation phenomena and can also predict the spinodal. DFT was initially developed by Oxtoby, Evans, and Zeng, approached the problem based on a density functional approach that expresses the system's intrinsic free energy as the function of molecular number density [183-186]. The theory assumes that the free energy of the nucleus (same as ΔG^*) depends on the average spherical density profile rather than the radius. The density of a new phase at the center of the nucleus is not the same as that in the bulk of a new phase (Figure 2.14). They located the saddle point in the functional space. It is the point at which the growth of a new phase is favored when the cluster reaches the critical density profile $\rho_c(r)$.

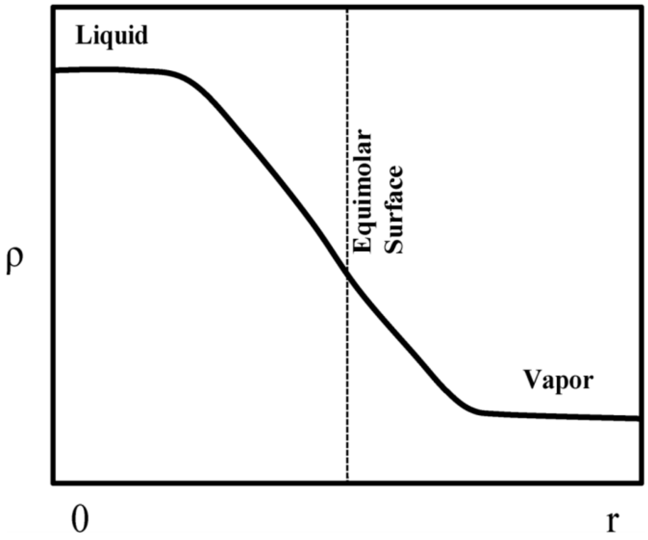

Figure 2.14. The density profile ρ(r) of the nucleus of the vapor−liquid system changing from liquid-like at the center to the bulk vapor density far from it [173].

The predictions of CNT show an error of several orders of magnitude for the experimental vapor condensation data due to the assumption that the thickness of the interface is small compared to the size of the nuclei. The phenomenological diffuse interface theory (DIT) tries to improve the droplet model by considering the interface between solid−liquid, and liquid−vapor systems, which extends to several molecular layers in contrast to the assumption of a sharp interface of the classical droplet model [187]. The DIT considers a strongly curvature-dependent surface tension related to a characteristic interface thickness. The model takes into account the bulk solid and liquid values of enthalpy and entropy within the interface region.

All the above theories have limited success since the evolutionary stages leading to the critical nucleus are not captured adequately in the treatment. CNT assumes that the clustering and reorganization to the new phase occur simultaneously, and density is the single-order parameter that differentiates old and new phases. But the growing experimental evidence of nucleation events in crystallizing solutions has shown that forming a cluster with a higher density and its structural reorganization to form a crystal requires at least two order parameters, namely density and structure, to differentiate old and new phases. This has led to the evolution of the concept of a non-classical two-step pathway nucleation.

Recent experiments have revealed that the nucleation process in solution crystallization proceeds through intermediate stages before reaching a thermodynamically stable phase. Complex materials like proteins, colloids, minerals, and polymeric solutions show that this behavior can be interpreted in terms of the rule of stages. Oswald's rule of stages states that in transforming from an unstable or metastable system to a stable one, the system does not go directly to the most stable conformation but prefers to reach intermediate stages having the closest free energy to the initial state [188]. According to Stranski and Totomonow, the phase that emerges is the one that separates from the parent phase by the smallest free energy barrier [189]. The occurrence of metastable intermediates was initially proposed for protein crystallization [190, 191].

In a non-classical approach, the nucleation is considered to proceed in two steps. Two-step mechanism has been observed in the colloidal model system [192-194], metastable phases in the glass system [195, 196], biomimetic mineralization [197-199], salt solution [200], open framework materials [201-204], and solid-solid phase transition [205]. The two-step mechanism assumes that the first step of nucleation is the formation of droplets of dense liquid called clusters/precursor phases/prenucleation clusters (PNCs) due to the critical density fluctuation or phase separation followed by the second step, which is the appearance of crystal nucleus due to structural ordering of molecules [190, 206, 207]. For example, calcium carbonate ($CaCO_3$) mineralization is studied extensively, and the prenucleation stage of amorphous calcium carbonate (ACC) before $CaCO_3$ mineralization has been seen in the literature [208-211].

The progress of two-step mechanisms can be tracked by following the typical trend in the overall kinetics of the system, which reaches a maximum when the intermediate quantity is maximum, after which a plateau develops due to the consumption of intermediates for growth [212]. Indeed, the non-classical pathway is favored when the sum of the energy barriers in two-step nucleation is less than the single energy barrier of CNT.

3. Experimental methodology

This chapter is devoted to the experimental approach and methodology used to study the interfacial behavior of water. First, the samples (fluid inclusions) will be carefully introduced. The second part deals with the vibrational spectroscopy methods, focusing mainly on FTIR micro-spectroscopy. Finally, the partitioning function used to convert the FTIR results to the thermodynamic properties will be detailed.

3.1. Samples

3.1.1. Fluid inclusions

As we already presented in chapter 1, fluid inclusions (FIs), natural (NFI) or synthetic (SFI), are closed micro-cavities occluding liquid-vapor assemblage present inside a crystal (i.e., typically quartz, calcite, fluorite, barite). These microsystems contain a liquid (water or solution) with constant composition and constant total volume [213-216]. In natural systems, this fluid circulates when the rock is formed or fractured. Despite their small size (usually less than 20 μm), the chemical composition and physical properties of NFI can be readily determined, and the data may be used to estimate the temperatures, pressures, and physicochemical nature of the fluid at the time of trapping in geological systems [213-216]. Fluid inclusions are also used to study water metastability, particularly superheating metastability [58, 216-218]. Synthetic fluid inclusions can be considered as an analogy of the natural water-rock interactions in porous media at the one-pore scale without any complexity of the natural porous media, such as varying size, shape, composition, tortuosity, etc.

3.1.1.1. Synthetic fluid inclusions (SFIs)

Synthetic fluid inclusions used in this study were produced in a solid quartz crystal by hydrothermal synthesis process in the framework of collaboration with the Institute of experimental mineralogy (Russia) [56, 218, 219]. The quartz was chosen as a hosting mineral since it is poorly twinned, poorly soluble in saline solutions, and transparent in a wide range of electromagnetic radiation. As we will show further, transparency is a crucial property for micro-FTIR measurements performed in the transmission mode.

The occluded liquid in the SFIs shown in Figure 3.1 was initially pure water, certainly "contaminated" during the hydrothermal synthesis (41 days at 610 MPa and 458°C) with silicic acid, and some cations naturally present in the crystalline quartz put in the capsules. As the quartz solubility under hydrothermal conditions largely exceeds the room's ones, a quartz reprecipitation onto the cavity walls during and after the cooling/depressurizing process is expected. This situation promotes both smooth inner walls and an equilibrium shape of the inclusion, and a fluid composition at the RT solubility level in the inclusion (10^{-4} mol/kgw). Consequently, the SFIs located in quartz fragments containing liquid water (**not pure water** but a dilute aqueous solution (~ 100 μM) of silicic acid) were employed as the main samples of this study.

As shown in Figure 3.1, there are three different phases in each fluid inclusion: solid quartz, liquid water, and gas bubble of saturated water vapor (the spheres inside the inclusions are the vapor bubbles). These SFIs are closed pores with constant composition and well-defined solid-liquid and liquid-gas interfaces. Several criteria, such as the thickness, geometry, and bubble position, are considered in the choice of fluid inclusions to be studied. The position of the vapor bubble during the measurement plays a crucial role. The bubble should remain stationary during the acquisition of the spectra. Indeed, the bubble of certain inclusions might follow the IR/laser beam, which masks the desirable spectral feature within the fluid inclusion because the beam constantly probes the same phase (i.e., vapor bubble). The geometry of inclusion is the last item, in which we have selected inclusions with different shapes and dimensions (morphology) to investigate the spectral feature dependency on the pore size/shape.

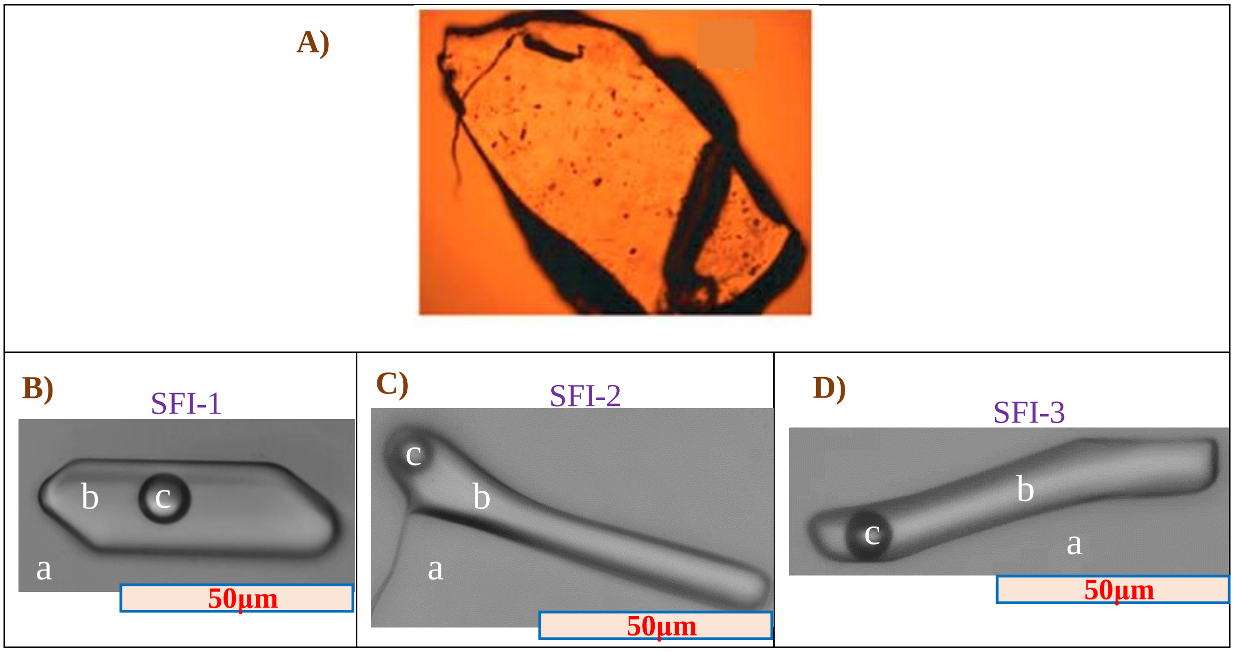

Figure 3.1. Micrographic images of A) the quartz fragment bearing different synthetic fluid inclusions: B) SFI-1, the reference sample of this study, C) SFI-2, and D) SFI-3. Each SFI includes three distinct phases: a) solid (quartz), b) liquid (water), and c) gas (bubble of saturated water vapor).

Among the employed SFIs (Figure 3.1), we chose the **SFI-1** as the **reference SFI**. Its transparency, dimension, and well-established geometry allowed us to precisely align the infrared beam and record spatially resolved vibrational features (absorption signature of water and quartz). As mentioned above, the SFI-1 does not contain pure water but a liquid with silicic acid and other impurities initially present in the quartz matrix and dissolved with time. In this study, we were particularly interested in the solid-liquid (dash line) and liquid-gas (dot line) interfaces (Figure 3.2). The length, width, and depth of the SFI-1 are 60, 20, and 5 µm, respectively. The diameter of the bubble is equal to 10 µm, and its depth is 5 µm. X-ray tomography measurements (ESRF, ID 21) with sub-micron accuracy confirm the planar shape of the fluid inclusion and its dimension (Figure 3.2B) [56].

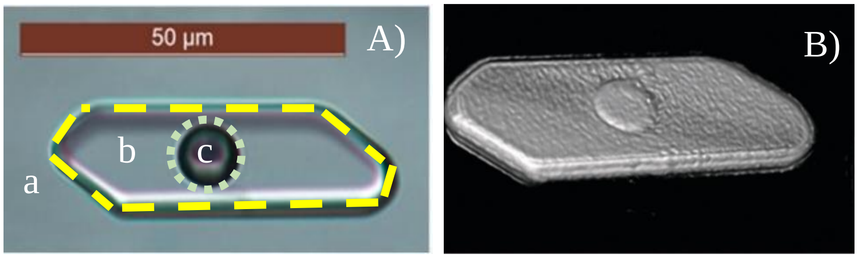

Figure 3.2. A) Micrographic image of the ***reference synthetic fluid inclusion (SFI-1)****. The yellow dashed line shows the solid-liquid interface and the green dot line shows the gas-liquid one. B) X-ray tomography image at 0.5 µm spatial resolution (ID21 beamline, ESRF; [56]).*

In order to investigate the effect of fluid composition on the interfacial properties, besides the SFIs composed of liquid water (Figure 3.1), the series of SFIs with saline solution have also been investigated. Figure 3.3 shows several SFIs located inside the quartz fragment containing NaOH solution with different concentrations: 0.5, 1, and 2 M. The SFI-4 and SFI-5 contain only a liquid phase, while SFI-6 includes a vapor bubble as well.

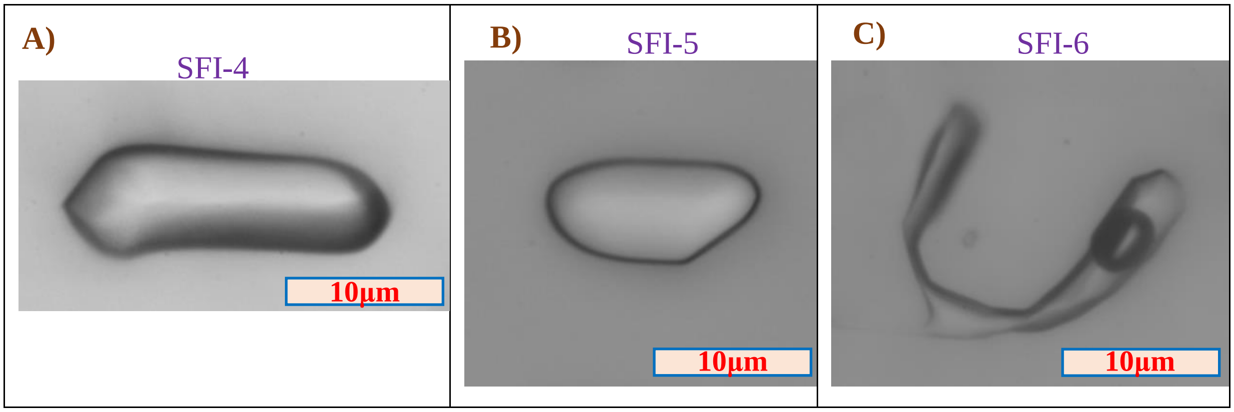

Figure 3.3. Micrographic images of SFIs located in the quartz fragment and including NaOH solution with the following concentrations: A) 0.5 M (SFI-4), B) 1 M (SFI-5), and C) 2M (SFI-6).

3.1.1.2. Natural fluid inclusions (NFIs)

Natural fluid inclusions (NFIs) were employed in this study to investigate the effect of the solid surface of a hosting mineral "container" property on water behavior. Alexander Tarantola, associated professor in University of Lorraine, sent us adequate number of calcite and fluorite fragments, where several natural fluid inclusions were located inside them (Figure 3.4). As shown in Figure 3.4, there are three phases in all chosen natural fluid inclusions: solid ($CaCO_3$ or CaF_2), liquid (water), and gas (bubble of saturated water vapor). The geometry of these NFIs is not as perfect as that of SFIs, and the solid-liquid interface is far from well-defined and sharp. This should be considered as a typical situation in the case of natural samples.

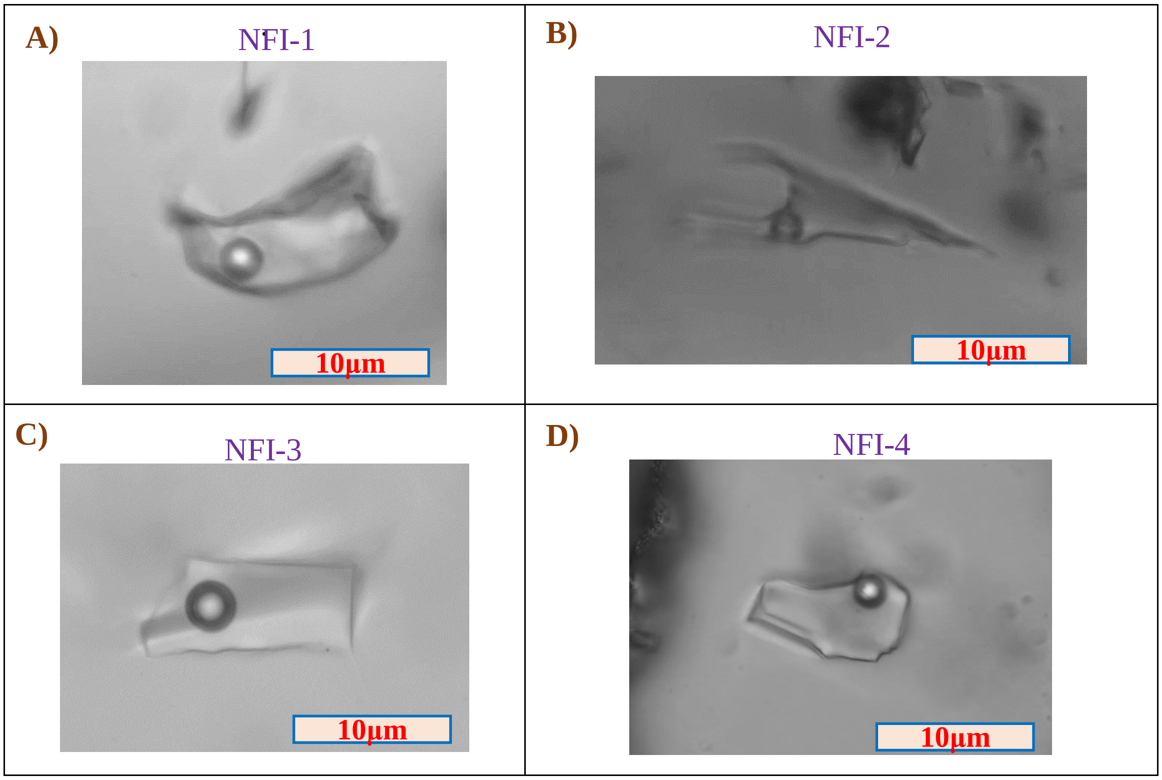

Figure 3.4. Micrographic images of several NFIs, including water, located in the calcite ($CaCO_3$): A) NFI-1, B) NFI-2, or in the fluorite (CaF_2) fragment: C) NFI-3, and D) NFI-4.

3.2. Microthermometry measurements

Almost all the FIs presented in the previous section are characterized by the co-existence of liquid-vapor at equilibrium and room conditions. As shown in Figure 3.5, for the SFI-1, the liquid-vapor assemblage stable at room temperature (RT) is controlled by the temperature and follows the water-vapor saturation curve up to homogenization temperature (T_h). T_h is a unique temperature where the bubble of saturated water vapor disappears, and the system becomes single-phase (fluid inclusion contains only liquid phase) (see Refs. [218, 220] for further details). T_h was determined by the microthermometry measurements.

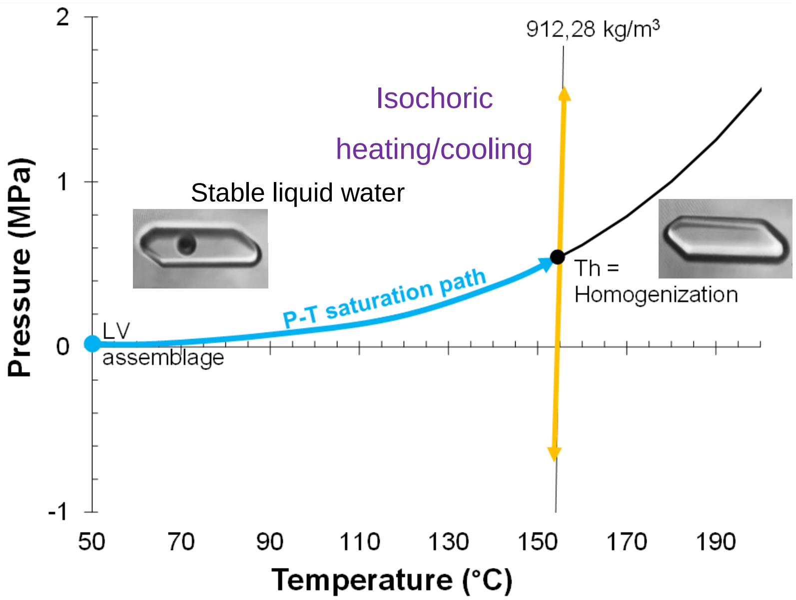

Figure 3.5. Phase diagram of the SFI-1. The coexistence of liquid water and a bubble of saturated water vapor following the water-vapor saturation curve (blue line) up to homogenization temperature (Th = 155°C) and pursuing the isochoric curve (orange line) to nucleate.

Microthermometry measurements make it possible to define phase transition temperature during the cooling and heating of a fluid inclusion-bearing sample at the given heating/cooling rate (°C/min) [221]. Herein, microthermometry measurements were conducted with 10 (°C/min) heating rate using THMS-600, LINKAM stage (Figure 3.6) coupled to the Leica optical microscope equipped with a 50X objective (numerical aperture (NA) = 0.50) and matching condenser. This device allows to work in a wide temperature range from -196°C up to 600°C with a high accuracy of ±0.1°C. THMS-600 device consists of a stage, system controller, and liquid nitrogen cooling system, which allow us to control the temperature of samples during measurements. Before starting the measurements, the instrument was calibrated using a reference sample, containing FIs of pure water with a known phase diagram.

It should be noted that each microthermometry experiment was repeated at least ten times to confirm the value of the homogenization temperature, which is equal to 155±1°C in the case of SFI-1. Determination of the T_h is very important for further spectroscopic analysis. Namely, heating beyond T_h makes the monophasic liquid to follow the isochoric curve, along which the pressure change predominates over the thermal one, putting the SFI at risk of what is called decrepitation, an irreversible cracking of the quartz container [222]. Consequently, we limited the studied temperature interval from RT to T_h.

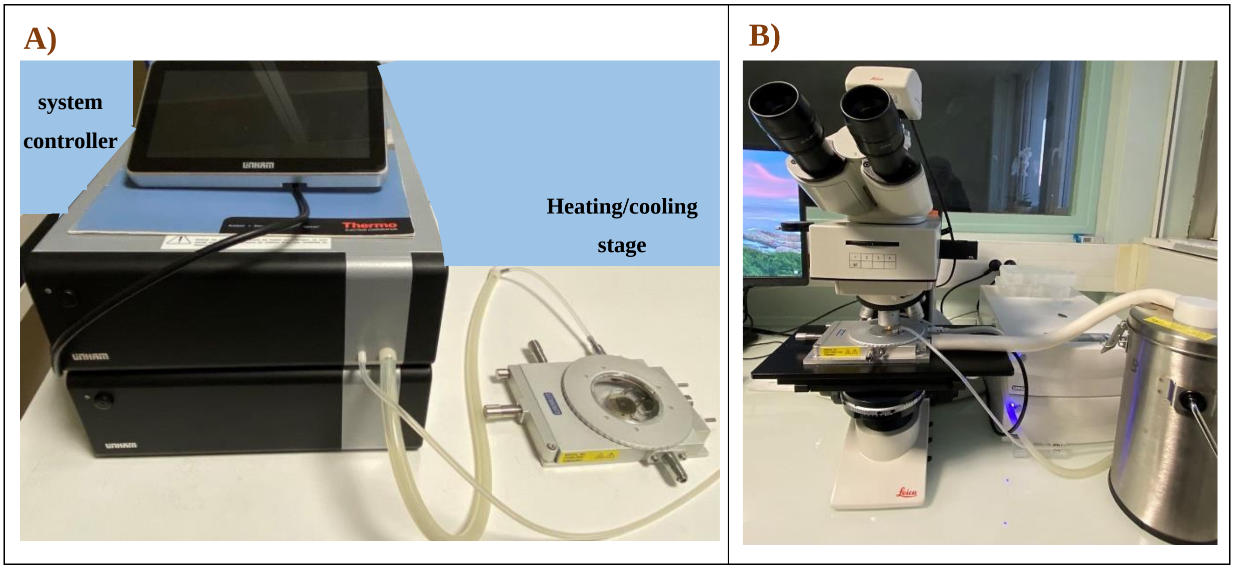

Figure 3.6. A) THMS-600, LINKAM heating-cooling stage, and a temperature controller. B) Linkam stage fixed under the Leica microscope to monitor the variation of sample behaviors optically as a function of temperature.

3.3. Vibrational micro-spectroscopy measurements

3.3.1. Diffraction-limited FTIR micro-spectroscopy

Mid-infrared micro-spectroscopy (micro-FTIR) is a well-established, non-destructive method for high-resolution measurements, which enables chemical analysis of samples, qualitatively in general or quantitatively, up to diffraction-limited spatial resolution [223]. According to Abbe equation ($d = 1.22\ \lambda / (2\ NA)$), the diffraction-limited resolution is commensurable with the wavelength (λ) of the spectral region of interest and with the numerical aperture (NA) of the applied objective. Micro-FTIR has been widely applied to study biological samples in the past 40 years. The employment of a diffraction-limited μ-beam allowed exploring the chemical composition of individual cells [224, 225], diagnosing diseases [226-230], studying microbiology and bacteria [231-235], biochemical and biophysical modification processes [236-241], and variation of chemical composition [242-245]. Furthermore, this method has been used in material science [246, 247], food industry [248-250], astrophysics [251], and geoscience [252]. In earth science and porous media, high-resolution micro-FTIR was exploited especially for microanalysis of fluid inclusions, which displayed various heterogeneities at the micrometric scale [59, 253, 254].

In micro-FTIR setups, the optical arrangement of microscopes might have different modes, such as confocal, semi-confocal, and aperture-less. The standard confocal mode consists in positioning an aperture (mask) in front of the detector in the focal plane of the objective. The aperture defines the beam size, creating a diffraction pattern that limits the actual spatial resolution. Some studies have shown that the higher-order diffraction was limited by utilizing two apertures, the first between the sample and the detector and the second between the IR source and the sample, called dual confocal mode [255, 256].

The dual confocal configuration allows the beam to be focused on the sample while eliminating most of the diffraction pattern, but it incurs tremendous photon losses degrading the signal-to-noise ratio (SNR). The principle of this configuration is based on the so-called infinity-corrected Schwarzschild objective and the associated condenser composed of two concentric mirrors with different diameters (Figure 3.7). The primary convex mirror has a smaller diameter than the secondary concave one. The light enters the objective through the central opening of the secondary mirror. It is first reflected from the primary mirror to the secondary mirror and then from there to the sample. The Schwarzschild configuration allows the light to be perfectly focused on the sample. The area on which the light is focused can be modeled by the point spread function (PSF). Figure 3.7A illustrates the simulated PSF of a Schwarzschild objective (32X, NA = 0.65) applied in transmission mode [256]. As shown in Figure 3.7B, it is worth noting that the sensitivity of non-confocal setups can achieve 50% near the center diffraction and reaches 80% at a 10 mm radial distance only. On the contrary, within a 4 mm radius, the confocal arrangement narrows the center maxima and achieves 90 % sensitivity [256-259].

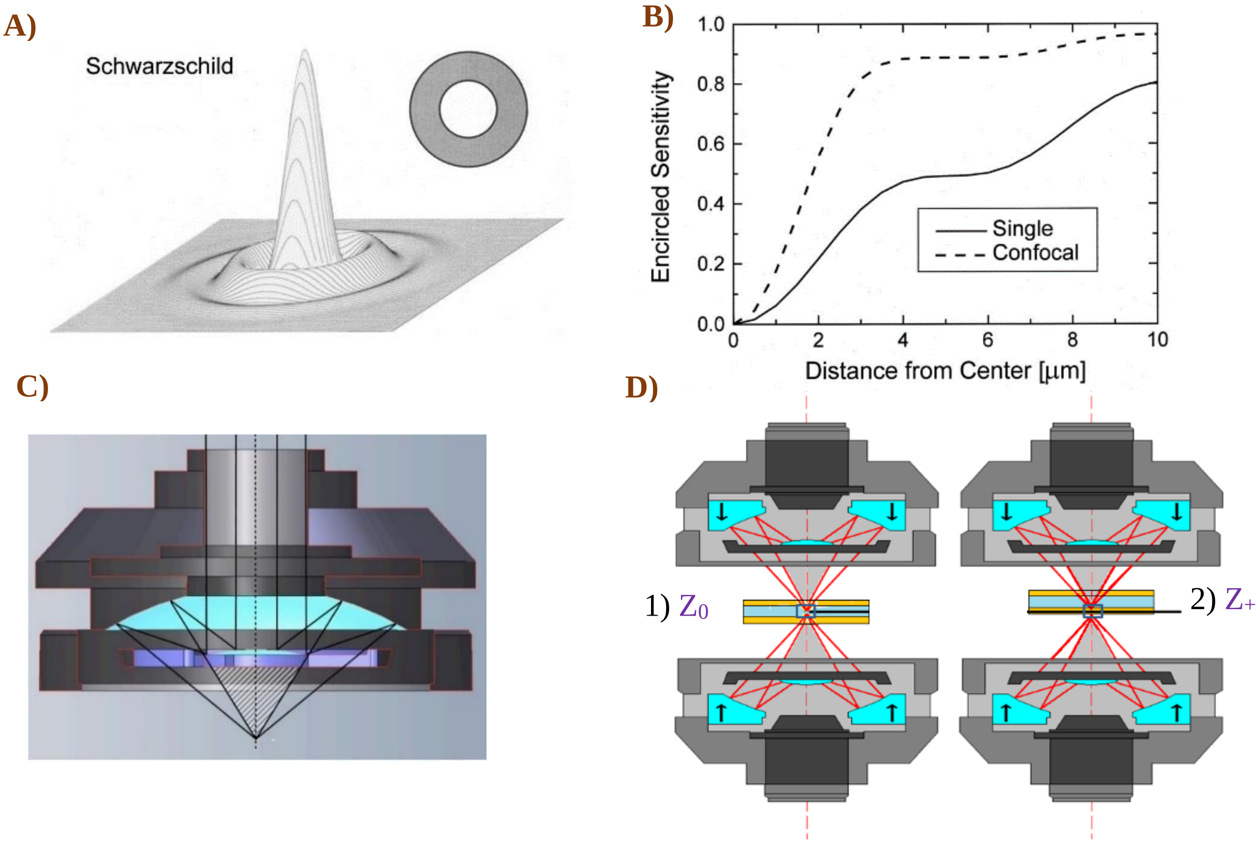

Figure 3.7. A) The diffraction pattern (point spread function) for an optic with a secondary mirror (central) obscuration. The gray area in the top right indicates the aperture [256]. B) encircled sensitivity in the case of single and confocal configuration, C) An infinity-corrected Schwarzschild objective. The hatched area is the shadow area formed under the primary mirror [255]. D) Confocal geometry of the acquisition setup allowing to work in the vertical dimensions (different Z levels): 1) at the focal plane (Z_0) and 2) at the bottom of a sample (Z_+) [256].

In consequence, the PSF of a Schwarzschild objective shows a narrow peak at zero-order and higher-order diffraction limits than the conventional visible microscope objectives. This is because the primary mirror causes a shadow zone (hatched zone in Figure 3.7C). As shown in Figure 3.7D, this configuration provides the confocal mode, which allows us to work in the vertical dimensions (different z levels) and makes it possible to obtain a 3D FTIR tomographic map of occluded water.

There is a strong dependency between spatial resolution, aperture size (field of view), NA of the objective, SNR, and acquisition time (number of scans). The final beam size and then the best spatial resolution achievable by a given equipment result from combining all these factors [260]. In this way, a bigger aperture size is suggested for acquiring the hyperspectral data with high SNR at a shorter acquisition time. However, spatial resolution moves away from the diffraction limit.

In order to record high-resolution measurements down to the diffraction limit, an IR source with high brilliance and collimation is required. Generally, the classical micro-FTIR setup exploits a thermal emitter (Globar), constructed of silicon carbide heated to very high temperatures (1000 to 1650°C) and emitting IR radiation depending on its temperature, like a black body. This infrared source is the most often used in the MIR range (4000 - 400 cm^{-1}). In many studies, the Globar source works properly down to an aperture of around 15×15 μm^2; below this value, the SNR of the recorded spectrum decreases because of the low photon count [261-264]. Since the radiations are emitted in all spatial directions (no angular dependence and no polarization), only a small fraction can be efficiently collected and collimated in the spectrometer and microscope apertures. Using a collimated infrared source such as supercontinuum laser or a synchrotron source allows for easier and more efficient collimation in the microscope optics and reduces photon losses [262-264].

Synchrotron sources use the property of charged particles that lose kinetic energy by emitting highly directional photon beams (emission of ‘Bremsstrahlung’ or ‘braking radiation’) when the particles are first accelerated at relativistic speeds and deviated in a magnetic field. The Brehmsstralung emission has several interesting properties for infrared microscopy: it covers an ultra-broadband spectral range from the Terahertz (mm wavelengths) to the near-infrared (1 µm wavelength), and it can be efficiently collected and focused in microscope optics thanks to its small emission angle. Therefore, synchrotron-based measurements are often employed for high-resolution micro-MIR measurements. They allow to achieve the diffraction-limited spatial resolution (aperture size 3×3 μm^2) for 2.53 µm wavelength of IR radiations [56, 265-267].

Meanwhile, combining separate laser chips and quantum cascade lasers (QCL) in the mid-infrared (MIR) has made remarkable progress, with tunability throughout a relevant range of 3–13 µm. Using QCL sources, discrete-wavelength imaging systems are now commercially accessible [268, 269]. Nonetheless, the multidimensional nature of the information required encourages the usage of broadband sources. Moreover, the coherence of QCLs is frequently harmful to the quality of infrared images. Therefore, micro-spectroscopy investigations need powerful broadband laser sources with constant spectral power density in the mid-infrared, spatial coherence, and temporal incoherence to complement the synchrotron source.

Supercontinuum generation (SCG) is established when a narrowband short laser pulse experiences significant spectral widening due to exaggerated optical nonlinearities [265, 270]. Consequently, the supercontinuum generation (SCG) of lasers has been employed as an alternative high-brilliance micro-MIR radiation source [260, 265, 271-273]. SCG combines the primary benefits of a synchrotron light source, namely a high brilliance, high collimation, broad bandwidth, and diffraction-limited spatial resolution, in a compact structure. However, their spectral bandwidth is still limited compared to the ultra-broadband synchrotron sources.

Most infrared micro-spectroscopy setups employ confocal microscopes and single-element mercury cadmium telluride (MCT) detectors. Infrared photon detection is challenging due to its low energies. Many standard detectors, such as bolometers or deuterated L-alanine doped triglycine sulfate (DLaTGS), rely on thermal detection mechanisms, while the very common mercury cadmium telluride (MCT) detector relies on photoconduction. MCTs offer high sensitivity/detectivity (D^*), units $cm\, Hz^{1/2} W^{-1}$, compared to thermal detectors while still spanning the MIR spectrum. Furthermore, they respond rapidly (typically microseconds), allowing rapid data collection and time-resolved spectroscopies. In a photoconductive MCT detector, a voltage is applied to the semiconducting MCT element. When infrared photons strike the sensor, electrons in the conduction band are excited into the valence band and travel in the potential gradient as a photocurrent. Because of their very low bandgap, such detectors are highly susceptible to thermal noise. In order to improve SNR, MCT detectors must be cooled with liquid nitrogen.

Using MCT detector, the hyperspectral maps are acquired via point-by-point measurements. However, another type of detector called focal plane array (FPA) comprises multiple small detector components organized in a two-dimensional grid on a focal plane. FPA-based systems produce high-definition spectral images (definition being the number of pixels in the image). Each pixel corresponds to the projected region of the sample and represents a distinct, full infrared spectrum [274-277].

3.3.2. Micro-FTIR spectroscopy: Experimental setups and conditions

One of the main goals of this study was to compare the efficiency of the micro-FTIR setups to deal with the interfacial water layer signatures. Four different experimental setups (Table 3.1), based on three different infrared sources (Globar, supercontinuum laser, and synchrotron), two optical arrangements (confocal and apertureless), and two detectors (MCT and FPA), were employed to explore the interfacial signature of water near the solid boundary (water-solid interface).

Table 3.1. The detailed information of four micro-FTIR experimental setups employed for recording the interfacial signature of water near the solid boundary (water-solid interface) in transmission mode.

Setup	**IR source**	**Spectrometer**	**Microscope**	**Microscope optical arrangement**	**Detector**	**The smallest beam size**	**Spectral range (cm^{-1})**
I	Globar	Cary 670	Cary 620 (Agilent)	Apertureless	Focal Plane Array (FPA)	0.65×0.65 (projected pixel size)	900-3950
II		Nicolet 6700	Nicolet Continuμm	Confocal (single aperture dual path mode)	single element mercury cadmium telluride (MCT)	15×15 μm	2800-4200
III	Supercontinuum laser					5×5 μm	
IV	Synchrotron	Nicolet 8700				3×3 μm	

All the micro-FTIR measurements for studying the water behavior have been conducted in the transmission mode, where the beam passes through a sample before reaching the detector. The Globar source was used with an FPA detector and an apertureless microscope in setup I. In setups II, III, and IV, we compared three infrared sources: Globar, supercontinuum laser, and the synchrotron radiation beam, respectively, with the same MCT detector and confocal microscope. The main differences between the sources were their brilliance and collimation, which allowed us to obtain a high SNR at various beam sizes (from 15×15 to 3×3 μm). Experiments using setups

I and IV were conducted at the SMIS beamline at the SOLEIL Synchrotron facility (Gif sur Yvette, France), whereas those based on setups II and III were performed at the Earth Sciences Institute of Orléans, ISTO (Orléans, France).

During all micro-MIR experiments (Table 3.1), the spectrum of water in the fluid inclusion was recorded in the spectral range from 2800 to 4200 cm^{-1} covering the OH stretching band. This is because the quartz cut-off occurred at the wavenumbers below 2000 cm^{-1}; consequently, the quartz absorption masked all low-wavenumber features. The background spectrum was recorded through the surrounding matrix before each set of spectra to remove the effects of any changes in atmospheric CO_2 and water vapor. All spectra were recorded in transmission mode at 8 cm^{-1} spectral resolution with 256 scans.

In the following parts, each experimental setup, which is employed in this study, is carefully detailed.

3.3.2.1. Globar source with FPA detector (setup I)

As shown in Figure 3.8, the set of infrared transmission spectral images was taken on a Cary 620 series FTIR aperture-less microscope (Agilent, Courtaboeuf, France) equipped with a liquid-nitrogen cooled 128×128 pixels Lancer FPA detector and coupled to a Cary 670 FTIR spectrometer using a KBr beamsplitter and a Michelson interferometer with an internal source (Globar). The microscope was equipped with a 25X objective (NA = 0.81) and matching condenser amplified by high magnification optics giving a final magnification of 62.5X. The FPA detector and the high magnification optics provide the theoretical projected pixel size of 0.65×0.65 μm^2 and a field of vision of 84×84 μm^2.

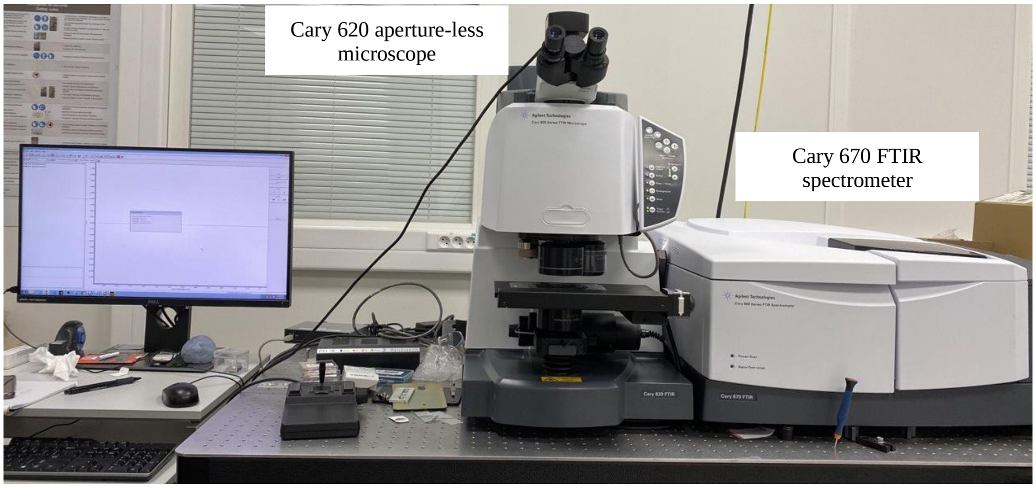

Figure 3.8. Photography of Setup I: Cary 620 series FTIR aperture-less microscope equipped with a liquid-nitrogen cooled Lancer FPA detector. at the SMIS beamline at the SOLEIL Synchrotron facility (Gif sur Yvette, France).

3.3.2.2. Globar source with MCT detector (setup II)

Setups II was based on a Continuμm microscope coupled to a Nicolet 6700 FTIR spectrometer (Thermo Fisher Scientific, USA) with an internal source (Globar). As shown in Figure 3.9A, the microscope was equipped with a liquid-nitrogen cooled 50 μm MCT detector, a 32X infinity-corrected Schwarzschild type objective (NA = 0.65, WD = 7mm, allowing a maximum beam size of 50×50 μm^2), and a matching 32X condenser that worked in the confocal mode [255]. Herein, the Continuμm microscope uses a special optical configuration called ‘single aperture dual path mode’ to obtain a confocal arrangement. This mode consists of a single aperture, while confocality is obtained by passing the IR beam twice through the single aperture, once before the sample and once after transmission through the sample. This configuration gives a fully confocal measurement, reduces diffraction, and improves X, Y, and Z spatial resolutions [255, 278]. The minimum beam size acquired by this setup, concerning the SNR and the light transmittance value, is equal to 15×15 μm^2. Figure 3.9B shows the optical pathway of the FTIR Continuμm microscope, which works in the transmission and confocal mode.

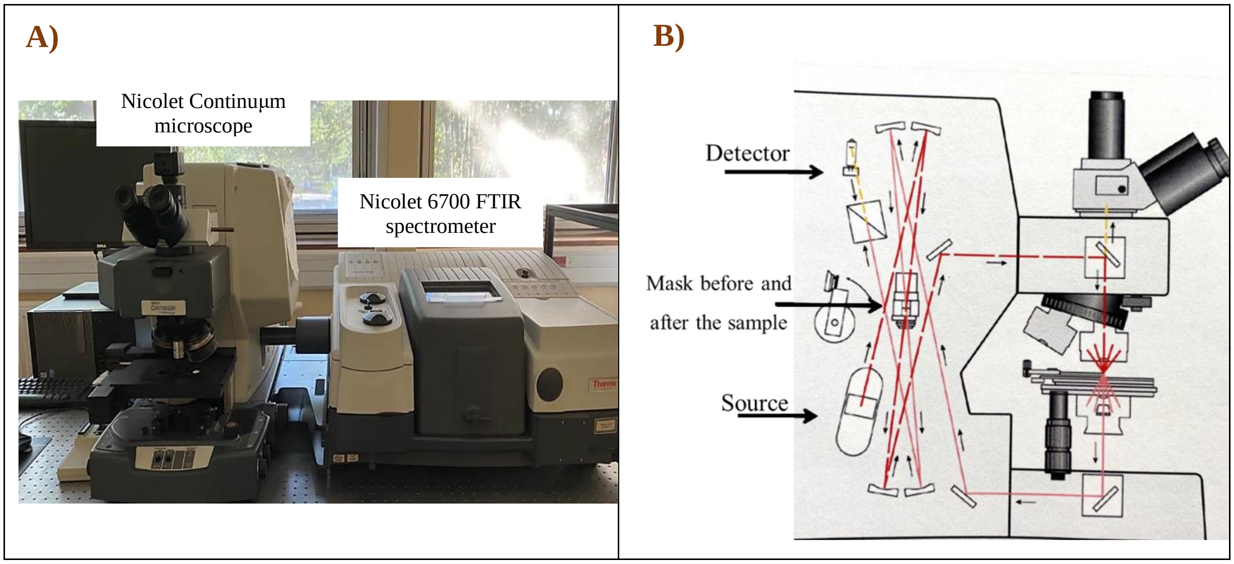

Figure 3.9. A) Photography of Setup II: Nicolet 6700 FTIR spectrometer with Nicolet Continuμm microscope with MCT detector at the Earth Sciences Institute of Orléans, ISTO (Orléans, France). B) The simplified scheme of the FTIR Continuμm microscope in transmission and confocal mode.

3.3.2.3. Supercontinuum laser source with MCT detector (setup III)

Figure 3.10 shows setup III, based on the configuration very similar to setup II except for the IR source. In this setup, the unpolarized supercontinuum laser (Coverage, Novae) was employed as an infrared source [270, 271]. Coverage is the turn-key supercontinuum source emitted a continuous spectrum from 1.9 μm up to 4.0 μm (5260 to 2560 cm^{-1}) in the LP01 emission mode. The very high brightness associated with the collimated laser, high output power (>1.5W), and average spectral power density (up to 0.5 mW/nm) make this all-fiber integrated laser a suitable device for a wide range of μ-beam applications. Although this high-power level is needed to enable and fully use the non-linear processes in the optical fiber, it could damage optical parts, especially the aperture blades, the detector, and the sample. To avoid potential damage, we used a reflective IR neutral density filter (ND=0.3, NDIR03A, Thorlabs) to decrease the intensity of the source. The Coverage laser source had been coupled to the Nicolet spectrometer in the Earth Sciences Institute of Orléans, ISTO (Orléans, France) in the “home-made way.” Due to the high brightness and collimation of this laser source, the aperture size of 5×5μm^2 has been reached with a high SNR. The hyperspectral data (rectangular and linear maps) of the SFI were recorded with a 2 μm and 1 μm step size (smaller than the beam size), respectively. Also, polarized FTIR spectroscopy measurements have been done by adding the polarizer parallel (0°) and perpendicular (90°) to a beam direction.

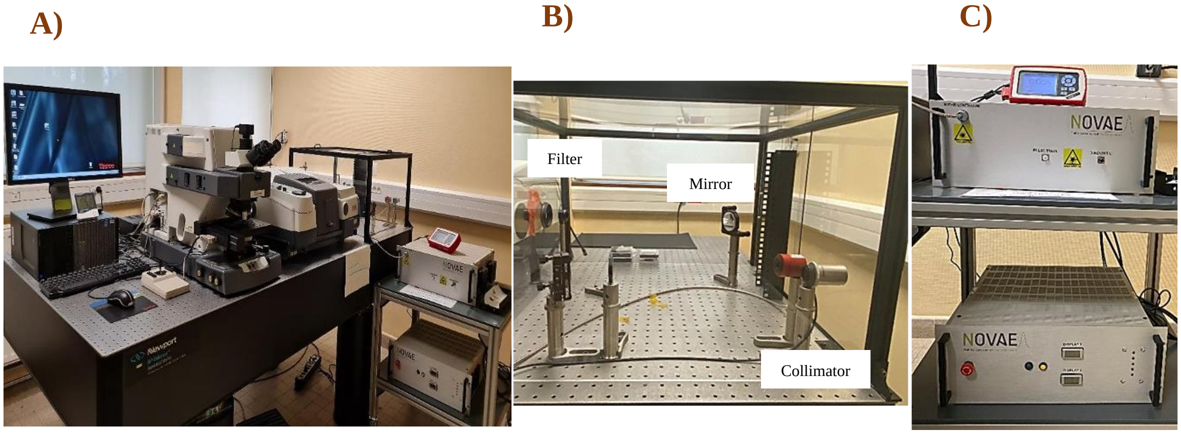

Figure 3.10. Photography of Setup III: A) Nicolet 6700 FTIR spectrometer with Nicolet Continuμm microscope coupled through the “home-made way” optical configuration (B) to the external supercontinuum laser source (C) at the Earth Sciences Institute of Orléans, ISTO (Orléans, France).

3.3.2.4. Synchrotron beam with MCT detector (setup IV)

As shown in Figure 3.11, the micro-FTIR setup in the SMIS beamline was equipped with the same Continuμm microscope as the setup II and III and coupled to a Nicolet 8700 FTIR spectrometer (Thermo Fisher Scientific, USA). For the infrared source, the synchrotron radiation at the SMIS beamline of the SOLEIL Synchrotron Facility was exploited at the SMIS 2 branch. The principle of synchrotron radiation is based on radiation emission by moving charges. While an electron oscillating in a vacuum emits a dipole radiation pattern, accelerating it to near relativistic speeds and forcing it to travel through a bending magnet resulting in a significant compression of the radiation pattern leading to a highly collimated, intense beam of light. During the beamtime, the synchrotron emitted at a constant current of 500 mA [258, 279]. The edge radiation is mainly circularly polarized, but the beam also contains an undefined proportion of bending radiation, which is linearly polarized.

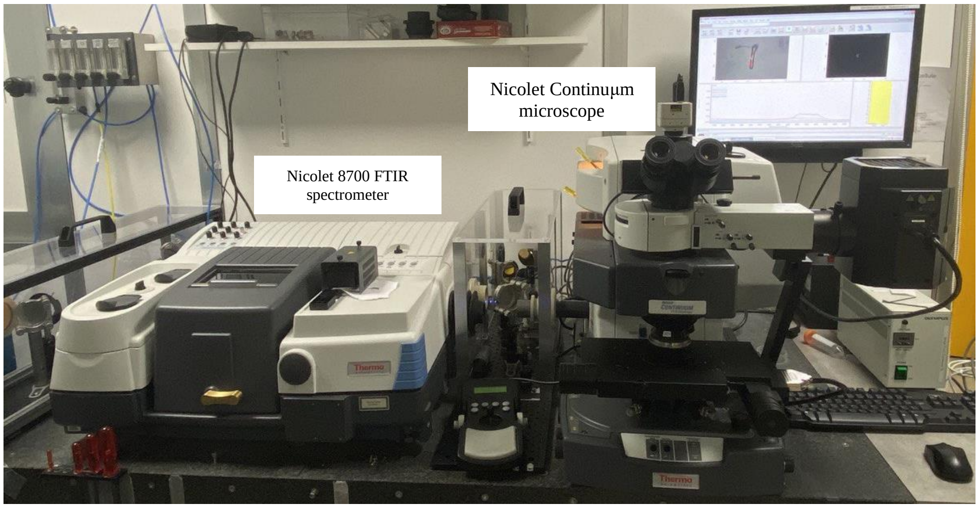

Figure 3.11. Photography of Setup IV: Nicolet 8700 FTIR spectrometer with Nicolet Continuμm microscope coupled to the synchrotron radiation at the SMIS beamline, SOLEIL Synchrotron facility (Gif sur Yvette, France).

The synchrotron radiation is emitted with an angular dependence; longer wavelengths are emitted at higher angles. This may result in chromatic aberrations, especially through high refractive index materials. Due to the high quality (in terms of brightness and collimation) of the radiation source, the beam size of 3×3 μm^2 was achieved. This IR μ-beam approached the diffraction limit, which is 2.61 μm at 2.7 μm wavelength (using Abbe equation $d = \lambda / (2 \text{ NA})$). For recording the spectral rectangular and linear maps of SFI, the step size was defined as 2 µm and 1 µm, respectively.

3.3.3. Raman micro-spectroscopy: Experimental setups and conditions

Although Raman spectroscopy is less sensitive to study the vibrational signatures of water molecules, the high potential of Raman micro-spectroscopy offering a spatial resolution of 1 µm was also employed in this work. The preliminary, punctual Raman scattering measurements were conducted at the Earth Sciences Institute of Orléans, ISTO (Orléans, France) using the Andor Shamrock 500i Raman spectrometer equipped with Andor Newton scientific back-illuminated CCD detector and the coherent Genesis MX SLM laser source (wavelength 532 nm) (Figure 3.12). This Raman setup is coupled to the Nikon ECLIPSE Ni-U microscope. Using a long working distance Nikon objective (100×, NA = 0.8) allows micro-scale analysis with a lateral resolution down to 1–2 µm^2.

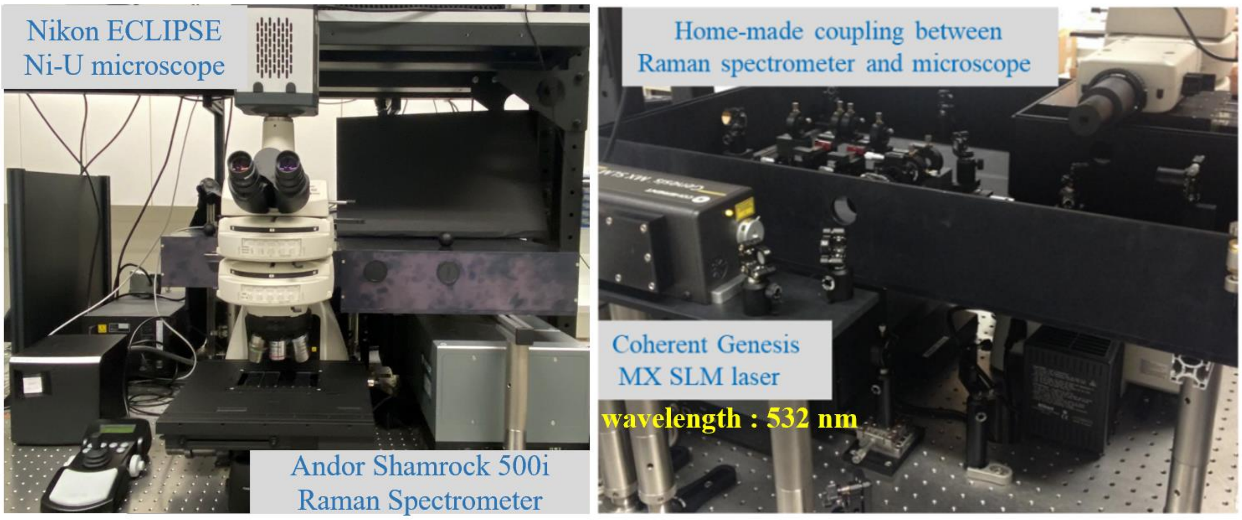

Figure 3.12. The photography of the micro-Raman setup used in the Earth Science Institute of Orleans (ISTO).

Further on, Raman imaging and cartography measurements allowing to record the numerous spectra of the bulk and liquid-solid interface with a resolution of 1 µm were performed at CEMHTI CNRS (Orleans, France), with a set of Renishaw Invia Raman micro-spectrometers (Reflex and Qontor) equipped with different laser sources spanning from the near-UV (355nm) to near-IR (785nm). The principal experiments were recorded by Invia Qontor Raman spectrometer coupled to a DM 2500 Leica microscope (100X objective, NA = 0.85). The maps were recorded in the backscattering geometry, in confocal mode, using 1800 grooves per mm grating and a 633 nm excitation of He-Ne laser (power on sample 10 mW). Detailed information on the Qontor Raman spectrometer and DM 2500 Leica microscope is shown in Figure 3.13. The spectral maps were recorded over a rectangular zone of 1971 points with a step size of 1 µm. It is worth mentioning that the exposure time for each spectrum was 15 seconds. This system has a particular automatic focus device. This feature allows one to record the spectra at the defined distance from the surface (at the given depth across the SFI). Also, the polarization filters were used at horizontal-horizontal (0°) and vertical-vertical (90°) conditions to detect the micro-scale water molecules directionality.

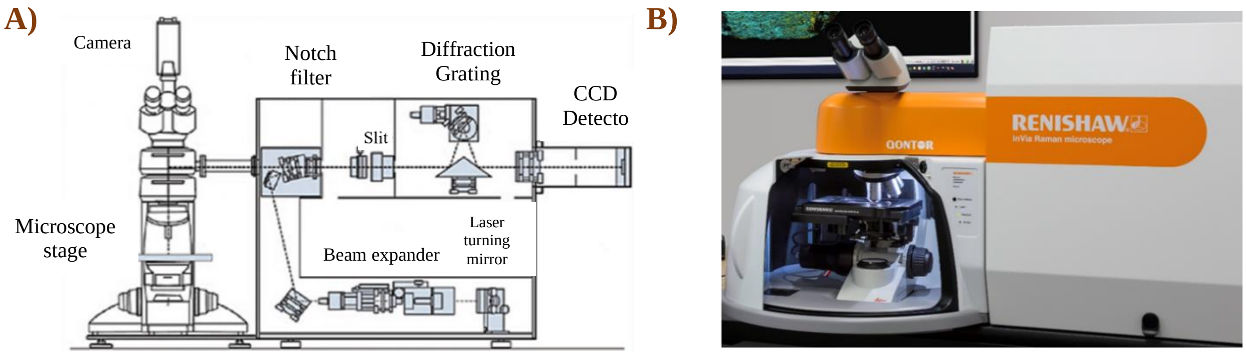

Figure 3.13. A) Different components of the Qontor Raman spectrometer and DM 2500 Leica microscope. B) Overall view of the experimental setup in CEMHTI, Orleans.

3.3.4. FTIR and Raman micro-spectroscopy measurements at different temperatures

In order to determine the impact of the thermal effect on the interfacial spectral signatures of water, the FTIR and Raman spectra were recorded from room temperature (RT) to homogenization temperature (T_h) (see section 3.2). THMS-600, Linkam stage, previously described in section 3.2, was used to record the micro-Raman spectra. Regarding FTIR measurements, the INS1402036, INSTEC heating-cooling stage was employed (Figure 3.14A). The change of stage was necessary in order to use the FTIR 32X objective described in the previous section. The working distance of this objective is not compatible with the geometry of the Linkam stage under the Continuµm IR microscope. The Instec stage works very similarly to the Linkam one. It allowed high accuracy (± 0.1°C) measurements in a temperature range from -196°C up to 600°C. It is equipped with a system controller and liquid nitrogen container for controlling the heating/cooling rate (°C/min). As shown in Figure 3.19, the heating stage was installed on the Continuµm microscope stage, and the sample was placed within the silver block of the stage between two CaF_2 windows (Figure 3.14B).

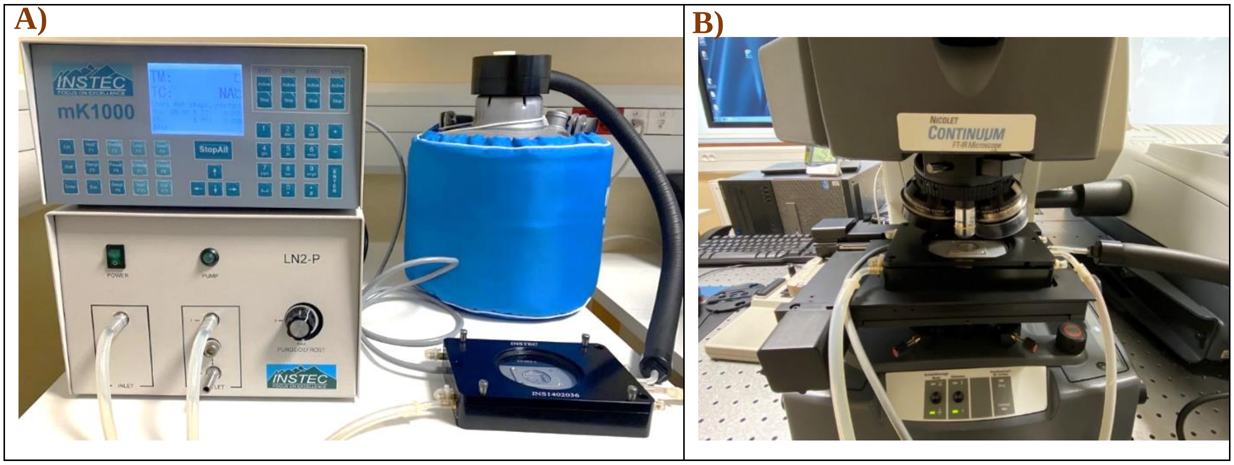

Figure 3.14. A) Photography of INSTEC heating-cooling stage used in the case of the high-temperature micro-FTIR measurements. B) INSTEC stage fixed under the Continuum FTIR microscope.

3.3.5. Raw data processing of FTIR and Raman micro-spectroscopy

All spectra of bulk and near the interface (see further in the Chapter 4), acquired with the four micro-FTIR setups and Raman scattering, are shown after processing, including baseline correction (by subtracting a linear baseline in the 2800 - 4200 cm^{-1}), and normalizing the absorbance value with respect to the highest absorbance (i.e., ranging the spectra between 0 and 1 (arb. Units)) using OriginPro v.2021 software. In the case of the FTIR spectra recorded by setups III and IV, additional processing methods, such as interference fringe removal and Mie-scattering correction, were done by implementing an algorithm in Igor Pro 9.0 software (kindly see Appendix A for further information) and deep learning-based modelling, respectively. For the interference fringe removal, the method illustrated in Ref.[280], and for Mie-scattering correction, the method presented in Ref.[281] were applied to the raw spectra as described in section 4.1.2.

Moreover, there were some small peaks parasites on the top of the bulk water spectrum acquired by setup III and IV, which might relate to the saturation issue. In this way, after checking the raw spectra we observed that the spectra are not saturated, i.e. the raw absorbance values never exceed 1.3 (arb. units), and the transmittance value is 5% at minimum. However, even if this positive value guarantees that the spectrum expresses the IR absorbance dynamics of liquid water, it is small enough to give birth to the small parasitic peaks observed at the top of the OH-stretching band. To avoid altering the spectra with this artefact, while keeping the full meaning of the spectra shapes, the FFT filter method (OriginPro v.2021 software) with 15-20 points within the window was employed to smooth all the spectra affected, namely bulk and normal water, before decomposing the water spectra (kindly find Appendix B for further information).

The decomposition of OH stretching band of FTIR and Raman water spectra at different temperatures was done using the peak analyzer function tool of OriginPro software v.2021, which fits components of the Gaussian algorithm to the band using the least square regression value. The most suitable and accurate model was chosen by least square regression higher than 0.993. The deconvolution process allowed to determine for each characteristic band: the exact wavenumber position, the full width at half maximum (FWHM), indicating the energetic distribution for the corresponding sub-band molecules, and integrated surface area, proportional to the sub-band molecular population. During the decompositions, the wavenumber values of each sub-band were partially fixed/restricted, such as 3150-3350, 3350-3550, and 3550-3750 for the first, second, and third sub-band, respectively. In addition, each sub-bands contribution (sub-band fraction) corresponding to the ratio between the integrated area of each sub-band (A_{iW}) and the total integrated area ($\sum A_{iW}$) (the sub-band fraction of NW: $A_{NW}/(A_{NW} + A_{IW} + A_{MW})$) was determined (please see Appendix C for additional information).

Finally, a statistical technique called non-negative matrix factorization (NMF) was employed in this study to reduce the dimensionality of the dataset and increase the interpretability while preserving the maximum information based on the multivariant analysis to investigate different components within the FTIR and Raman scattering hyperspectral data [282-284]. NMF analysis was done by implementing a script/algorithm in Python v.3.11.1., Jupyter Notebook platform. This script was developed by Raoul Missodey in the framework of Master-1 internship at CEMHTI, CNRS, Orléans. Kindly find following link to access to its Python code: https://github.com/CEMHTI/Raman_Analysis

3.4. Partition function for converting the vibrational spectroscopy to thermodynamic properties

The partition function converts the microscopic properties of a system to its macroscopic ones. In addition, it plays a fundamental role in statistical physics since all physical quantities at equilibrium can be written through it. If the different forms of energy in the system are independent, the total energy can be written as:

$$E_{tot} = E_n + E_{el} + E_{trans} + E_{vib} + E_{rot} \qquad (3.1)$$

Where E_n is nuclear energy, E_{el} the electronic energy, E_{trans} the energy of translation, E_{vib} the energy of vibration and E_{rot} the energy of rotation. In this way, the energy levels of the molecules are quantified and: $E_{el} > E_{vib} > E_{rot} > E_{trans}$ [285, 286]. It should be noted that the translational energy levels are very close to each other; consequently, the translational energy is not quantified frequently [285].

The partition function is written as the product of the partition functions of each energy forms in the system:

$$Z_{tot} = Z_n . Z_{el} . Z_{trans} . Z_{vib} . Z_{rot} \qquad (3.2)$$

For water, the nuclear and electronic partition functions (E_n, E_{el}) are equal to 1 [287]. Moreover, the first order of E_{rot} is negligible. The vibrational energy, which we measure in FTIR, is the dominant contribution for the calculation of the partition function.

The partition function that we use in this study was developed by Bergonzi et al. [56, 57], which is derived from the partition function of Griffith and Scheraga [288], and Néméthy and Scheraga [289]. Indeed, Bergonzi et al. modified Griffith and Scheraga partition function to take into account the intramolecular modes of water as well as fractions of populations of water molecules obtained experimentally instead of calculated manner. The modified partition function is written in the following form:

$$Z = \sum_{N_i} g \left[\prod_{i=1}^{3} \left[f_{i,inter} \exp\left(-E_i/RT\right)\right]^{N_A x_i} \prod_{i=1}^{3} \left[f_{i,intra} \exp\left(-E_i/RT\right)\right]^{N_A x_i}\right] \qquad (3.3)$$

Bergonzi et al. model only employed three populations of water molecules obtained from the decomposition of the OH stretching band. The fraction of each population was obtained by decomposing the OH stretching band into three Gaussian components. The g factor is calculated from these three populations as shown in the following equation:

$$g = \frac{N_A}{N_{NW}! N_{IW}! N_{MW}!} \qquad (3.4)$$

Where $N_{NW} = N_A x_{NW}, N_{IW} = N_A x_{IW}, and\ N_{MW} = N_A x_{MW}$.

N_A is the Avogadro number and $N_i = N_A x_i$ with $\sum N_i = N_A$ are the number of each species per mole of water; x_i is the mole fraction of each species.

Likewise, the weighting factors f_i is also modified. They exploited three intermolecular factors $f_{i,inter}$, one for each of the three populations, and three intramolecular factors $f_{i,intra}$. The modified weighting factors are written as follows for the intermolecular and intramolecular factors:

$$f_{i,inter} = \left[1 - \exp\left(-h\upsilon_i^{(T)}/\kappa_B T\right)\right]^{-3} \left[1 - \exp\left(-h\upsilon_i^{(L)}/\kappa_B T\right)\right]^{-3} \ (\mathrm{i} = 1, 2, 3) \qquad (3.5)$$

$$f_{i,intra} = \left[1 - \exp\left(-h\upsilon_i^{(S)}/\kappa_B T\right)\right]^{-3} \left[1 - \exp\left(-h\upsilon_i^{(B)}/\kappa_B T\right)\right]^{-3} \ (\mathrm{i} = 1, 2, 3) \qquad (3.6)$$

${\upsilon_i}^{(S)}$ the wavenumber assigned to the OH stretching mode, while the ${\upsilon_i}^{(B)}$ the wavenumber attributed to the bending mode. In this way, it is crucial to measure the wavenumbers of each mode experimentally and not calculate them to adjust the results with the reference values. In addition, it is necessary to experimentally obtain the fraction of each of the three populations and insert these parameters as an input of the model. These parameters were obtained from the infrared measurements presented above.

Bergonzi et al. validated their partition function by employing two different setups. In the first one, the connectivity and libration band are recorded from -6 to 30°C. Then, the partition function was calculated entirely from the experimental data. But, in the second, the connectivity and libration band was not recorded because of signal cutting at low wavenumbers. For this second case, certain assumptions were applied in order to calculate the partition function [57]. It should be noted that in this study, we use the reference value of Bergonzi's results for connectivity, libration, and bending mode of water molecules. In addition, the provided data in that work was extrapolated to obtain the values at the higher temperature (up to 155°C).

In this model, the population of NW ($n_h{\sim}4$) is considered as the fundamental level, i.e., $E_{NW} = 0$. The energy assigned to the level of IW is the energy required to transform a bond $O - H \cdots O$ of ice in a free OH bond, estimated for liquid water equal to $E_H = 23.3\ kj.mol^{-1}$ [57, 69, 290, 291]. Finally, the energy allocated to the energy level of the MW population must be a combination of the energies required to break 2, 3, and 4 hydrogen bonds with this form $E_{MW} = x_2 2E_H + x_1 3E_H + x_0 4E_H$. However, the fractions of the 2-, 1- and 0-linked populations contained in the MW fraction are not well-defined separately in the literature. That is why Bergonzi et al. assumed that in MW, the molecules create 2 hydrogen bonds in the maximum. This hypothesis is verified by different studies [292-295]. Therefore, the energy assigned to the MW population is the energy required to break 2 hydrogen bonds and is equal to $2E_H$.

As was shown, Bergonzi's partition function was developed from the Maxwell-Boltzmann distribution and considered for the system characteristic properties at constant temperature and volume. Also, Helmholtz free energy (F) is the thermodynamic function directly related to Z. As a result, the thermodynamic potential at constant (T, V) can be written as $F = -\kappa_B T \ln Z$. In addition, the Gibbs free energy (G) can be obtained from this equation: $G = F + PV$ (please find Appendix D for additional information); therefore

$$G = -\kappa_B T \ln(Z) + \kappa_B T V (\frac{\eth \ln(Z)}{\eth V}) \qquad (3.7)$$

After evaluating the sensitivity of the model, Bergonzi et al. declared that the correction allowing us to pass from the Helmholtz free energy to the Gibbs free energy since the $P.dV$ is negligible, approximately $2\, J.mol^{-1}$ on the range of temperatures -6 to 90°C. Consequently, we report the Gibbs free energy (G), which is the suitable thermodynamic potential for constant (T, P) transformations, as we most often have in the field of geoscience.

4. From the cavity center to the borders: Infrared measurements of the bulk (in-pore) water

After introducing the materials and methods, we gather in this chapter all the results giving evidence on the spectral signatures of water located in the fluid inclusions, which are shown to depend on the distance to the solid wall (solid-liquid interface) and to the water vapor boundary (liquid-air interface). Our study starts from the results already acquired by Bergonzi et al. [56, 91], particularly bearing on the two main specificities of our team: 1) working with micro-beam down to the diffraction limit using synchrotron radiation source [56-58, 255], hereafter with an additional approach owing to supercontinuum laser source; 2) probing water occluded in one closed micro-cavity formed as intra-minerals pockets. In what follows, we systematically compare our measurements to the previous ones, especially when using the same inclusions, to reach a comprehensive discussion and conclusion at the end of this chapter.

4.1. Normal vs. bulk (in-pore) water

As discussed in chapter 1, normal water refers to water that is not confined within a fluid inclusion or any closed medium. Its properties have been extensively described using vibrational spectroscopy methods, as outlined in section 2.2.1. On the other hand, bulk (in-pore) water specifically pertains to water located within the fluid inclusion, which is a micrometric closed medium isolated from any solid-liquid or liquid-gas interfaces.

4.1.1. FTIR spectra of normal *versus.* bulk water at room temperature

For recording the spectrum of normal water, the acquisition setup bears upon sandwiching water between two solid plates. In this way, Bergonzi et al. used a fluid cell composed of two ZnSe windows. ZnSe is a semi-conductor window, and water is deposited with a thickness of almost 1 μm to prevent the saturation of the FTIR absorption when crossing the fluid cell. Also, they employed a Globar source with MCT detector for recording the stretching band of water; however, the beam size was not mentioned.

In our study, we deposited a drop of water between two CaF_2 windows (13 mm × 2 mm) in a similar way. The pristine CaF_2 window is the most commonly used window because it is transparent in a wide range of infrared radiation. For recording the spectrum of normal water, a supercontinuum laser source with MCT detector (setup III, section 3.3.2.3) with a beam size 5×5 μm was employed, and the spectrum was recorded in the spectral range from 2800 to 4200 cm^{-1}, which corresponds to the OH stretching. It is worth noting that the acquired normal water is limited only in the Z direction and is unlimited (interface-free) in the X and Y axis.

As mentioned in section 2.2.1, the OH stretching band (c.a. 3400 cm^{-1}) predominates in the FTIR spectrum of normal water and is significantly modified by the varying molecular network connectivity (i.e., changing H-bonds network). The coordination number of H-bonds among the water in liquid form is generally very close to the ice. Indeed, the average coordination number of normal water molecules is equal to 3.4 ± 0.1 at 22°C [88, 89] or 3.8 [93], which means that the water molecules, on average, are tetrahedrally coordinated. This number shows the predominance of well-connected molecules contribution (network water, NW). The absence of any dangling OH mode, centered around 3700 cm^{-1}, suggests that the “free” water molecules (0-connected) are in very low concentration in the normal water, less than 1% [68].

To record the spectrum of bulk water, Bergonzi et al. exploited the synchrotron beam, while in our case, the bulk spectrum was acquired by four different experimental setups (setup I to IV). Figure 4.1 compares the OH stretching band profile of normal water with the bulk water obtained by the presented methods. The spectrum of bulk water recorded in the middle of fluid inclusion is considered as the reference spectral signature of water in this study. As shown, our normal and bulk spectra in terms of the main peak position are identical to the previous study done by Bergonzi et al. [56]. However, comparing the FTIR absorption spectra characteristic of normal and bulk water demonstrates that the behavior of water inside the micrometric closed media (fluid inclusion) substantially differs from the normal water (interface-free water). As shown, the bulk water's main peak position slightly shifted toward a higher wavenumber (from 3430 cm^{-1} in normal to 3500 cm^{-1} in bulk (blue-shifted)). Also, the OH stretching band of the bulk water clearly broadens (namely, the FWHM substantially increases, suggesting that the energetic level of H-bonding is enhanced).

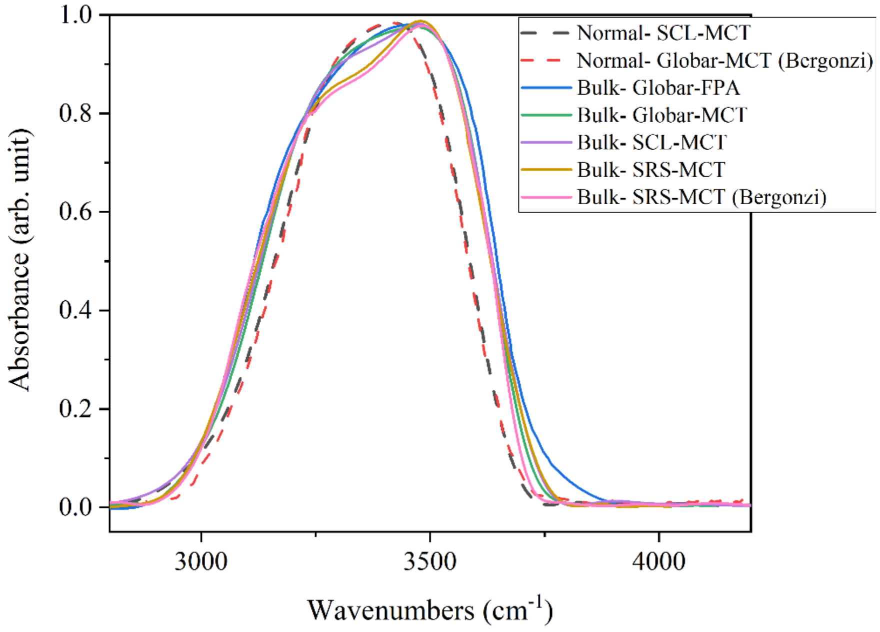

Figure 4.1. The comparison of the mid-infrared absorption spectra characteristic of normal water (not located inside the fluid inclusion or any closed media) and of bulk (in-pore) water (water located in the center of SFI (micrometric closed media)).

We have no unambiguous explanation about the main reason for this discrepancy between bulk and normal water in terms of water physics. However, this modification of the OH stretching band might be due to the geometrical effect of the fluid inclusion since it has a geometry limited in x, y, and z with a certain shape and curved pore walls, compared to the setup for normal water, where the water is limited only in z, with planar windows perpendicular to the radiation. Another assumption would relate to the optical pathway of the radiation through the fluid inclusion and the different media it has to cross. As shown in Figure 4.2, the variation of refractive index from quartz to liquid or air, then to quartz again, can modify the optical pathway. This modification does not seem to be huge; however, it might affect the final spectral profile. In general, the dimensions of the cavity, the distance between pore walls, or the bubble size can affect the high-resolution FTIR measurements and trigger optical aberrations.

4.1.2. Optical aberrations

The collimation of infrared radiation emerging from a synchrotron and supercontinuum laser offers many significant benefits. However, from a physical point of view, the interaction between a small beam and micrometric objects can create artifacts such as interference fringes, called also sinusoidal waveform or oscillations [296, 297]. Their presence is detrimental since they can be at the origin of incorrect features such as peak shifts, baseline drifts, shoulders, noise, and dispersion in the final spectrum [296]. This can be more prominent when one deals with samples such as spheres or rods with sizes similar to the beam size, where Mie-type scattering may occur [298, 299]. This can significantly affect the SNR of diffraction-limited spatial resolution measurements since scattering may direct the main intensity of the beam out of the confocal aperture.

4.1.2.1. Interferences fringe

Probing samples with plane-parallel sides, such as the upper and lower quartz surface in a distance of micrometers in mid-infrared spectroscopy transmission measurements, may lead to multiple reflections of the beam and broad sinusoidal trends in baselines called interference fringes that overlay with chemical spectral features [300, 301]. Figure 4.2 shows the optical pathway in the sample (SFI-1) schematically.

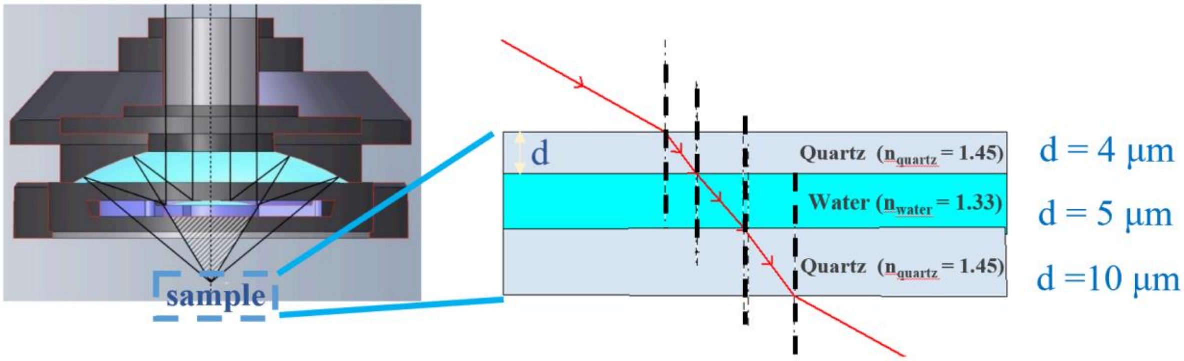

Figure 4.2. Schematic of the optical pathway in our sample (SFI-1), which provided the interference fringes in the acquired spectra because of the multiple reflections.

Figure 4.3A shows a sinusoidal baseline with an almost constant period (harmonic trend) recorded in all our spectra. The period of the sinusoid can be used to compute the distance between the two semi-reflective surfaces using the following equation: $\Delta\upsilon = 1 / (2dn)$, where $\Delta\upsilon$ = the increment in wavenumber between successive interference fringes, d = thickness of the fragment, and n = refractive index of the material [302]. According to this equation, the thickness of the quartz fragment hosting the SFI-1 can be estimated at around 18 µm, which is in good agreement with its actual thickness according to CT tomography (19 ± 1 µm).

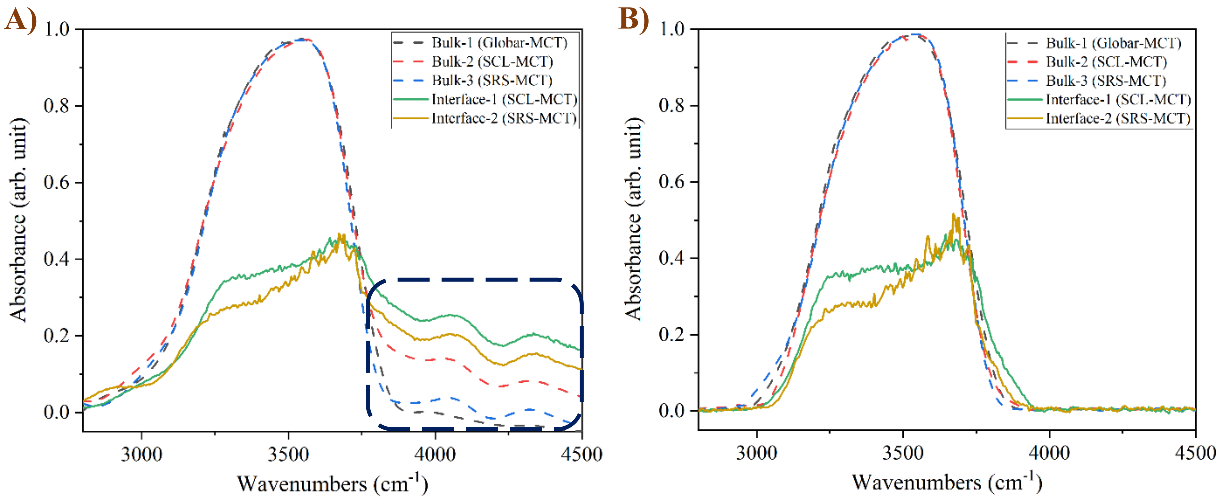

Figure 4.3. A) Mid-infrared spectra of water recorded with setups II (Globar-MCT), III (SCL-MCT), and IV (SRS-MCT) showed the oscillating interference fringes. B) The corrected spectra of bulk and interface water after interference fringes removal processing according to Faggin and Hines's method [280].

Processing the acquired data is necessary to define and quantify the various absorbance spectrum contributions individually in the hyperspectral data. Some models allow suppressing the interference fringes in FTIR data [300, 301, 303, 304]. A modified interferogram can suppress interference fringes in the absorption/transmission spectrum by replacing the sinusoidal trend in the interferogram with a horizontal line [305]. Using the central burst to model and eliminate the side bursts is another approach to directly edit the interferogram for rectification [306]. Other correcting methods take advantage of the fact that interference fringes have much lower intensity than desired spectral features; therefore, exploiting the filtering techniques either in the spectral domain, such as a series expansion of the spectrum to eliminate low-frequency terms [307] or in the Fourier domain [308] can remove the fringes. Likewise, some methods employ a partial least-squares method to eliminate interference fringes and noises [280, 309-311].

In this study, the same procedure as Faggin and Hines was applied, determining the amplitude and period for every fringe in the absorption spectrum [280]. This procedure first defines sharp and broad absorption features relative to the frequency of the interference fringes (harmonic trend). Following this step, we worked on the interferogram, and the frequency of the components related to the interference fringes was identified. After isolating the remaining components, the interferogram was Fourier-transformed to create the pure spectrum of the interference fringes. Finally, the isolated pure interference fringes were subtracted from the original spectrum (Figure 4.3A). Figure 4.3B shows the corrected spectra after the data treatment by implementing an algorithm in Igor Pro 9.0 for removing the interference fringes and baseline correction with the OriginPro v.2021 (peak analyzer function).

4.1.2.2. Mie scattering

The phenomenon called Mie scattering was first studied analytically by Gustav Mie, as he presented the mathematical description of light scattering of an electromagnetic plane wave by a homogeneous sphere of arbitrary size (Figure 4.4A) [312]. Mohlenhoff and Romeo et al. were the first to report on Mie scattering in mid-infrared microspectroscopy of biological cells [298, 299]. Mie scattering is seen mostly as large and highly non-linear baseline fluctuations in the absorbance spectra. In addition, strong peak distortions are observed since absorption and scattering are highly entangled in Mie-type scattering, where the scattering depends on the complex refractive index whose real part determines the optical properties and the imaginary part to the absorption properties. The real and imaginary part of the refractive index are related through a Kramers-Kronig relation. Mie scattering is particularly pronounced where the surface of an object has a local curvature with a radius that is on the same order of magnitude as the wavelength of the radiation. This phenomenon happens in the fluid inclusions, where there is sphere-like water vapor with a size commensurable to the wavelength (λ) of the incident radiation. Figure 4.4B shows the Mie scattering effect (large and broad undulation of the baseline c.a. 3700 cm^{-1}).

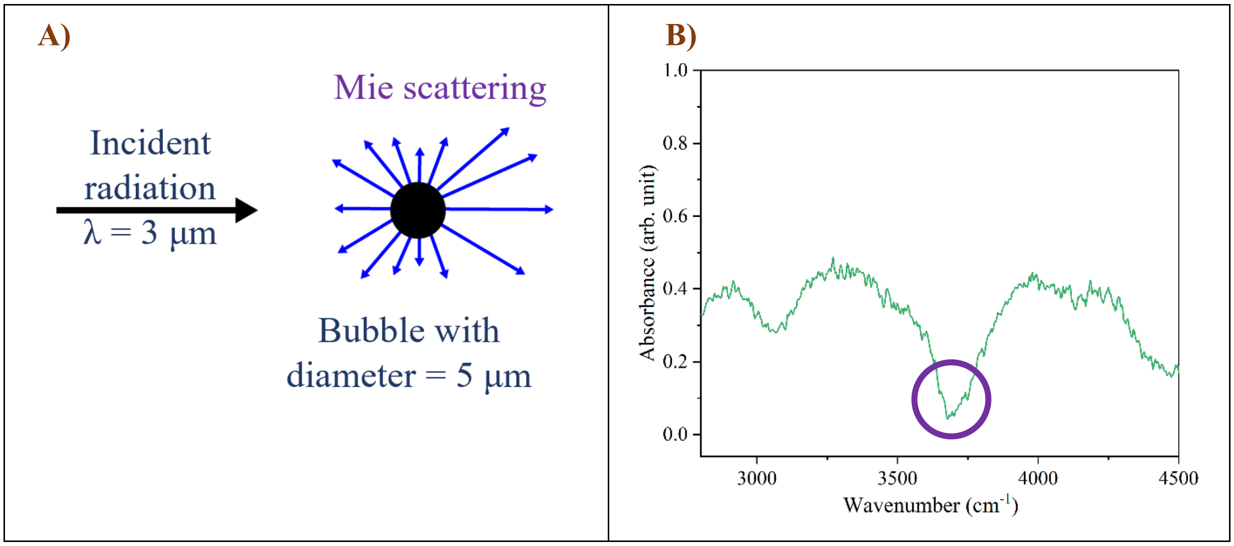

Figure 4.4. A) Schematic of Mie scattering phenomenon: scattering of radiation by a bubble with size (diameter D) comparable to the wavelength (λ) of the incident radiation. B) Spectral signature of Mie scattering.

Practical approximation theories have been established for the intricate Mie formalism, which captures many important scattering aspects [313, 314]. Generally, it is necessary to disentangle Mie scattering and other physical effects from the molecular absorption in FTIR absorbance spectra to make conclusions about the chemistry of the samples. There are several correction methods for handling physical effects in FTIR spectroscopy. The most used is the Extended Multiplicative Signal Correction (EMSC), a flexible approach for correcting FTIR spectra, and in particular, the Mie Extinction EMSC has been used for several cases to remove Mie scattering efficiently [315-320]. Recently, deep learning-based approaches for Mie scattering correction have also been employed to successfully disentangle absorption and scattering contributions in the hyperspectral FTIR data and, in some cases, even outperform the EMSC-based algorithms [281, 321].

As seen in Figure 4.5A, there is a large baseline undulation in the spectra taken in/around the bubble. To correct these spectra, we trained a scatter correction model on simulated spectral data similar manner to Ref.[281], where a deep learning model is trained to solve the IR spectroscopic inverse scattering problem. We built a deep convolutional neural network (DCNN) to infer the pure absorbance spectra as well as give an estimate of the refractive index and the radius of the curvature on which the light scatters. Then, Figure 4.5B shows the water spectra in/around the bubble after Mie scattering correction.

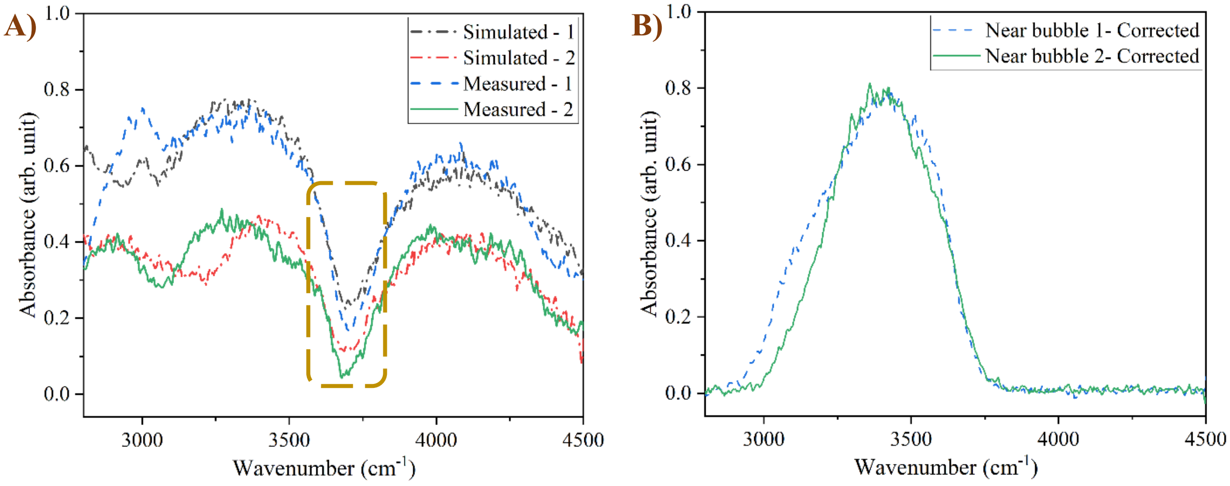

Figure 4.5. A) The measured and simulated mid-infrared spectra with the Mie scattering effect occurred inside/around the bubble (acquired by SCL-MCT (setup III)). B) The corrected spectra after Mie-scattering correction.

Herein, the model was trained on data created by simulating IR spectroscopic measurements. Due to the relative simplicity of the IR spectra of water, we trained our model on completely simulated absorbance spectra, where we simulated the water spectra as superpositions of three Gaussian curves. Indeed, decomposing the OH stretching region with three Gaussian components is a very classic scheme,[57, 103] providing excellent fits of the data with a minimum number of parameters (Okham's razor principle). We created the training data for our DCNN by simulating the bulk water spectra as three Gaussian sub-bands with randomly varying widths and heights and then calculating the scatter-distorted spectra for different spherical scatterers with radii between 2 and 13 microns and refractive index ratios between 0.2 and 1.3 by solving Maxwell's equations and calculating the loss of radiation as the light passes through the sample [314, 322]. Thereafter, we trained the model to solve the inverse problem and infer the absorbance spectra from the scatter-distorted spectra and the physical properties of the sample. The architecture of the DCNN is essentially the same as in Ref.[281], apart from the fact that we only have one spectral output channel since we need consider only a single sphere.

After completing training, we have a model that corrects the measured spectra, gives us the absorbance spectra, as well as predicting the radius and refractive index ratio. Thus, it can correct the scattering in the measured spectra in/around the bubble. We also used the corrected spectra and predicted physical parameters and simulate the scatter-distorted spectra to check that this is similar to the measured spectra and thereby demonstrate that our corrected spectra are viable and that Mie scattering can indeed explain the undulations seen in the measured spectra. It is crystal clear in Figure 4.5A that the simulated spectra are reasonably similar to the measured spectra in/around the bubble.

4.1.3. Thermal effect on the FTIR spectra of normal and bulk water

To deal with the various environments of a molecule concerning the H-bond connectivity, the OH stretching band is frequently decomposed into three Gaussian components (section 2.2.1.4). After decomposing the bulk water spectrum at different temperatures and compared with the normal one reported in the literature [57], the same thermal dependency is observed, even if bulk water is slightly NW-enriched (5%) and IW-depleted (4%) with respect to normal water (Figure 4.6 and Table 4.1).

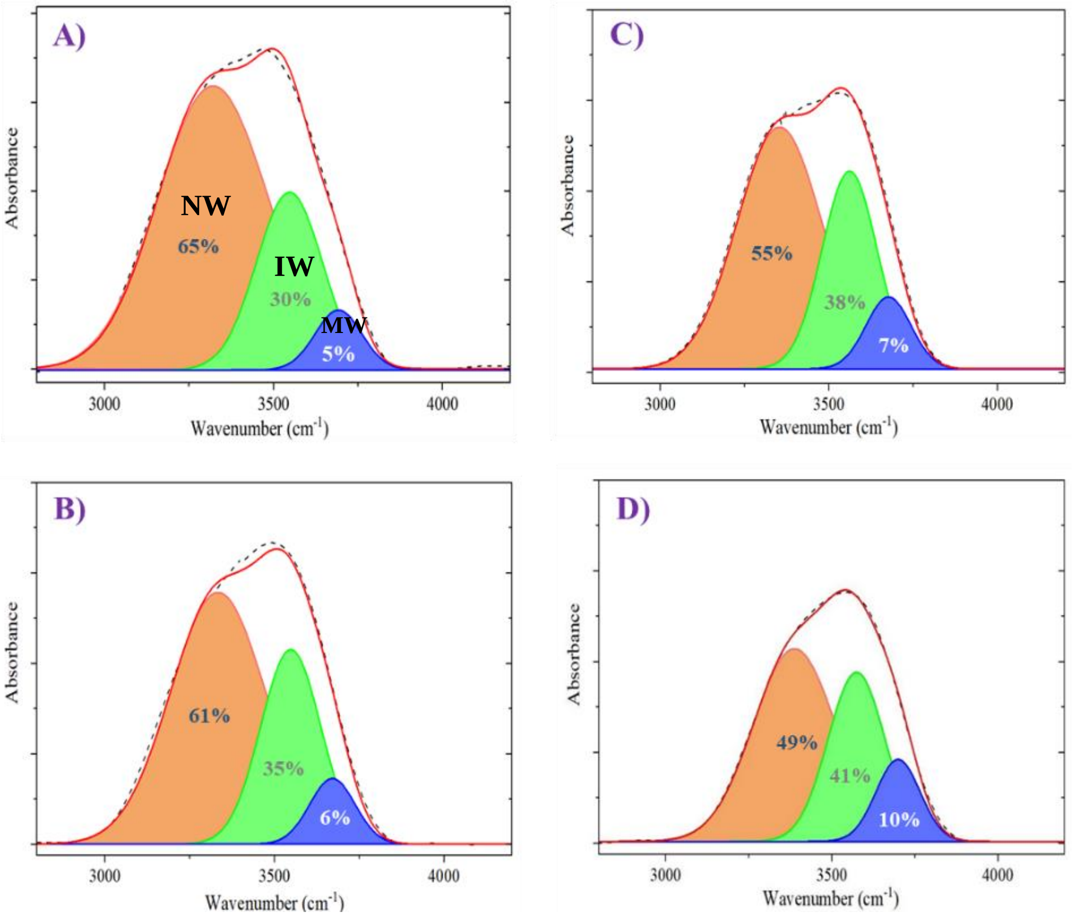

Figure 4.6. The decomposition model of bulk water spectra in the spectral range from 2800 to 4200 cm^{-1} at A) 22°C, B) 55°C, C) 85°C, and D) 155°C. The experimental data are the dotted line, and the solid line corresponds to the fitting curve. The decomposition into three Gaussian components, such as NW, IW, and MW, illustrates the percentage of their respective population.

Similar to normal water (see section 2.2.1.2), the first-order features of bulk condition consist in the blue-shift behavior of the three sub-bands peak position, demonstrating a connectivity loss with T as liquid water becomes more volatile (Figure 4.6). We can also mention that the band intensity (absorption value) decreases (from 0.87 arb. unit at RT to 0.71 arb. unit at T_h), an ordinary observable when liquid water is heated (i.e., the enthalpy diminishes and the entropy increases) [57].

Table 4.1 compares the contribution of each sub-band in bulk (Figure 4.6) with the reported value for normal water [57, 91]. It illustrates that increasing the temperature reduces the average coordination numbers of each H_2O molecule to its adjacent H_2O neighbors, even in bulk, which is expected due to the enhancement of vibrational energy with the thermal energy kT [323]. Generally, both normal and bulk water are characterized by the predominance of well-connected NW molecules, which is one of the most basic features of liquid water and makes it an 'associated liquid' [324].

Table 4.1. Comparing the each sub-band contribution (sub-band fraction) of bulk water with the reported value for normal water [57] at different temperatures.

Contribution of each sub-band	Bulk water		Normal water [57]	
	@ RT	@ 85°C	@ RT	@ 85°C
Network water (NW)	65%	55%	60%	52%
Intermediate water (IW)	30%	38%	34%	37%
Multimer water (MW)	5%	7%	6%	11%

To analyze more meticulously, three different parameters were drawn as a function of T for each sub-band of bulk water (Figure 4.7). Besides the blue-shifted behavior of each sub-band by increasing the temperature (already above-mentioned), the FWHM of the NW sub-bands shows a decreasing trend, making clear that the tetrahedrally connected molecules are less and less active with T. This change is also visible with the fraction of each sub-bands with enhancing T, which shows a significant decrease of the NW fraction while the other two increase (Figure 4.7C). As a result, temperature promotes a certain disorder in the H_2O network, which is well in line with the decreasing latent heat of vaporization. In conclusion, we can say that bulk water has certain specificities to be studied closely, but within a first-order interpretation, it behaves quite similar to normal water at RT and with increasing T.

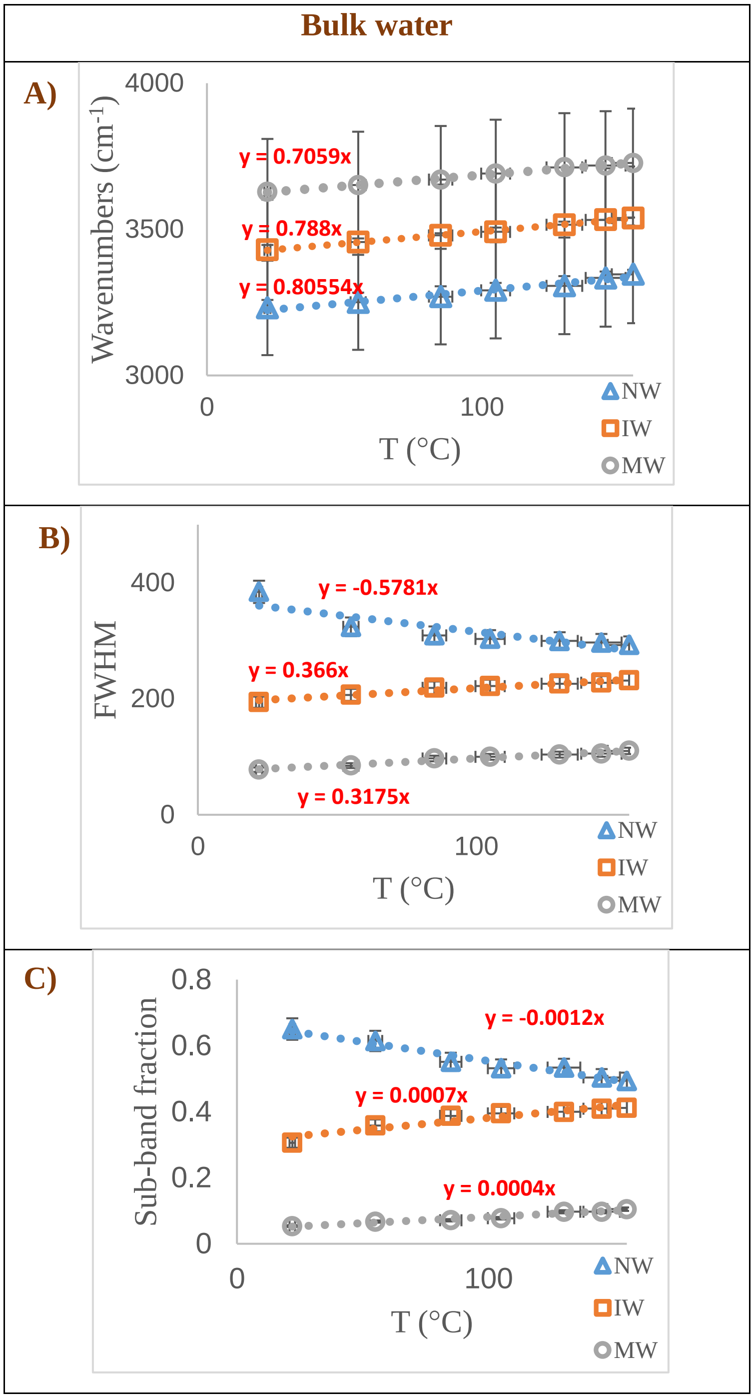

Figure 4.7. The main peak parameters of micro-FTIR bulk water spectra, such as A) peak position, B) FWHM, and C) sub-band fraction (contribution of each sub-bands) from RT to T$_h$.

4.2. Bulk vs. Interfacial water

Interfacial water is defined as water located along a solid wall (solid-liquid interface) or water vapor boundary (liquid-gas interface). The most questioning measurements we got with these fluid inclusions were acquired along the interfaces, displaying spectral signatures very different from the bulk ones, and whichever the type of interfaces (liquid-air and liquid-solid), the P-T conditions, the host minerals, and the fluid composition including the pH variation.

4.2.1. Spectral signature of water along a solid boundary

In this study, we employed 4 different micro-FTIR setups to record the variation of the OH-stretching band of water from the center to the boundaries at the optical plane, at different Z levels across the fluid inclusions (top to bottom cross-section), at various temperatures (with a small variation of the internal pressure: liquid-vapor saturation conditions), and with diverse polarizations of the incoming radiation. As mentioned earlier, the bulk water spectrum is considered as the reference spectral signature of water, and its spectral profile (peak shape and position) is carefully compared to other spectra recorded as a function of distance from the solid boundary or the bubble surface. In this way, different micro-FTIR experimental setups (with different infrared sources and detectors, see Table 3.1) are employed. All the micro-FTIR setups are evaluated based on their potential to capture the interface signature, defined as an additional band appearing in the OH stretching region between 3650 and 3750 cm^{-1}, either broadening the OH-stretching band or as a distinct dangling-type free OH band (see chapter 2).

Figure 4.8 compares the average/representative spectra of the OH stretching band recorded in the middle of the reference fluid inclusion (SFI-1) and near the quartz-water interface using four different micro-FTIR setups. Further on, Figure 4.9 demonstrates that the band shapes and the absorbance values change as a function of the beam location in the SFI-1, i.e., from the bulk (middle of inclusion) to the water-quartz interface (quartz boundary). In Figure 4.9, by showing the series of vertical linear maps across the SFI-1, the characteristic spectra of quartz, quartz-water interface, and bulk water can be well distinguished.

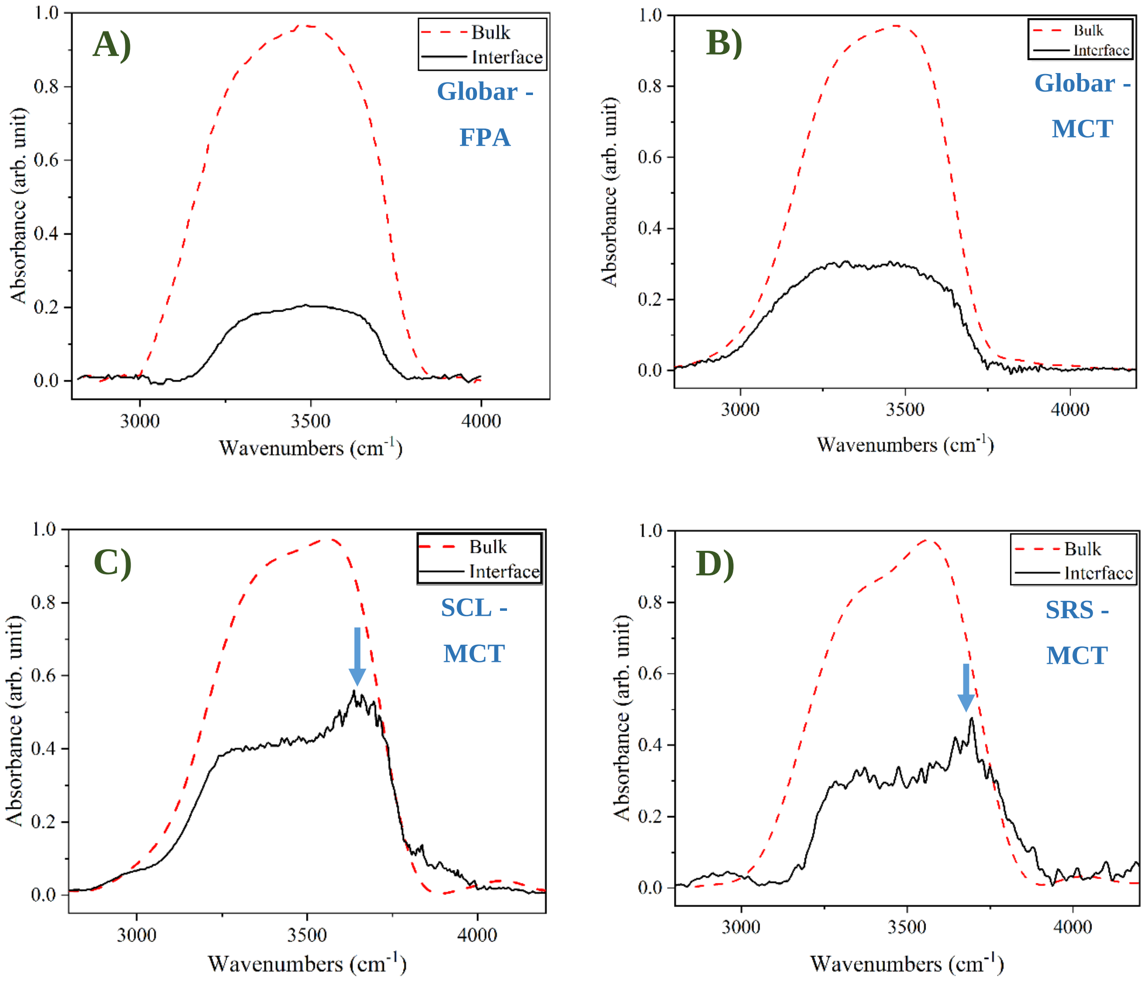

*Figure 4.8. The representative spectra of bulk and interface water (along the quartz boundary) using A) Globar source with FPA detector (**setup I**), B) Globar source with MCT detector (**setup II**), C) supercontinuum laser with MCT detector (**setup III**), and D) synchrotron beam with MCT detector (**setup IV**). The spectra were normalized, and the baseline was corrected. The arrows show the interfacial signature of water recording with setups exploiting supercontinuum laser and synchrotron beam as an infrared source.*

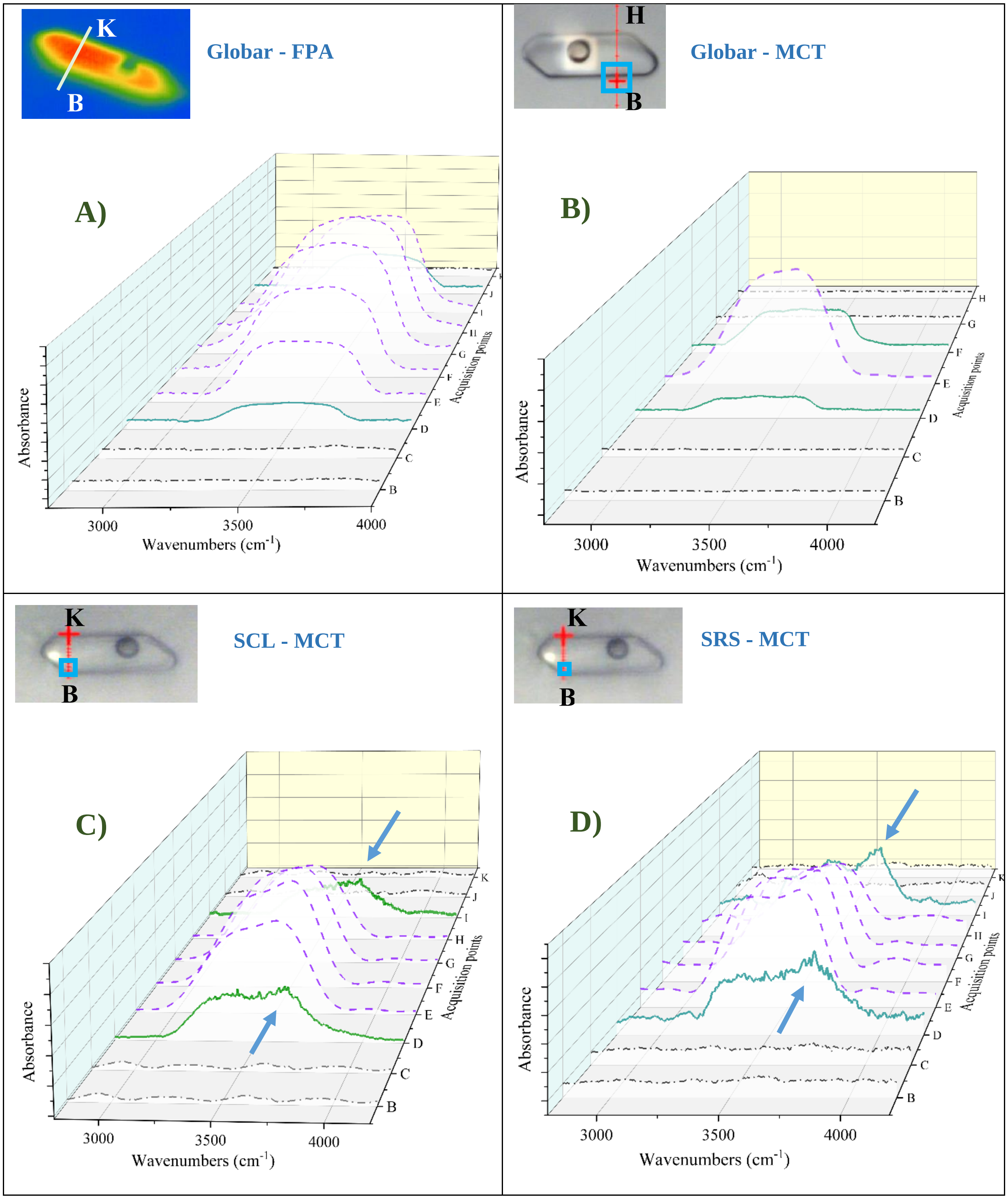

Figure 4.9. The variation of OH stretching band recorded across the SFI-1 before processing steps (from point B to point H or K) with A) Globar source with FPA detector (aperture-less microscope), B) Globar source with MCT detector, C) supercontinuum laser with MCT detector, and D) synchrotron beam with MCT detector. Black lines (dash-dot line) correspond to quartz, green (solid line) to the near liquid-solid interface, and purple (dash line) to bulk water behavior. The blue squares in panels B, C, and D correspond to the aperture size.

Setups exploiting the supercontinuum laser (SCL) and synchrotron radiation source (SRS) as an infrared source and using MCT detector (i.e., **setup III and IV**), providing the aperture sizes of 5×5 μm and 3×3 μm, respectively, revealed the presence of the sharp deformation of the water spectrum at c.a. 3700 cm^{-1} when approaching the quartz boundary (solid-liquid interface). In detail, the setup IV (Figure 4.8 & 4.9 D) based on a SRS allowed to record the sharpest, well-resolved band near 3700 cm^{-1}. This is related to the high spatial resolution down to the diffraction limit (equal to 2.53 μm at 2.7 μm wavelength) offered by the SRS coupled to the confocal microscope. These new results are the same as those of Bergonzi's, already performed with SRS, which was the first to reveal the specific interfacial behavior of water molecules at the micrometric scale along a solid wall [56]. Likewise, the setup III (Figure 4.8 & 4.9 C) can record similar signatures based on the mid-infrared fiber-based supercontinuum laser that allowed to achieve beam size of 5×5 μm in the laboratory condition. This conclusion aligns with the findings of Borondics et al. and Kilgus et al., who also observed the effectiveness of supercontinuum laser sources in facilitating high-resolution micro-FTIR measurements [260, 265].

In contrast, the Globar source with the FPA (setup I (Figure 4.8 & 4.9 A)) and MCT detectors (setup II (Figure 4.8 & 4.9 B)) did not allow to record the interface signature accurately because the interface domain is smaller than the actual spatial resolution of the system. Nevertheless, the aperture-less microscope with the FPA detector allows substantially faster data gathering at a spatial resolution two or three times bigger than the diffraction limit. These results confirm previous experiments, which demonstrated that the FPA detector may not always be suitable for exploring the chemical or physical features at the diffraction limit [277]. This may be counterintuitive as the area on the sample covered by each detector element has a dimension below the diffraction limit. However, because of the diffraction, each detector element receives a contribution from an area bigger than the area on the sample nominally covered by each element.

The microscope aperture of a confocal microscope employing synchrotron-based radiation or a supercontinuum laser source allows to control the spatial resolution at the diffraction limit and consequently records the interfacial signature. In the FPA detector-equipped microscope, physical apertures do not limit the IR beam illuminating region. Instead, the projected image of the unmasked IR beam on the sample is collected using an array of IR detector components;

therefore, the precision of aperture-less images is highly dependent on the optical system magnification and numerical aperture [277, 325, 326].

According to our main findings of reference fluid inclusion (SFI-1), the supercontinuum laser can be employed as a laboratory alternative to the synchrotron radiation source to conduct high-resolution micro-FTIR measurements down to the diffraction limit. This series of measurements proved that exploiting the μ-beam down to the diffraction limit is crucial for recording the interfacial behavior of water molecules [327].

Figure 4.10 shows the bulk and interface water spectra in the SFI-1 recorded with setups III and IV after applying the processing methods to eliminate the interference fringes and Mie scattering contributions. As can be seen, both experimental setups with diffraction-limited spatial resolution reveal evident differences between the bulk and interface as well as the presence of the particular spectral signature of water in the vicinity of the micrometric scale solid boundary. It is worth noting that the interfacial contribution is much more detectable after processing. This confirms unambiguously that the origin of the recorded interfacial signature is not related to any parasitic issues.

Almost the same spectra of bulk water were recorded using setups III and IV. However, there is a slight discrepancy between the interface signatures. This difference in the spectral profile (band shape and intensity) can be related to the smaller aperture size and higher spatial resolution provided by setup IV. In this setup, the integrated area of the interface spectrum and its absorption value are lower than those obtained by setup III. Also, it can be related to the geometry of the fluid inclusion, especially near the edges where the beam size is commensurate with the depth of SFI-1. Nevertheless, the main peak position locates in the same wavenumber (c.a. 3700 cm^{-1}) for both interface spectra (either setup III or IV).

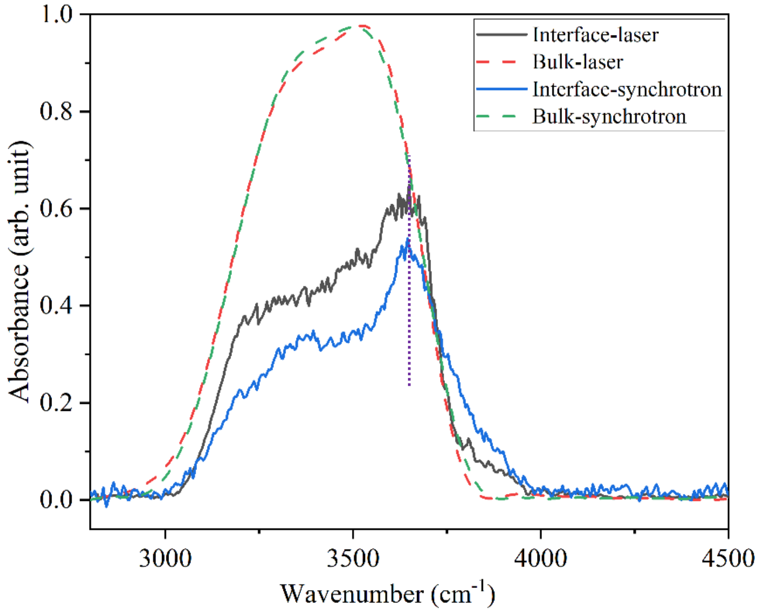

Figure 4.10. The average/representative mid-infrared spectra of bulk and interface water in the SFI-1 after processing acquired by laser (setup III) and synchrotron (setup IV) as infrared source.

The peak recorded c.a. 3700 cm^{-1} is assigned to the interfacial signature of water. This peak might be interpreted as dangling OH groups (i.e., molecules without any H-Bonding with their adjacent molecules). Bergonzi et al. justified their results by the presence of dangling OH mode within this surface water. At that time, it was unclear whether the small peak Bergonzi et al. recorded at 3700 cm^{-1} was distinct from the OH-stretching band itself (as is expected from dangling free OH mode) or belonged to it [56]. According to the non-linear spectroscopy methods (like the sum frequency method [328], Figure 4.11), the free or dangling OH mode appears as a distinct peak, separated from the OH stretching band when the liquid water is in contact with the hydrophobic interfaces.

In Figure 4.10, it is more evident that we have an additional peak within the stretching modes of water, and the superposition of the bulk and the interface spectra. As a consequence, the peak is not interpreted as detecting a pure dangling OH mode, which would be really unexpected and physically hard to conceptualize with a significant number of 0-connected molecules in a large amount of H_2O permanent dipoles. Indeed, we are probably not recording the presence of enormous amount of free H_2O molecules over a thick layer. The interfacial domain is rather characterized by an enrichment of the less-connected molecules (1 or 2-connected; see the “decomposition” section below). This observation suggests that the hydrophobicity along the solid-liquid interface promotes a chaotropic effect on the water molecule network, enriching the **less-connected molecule fraction.**

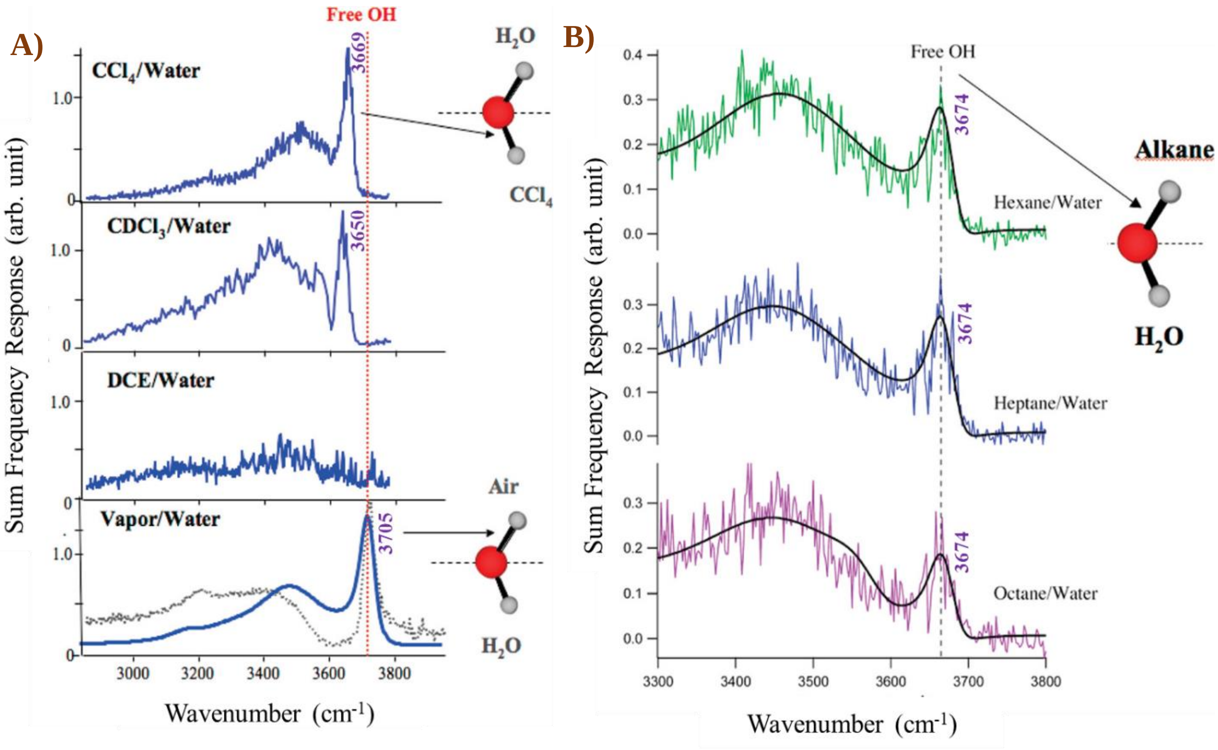

Figure 4.11. A) Sum Frequency spectra of water at three organic/water interfaces and the air/water interface. B) spectra of water at the interface of three alkane/water systems. Taken with SSP polarization [328].

4.2.2. Hyperspectral map of the reference fluid inclusion

A rastered hyperspectral map provides an opportunity to detect the interfacial effect, evaluate its scope of propagation in the fluid inclusions, and compare the spectra more meticulously as a function of the beam location.

4.2.2.1. Insight from supercontinuum laser

Figure 4.12 shows the rectangular spectral map of SFI-1 recorded with setup III in the laboratory after a few processing steps (baseline correction, normalization, and interference fringes removal). Two different absorbance distribution maps are presented with respect to the two characteristic wavenumbers: i) 3400 cm^{-1}, which corresponds to the bulk signature of water, and ii) 3700 cm^{-1} assigned to the interface signature, as previously presented in Figure 4.10. As shown in Figure 4.12, the bulk-like water spectra with maximum absorption values were observed in the middle of inclusion (far from the liquid-solid and liquid-vapor interfaces). Regarding the absorption value in bulk, this value gradually diminished toward the SFI boundaries, most likely because of reduced water quantity in the SFI borders.

Figure 4.12A shows the absorbance distribution maps before Mie scattering correction in which the interfacial behavior is observed in/around the bubble and along the quartz boundary. This is related to a large undulation detected at almost the same wavenumber as the interfacial signature (c.a. 3700 cm^{-1}) appearing in/around the bubble, which, as previously shown (Figure 4.5A), corresponds to the Mie scattering effect. By applying the Mie scattering correction method on all hyperspectral data, the interfacial behavior of water is observed neatly near the quartz boundary, i.e., along the water-solid interface, and around the bubble (water-air interface) (Figure 4.12B).

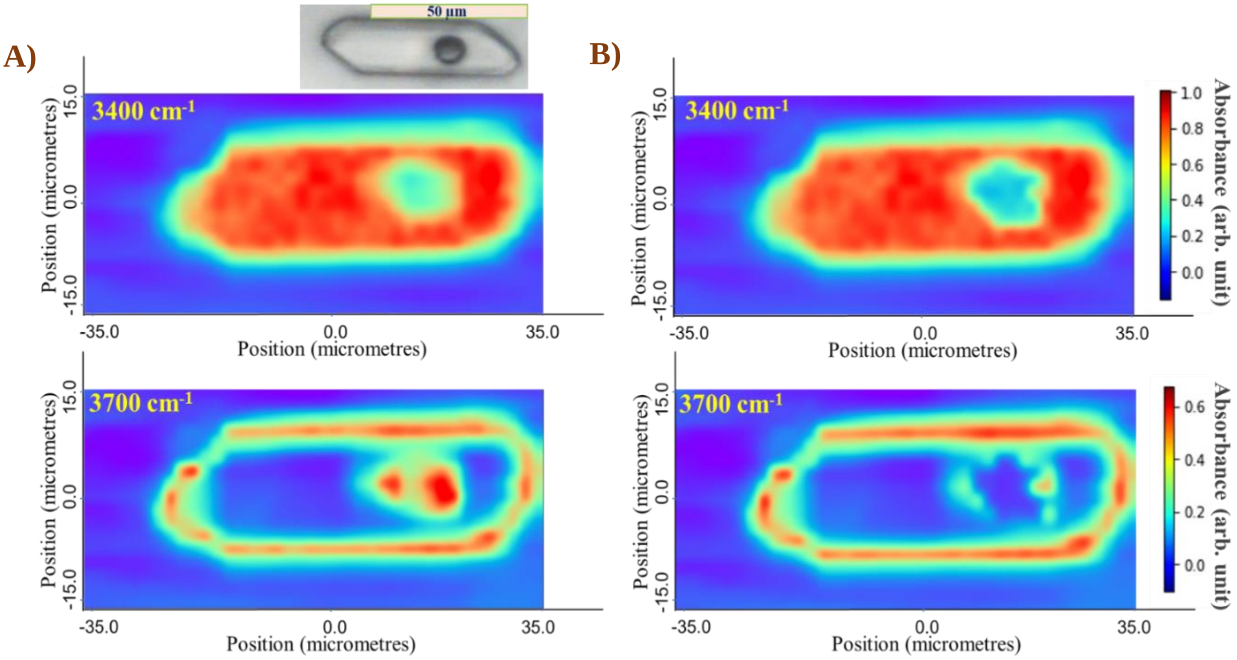

Figure 4.12. Hyperspectral maps of the SFI-1 acquired by setup III showing the distribution of absorbance at two characteristic wavenumbers: 3400 cm^{-1} related to the bulk and 3700 cm^{-1} representing the interface water behavior A) before and B) after Mie scattering correction.

4.2.2.2. Insight from synchrotron radiation

Hyperspectral maps were also recorded using synchrotron radiation as an IR source. Because of the higher brilliance and collimation, the beam size could be reduced to 3×3 µm. With this setup, the spectral maps were taken exclusively along the half-left part of the SFI-1 to avoid undesirable movement of the bubble. It is important to note that high energy and heat transfer of the synchrotron source caused a rapid movement of the bubble when the beam was focused on it. Since the bubble follows the beam location when getting in focus, we tried to avoid approaching too close to the bubble because such a situation significantly masks either the bulk or the interface features. Figure 4.13 shows the absorbance distribution maps of the half fluid inclusion after processing (baseline correction, normalization, and interference fringes removal) at the two characteristics wavenumbers representing the bulk (c.a. 3400 cm^{-1}) and interface (c.a. 3700 cm^{-1}) water behavior (as shown before in Figure 4.10). The interfacial spectral signature appears very sharp due to the higher spatial resolution of this method. As can be seen in Figure 4.12 and Figure 4.13, there is a good agreement between the hyperspectral maps obtained from setup IV and setup III.

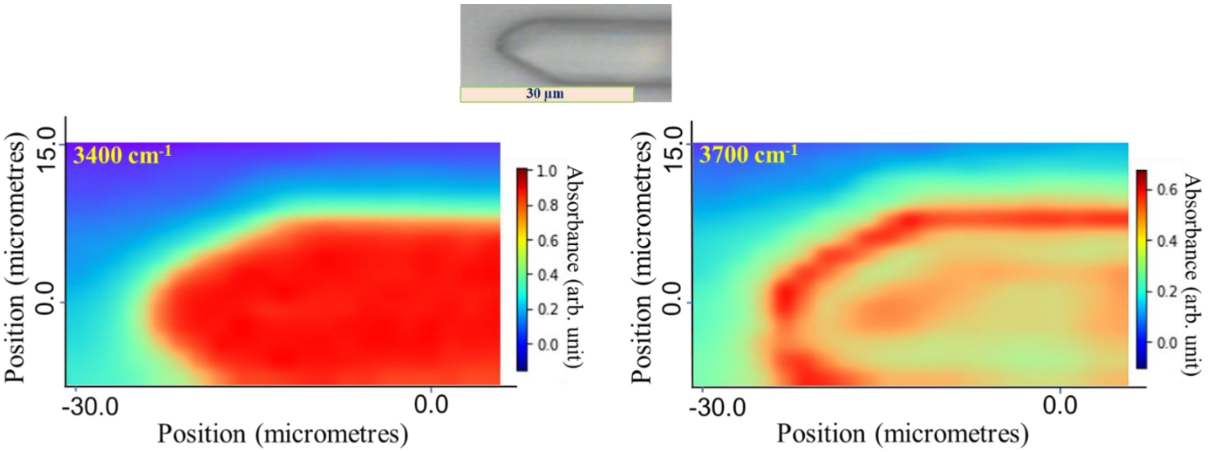

Figure 4.13. Hyperspectral maps of the SFI-1 acquired by setup IV (synchrotron beam) showing the absorbance distribution at two characteristic wavenumbers: 3400 cm^{-1} related to the bulk and 3700 cm^{-1} representing the interface. This hyperspectral map is not corrected by Mie scattering correction method.

4.2.3. Thermal effect on FTIR spectra of interfacial water

In this section, we specifically focused our study on the effect of temperature on the interfacial behavior of water using the reference SFI. In this way, a series of micro-FTIR measurements were acquired along the biphasic equilibrium (water-vapor saturation) curve at different temperatures from RT to T_h (155°C) (section 3.2 for further information).

As shown in Figure 4.14, the peak position (wavenumber), band shapes, and absorbance values vary with temperature, for both a bulk (middle) and an interfacial (edge) signature. It is well-established that increasing the temperature leads to a blue shift of the OH stretching band of water spectrum, with the peak position going toward a higher wavenumber (section 2.2.1.2) [57, 60, 66, 103, 104, 112, 329-334]. Herein, the interface signature behaves in that way as well (following the rear arrow in Figure 4.14B). It should be noted that the SNR decreased from 105 to 130°C due to the instability of the bubble (i.e., the bubble became smaller and smaller with T and disappeared at 155°C) that no longer adheres to pore walls and can move freely. In this condition, the bubble starts to follow the IR beam and superimposes over the water spectra, which decreases the SNR.

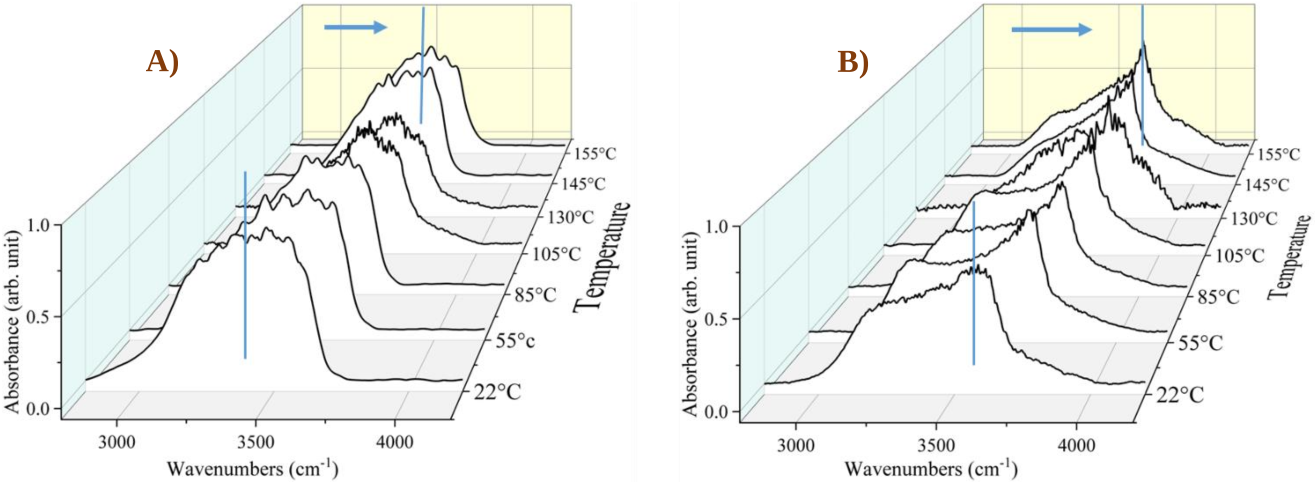

Figure 4.14. A) The representative/average spectra variation of SFI-1 at seven different temperatures (from RT to T_h) in the A) bulk and B) interface after processing steps, such as baseline correction, normalization, and interference fringes removal.

Figure 4.15 demonstrates a direct comparison of the hyperspectral maps between the two extreme temperatures (RT and T_h), which reveals major features: 1) the thickness of the interface-driven effect, i.e., the distance over which the interface signature is recorded, kept almost constant, possibly slightly increasing. 2) the intensity of the surface-imprinted signature increases with T, resulting in a denser, more marked surface-water layer.

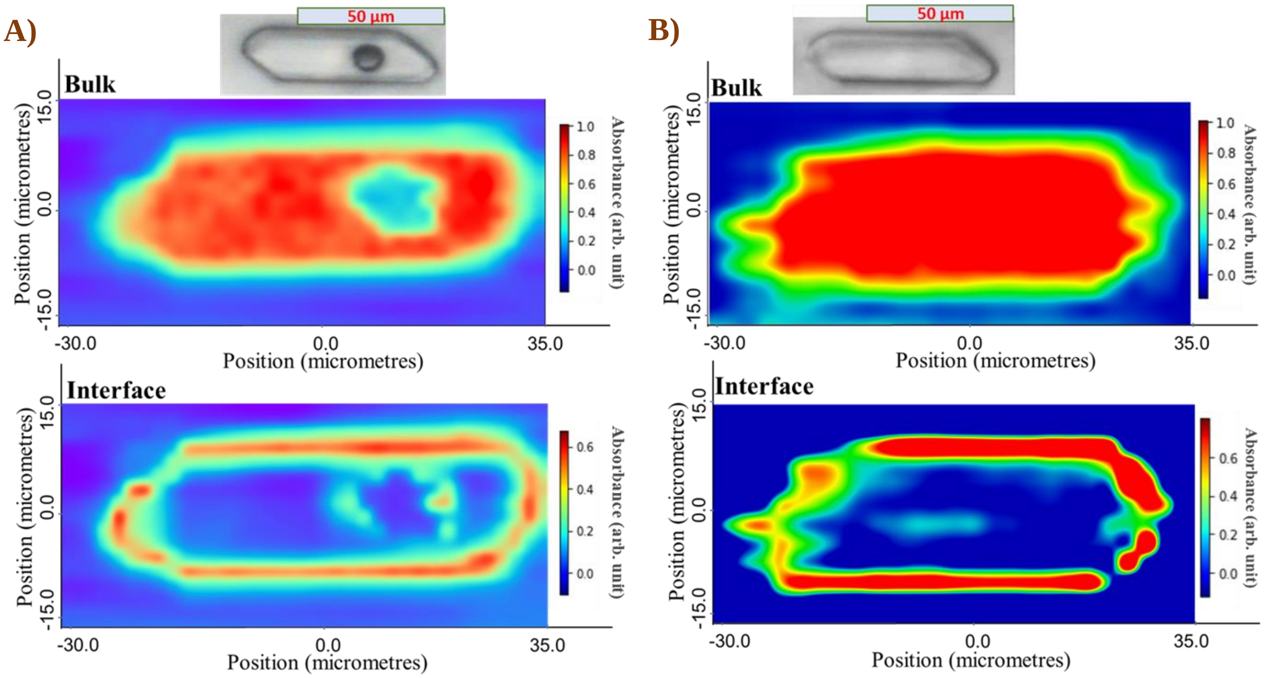

Figure 4.15. The absorbance distribution map of the SFI-1 at A) RT and B) T_h after data processing (baseline correction, normalization, and interference fringes removal) regarding the two main characteristic wavenumbers related to the bulk (c.a. 3400 cm^{-1}) and the interface (c.a. 3700 cm^{-1}). Both maps are not corrected by Mie scattering correction method.

4.2.3.1. Statistical analysis of the thermal effect

Moreover, the statistical analysis of the hyperspectral maps was done to investigate the spectral profile variation along the SFI-1. To do so, a statistical technique called non-negative matrix factorization (NMF) was employed in this study to reduce the dimensionality of the dataset and increase the interpretability while preserving the maximum information based on the multivariant analysis to investigate different components within the hyperspectral data [282-284]. NMF decomposes a dataset matrix into its non-negative submatrix whose dimensionality is uneven and chooses the best factorization rank and the number of components that is meaningful to the analysis. In NMF analysis, scores and loading are two main terms, which mainly correspond to the concentration and shape of the representative/average spectrum, respectively.

As shown in Figure 4.16, the NMF analysis of micro-FTIR measurements at RT and T_h represents the loading (principal component) as a function of beam location in the SFI-1. We are dealing with two main features at each temperature, corresponding to bulk and interface behavior of water molecules. This statistical analysis confirms that by approaching the quartz boundary (interface), the spectra of water are modified, and an additional peak from 3650 to 3750 cm^{-1} appears with respect to the bulk condition in the middle of SFI-1. Indeed, the NMF1 corresponds to the usual bulk behavior of water molecules, and the NMF2 represents the interfacial behavior of water molecules appearing along the quartz boundary. Moreover, it is evident that increasing the temperature shifts the main peak position toward a higher wavenumber, and the integrated area becomes smaller. Both these loadings are coherent with Figure 4.14 and enforce the self-consistency of the whole reasoning.

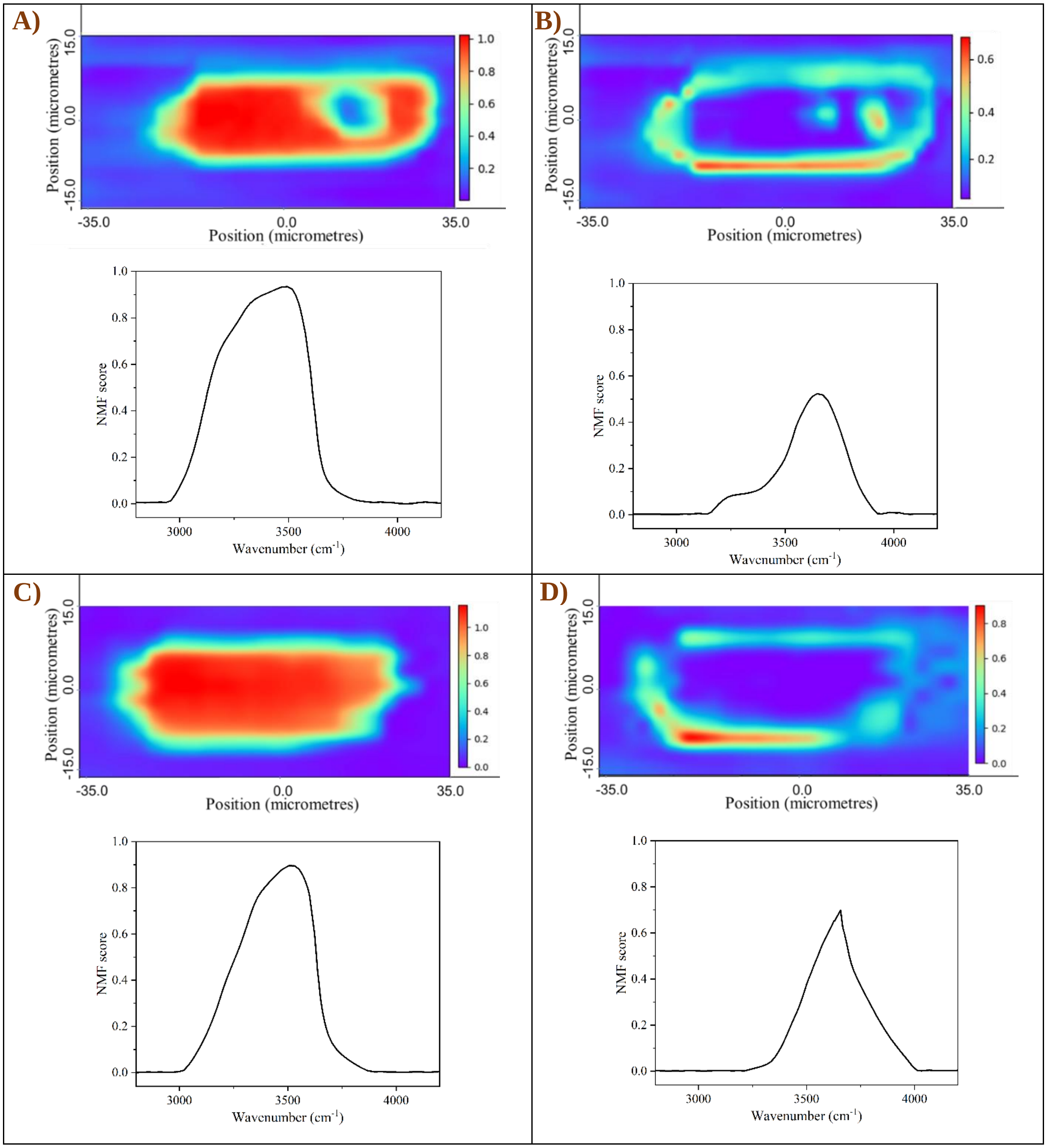

Figure 4.16. NMF analysis of micro-FTIR measurements. NMF1 (representing the bulk) at A) RT and C) T_h. NMF2 (defining the interface signature) at B) RT and D) T_h with their representative/average spectra.

4.2.3.2. Decomposition model of OH stretching band at different temperatures

After decomposing the OH stretching band into three Gaussian components, Figure 4.17 directly compares the three fitting parameters of bulk and interfacial water, such as peak position, FWHM, and sub-band fraction, for each sub-band as a function of T.

The vibrational energy is adequately expressed by the peak position of each sub-band and the blue shift trend of normal water with T is already highlighted (see section 2.2.1.2). Herein, along the interface, each sub-band shifts toward higher wavenumbers with T like the bulk, but either more than the bulk (IW and also NW) or less than the bulk (MW) (Figs 4.17A). But the difference between bulk and interface remains relatively negligible.

In terms of FWHM, the IW sub-band of interfacial water at RT overcomes neatly its NW counterpart indicating the energetic contribution of these connectivity strongly controls the average percolation of H-bonds. As T changes, both sub-bands exhibit similar patterns, but there is a noticeable gap intensification between them. This occurs because FWHM of the NW decreases to a greater extent than in the bulk, whereas the FWHM of the IW experiences a considerably larger increase compared to the bulk (Figure 4.17B). Likewise, the IW peak shift explains most of the interfacial sensitivity to T even if the NW behavior contributes to the energetic interfacial signature. As a direct consequence, the IW predominance at RT is enhanced with T with interfacial water becoming more and more active compared to the bulk. Very interestingly, the MW signature, which was assumed responsible for most of this interface-driven effect [56], is actually less sensitive to T change than the bulk, which points to a less active role in the energetic landscape of the interfacial water. At 155°C, the two FWHM of NW and MW covers together only half the FWHM of IW. It may be interpreted as decreasing the coordination number of water molecules along the quartz boundary, and that effect is enhanced by increasing T.

The most illustrative part comes probably from comparing how the fraction of each sub-band are modified with T for the bulk and the interfacial water (Figure 4.17C). The first and most striking outcome is that surface-imprinted liquid water is again dominated by IW over NW fraction even at RT (Figure 4.17C). The well-known predominance of NW water in liquid at the origin of many of its specific properties is no more met. The slope of variation with T (i.e., T-dependence variation) is similar for the bulk and interface water, meaning that the source of the H-bonding disruption is permanent and of similar intensity along a T range. The chaotropic effect of T is not the source nor increases the interfacial effect. Additionally, the initial small fraction of NW (abnormal feature with respect to bulk) and its negative slope with T (a classic trend with respect to bulk), compared with the MW's same features (all the same from bulk to the interface), makes the MW/NW ratio to change from 0.5 at RT to 1 at 130°C, the MW predominating over the NW fraction beyond 130°C.

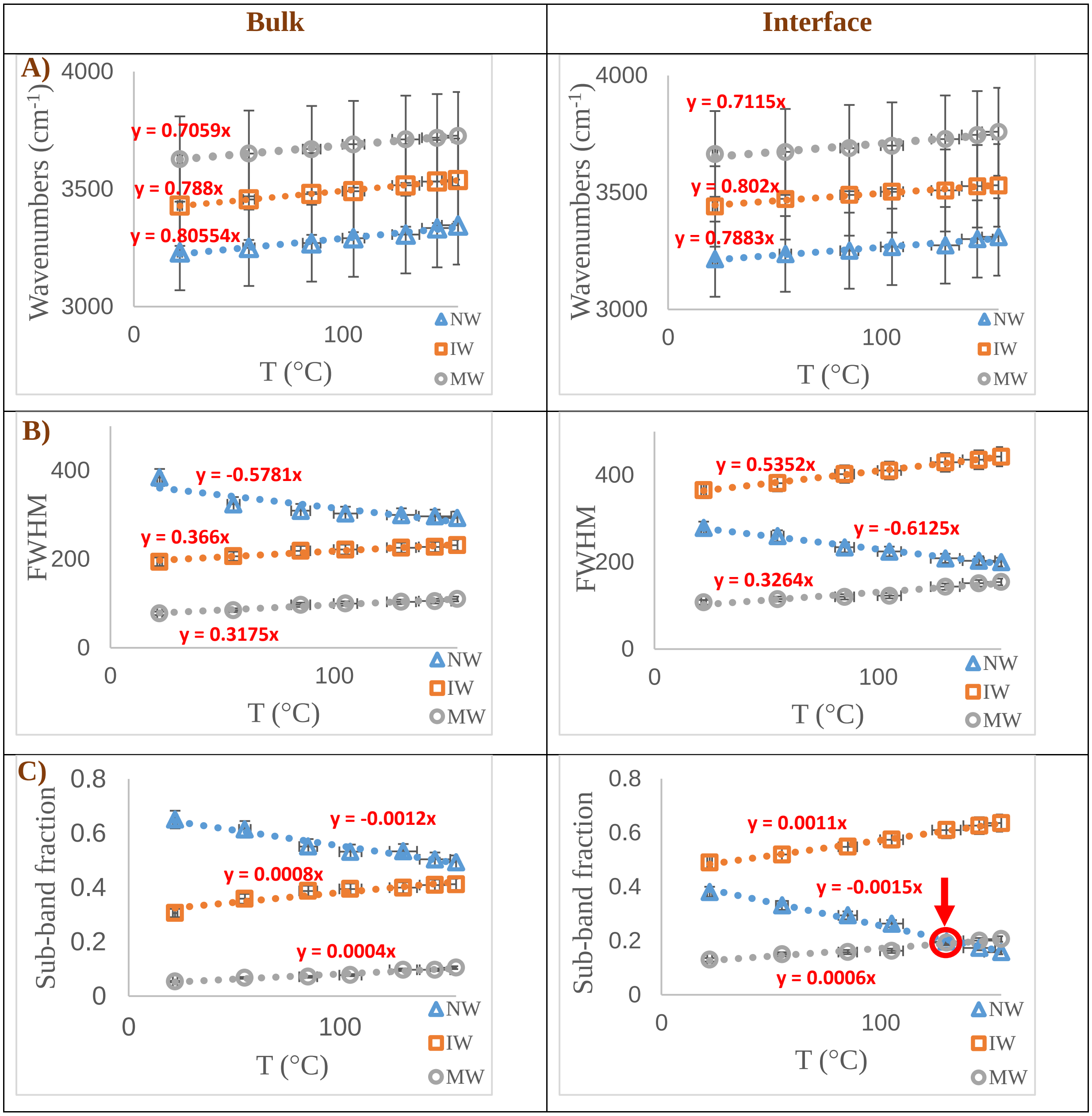

Figure 4.17. The main peak parameters of micro-FTIR water spectrum, such as A) peak position, B) FWHM, and C) sub-band fraction (contribution of each sub-bands) in bulk and interface (near the quartz boundary) at different temperatures. The circle in panel C shows the temperature at which the sub-band fraction of MW becomes more dominant than the NW.

The fraction ratios can be used to visualize the variation from bulk to the interface and adequately estimate its intensity. For instance, the MW/NW ratio can be mapped at the scale of the water-bearing cavity (Figure 4.18) and clearly outlines the interfacial border along the whole T range. Overall, the molecular networking of interfacial water is dominated by the IW (3-connected molecules) instead of the bulk feature, which is the NW predominance. Changing T does not provide a significant change in this behavior.

The most significant fact is that this disorganization among the H-bonds of water molecules percolates over almost thousands of monomolecular water layers, corresponding forcibly to an enthalpic penalty (disruption of H-bonds). This chaotropic effect is enforced with T, as shown with the slope of FWHM and sub-band fraction for the NW, IW, and MW sub-bands, which all change more at the interface than far from it (Figure 4.17). It demonstrates that the interfacial water is more sensitive to the T-driven chaotropic impact than the bulk at an identical thermal supply. The diminishing average connectivity throughout the molecular network favors its ability to exploit entropic supply by the thermal stage. This may be interpreted as a signature of a diminished heat capacity at the interface.

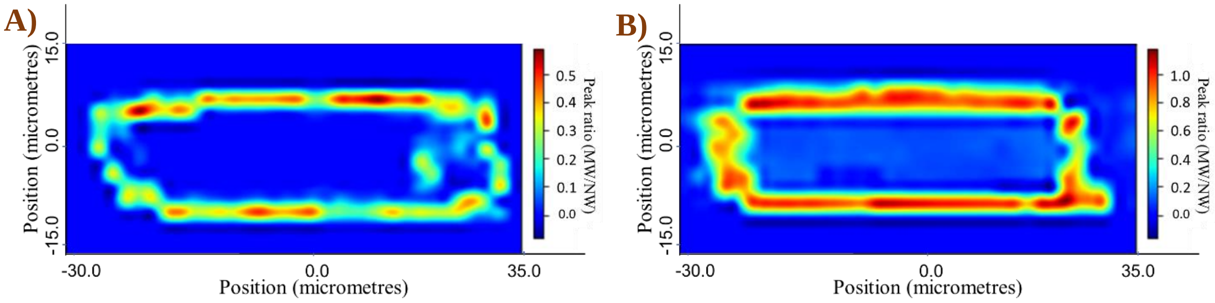

Figure 4.18. Mapping the peak ratio of the third to first sub-band (MW/NW) at A) RT and B) T_h*, which represent the contribution of the less-connected (two to zero H-bonds) water molecules with respect to the well-connected ones (four H-bonds).*

In molecular terms, Figure 4.18 corresponds to an increasing distance between neighbor molecules and varying $O - H \cdots H$ bonds [335]. Herein, this variation occurs over thousands of molecules, indicating that the average intramolecular force decreases, leading to weakening of the H-bonds of each molecule created with its possible neighbors. The best analog situation at the larger scale, though more or less exactly the reverse, corresponds to water confined in nanoporous hydrophilic silica materials. The measurements recorded decreasing density and surface tension [335, 336], increasing heat capacity of water [337], and red-shift of the OH-stretching band with NW increase and IW decrease [107]. In the latter study, the authors postulated that their whole measurements correspond to a surface shell of water molecules superimposed to a bulk-like behavior in the rest of the nanopore (from 8 to 320 nm). They found out that this surface layer varies with the pore size from 3 nm to 30 nm. In parallel, the silanol surface groups are assumed to play a role in that confinement effect, congregating highly coordinated water molecules [335], while we are postulating that the hydrophobic interactions disrupt the water H-bonding and diminishes its cooperativity. As a consequence, the interface-driven effect would be dominated by a surface component, visible as a kosmotropic enhancement with hydrophilic pore walls owing to confinement, but revealable as a chaotropic disorder and H-bonds loosening along hydrophobic pore walls with a sufficiently small beam.

Indeed, there are two synergistic effects on micron-thick water layers along a solid boundary: 1) thermal effect and 2) interface-driven effect. According to our findings, the interface-driven effect is enforced by the temperature, and both have a chaotropic effect on water molecules by disorganizing their molecular networking. However, we observed that the interface-driven effect plays a prominent role compared with the thermal one. Clearly, the physical realm of IW predominance is already installed at RT, and keeps stable and (even increasingly) visible along the 130°C range of our present study. Additionally, we can expect that our dataset minors the reality due to our methodology, the hydrostatic pressure increases along the thermal ramp, forcibly promoting connectivity and diluting the T-based synergy to the interface-driven signature.

4.2.4. 3D measurements of the interfacial effect

By now, all the presented data were recorded at the focal plane (constant Z level, equal to Z_0), and beam location was changed along the X-Y axes (2D measurements). We decided to perform 3D measurements, taking benefit of the confocal geometry of the Nicolet microscope allowed by the curvature of its Schwarzschild mirrors (section 3.3.1, [255]). The main objective of this study was to avoid the issues related to the curvature of the side interface, with the Mie scattering issue. The top and bottom interfaces in our reference inclusion give the opportunity to prospect what spectral signatures are recorded when IR-beam probed on almost planar interfaces.

We chose a point at given (X, Y) coordinates, and the acquisition was taken every 0.5 µm (normalization of the Z-step scale in the microscope) from the top to bottom water-quartz interface. It should be noted that Z_+ means the displacement of the microscope stage from a focal plane (Z_0) to the bottom of SFI-1 (bottom interface), and Z_- defines as changing from a Z_0 to the top of SFI-1 (top interface).

Figure 4.19 shows the variation of water spectral profile at different Z levels across the whole thickness of SFI-1 in three chosen points at given X-Y value in the bulk region (points (i), (ii), and (iii) in Figure 4.19A). As already mentioned in chapter 3, since SFI-1 is located inside the quartz fragment, it has an interface with quartz at two different Z levels. The total thickness of the fragment is 19 ± 1 µm with a thickness of quartz above the fluid inclusion at 4 µm and below the fluid inclusion at 10 µm. The blue lines (Figure 4.19) delimit the last water-bearing spectra in the crossing. Namely, they are the spectra that can be most easily associated with the top and bottom water-quartz interfaces. The top water-quartz interface displays the classic interfacial signature, predominating the higher wavenumber component. The bottom interface is not marked by this signature but displays a clear Mie scattering phenomenon with a large baseline undulation, especially marked c.a. 3700 cm^{-1} wavenumbers. This result showed that the methodology with the planar interfaces does not guarantee the absence of Mie scattering. We are still working with our Norwegians collaborators (BioSpec group) on the post-treatment of this dataset to investigate whether the undulation turns into a high wavenumber peak characteristic of the interfacial domain. It is also interesting to note that the interfacial signature is visible top-wards only at 0.5 µm of the solid surface and is no more visible at 1 µm. Bottom-wards, the interface is less marked but seems to extend over 1 µm.

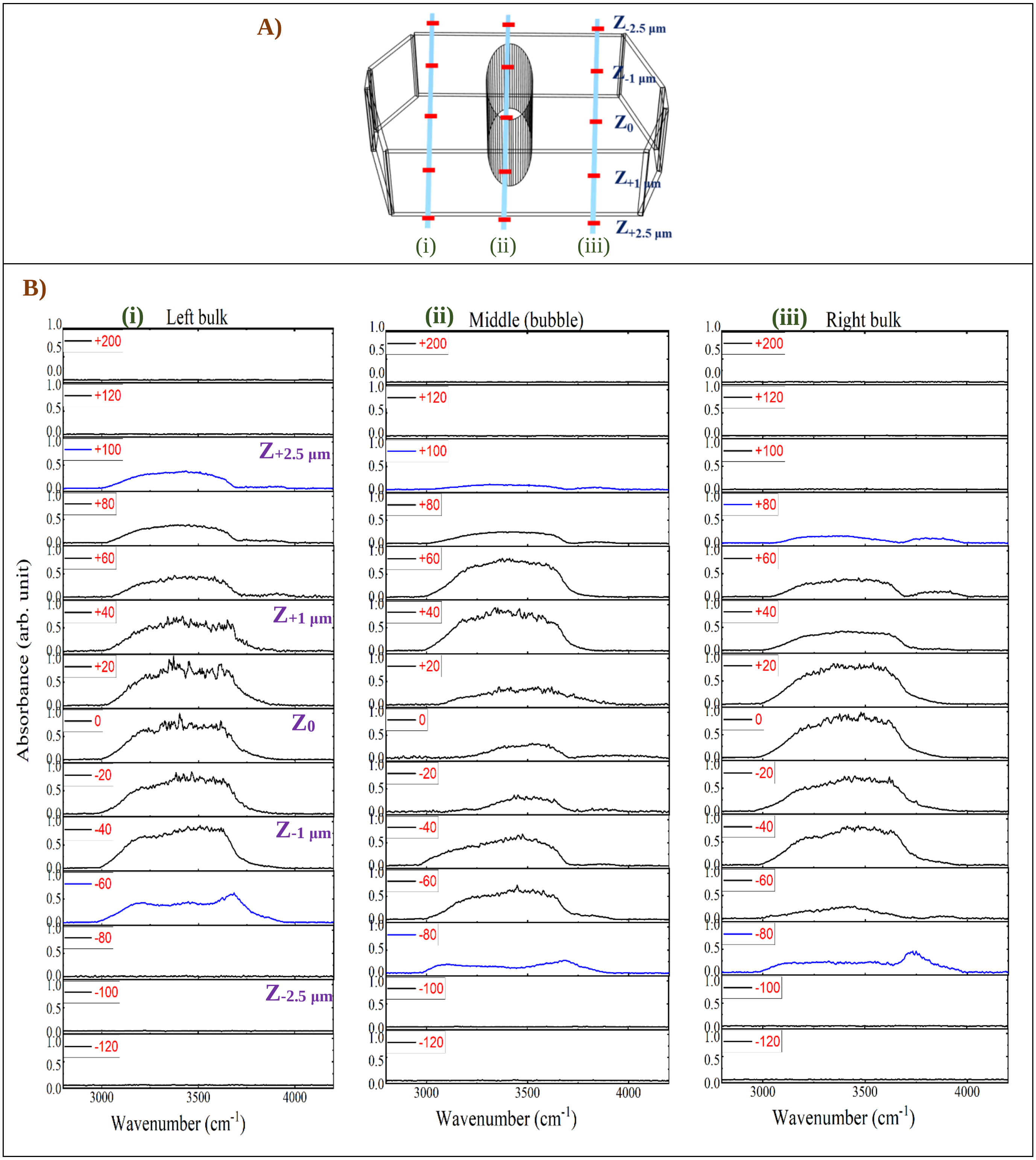

Figure 4.19. A) location of acquisition points in the reference fluid inclusion. B) The variation of micro-FTIR spectra of water in the three points, namely (i), (ii), and (iii) at different Z levels across the thickness of SFI-1 (3D measurements). Numbers inside the graphs represent the Z steps (every 20 steps ≈ 0.5 µm).

Moreover, it is possible to measure the thickness of the SFI-1 by recording the water spectra at different Z levels (3D measurements) and comparing the results with the value acquired by X-ray tomography measurements with sub-micron accuracy. As shown, the quartz spectra appear at the Z_{+120} & Z_{-80} on the left and Z_{+100} & Z_{-100} on the right side of SFI-1. It illustrates that the SFI-1 does not have a perfect horizontal shape (it has a slight slope, $\theta = 4°$). It is demonstrated by the presented spectra, where the left part of the SFI-1 shows the water spectrum at more positive Z levels than the right side. Also, we can deduce that the thickness of SFI-1 is equal to almost 5 ± 0.5 µm, which is consistent with tomography measurements.

4.2.4.1. Statistical analysis of 3D displaying of interfacial effect

Two hyperspectral maps of SFI-1 are recorded at two different Z levels for probing the interface behavior. Figure 4.20 shows the NMF analysis of micro-FTIR measurements at $Z_{+1\mu m}$ and $Z_{-1\mu m}$, representing the loading (principal component) as a function of beam location in the SFI-1. As shown, we are dealing with two main features at each Z level, corresponding to the bulk and interface behavior of water molecules. Indeed, there are two sets of NMF in this data series. The NMF loading varies depending on where the infrared beam is located in the inclusion, demonstrating a considerable shift from the center to the solid boundary walls. Surprisingly, whereas the NMF1 reveals a thick layer of water molecules in bulk, the NMF2 shows the transition from bulk liquid to solid, which may be considered an interface signature at $Z_{-1\mu m}$ and a Mie scattering signature at $Z_{+1\mu m}$.

This statistical analysis confirms that by approaching the quartz boundary (interface), even at $Z_{\pm 1\mu m}$, the spectra of water are modified, and an additional peak c.a. 3700 cm^{-1} appears with respect to the bulk condition in the middle of SFI-1. Indeed, the NMF1 corresponds to the usual bulk behavior of water molecules, and the NMF2 represents the interfacial behavior of water molecules appearing along the quartz boundary and the Mie scattering effect occurring on the bottom side of the SFI-1. Both these loadings are coherent with spectra, shown in Figure 4.19.

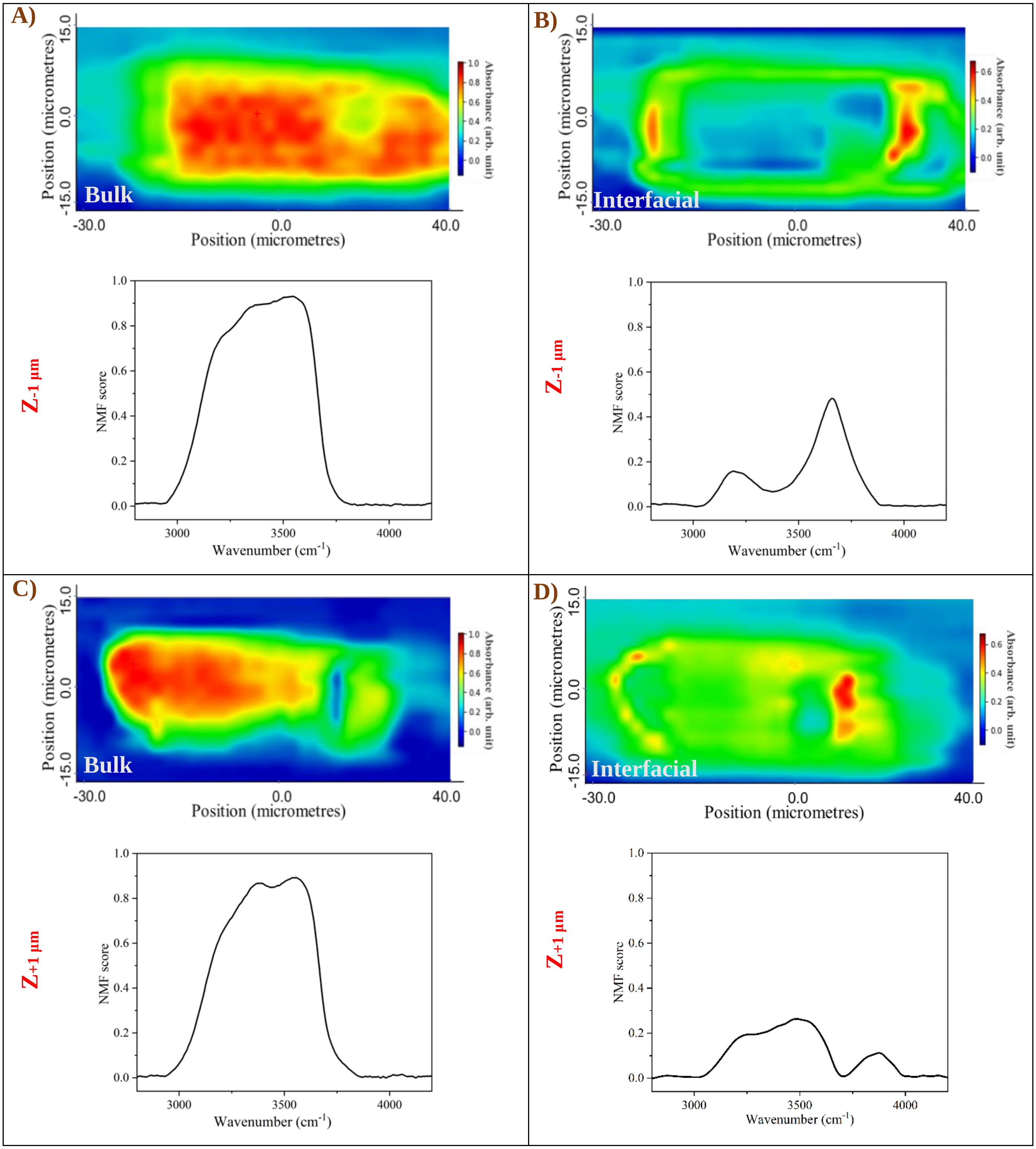

Figure 4.20. NMF analysis of micro-FTIR measurements at two Z levels proportional to the well-focused plane (Z_0). NMF1 at A) $Z_{-1\ \mu m}$ and C) $Z_{+1\ \mu m}$ & NMF2 at B) $Z_{-1\ \mu m}$ and D) $Z_{+1\ \mu m}$ with their representative/average spectra.

4.2.5. The effect of polarized incident radiation on interfacial water

Polarized FTIR spectroscopy has been used extensively to study the orientation at the molecular level of samples showing optical anisotropy, such as oriented polymers and thin films [338]. Herein, polarized micro-FTIR is employed for recording the spectra with the polarized infrared radiation parallel (0°) and perpendicular (90°) to the beam direction. As shown in Figure 4.21A, almost the same representative spectra have been recorded for the bulk water in the SFI-1 in the polarized (0° and 90°) and non-polarized mode at the focal plane (Z_0). Moreover, the representative spectra of bulk and interface were recorded at the ±1 µm far from the Z_0 to compare the polarization effect on the behavior of water spectra at different Z levels (Figure 4.21 B&C). As presented, there are no significant differences between the water spectra in bulk with or without the polarization at $Z_{\pm 1\mu m}$ far from the Z_0.

Nevertheless, slight discrepancies regarding the spectral profile (band shape and peak ratio of MW/NW) appeared near the solid-liquid interface. Indeed, the main change in the interfacial spectrum is a decreasing intensity of the whole band under polarization, obviously related to the diminished number of photons. But the low-wavenumber part of the band decreases more than the high-wavenumber part, meaning the polarization (regardless the direction) highlights the loss of order. However, the absence of sensitivity to the polarization angle prevents us from concluding something linked to orientational disordering/ordering along the water-solid boundary.

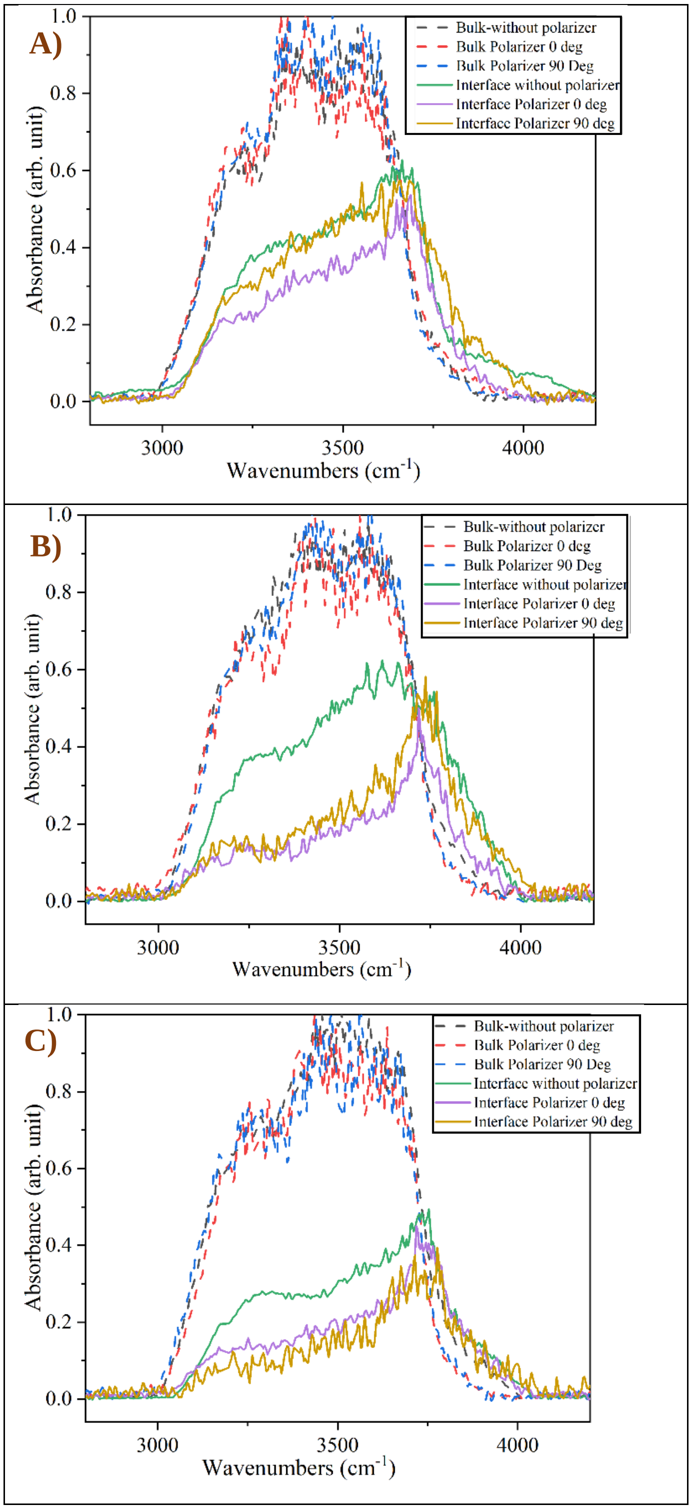

Figure 4.21. The effect of the polarization on the representative micro-FTIR water spectra in bulk and near the solid-liquid interface at A) Z_0, B) Z_{+40} steps (+1 μm), and C) Z_{-40} steps (-1 μm) after processing steps, such as baseline correction, normalization, and interference fringes removal.

4.2.6. Raman micro-spectroscopy measurements

A complementary Raman scattering study was conducted only on the SFI-1 (reference SFI) since Raman scattering measurements provides spatial resolution of 1 µm. As discussed in section 2.1.3, since water molecules have a strong dipole moment and weak polarizability variation, Raman scattering has less sensitivity to water. Indeed, water is considered as a “weak Raman scatterer.”

4.2.6.1. Interfacial signature near solid boundary

Raman scattering spectra of water in the OH stretching region were recorded over the entire surface of the SFI-1, taken in the focal plane (Z_0). Regarding the spectral profile variation, as shown in Figure 4.22, the intensity of the band decreased near the water-quartz interface. A detailed observation of the band shapes showed that the peak ratio of the first to second sub-band (3250/3450 cm^{-1}) was significantly higher at the interface than at the bulk. In Figure 4.22A, each spectrum was normalized by the spectrum, which has the highest Raman intensity. However, in Figure 4.22B, each spectrum was normalized by its own intensity to show the peak ratio variation more meticulously. As shown, no interfacial signature of the water molecule (less-connected water molecules, dangling OH mode) was detected regardless of the beam location. It might be related to the fact that Raman spectroscopy has a lower sensitivity to changes in the molecular environment with respect to micro-FTIR spectroscopy.

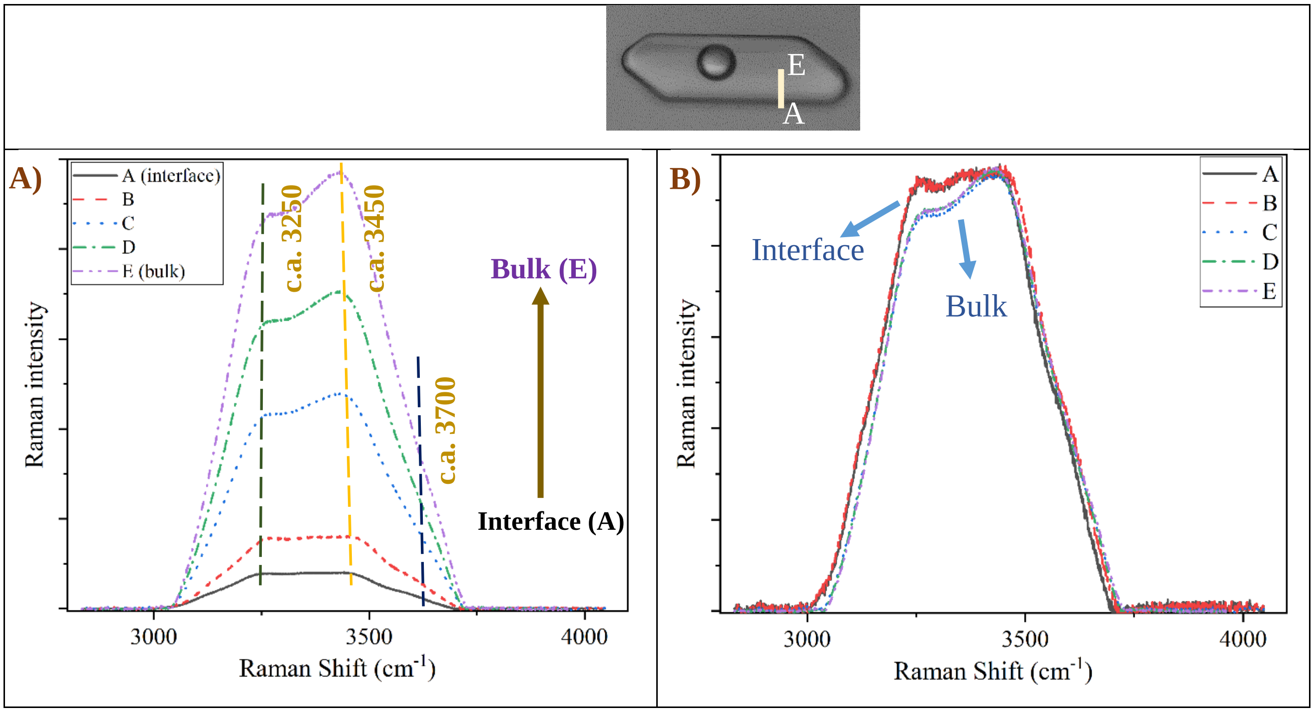

Figure 4.22. Raman spectra variation by approaching the solid surface (from A→ interface to E→in bulk) after processing steps, such as baseline correction and normalization to A) the spectra having the highest intensity and B) each spectrum by itself.

4.2.6.2. Effect of the temperature on the Raman spectra

Figure 4.23 shows the bulk water spectra variation at different temperatures from RT to T_h. The blue-shifted behavior is observed by increasing the temperature, similar to the micro-FTIR measurements (i.e., the peak position shifts toward high wavenumbers (Figure 4.14)). Besides the peak shift, the low-wavenumber part of the OH stretching band (network water, c.a. 3250 cm^{-1}) is suppressed by increasing the temperature. Raman spectra variation by increasing the temperature confirms the assumption acquired by micro-FTIR measurements that the temperature has a chaotropic effect on the water molecules network (the fraction of less-connected water molecules enhances with temperature), which is expected due to the enhancement of vibrational energy with the thermal energy *kT* [323].

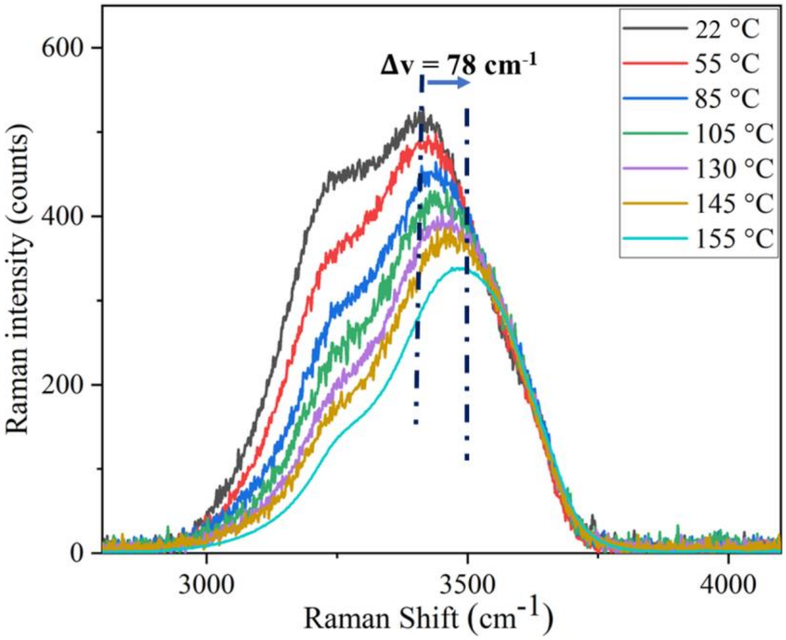

Figure 4.23. Comparison of bulk water spectra at different temperatures, from RT to T_h.

4.2.6.2.1. Statistical analysis of Raman spectra at different temperatures

The statistical analysis (NMF) of the hyperspectral maps of Raman scattering measurements has been performed at RT and T_h (Figure 4.24). As shown, one NMF loading has been acquired for the SFI-1 at each temperature with respect to the spectral variation (i.e., corresponding to the bulk behavior of water molecules). This statistical analysis confirms that Raman measurements cannot detect the interfacial behavior of water by approaching the quartz boundary (interface) (i.e., the interfacial signature with an additional peak 3650-3750 cm^{-1} does not appear). Indeed, the presented loading is coherent with Figure 4.22, where the interfacial signature of water spectra has not been observed by approaching the water-quartz interface.

This analysis somehow contradicts a previous analysis performed by Bergonzi et al., using a PCA (principal component analysis) method [56]. According to their statistical analysis, the interfacial behavior of water was detectable, so they used Raman scattering measurements to estimate the thickness of the interfacial water, resulting in a 1 μm distance from the quartz boundary.

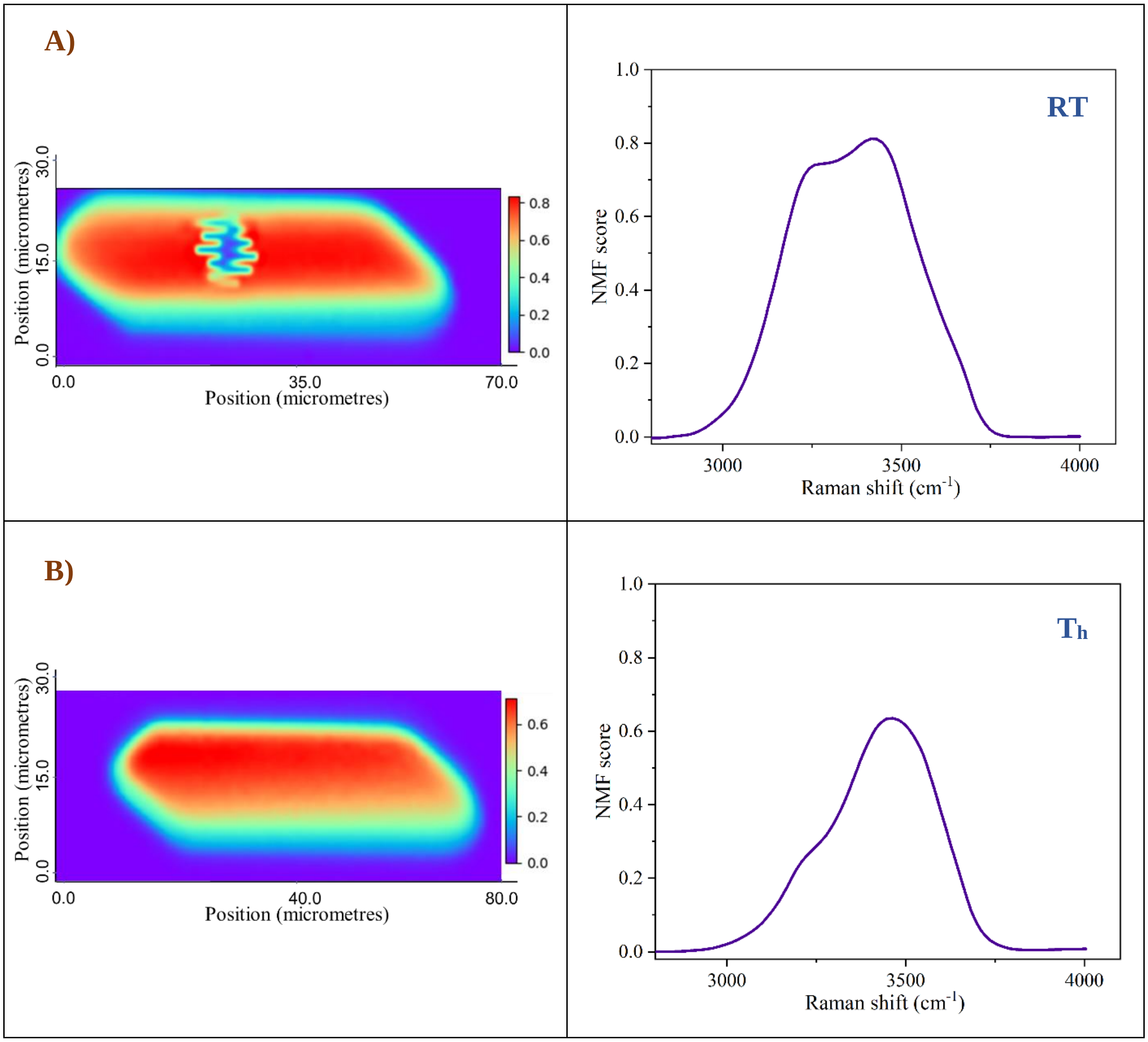

Figure 4.24. NMF analysis of micro-Raman measurements. A) NMF1 at RT and B) NMF1 at T_h *with their representative/average spectrum.*

4.2.6.3. Effect of the polarized radiation on Raman spectra

A series of Raman scattering measurements were conducted by adding the polarizer in two different parallel-polarized conditions (horizontal-horizontal (HH) and vertical-vertical (VV)) in the comparable mode to the micro-FTIR experiments with the 0° and 90° polarizer angle. A major drawback of the polarized Raman scattering method was the extreme weakness of the signals, which led to a lower SNR. Figure 4.25 shows the Raman spectra variation through the linear map from the quartz-water interface to the bulk (from points 1 to 9). As shown near the solid surface (points 1 and 2), the changes from the spectrum of bulk water are evident in the vertical-vertical polarized spectrum. However, the system shows almost the same spectra for the horizontal-horizontal polarized condition with respect to the normal one (non-polarized state). The variation of the vertical-vertical polarized spectrum is observed especially regarding the peak ratio of the first to second sub-band (NW / IW) between the vertical-vertical polarization mode and the horizontal-horizontal one. The variation of (NW / IW) in water spectra with the vertical-vertical polarizer has already been reported for normal water and through theoretical calculation [116].

It should be mentioned that the spectra are shown after baseline correction, and the step size (distance between two consecutive beam locations) is 0.5 μm. Therefore, we can define the propagation scope of the solid surfaces so that after 1 ± 0.5 μm far from the quartz-water interface, the bulk water behavior is observed, where there are no differences between the polarized and depolarized Raman spectra of water.

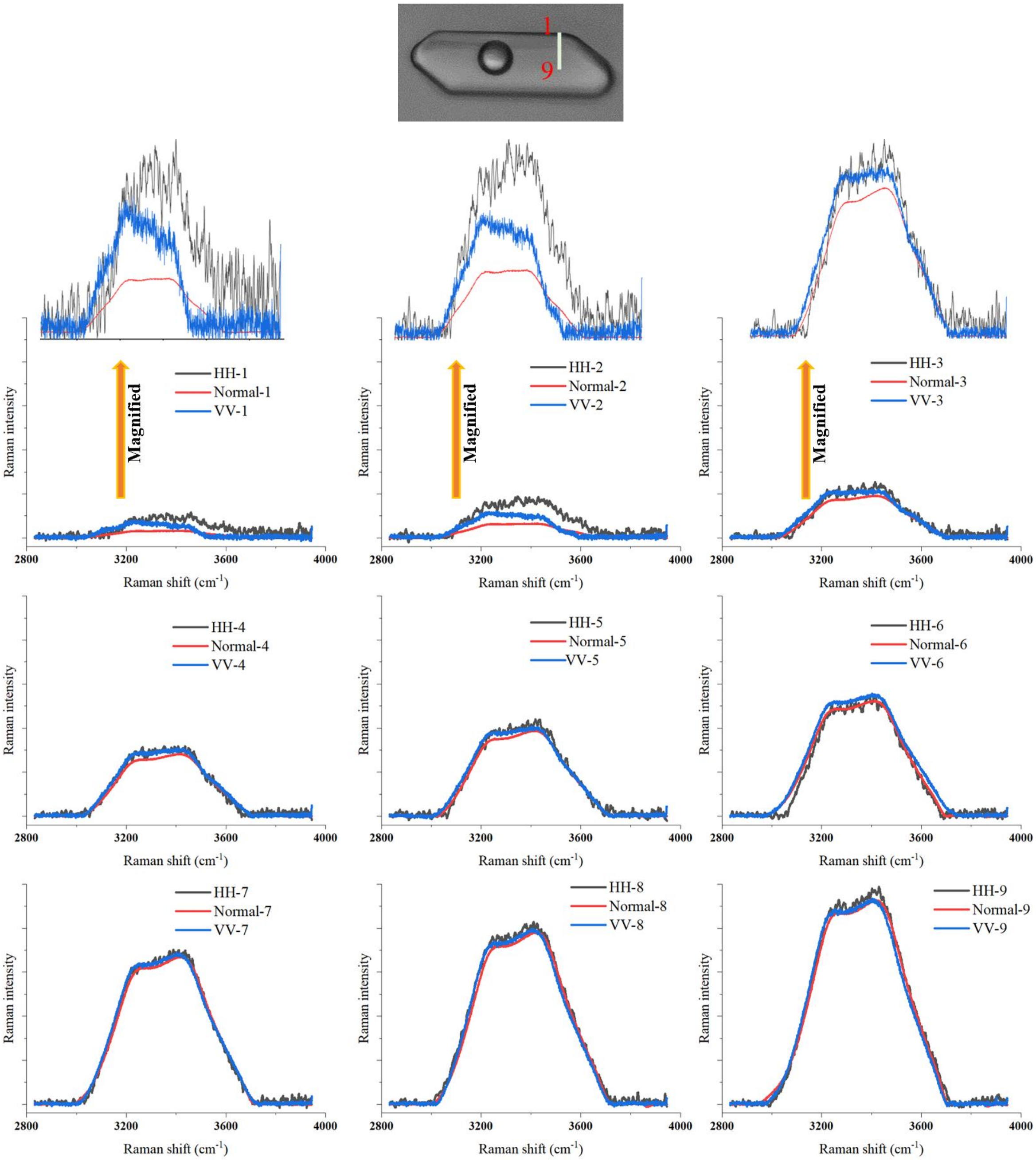

Figure 4.25. Raman spectra variation of water located in SFI-1 from points 1 to 9 at two different polarization conditions (vertical-vertical (VV) and horizontal-horizontal (HH)) and without polarizer (normal).

4.3. The origin of the interfacial signature

In this section, the possible origins and/or control parameters of the interfacial signature in the micro-FTIR water spectra along the solid boundary are presented.

4.3.1. Morphology of closed cavity

Herein, we investigate the role of the morphology of the inclusion cavity by exploring three different inclusions formed in the same quartz fragment. These SFIs have different sizes/shapes but have the same mineral host and fluid composition. Figure 4.26 A&C show the representative bulk and interfacial water spectra near the quartz boundary (solid-liquid interface) in the SFI-2 and SFI-3, acquired by SRS (setup IV) and SCL (setup III) as an infrared source, respectively. Also, Figure 4.26 B&D illustrate the absorbance distribution maps of these two SFIs concerning the two characteristic wavenumbers corresponding to the bulk (c.a. 3400 cm^{-1}) and interface (c.a. 3700 cm^{-1}) signature. The bulk and interface spectra are substantially different within these two SFIs, regardless of their dimensions and shapes. The representative spectra and the hyperspectral maps show that the absorbance value varies from bulk-type water far from the liquid-solid and liquid-gas interface to a specific blue-shifted spectrum along the quartz boundaries, with an additional peak between 3650 and 3750 cm^{-1}. The step between the two types of spectra is observed at 1 ± 0.5 μm far from the solid boundary (at the beam size resolution) regardless of the pore shape and dimension. As a result, the thickness over which the infrared beam can record the interfacial water is almost constant for the SFIs (see Figure 4.12 for SFI-1). Therefore, any interface-driven cause responsible for such an effect has a propagation scope that is not shape or pore dimensions-dependent.

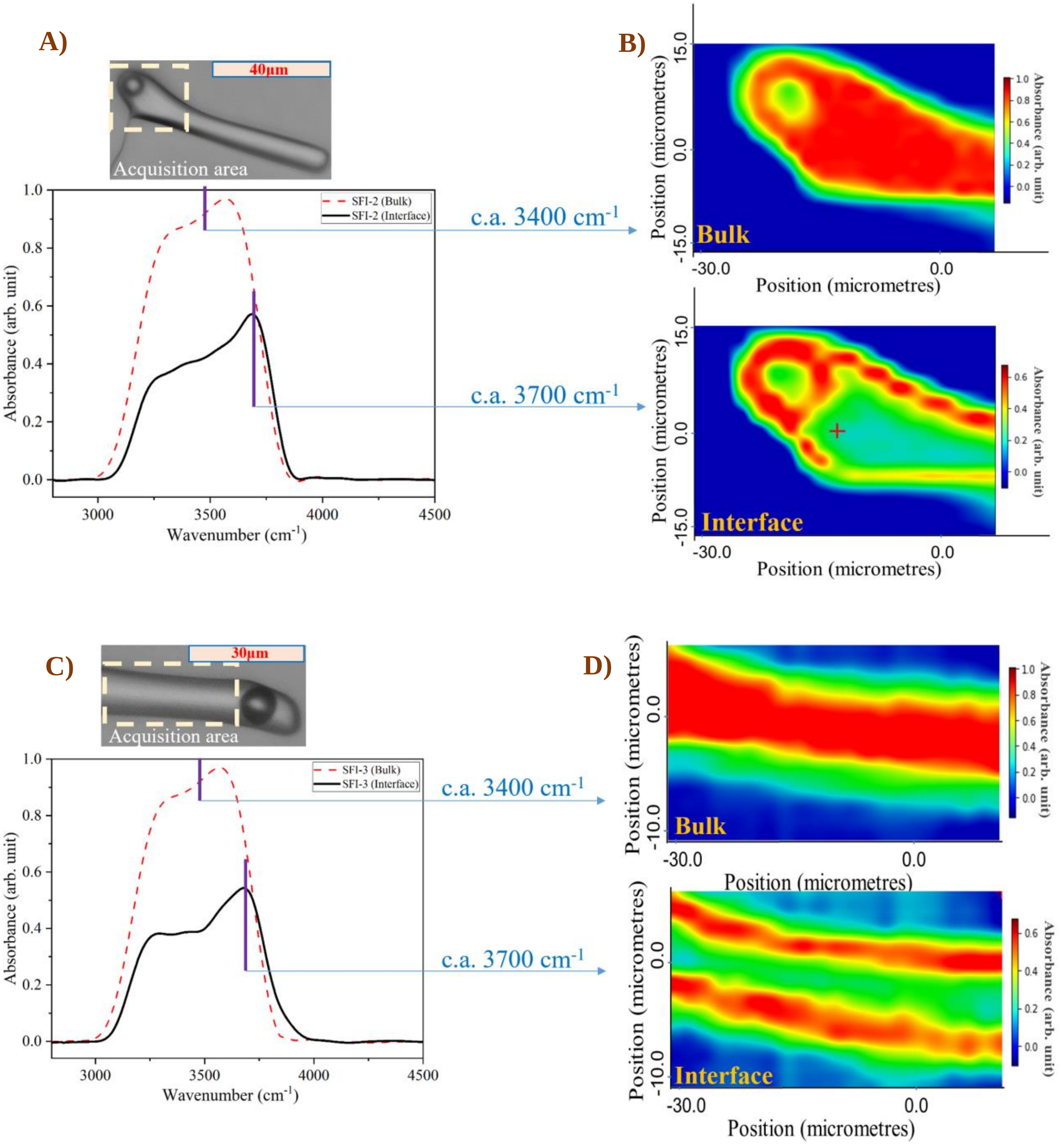

Figure 4.26. The representative/average spectra of bulk and interface after processing steps in A) SFI-2 (acquired by setup IV (synchrotron beam)) and C) SFI-3 (recorded by setup III (supercontinuum laser)). The absorbance distribution maps of B) SFI-2 and D) SFI-3 regarding the two characteristic wavenumbers correspond to the bulk (c.a. 3400 cm^{-1}) and interface (c.a. 3700 cm^{-1}).

4.3.2. Composition of occluded liquid

Changing the composition of the occluded liquid in the fluid inclusion is another important feature that can be the origin of the water spectral signature by approaching the solid boundary. We employed the SFIs, including the NaOH saline solution with different concentrations. Figure 4.27 compares the Raman scattering and micro-FTIR spectra of NaOH solution from 0.5M to 2M, namely very basic solutions, close to pH 14, with the water spectrum (pH 7). For Raman scattering spectra, the low-wavenumber part of the OH stretching region (c.a. 3250 cm^{-1}) of bulk solution is suppressed by increasing the NaOH concentration, and the peak c.a. 3450 cm^{-1} becomes more predominant; however, there are no sharp differences between bulk solution spectra acquired by micro-FTIR technique. Meanwhile, by increasing the concentration, the micro-FTIR interfacial spectra show slight variation in a way that the highest concentration leads to a higher absorption value and bule-shifted behavior around 20 cm^{-1} with respect to the others. The trend of Micro-FTIR findings outlines the sensitivity of interfacial water to the concentration of the occluded saline solution and/or to its pH. In the present case, the pH and the composition of occluded solution do not change significantly. Therefore, a larger variety of occluded solutions should probably be tested before advancing conclusions.

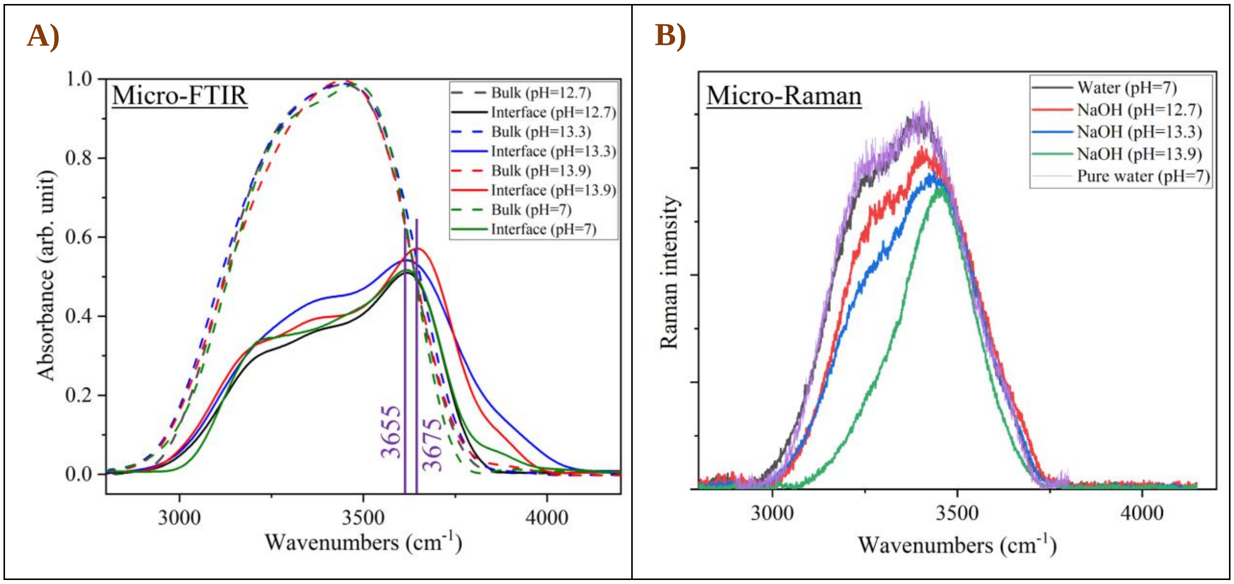

Figure 4.27. A) micro-FTIR spectra of water and NaOH solution with different concentrations in bulk (dash line) and near the solid-liquid interface (solid line) after processing steps, such as baseline correction, normalization, and interference fringes removal. B) Raman spectra of water and NaOH solution with different concentrations (from 0.5M to 2M) in bulk.

Linear micro-FTIR maps can be recorded from one wall to the other at a constant Z plane for the SFI-4, SFI-5, and SFI-6 inclusions. Figure 4.28 and Figure 4.29 demonstrate that the band shapes and the absorbance values change from the bulk to the interface in the SFIs, occluding the 0.5, 1, and 2M NaOH solution, respectively. By showing the series of vertical linear maps across the SFIs, these figures well-distinguished the characteristic spectra of quartz, quartz-NaOH solution interface, and bulk NaOH solution. In Figure 4.29B, we recorded the linear map across the region with 3 µm length to investigate the spectral profile variation regarding the size of the closed media. As shown, we retrieved bulk behavior almost 1 µm from the solid walls. Consequently, we confirmed that the pore size seems not to affect the scope of the interfacial signature.

Although the dimensions of these inclusions are small, the one of SFI-5 is big enough to record the hyperspectral map, which provides an opportunity to investigate the spectral signature of water along the whole solid surface. Figure 4.30 shows two different absorbance distribution maps with respect to the characteristic wavenumbers: A) 3400 cm^{-1}, which corresponds to the bulk, and B) 3700 cm^{-1} assigned to the interface signature.

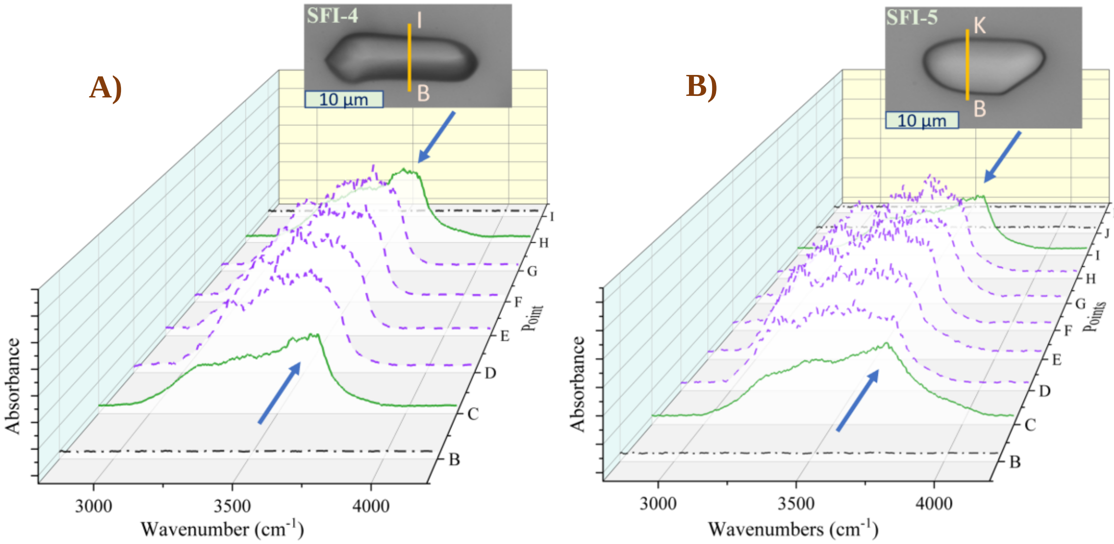

*Figure 4.28. The variation of the OH stretching band recorded across the A) SFI-4 (**NaOH 0.5M**) (from point B to I)) and B) SFI-5 (**NaOH 1M**) (from point B to point K). Black lines (dash-dot line) correspond to quartz, green (solid line) to the near liquid-solid interface, and purple (dash line) to bulk behavior.*

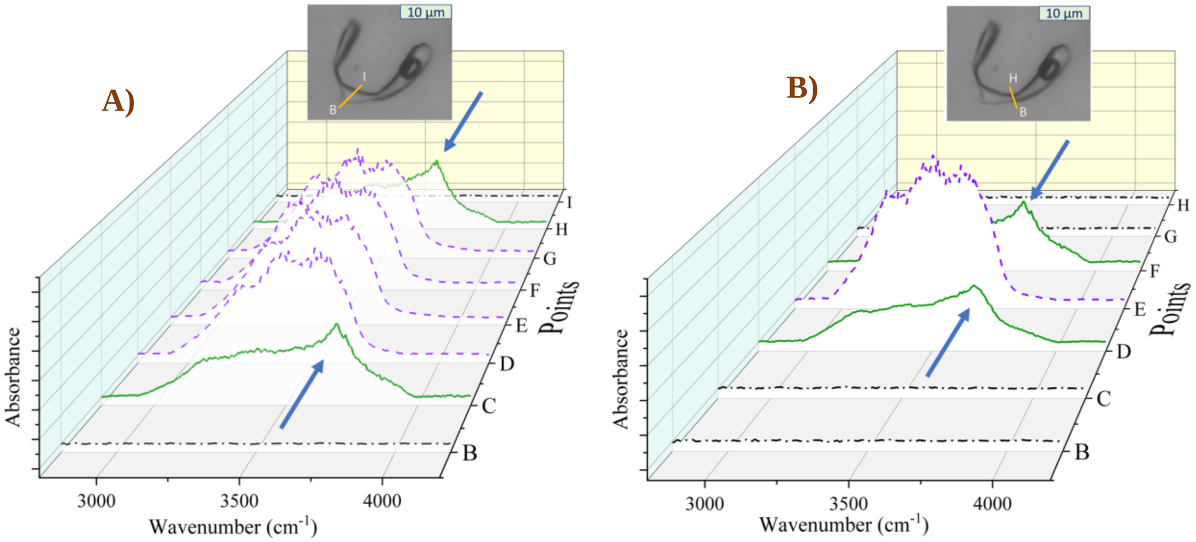

*Figure 4.29. The variation of the OH stretching band recorded across the **SFI-6 (NaOH 1M in quartz fragment)** A) In a broader area (6 μm length, from point B to point K) and B) In a narrower scope (3 μm length, from point B to point H). Black lines (dash-dot line) correspond to quartz, green (solid line) to the near liquid-solid interface, and purple (dash line) to bulk behavior.*

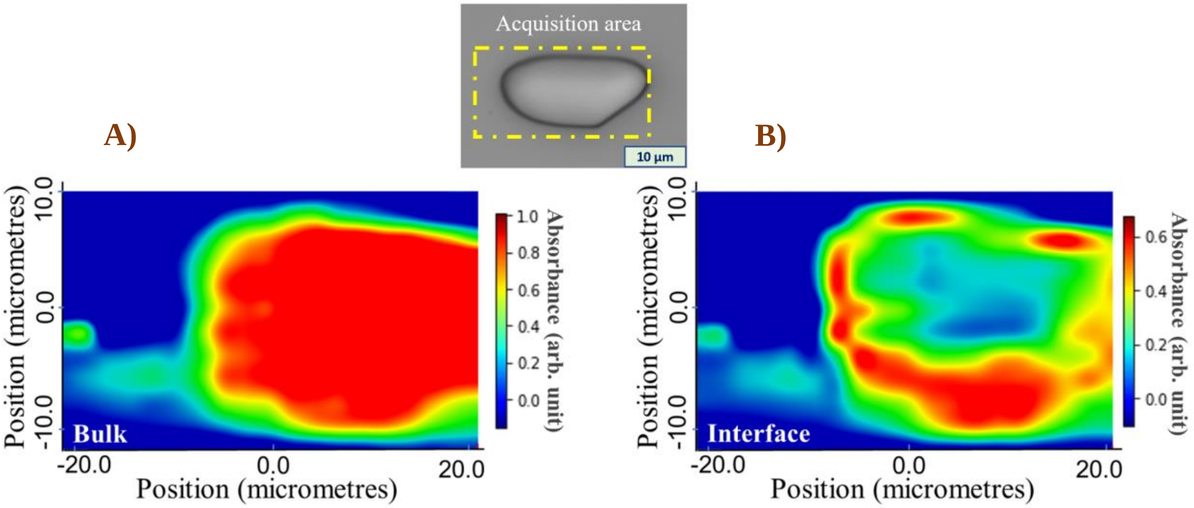

Figure 4.30. The absorbance distribution maps of SFI-5, regarding the two characteristic wavenumbers, correspond to the A) bulk (c.a. 3400 cm^{-1}) and B) interface (c.a. 3700 cm^{-1}) after processing steps, such as baseline correction, normalization, and interference fringes removal.

4.3.3. Nature of host mineral “container”

Since the solid surface properties, especially the hydrophobicity of a siloxane-dominated quartz, was proposed to play a role in the interface-driven effect, complementary studies were carried out on hydrophilic and hydrophobic FIs. To do so, the natural fluid inclusions (NFIs) with different host mineral “container” are employed in this study to investigate the effect of solid surface properties on the bulk and interfacial behavior of water. Figure 3.4 shows two natural fragments, such as calcite ($CaCO_3$) and fluorite (CaF_2), bearing the fluid inclusions of occluded water and saturated water vapor.

4.3.3.1. Calcite fragment

Figure 4.31 shows the series of vertical linear maps across the NFI-1 and NFI-2. Also, the characteristic spectra of calcite-water interface and bulk water are well discerned by showing in Figure 4.32A&B. As is shown, deformation of water spectra has been seen near the calcite-water interface in the way that the absorbance value was decreased slightly and the peak ratio of well-connected molecules to less-connected ones increased (e.g., point D in Figure 4.31A&B). Indeed, the spectral profile near the calcite surface indicates the enrichment of the well-connected water molecules (NW, c.a. 3250 cm^{-1}) compared to the less connected ones (IW and MW, c.a. 3450 and 3700 cm^{-1}, respectively).

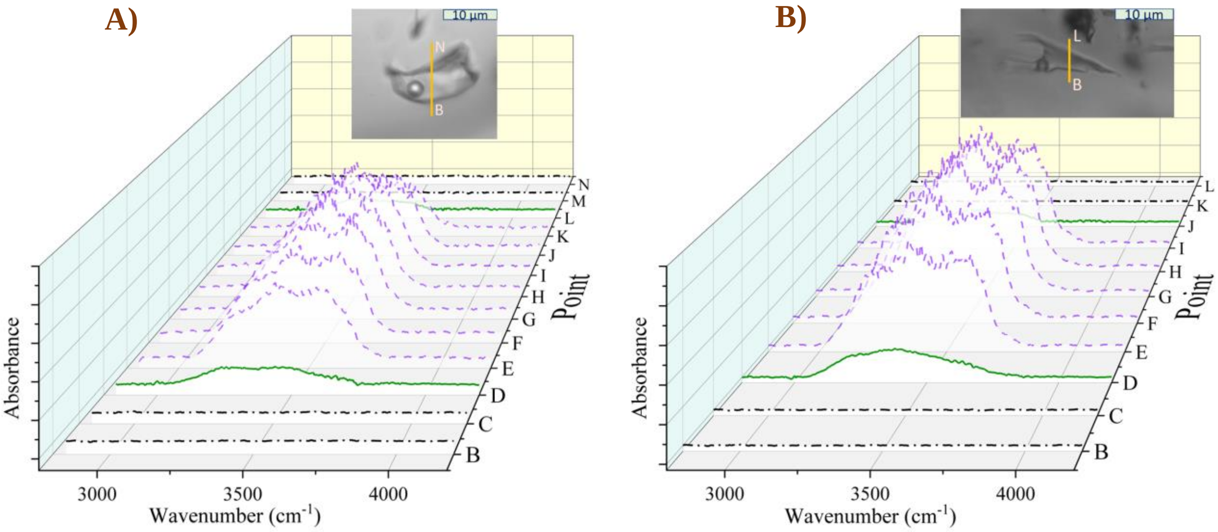

Figure 4.31. 3D view of the variation of OH stretching band recorded across the A) ***NFI-1 (liquid water in natural calcite fragment)*** *(from point B to N) and B)* ***NFI-2*** *(from point B to L) after processing steps. Black lines (dash-dot line) correspond to calcite, green (solid line) to the near water-calcite interface, and purple (dash line) to bulk behavior.*

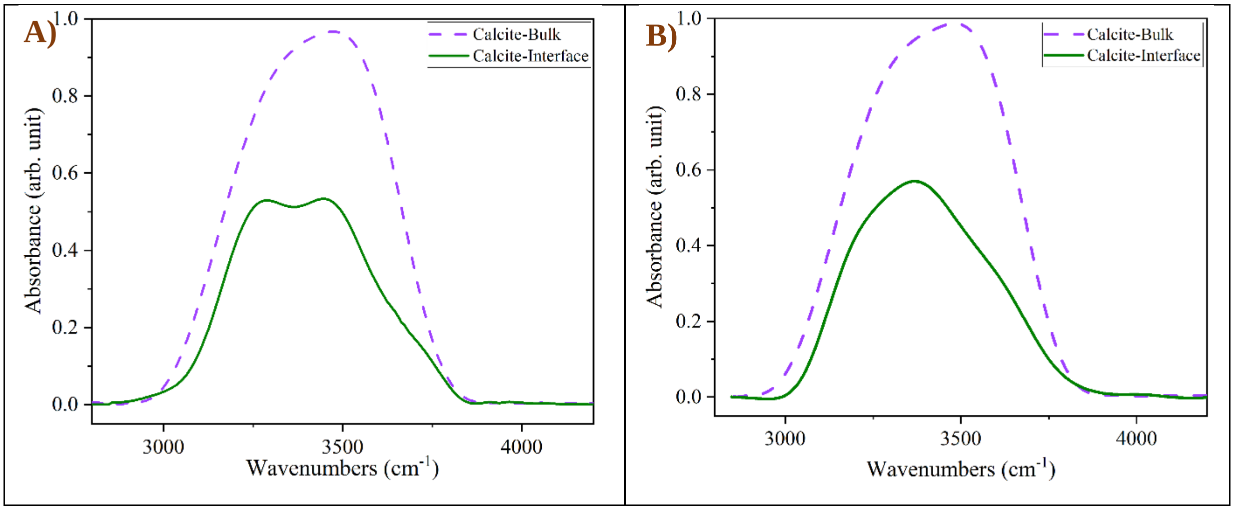

Figure 4.32. The representative/average spectra of calcite-water interface and bulk water in A) NFI-1 and B) NFI-2 after processing steps.

4.3.3.2. Fluorite fragment

The same set of experiments as calcite has been conducted for the natural fluorite fragment. As shown in Figure 4.33 and Figure 4.35A&B, the two distinct spectral profiles (i.e., water-fluorite interface and bulk water) have been observed by recording the linear hyperspectral map across the NFI-3 and NFI-4. As shown, the additional peak c.a. 3700 cm^{-1} was observed clearly in the OH stretching band of water by approaching the water-fluorite interface. This signature is quite similar to quartz-water interface; however, there is a slight difference in the intensity (absorption value) of the interfacial water. In this way, NFI-3 and NFI-4 shows a bit higher intensity with respect to the interfacial signature already shown for the SFI-1, SFI-2, and SFI-3. This finding suggests that the solid surface properties play a major role in getting the interfacial signature of water molecules since the solid can modify the H-bonding among the water molecules.

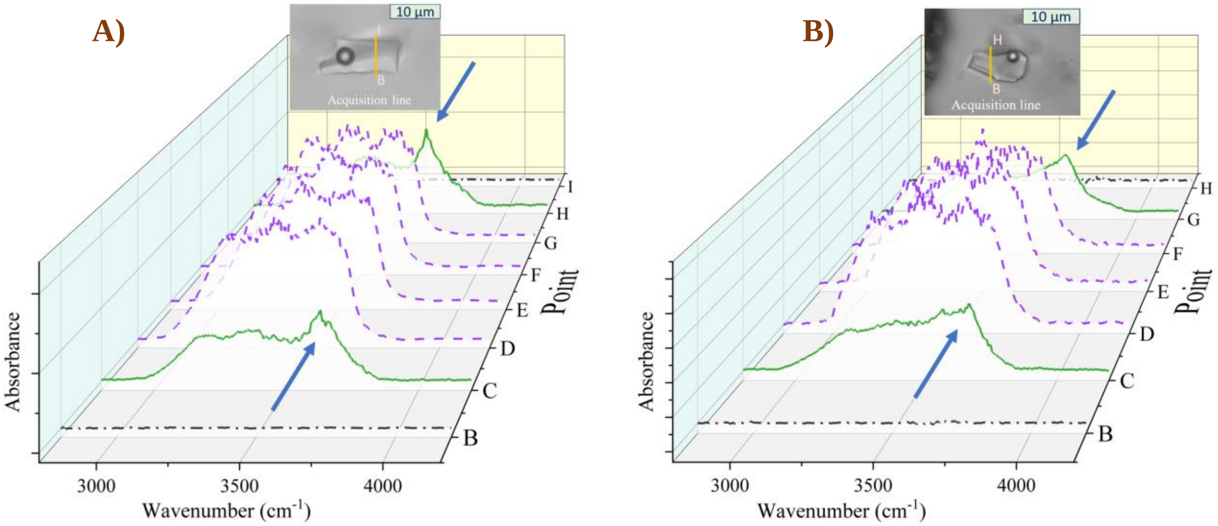

Figure 4.33. The variation of OH stretching band recorded across the A) ***NFI-3 (liquid water in natural fluorite fragment)*** *(from point B to I) and B)* ***NFI-4*** *(from point B to H) after processing steps, such as baseline correction, normalization, and interference fringes removal. Black lines (dash-dot line) correspond to fluorite, green (solid line) to the near water-fluorite interface, and purple (dash line) to bulk behavior.*

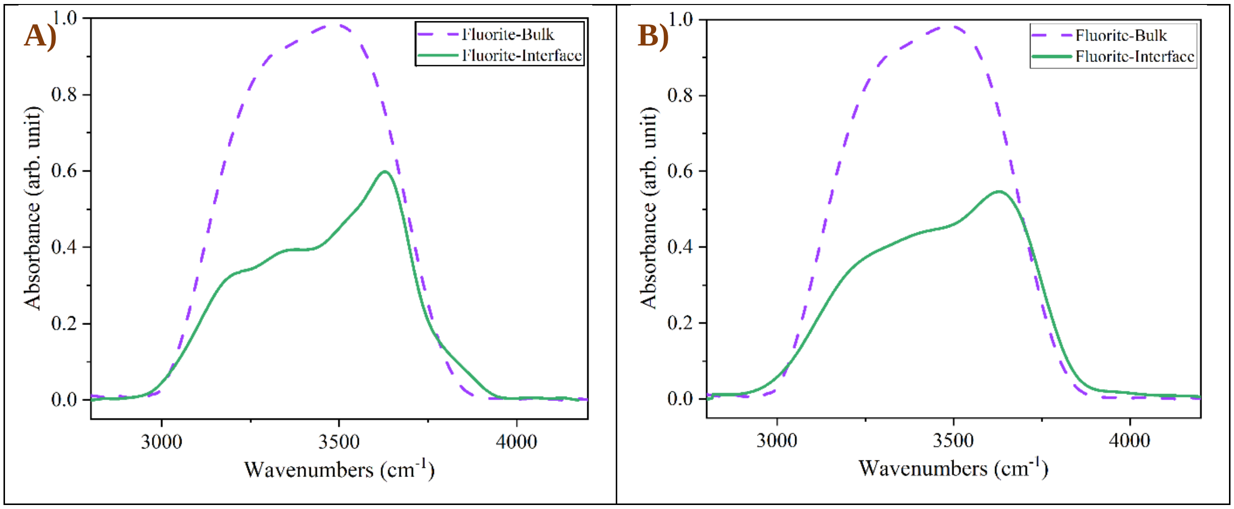

Figure 4.34. The representative/average spectra of fluorite-water interface, and bulk water in A) NFI-3 and B) NFI-4 after processing steps.

Through the plotting of bulk and interfacial behavior of water on various solid hosts (Figure 4.35), it becomes evident that the interfacial behavior is significantly influenced by the properties of the solid surface. The observation of interfacial signatures can be attributed to hydrophobic forces acting through the disjoining pressure, as explained in section 2.2.3.2. These forces may provide insights into the disordering of water molecules. A more comprehensive discussion on this aspect will be presented in chapter 5, offering further elaboration and analysis.

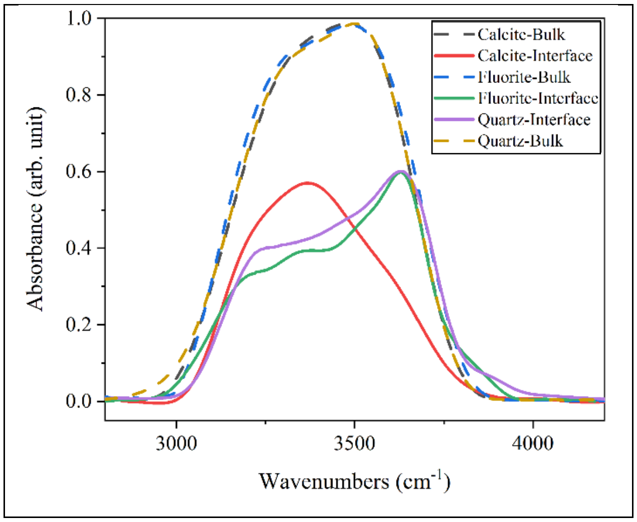

Figure 4.35. Comparing the representative/average spectra of fluorite-water, calcite-water, and quartz-water interface with bulk water after processing steps.

4.4. Bulk vs. interfacial water along the bubble boundary

Since the water-vapor interface is well-known as a hydrophobic interface [339-341], recording the micro-FTIR spectra around the water vapor boundary gives a ground for justifying our above outcome with respect to the prominent role of the hydrophilicity/hydrophobicity scale of the surface. As discussed in the introduction, there is a large baseline undulation called Mie scattering phenomenon around/inside the gas bubble because of its geometry. After correcting the acquired spectra using deep learning-based modelling, we observed a distinct additional peak between 3650 and 3750 cm^{-1}.

Figure 4.36 shows the spectra acquired around/inside the bubble after applying the Mie scattering correction method. The green solid lines in this figure show the spectra of the water-vapor interface and the black lines indicated the spectra recorded inside the bubble. As the absorption of liquid water is much higher than the water vapor, it suffices that the light crosses a small amount of liquid (either through the films at the apex, or by crossing the bulk liquid if the beam illuminates it) for the corrected spectra to look essentially like a liquid spectrum instead of the vapor one. It should be noted that the location of the green spectra is indicated by a yellow circle in Figure 4.37B.

When we meticulously compared the spectral signature of the water-quartz and water-air interface (Figure 4.38), we found differences between these interfacial behaviors. In the water-quartz interface, the spectral signature shows an additional peak at the end of the OH stretching band of water; however, in the water-vapor interface, the peak appears separately from the OH stretching band, which represents dangling OH mode (very similar to the spectra acquired by SFG method, see section 2.3.2). The signature of interfacial water is pretty straightforward and fully compatible with the free OH molecules present at the liquid-air interface. Although, it cannot be so evident that these free molecules could develop over a large thickness, away from the interface towards the liquid side. It demonstrates the sensitivity of the technique to record the dangling OH-modes, which seem to be able to absorb radiation at various wavenumbers. It becomes difficult to assign the extra band to a pure dangling mode or to the 1-connected molecules.

What is especially interesting is the clarity of the liquid-air signature retaining the enrichment in no or less-connected molecules as a primary feature. This has two important consequences: First, liquid water along the interface is clearly (at a macroscopic scale) impacted by the presence of vapor boundary. Second, the liquid-air and the liquid-quartz/fluorite interface share the same characteristic of disconnected H-bonding and increased less-connected molecules. This is interestingly linked to the commonplace statement that hydrophobic surfaces promote a surface gaseous-like or low-density layer when interacting with water [342]. The "phobia" comes out from this ability to repel liquid water at a distance, while it must be outlined that water keeps contacting the surface since the interface term would be totally inadequate. The following chapter tries to combine the present findings with some main features of what is known as the hydrophobicity effect.

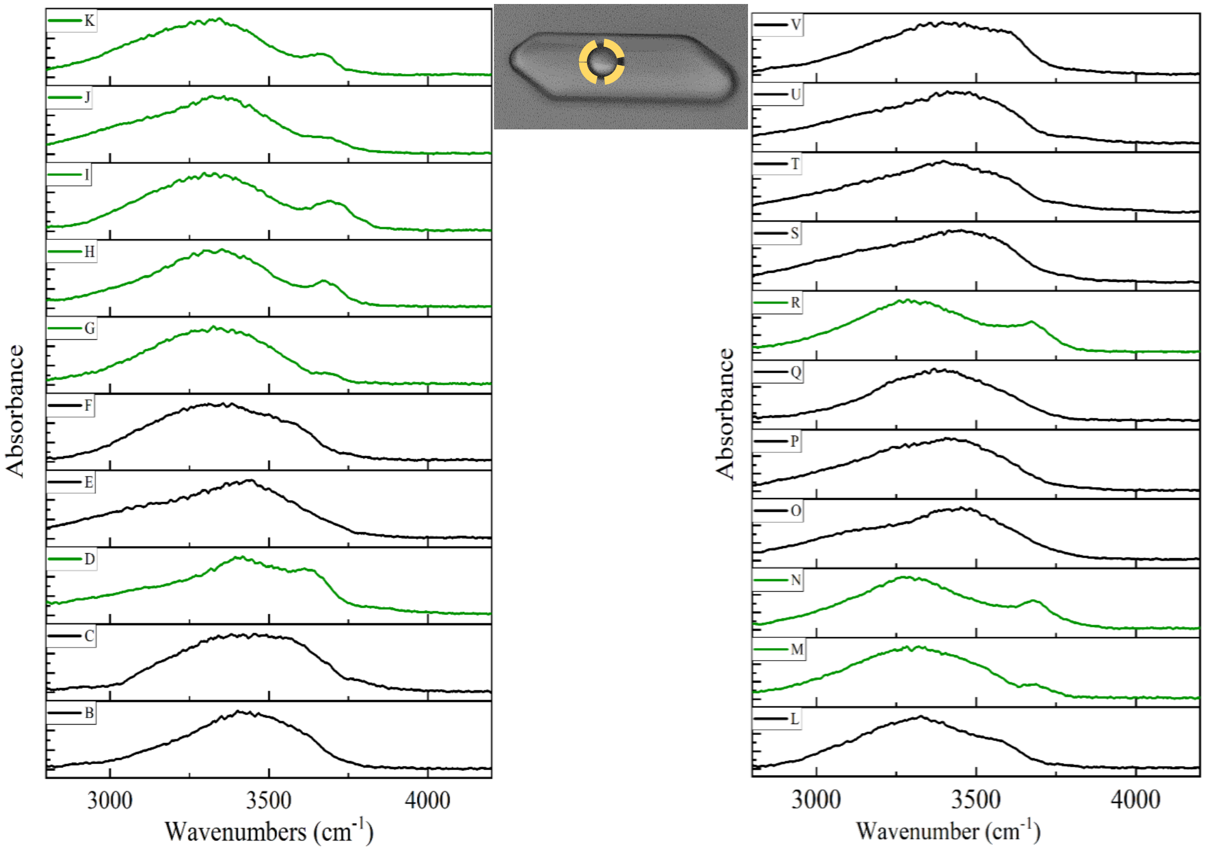

Figure 4.36. The random representative Mie-scattering corrected spectra recorded around/inside the saturated water vapor (gas bubble, yellow dash-line in the picture). Black solid lines correspond to the water spectra inside the bubble and green lines represent the interfacial spectra around the liquid-gas interface.

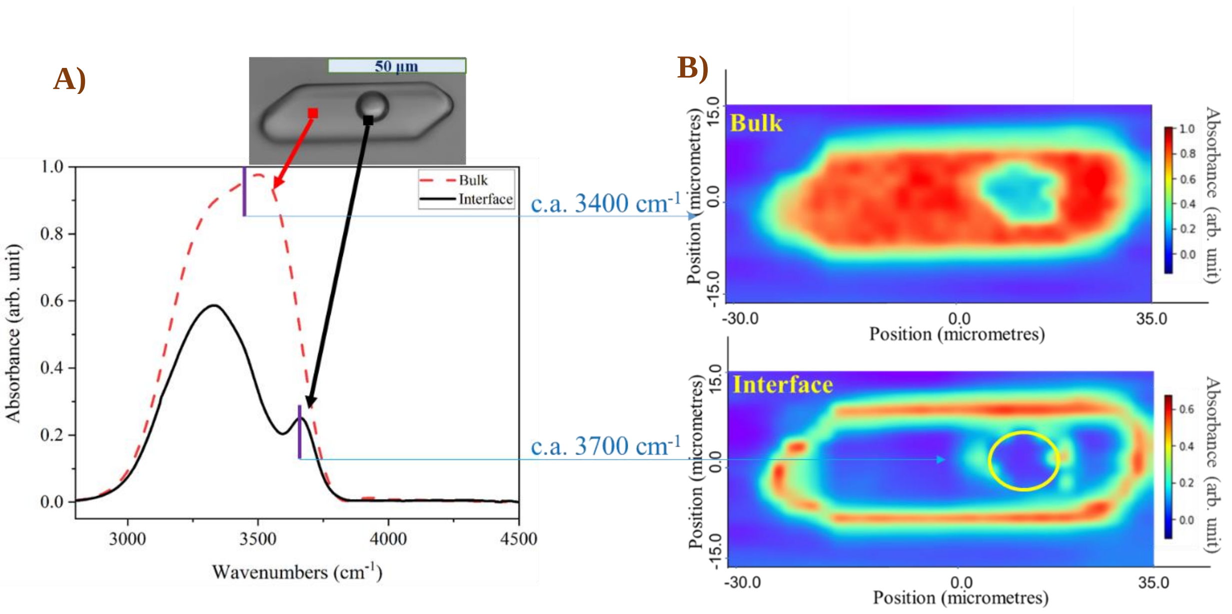

Figure 4.37. The representative/average spectra of bulk and liquid-air interface after processing steps, including Mie scattering correction, in SFI-1 (acquired by setup III). B) The absorbance distribution map regarding the two characteristic wavenumbers correspond to the bulk (c.a. 3400 cm^{-1}) and interface (c.a. 3700 cm^{-1}). The yellow circle corresponds to the gas bubble location (liquid-air interface).

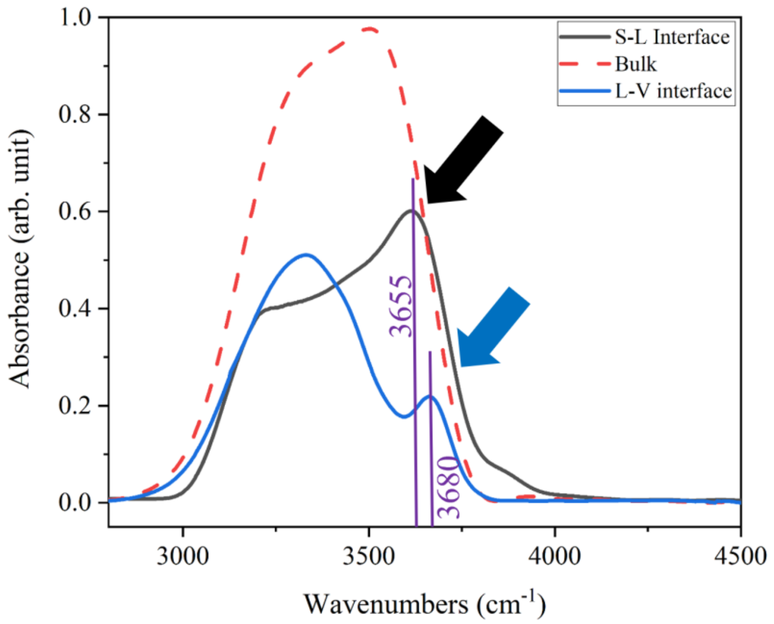

Figure 4.38. Direct comparison of water behavior in the bulk and at the solid-liquid and liquid-air interfaces.

4.5. Conclusion

The experiments performed in this study demonstrate that the micro-FTIR technique applied in the diffraction limit spatial resolution can be employed to study the water behavior in micrometric scale closed cavities (synthetic and natural fluid inclusions). The water behavior and corresponding spectra are highly affected when the beam approaches the solid surface and the gas bubble; however, they are partly influenced by optical aberration, such as interference fringes and Mie scattering. The former corresponds to the thickness of the fragment, and the latter relates to the shape of the bubble/interface. All these phenomena can overlay with chemical spectral features and may cast doubt that such signatures are a general feature, which have a systematic significance for the water-solid interphase as a whole. That is why two different methods were applied to suppress these trends. After processing the data, the variation of the spectral profile has been emphasized, revealing that an additional peak at c.a. 3700 cm^{-1} takes place systematically in the vicinity of the quartz and fluorite interface with water. As a consequence, the interfacial signature of water cannot be related to optical aberrations.

The existence of two contributions (c.a. 3400 cm^{-1} and c.a. 3700 cm^{-1}), one bulk-like and the other interfacial signature, can be assigned to the difference in H-bonding in the two areas. The OH stretching bands of normal and bulk water show a strong low-wavenumber component (c.a. 3250 and 3450 cm^{-1}), and they do not have a shoulder at higher wavenumbers (c.a. 3700 cm^{-1}) [103, 113]. A band detected between 3650 and 3750 cm^{-1}, visible along the quartz and fluorite boundary (water-quartz and water-fluorite interface), can be assigned to the absorption of less-connected water molecules (two to zero H-bonds, free-OH molecules (dangling OH mode)) near the hydrophobic surfaces [41, 56, 143, 146]. On the contrary, the enrichment of the well-connected water molecules (near four H-bonds) has been observed along the calcite boundary, which can be assigned to one hydrophilic surface (Figure 4.39).

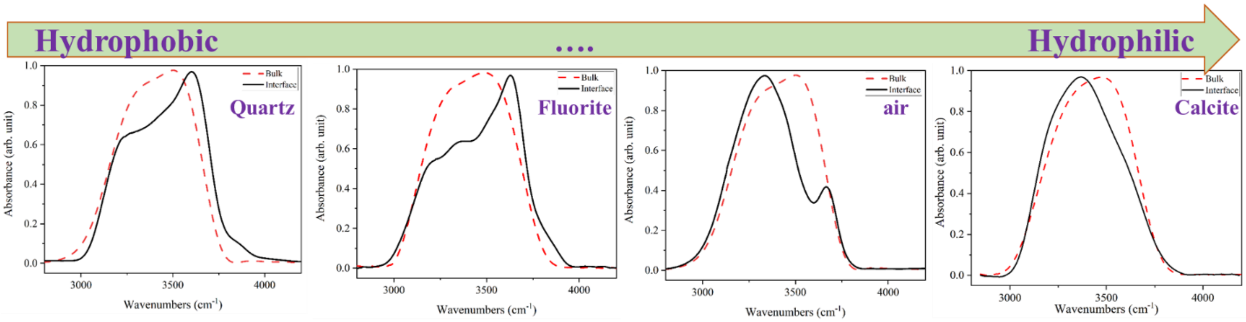

Figure 4.39. Variation of water behavior at the interfaces from hydrophobic surface to hydrophilic one (red dash lines relate to bulk behavior and solid black lines correspond to the interface behavior).

Indeed, the interfacial behavior is linked to the solid surface properties and active surface forces like the hydrophobic force (by considering Hamaker's constant and disjoining pressure) emanating from the surface and causing the disorganization (chaotropic effect) or organization (kosmotropic effect) of water molecules over a long distance. Herein, the scope of the interfacial effect recorded in the interval, at which has never been expected because the neutron measurements revealed that the variation of the H-bonding occurs up to 3 water molecule layers (almost 1 nm). However, we have observed that the bulk-like properties are recovered at around 1 ± 0.5 μm from the solid, which is coherent with the previous studies in this respect [56, 58]. Likewise, we showed that the scope of the interfacial domain is not affected by the morphology of the cavity, nor by the fluid composition, in the limits of what has been studied here.

Concerning the effect of increasing the temperature, we have observed that the interfacial water near the quartz surface in SFI-1 displays less hydrogen-bonded coordination number with respect to the bulk water (33% less well-connected water molecules at room temperature and 35% at 155°C). Moreover, the peak c.a. 3700 cm^{-1} becomes more intense at high temperatures (up to 155°C), which means that increasing the temperature has a chaotropic effect on the water molecular networking besides the solid boundary, decreasing their coordination number. Overall, the molecular networking of interfacial water is dominated by the IW (3-connected molecules), a fact promoted by T, strikingly different from bulk water dominated by NW even at high T.

Besides the micro-FTIR, the Raman scattering measurements were conducted only for our reference fluid inclusion (SFI-1) to investigate the spectral profile variation of water by approaching the solid surface. Our finding showed that the interfacial signature has not appeared in the Raman measurements; however, the peak ratio of intermediate to network water molecules drastically changed close to the water-quartz interface (up to 1 μm far from the solid surface). Also, a series of infrared and Raman water spectra were recorded by adding the polarization to the optical pathway (0° and 90° for infrared, and horizontal-horizontal and vertical-vertical polarizer for Raman). We observed that Raman scattering measurements are more sensitive to polarization in a way that the spectra of water acquired by V-V polarizer showed a substantially different spectral profile (peak ratio and peak position) near the quartz surface. Nevertheless, there are no striking differences between the H-H polarized and depolarized Raman spectra.

Last but not the least, the spectra of the NaOH saline solution with different concentrations (from 0.5M to 2M) bearing inside the quartz fragment were recorded by the micro-FTIR setup. Our findings emphasized the effect of ion activity on the water spectra by playing a chaotropic or kosmotropic effect. We showed that the saline solution with higher concentration leads to a higher absorbance value; however, the length scale over which the interfacial behavior of water was recorded was kept almost constant. It should be noted that this consistency of the interfacial domain can be related to the experimental methods, where the distance of two consecutive beam locations could not be lower than 1 μm.

5. Reactivity along a hydrophobic interface

5.1. The hydrophobicity effect: liquid water and the "hydrophobes"

Historically, the concept of the hydrophobicity effect emerged considering the low solubility of non-polar solutes in water or equivalently the tendency for oil and water to segregate. At ambient temperature and pressure, water molecules form a percolating, fluctuating network of hydrogen bonds (H-bonds) [343]. This self-associating nature of water governs its behavior near apolar compounds, which are incapable of forming H-bonds. Experimentally, it has been found that small apolar molecules exhibit a significant negative entropy of hydration, indicating a possible structural rearrangement of H-bonds between water molecules near the solute. It was early on proposed that a kind of "cage" by highly networked water molecules formed around the non-polar solute, what was called the "iceberg" model [344]. Since then, some studies [345-348] supported the existence of increased tetrahedral order around small hydrophobic groups in aqueous solutions, while some other studies, equally recent and well-conducted, concluded at odds with water destructuring [349-353]. In particular, neutron scattering hardly shows any difference in the state of water molecules when introducing a hydrophobe [351]. On the other hand, molecular dynamics calculations indicate that the structural changes of water near small non-polar solutes cannot be deduced from the water radial distribution functions, explaining why this increased ordering is not observed through neutron diffraction experiments [354]. The molecular dynamics study shows slower translational and re-orientational dynamics of water near hydrophobic groups, resembling water at low temperatures [346]. It remains that a dominant factor in hydrophobic hydration is the formation of a cavity of size and shape to accommodate a given solute molecule. The thermodynamics of cavity formation is intimately tied to the fluctuations in the local density of water [355].

To date, there remains strong debate around the "iceberg" model, even if hydrophobic interactions are classically regarded as entropy-driven. In the "iceberg" structural model, water molecules can rearrange around a small hydrophobic solute to enhance their average H-bonds network [356]. In that sense, the hydrophobic effect has a kosmotropic impact on water, associated with a large and positive free energy change ($\Delta G = \Delta H - T\Delta S$). This positive ΔG variation implies a poor interaction of the hydrocarbon fraction with water, accounting for their low solubility. Yet, Hildenbrand [357] early on highlighted that speaking in terms of phobia for water was inadequate because there was solubility, and a water-hydrophobe association was attractive. Tanford [358] argued that the underlying cause for the preference for like-like contacts (instead of "phobia") resides almost exclusively in the strong attraction of water for itself, which is expressed by its very large interfacial free energy that leads readily to a dewetting of the less attractive surface. This analysis implies that the high cohesive energy in liquid water is the cause for the low solubility of hydrocarbons in water, or the preference for like-like contacts. A direct and important consequence is that the surface area of the water-hydrophobe contact matters a lot in the reasoning. This question of size is of primary importance, and the hydrophobic interactions are nowadays known as hydrophobe-size dependent [359, 360]. Indeed, most of the literature about non-polar solutes refers to solutes having an infra-nanometric size, with concentrations lower than the aggregation threshold.

The hydration-free energy of large apolar solutes (roughly > 1 nm at ambient conditions) is dominated by a large positive enthalpy change, which is attributed to the inability of the water molecules close to the large solute to maintain their H-bond network [361]. Forty years ago, Stillinger [362] suggested that the difficulty experienced by water molecules to preserve the H-bonded network close to a large enough hydrophobic surface can facilitate density depletion near the surface, leading to the formation of a vapor−liquid-like interface. Subsequent theoretical work, substantiated by numerous simulation studies, has shown how such "soft" interfaces arise in practice and highlighted the central importance of large density fluctuations near extended hydrophobic surfaces [363].

The first model that successfully bridged the molecular and macro-scales and accounted for size-dependent wetting/dewetting was described by Lum, Chandler, and Weeks (LCW) [364]. To summarize [365], H-bonding between waters is hindered near the surface in small solutes. However, even a distorted H-bond network cannot accommodate solutes larger than 1 nm in diameter, and consequently, H-bonding is sterically depleted. The result is a reduction in the cohesive forces and a concomitant surface dewetting. The breaking of H-bonds is dominated by enthalpy, but the spatial arranging of H-bonds is dominated by entropy in a way that the latter outweighs the solvation of a small solute. On the other hand, the entropy of solvating a large solute is favorable. Therefore, there not only exists a wetting/dewetting transition but also an entropy-enthalpy crossover transition. These two types of solvation are fundamental to the assembly of hydrophobic solutes; the equilibrium is dominated by the difference between the entropically dominated solvation of the small solute and the enthalpically dominated solvation of the larger assembly. The crossover between small and large regimes occurs on the nanometer length scale.

Therefore, when studying either the solvation of a large solute in water or the interaction of water with an extended solid hydrophobic surface, the H-bonding of water may be broken at the surface of the hydrophobe, which may result in an enthalpic penalty. In such structures, the orientation of water molecules is biased so that hydrogen bonding groups (donor or acceptor) tend to avoid a direction toward the non-polar substrate, which cannot participate in hydrogen bonding. Consequently, the hydration of a planar hydrophobic surface of infinite extent is the opposite end member from the carefully explored small solute case [366]. The liquid structure nearest the surface is characterized by the dangling H-bonds; i.e., a typical water molecule at the surface has one potentially hydrogen-bonding group oriented toward the hydrophobic surface (section 2.3.2). This surface arrangement represents a balance between the tendencies of the liquid to maximize the number of hydrogen bonds on the one hand and the packing density of the molecules on the other. A detailed analysis shows that the structural properties of the liquid farther from the surface can be understood as effects imposed by this surface structure [366]. These results show that the hydration structure of large hydrophobic surfaces can be very different from that of small hydrophobic molecules. Also, an understanding of water density fluctuations near a surface serves to characterize its hydrophobicity. In particular, the free energetic cost of displacing interfacial waters to create a cavity next to a surface provides a general, unambiguous measure of its hydrophobicity; the easier it is to create an interfacial cavity, the more hydrophobic the surface [367]. The water coordination number and extent of H-bonding between interfacial waters decreased by moving from the bulk to the surface. Correspondingly, the models suggest an increasing probability of void formation closer to the surface [365]. The formation of surface nano-bubbles, giving birth to a layer of reduced density close to the solid surface, is one of the major models for the long-range attraction between hydrophobic solids in aqueous solutions [368] and to justify a very long propagation of the hydrophobic effect with impurities-bearing surfaces (> 100 nm [369], and even 650 nm [370]).

In addition to enhanced interfacial water density fluctuations and the corresponding facilitation of cavity creation, the disruption of water structure near hydrophobic surfaces is also reflected in other interfacial properties, such as isothermal compressibility, transverse density correlations, distribution of water dipole orientations, interfacial diffusivity, orientational relaxation times, hydrodynamic slip and Kapitza resistance [367]. In particular, an interesting manifestation of hydrophobicity at solid surfaces is their behavior in hydrodynamic flows [371]. For usual surfaces, a lateral flow of a liquid is described by the Navier–Stokes equation in conjunction with the “no-slip” boundary condition, which implies that the interfacial fluid layer is at rest relative to the surface. This boundary condition is violated for a water flow along a hydrophobic material, and the interfacial water layer moves relative to the surface [372, 373]. This slippage effect has important implications for the extreme mobility recorded in nanofluidic channels like carbon nanotubes [374]. In that last reference, an illuminating link is made between the high mobility in nanotubes and the infrared features of in-channel water. They are characterized by a predominant contribution of loose H-bonds even for fully hydrated states, irrespective of the nanotube size. While the dominating loosely bond signature is attributed to a one-dimensional chain structure for small-diameter nanotubes, this feature also results from a water layer with free molecules facing the nanotube wall for larger-diameter nanotubes [374].

5.2. Thermodynamics of the IR-based interfacial water

Micro-FTIR spectroscopy results can be expressed in terms of Gibbs free energy through an IR-to-thermodynamic conversion based on a partition function developed previously (equation 3.3) [56, 57, 91]. It consists in summing the frequencies of all the inter- and intramolecular water modes to deduce the Gibbs free energy by employing equation 3.7. In our case, we can only record the intermolecular stretching band because of both the limited IR laser wavelength and the quartz cut-off wavenumber (2000 cm^{-1}). As a result, the IR-to-thermodynamic conversion is performed assuming that all modes other than intramolecular stretching are constant and equal to the normal water value reported in the literature as a function of T [57, 91, 375]; we extrapolate the provided graphs for calculating these constant values at the 155°C. It should be noted that for the OH stretching band, we exploit the numbers given in Figure 4.17A&C.

The key characteristic of the conversion technique relates to work based on the relative value of Gibbs free energy instead of the absolute one due to the numerous uncertainties of the calculation process (see [57]). The procedure is directed to calculate how much ΔG changes with respect to a reference (dΔG) by subtracting the IR-based ΔG at any point from the reference value (i.e., the average of the IR-based ΔG obtained in the center of the SFI-1). This relative approach provides a logical way to conclude the Gibbs free energy variation based on the vibrational energy. The outcome indicates large differences in dΔG between bulk and interface regions, reaching 600 J/mol at RT (Figure 5.1A) and 1000 J/mol at T_h (Figure 5.1B) over an almost similar thickness of 1 ± 0.5 µm.

To visualize better how the T promotes the interface effect, a map of dΔG difference point by point between RT and T_h was drawn (Figure 5.1C). The bulk region is characterized by a zero-greenish color, demonstrating that the bulk region covers the same area at RT and T_h, and reacts identically to the different temperatures. When moving to the micron-thick interface region, the dΔG between the two different T reaches 300 J/mol, revealing two facts: 1) T promotes the interface effect but does not fabricate it; 2) the interface reacts more intensely to the T variation than the bulk water. This observation, similar to a conclusion inferred from the sub-bands examination (section 4.2.3), corresponds to a decreasing heat capacity and, therefore, a weakening of the enthalpic contribution. This conclusion is directly connectable with the lesser H-bonds network in the interphase (predominance of the IW component), corresponding to an enthalpic penalty for the hydrophobic effect. In the meantime, it is good to recall that the orientational order does decrease (no clear polarization, diminishing of the NW component), corresponding to an entropy increase. The water-hydrophobe interphase is characterized by the rise of the ΔG, which seems to be enthalpy-driven, with an opposite entropic contribution not strong enough to contradict the enthalpy trend. Working with polarized radiation in a more systematic and controlled way would shed light on all that enthalpy-entropy compensation topic.

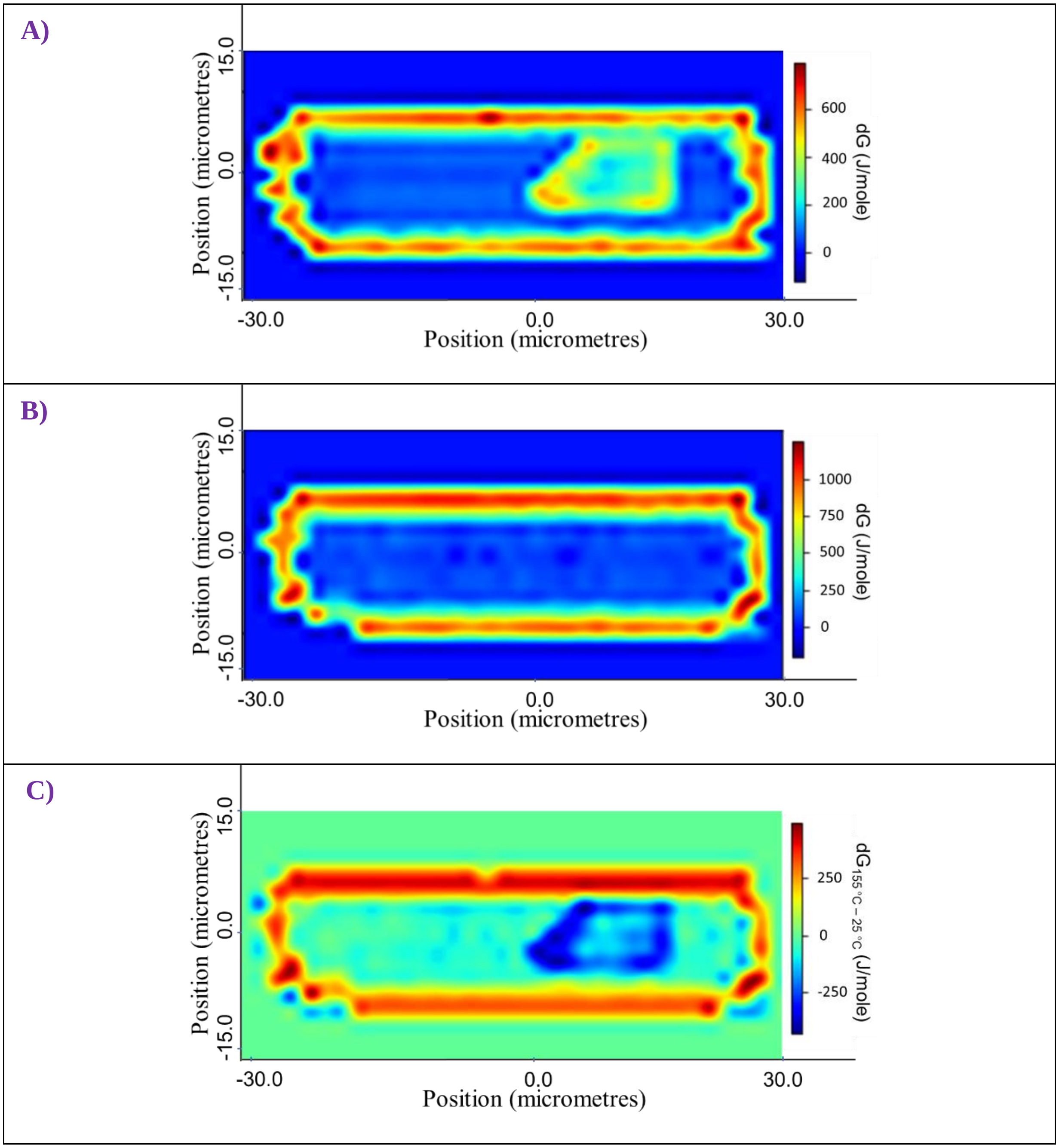

Figure 5.1. The map of Gibbs free energy variation all along SFI-1 at A) RT, B) T_h (155°C), and C) the point-by-point differences between Gibbs free energy value at RT and T_h (B-A).

The shift from bulk to the interface has been magnified with T, widening the gap between what is expected and what is experimentally measured. Interestingly, the decreasing heat capacity is the reverse of what was measured in hydrophilic nanopores [337], even if the link between the two situations remains debatable, with no confinement in our ultra-large (in terms of confinement threshold) liquid-bearing cavity.

Increasing the Gibbs free energy of a phase lead to enhancing its chemical potential and modifying the solubility levels (in the case of liquid water) of any solid and gas reacting in such conditions. Additionally, this significant change in the chemical reactivity of liquid water takes place over a micron-thick domain, rather defining an “interphase” domain than a sharp geometrically “interface” linked to the phase variation. This domain has a higher Gibbs free energy with respect to the bulk, with a gap enhanced by T. As a result, interfacial water has a larger chemical potential from RT to T_h; therefore, it is less stable than bulk water, which makes local water more reactive and more prone to dissolve the solid matrix than bulk water.

5.3. Consequences of the interphase on geochemical reactivity

These findings give birth to a new concept, the interphase, to be involved when interpreting water-rock interactions in pores, channels, and cavities. The key aspect is that this interphase, both on intensity and propagation scope scale, relates to the chemical nature of the pore walls. The pore-sized controlled solubility [178, 376, 377] or confinement effect [40-46] matter, as recently abundantly demonstrated. In that respect, both the thermodynamic potential and the active water give rise to modifying how to conceptualize a liquid-solid interaction at the multiphase boundary scale. Indeed, a significant mass transfer is required for the equilibrium to be reached. Due to the thermal sensitivity of this interface-driven effect, the practical consequences of the water-rock interactions will be maximized during the diagenetic or hydrothermal processes.

To try being more quantitative and illustrating in real terms the meaning of that interphase; although, this has already been partly published by our group [56], it is good here to review what can be the exact consequences of such a thermodynamic variation but also at which conditions it can be amenable to a macroscopic understanding of water-rock interactions.

The first aspect is considering the coexistence between interfacial and bulk water compatible with the recorded maps. It seems logical through the sharp interface to expect a surface field to provide additional energy to modify the chemical potential over a large but limited distance.

Therefore, we propose the coexistence of two types of water in the closed cavity, separated by a neat marked interface, instead of a continuous dielectric medium. The following section will discuss two different conceptualizations compatible with this first remark. The second point is to note that the thermodynamic change affects millions of molecules (1 µm thick interfacial water corresponds to roughly 3500 molecular layers) meaning that there is a specific phase, or a continuous extended interphase domain, standing between bulk solid and bulk solution. In terms of classic thermodynamics, the activity of this interphase water (a_w) is modified ($RT \ln a_w$ positive component for $a_w > 1$) when coming closer to a hydrophobic solid surface. This increases the Gibbs free energy, a well-known aspect of the hydrophobic effect, and means it is much more reactive than the bulk water. This may sound counter-intuitive since hydrophobicity is linked to a lack of interactions, but it has roots in the enthalpy-entropy compensation challenge that we discussed qualitatively. It would be interesting to note that we could design a quantitative test of the interphase thickness by using a nanofluidic chipset (see chapter 6), meaning etching channels at the infra-micrometric level, let's say 100 nm in width and height. Indeed, we can create geometries that are downscaled with respect to the hypothesized interphase. By functionalizing their inner walls to make them hydrophobic (etching process fabricate silica-based channels), we logically produced a hydrophobic effect in a cavity much thinner than the scope of the interfacial effect, therefore giving rise to actual confinement (and cooperative) effects, removing any bulk water inside the channel. We may delineate the threshold between interphase and bulk with a sequence of larger and larger channels. The big issue here would be the size of the IR beam (3 µm), which is much larger than any channel.

Second, the thermodynamic status of dissolved solutes should be impacted by the conceptualization of the interphase. Assuming that the surface fields affect only water networks, let the solutes with precisely the same thermodynamic properties. However, this approach is probably too simplistic. The thermodynamic properties of dissolved solutes involve their behavior in the presence of water. In such a view, it seems highly implausible to imagine that a strong variation in the energetics of the water network would not influence the reactivity of the solutes themselves. To properly tackle the solubility viewpoint from the present findings, we should have much more information about the unknown thermodynamic status of the silicic acid in the interphase area. The only information obtained is the record of phase transitions inside fluid inclusions containing saturated solutions coexisting with salts at equilibrium. It was very interesting to note that whenever the in-pore grain moved toward the interface, it started dissolving up to total disappearance, giving empirical evidence that something "weird" can happen along interfaces (Figure 5.2). It is not at all quantitative or even completely demonstrative, because of the difficulty of defining the grain location. Also, we did not have time to properly record the infrared map of this exact inclusion and check for the existence of a thick interphase. But this preliminary observation offers a perspective to progress on the macroscopic solubility viewpoint of the interphase and also to discuss whether or not the solute thermodynamics is cooperative or anti-cooperative to interphase water properties with respect to water-rock interactions.

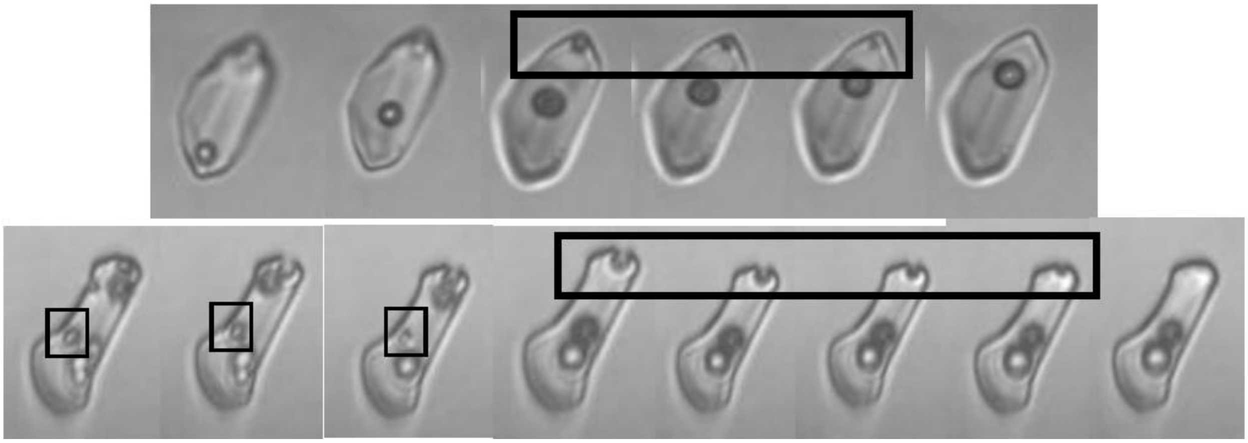

Figure 5.2. Photographic capture of the crystal growth in CsCl-bearing inclusions displaying crystal re-melting along solid-solution interfaces. The top photograph sequence lasts 20 seconds, while the bottom lasts 2 minutes. The photograph interval is not regular. On the bottom sequence, see particularly the stability of the crystal located in the center part of the inclusion, while the (having almost the same size) the other along interfaces dissolve rapidly.

Third, and letting open that problem of the dissolved solutes, we can approach the reactional driving force viewpoint. Eventually, the interfacial effect is thermodynamically characterized by a +0.6 to +1 kJ/mol shift in the Gibbs free energy, depending on temperature, which makes the vicinal water more reactive than the bulk. This effect is thermodynamically sensitive over relatively long distances but is steeply attenuated over 1 µm. Thus, a water layer of significant thickness undergoes this thermodynamic shift and is expected to behave differently than its bulk counterpart, which justifies introducing the "new" ΔG in a bulk thermodynamics framework.

Simple calculations can illustrate this statement, for instance, the shift of the phase transition temperature in water (Figure 5.3A) or the solubility with respect to the quartz host (Figure 5.3B).

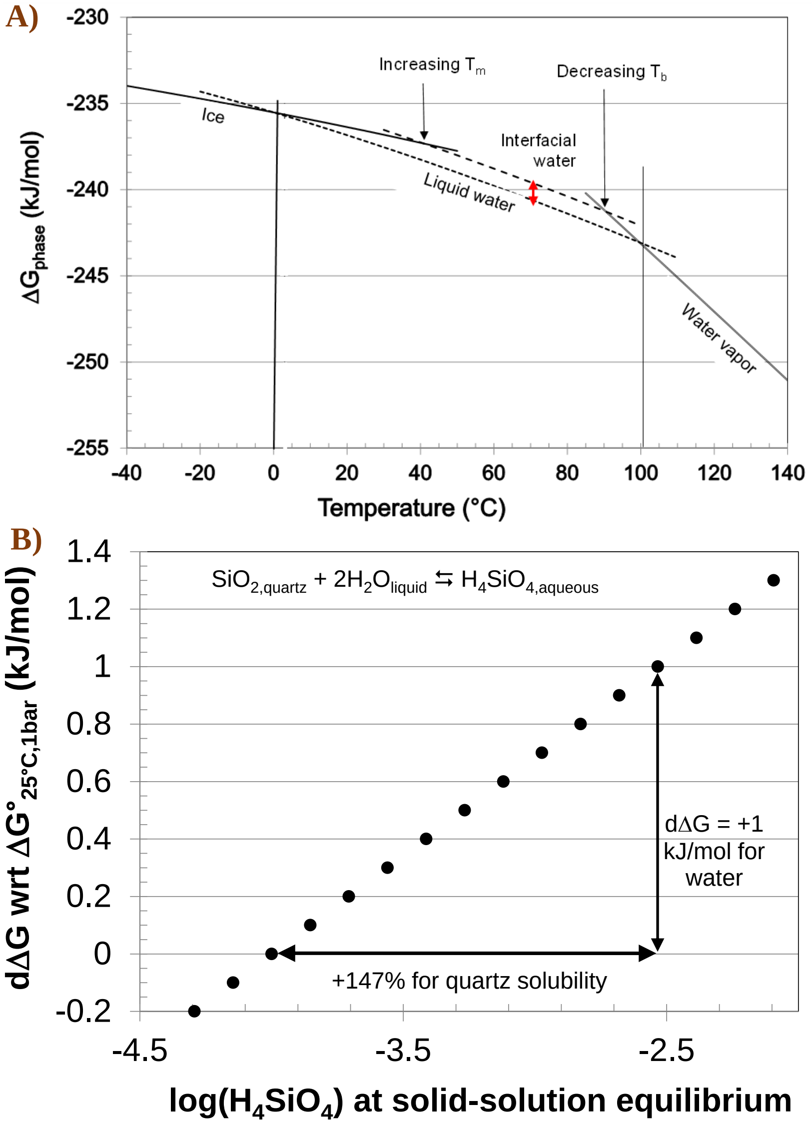

Figure 5.3. A) The estimated shifts of the phase transition temperatures and B) quartz solubility corresponding to the thermodynamic signature of interfacial water presently measured [56].

It appears that inside the interfacial region, the increasing Gibbs free energy of the liquid causes a depression of its boiling point, an elevation of its melting point, and enhances the solubility by a factor of + 147% for quartz if the Gibbs free energy of the interfacial water is increased by 1 kJ/mol (Figure 5.3B) at 25°C, +88% if the dΔG is equal to 0.6 kJ/mol. The decreasing boiling point corresponds to an upper displacement of the whole saturation curve (in a PT diagram), with

LV equilibrium obtained at a higher pressure than the bulk water. This fact is especially interesting because the hydrophobic interactions provoke a dewetting or cavitation [12] along the water-hydrophobe contact. It is important to note that an accurate calculation would require the heat capacity and the volume of interfacial-imprinted water since they control the variation of ΔG with T and P, respectively.

As early noted [56], the increased solubility of quartz due to the presence of water interphase offers an alternative to accounting for the well-known silica supersaturation in the old groundwaters of large sedimentary basins [33, 35]. An increase of 500 J/mol is required to meet the observed supersaturation in the Paris basin [56], which is reasonably consistent with the estimated interphase effect (without considering the silicic acid aspect).

5.4. Hydrophobicity effect: possible macroscopic surface fields

In what precedes, the in-pore water appears to have a varying chemical potential as a function of the distance to pore walls. Moreover, with the more accurate infrared maps, this frontier appears continuous all around the cavity, irrespective of the sides, top or bottom locations in the cavity. The signature is isotropic, making it possible to define an interphase domain wherein water is profoundly and equally disturbed with respect to the bulk position, with fewer H-bonds. Therefore, a diminished enthalpy, an increasing dangling-OH mode, and the predominance of IW components correspond logically to increased entropy. This leads us to conclude that there is a neat, steep frontier between the interphase and the bulk. At the precision of the infrared probe, there is no indication of a diffuse transition from the interphase to the bulk. Another point is that the presence of the bulk signature in the cavity center reveals that no confinement emanates from the cavity itself due to a wall-water-wall interaction, which is completely expected considering the dimensions at play. In this section, we are trying to review, qualitatively, which surface fields can account for the characteristics of our thick infrared layer.

Apart from the low-density layer at the hydrophobic interfaces, the main aspect is electrification along them. The surfaces of solid hydrophobes (as polypropylene, or some others) can be negatively charged, even in the air, due to surface-bound electrons [378]. When water comes into contact with these surfaces, the ions present in the water, such as H_3O^+, OH^{-}, and other cations/anions, form an electrical double layer with excess positive charges, and this charge separation is facilitated by the water's high dielectric constant. As a direct consequence, the hydrophobe-water continuum obeys the charged interface behavior. It is questionable that a silica surface can be strictly hydrophobic due to the well-known hydroxylation of silica with time. For instance, the measurement of dangling-OH mode on a quartz-water interface was obtained using functionalized silica surface with a silanization process [141]. Freshly cleaved silica exhibits coordinatively unsaturated Si−O bonds, which react rapidly with atmospheric moisture or liquid water, forming surface (Si−OH) groups [379]. The resulting acid−base chemistry of silica surfaces was studied theoretically, showing that silanol groups are only present on strained or defective surfaces [380]. Most probably, the very peculiar crystallographic status of our negative crystal-shaped cavity makes the surface reactivity of the inner walls quite different and the hydroxylation unfavorable. Indeed, the hydrophobic state of the pore walls is inferred by our recording of the less-connected water molecules, which are the particular features of such interfaces, though commonly recordable by nonlinear optical spectroscopies.

When considering the hydroxylated silica surfaces, a vast number of measurements and theoretical simulations, demonstrated the strong role of the water-silanol H-bonding. In particular, the two peaks characteristic of the OH-stretching band along such interface [140, 142] result from the silanol groups ability to donate or accept hydrogen bonds with different strengths, which consequently modulates the vibrational properties of the adsorbed water layer [93]. Alternatively, to limit increasing confusion, we can mention that the hydrophobic negative charging may come from an intrinsic anisotropic dipole orientation with the adsorption of hydroxide ions, the former causing the latter. According to Creux et al. and Lützenkirchen et al., [381, 382] preferential adsorption of hydroxide ions in the interfacial region of hydrophobic water interfaces is equivalent to enhanced autolysis of interfacial water molecules. It is an alternative mechanism to diminish the water density at the approach of a hydrophobic interface without requiring a boiling or still a repelling process.

Finally, we cannot tell that a precise mechanism of surface charging can be identified for our intra-crystalline silica surfaces, but we can evoke the consequence. The electrostatic attraction between a charged interface and counterions draws oppositely charged ions from the solution to the interface, competing with thermal effects that favor a more homogeneous, bulk-like ion distribution. The result is a charge distribution that is spatially inhomogeneous along the surface, with an associated electric field [383]. This field acts on the static water dipole, causing its preferential orientation near the interface. The interfacial ion distribution and the water molecules form the so-called electrical double layer (EDL). This classical mean-field description relies on average charge density, which is appropriate for various simple cases. However, it cannot capture the interaction of water with localized charges present at both mineral interfaces and bio-interfaces. Different observables question the mean-field theories, like the underscreening with salt concentration [384] or the opposite overscreening [385], as well as processes like overcharging or charge inversion due to preferential adsorption of co-ions [386]. The observations can be justified based on physical-chemistry considerations but cannot be explained by the classical mean-field models [383]. The result would be an ionic composition along the interfaces particular to the surface charge and the distribution of counterions/co-ions. The electrical potential at the proximity of the interface becomes the ideal mediator for disturbing the H-bonds network based on the dipolar nature of water. Interestingly, letting aside any hydrophobic interaction, a relationship between the surface charge density and the fluid supersaturation in micron-scale pores has been proposed to back-influence the crystal nucleation in pores [39].

To summarize, we come up with an interface characterized by a low-density (nano-bubbles) layer close to the interface and/or charged, namely being part of an electrical field. A first conceptualization of this situation would be to design the low-density layer as a gaseous-type layer. In that case, the water-hydrophobe interface would be formed as a liquid-air and air-solid interface sequence. In this way, it would become possible to model the interface as a three-dielectrics medium, meaning that the disjoining pressure may act throughout the interfacial layer (purposely equal to the interphase domain), modifying the Gibbs free energy with a $V.\Delta\Pi$ (Π the disjoining pressure) term. The disjoining pressure offers various interesting perspectives: 1) it can harness different components (hydrophobic interactions, electrostatic field, water structure, etc.), 2) it is a macroscopic term, equivalent to an internal pressure term, namely analogous to a density of cohesive energy parameter. It easily accounts for the increase of the surface tension linked to hydrophobic interactions since the surface tension is integral of the disjoining pressure over the film thickness (section 2.3.3.2). From a micro-macro viewpoint, it appears that the (certainly) a large number of dangling OH bonds gives rise to a large interfacial surface energy which may contribute to the Gibbs free energy of interfacial water [141, 342]. On one side, the bubbles would be stabilized by both the thermodynamic properties of the interphase water and by the electrical potential created at the surface, making it possible to record dangling OH modes even with the FTIR transmission mode. On the other side, the chemical potential of water would be, in that case, modified by a distance-dependent volumetric term depending on the Hamaker constant. This latter would measure the level of the 'pure' hydrophobic long-range force, with enhanced Hamaker constants possibly associated with the proton-hopping polarizability of water [369].

A second conceptualization track would be to assume that the low-density layer would be treated as a nano-bubbles alignment all along the perimeter of the water-quartz interface. It means the liquid water would be connected to the solid surface by successive punctuations separated by air pockets. An everyday life analog is a curtain suspended to a series of rings, themselves bearing on a curtain rod. In that case, the high surface tension of water, even diminished by the hydrophobic interaction, would allow sustaining of small capillary bridges depending not on the surface roughness and the presence of cracks but due to the limited connectivity of water with the surface. The bubbles here do not bridge two opposite planes as was envisioned for hydrophobic confinement (e.g., [369]), but their average size establishes the Laplace radius (weighted by the contact angle) and therefore fixes the internal pressure reigning in the interphase. This is again an internal pressure model, intrinsically long range, the intensity of which is highly dependent on the critical distance between anchorage punctuations.

5.5. Conclusion

We are positioning in that chapter our infrared findings within the framework of the hydrophobic interaction, which is far from being understood in general. Despite the possible superposition of various mechanisms and parameters, the presence of a stable interphase throughout an extensive range of geometries, occluded solutions (including pH up to 14), and mineralogical host postulates the existence of generic force fields systematically at play, able to propagate over the long-range here detected. The question of how to define hydrophobicity seems to be the real question behind this diversity of active parameters or possible force fields. It is also challenging to keep a conceptualization of the interfaces self-consistent from the macro-, to the meso-, down to the microscopic level/scale.

Due to the extreme length of what we measured, only very long-range forces can be proposed, which are not exclusive from each other. The surface tension approach associated with a capillarity/dewetting viewpoint, and an electrified process that modify the EDL, contributes to establishing a force field of thermodynamic significance and reaching the recorded scope.

We are aware of the speculative aspect of what is developed here, especially considering the enormous amount of data, interpretation, and simulations obtained over a large variety of situations. The hydrophobic puzzle is somehow confused by making the low-density layer and the dielectric effect interplay with a fluid composition, including the pH. The primary remark is that we are working with dirty materials (i.e., not pure ones), matching with the natural porous media characterization, which obscures the conclusions that can be inferred in terms of the law of physics. We cannot do better here to quote a very experienced team on those questions [369], though they were focusing instead on the hydrophobic confinement than purely interfacial hydrophobicity: “One of the few aspects that appear to be clear in the hydrophobic puzzle is the fact that the measured range of attraction decreases dramatically if great care is taken to eliminate electrostatic and capillary forces, for example, by rigorously deaerating the solutions. Deaeration has been found to significantly decrease the range of the extended long-range interaction between physisorption monolayers even though cavities no longer exist while bilayer domains still exist. Does this suggest that deaeration somehow removes the long-range electrostatic interaction? Deaeration has also been found to reduce the attraction and thickness of the vapor-depleted layer at hydrophobic–water interfaces but not the value of the hydrocarbon-water interfacial tension. Thus, the effects of deaeration on both the long- and short-range (adhesion) forces between hydrophobic surfaces in water are not currently understood [369].”

6. Reactivity at the nano-throat in heterometric pore networks: reactive role of the liquid-air capillary bridge

6.1. Introduction

The previous chapters quantitatively discussed the reactivity variation in the solid-liquid interface scale (nm-µm), also making some links between a hydrophobic solid-liquid interface and the liquid-air interface. Most of this manuscript thus discusses the phase boundary scale and supports the existence of a thick interphase layer that screens bulk water from solids. In this way, the water-rock interactions are no longer dependent only on the thermodynamic properties of the bulk phases. With the conceptualization envisioned for the hydrophobic boundaries, we came out with a low-density region, which might make capillarity a key player at the one interface scale. However, capillarity is commonly a matter of two walls, in which water bridges together, with a characteristic concave curvature. In this way, the internal pressure of capillary water diminishes with respect to the water behind planar liquid–vapor (LV) interfaces.

This self-consistent chapter intends to study the reactivity variation of liquid water **at the pore scale in the multiphasic situation** where capillary water takes place at nanometric pore throats (with intense capillary potential) coexisting with a massive amount of water occluded in large pore bodies. This is commonly called the ink-bottle effect (section 1.1, Figure 1.2).

As discussed in chapter 1, CO_2 injection in the deep aquifer (saline formations) is one of the possible ways to perform CO_2 storage and results in a complex multiphasic state (solid-liquid and liquid-air), especially near the caprock. We can conceptualize this aquifer-caprock interface as an ink-bottle type one (i.e., nano-throat and millimeter-scale pore assemblage), where the capillary bridge between the saturated caprock and the CO_2 bubble located in the aquifer can create considerable negative pressure (tensile state). Since the entire hydrosystem is hydraulically connected, the capillary pressure can propagate from the caprock-bubble pore to the macro scale of the whole caprock formation (Figure 6.1).

In order to better understand what happens at this precise location, considering the role of high capillarity explicitly, we designed specific experiments based on nanofluidic models etched in silicon materials, where nanoscale channels coexist with tens of microns-scale reservoirs (Figure 6.1). With these tools, we evaluate the role of relative humidity (RH) on a liquid-vapor capillary bridge in channels with nanometric thickness. First, we present how these nanocapillaries trigger water cavitation in the large reservoirs with which they are connected and describe the experimental protocol. Then, the kinetics of the nanocapillaries evaporation at different relative humidity ($RH < RH_{equil.}$) is discussed.

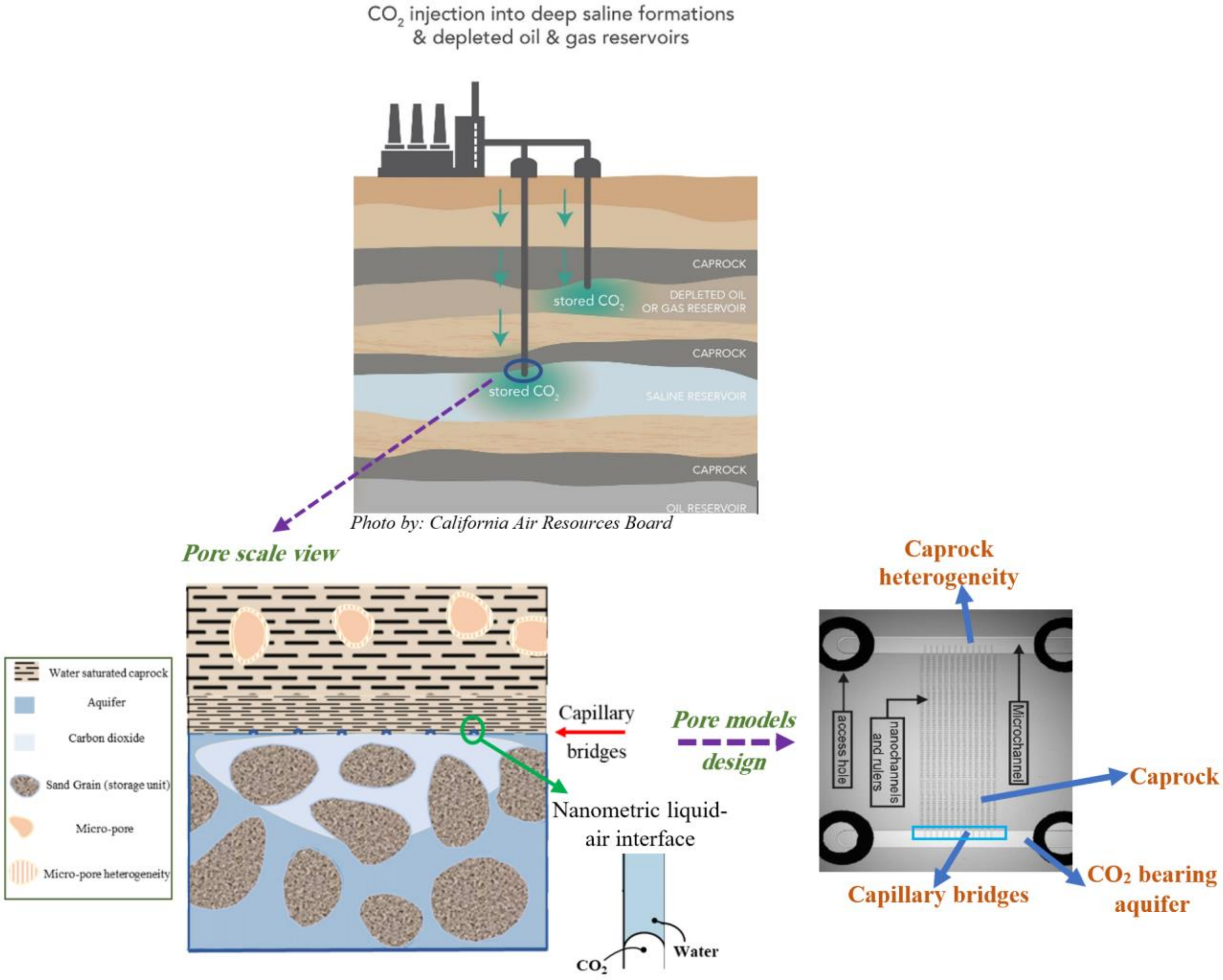

Photo by: California Air Resources Board

Figure 6.1. Schematic view of CO_2 storage situation in the subsurface and compared with our nanofluidic design.

As already explained in detail in section 2.2, the capillary bridges at the liquid-air interfaces control the mechanisms that occur in the porous media by generating a negative pore pressure. According to Young-Laplace law, this phenomenon occurs whenever the liquid is trapped in a pore smaller than 1.5µm. This negative pore pressure (water tension) is installed in the whole hydrosystem, but is stable only inside the nanometric spaces (Young-Laplace condition). Consequently, as soon as the tensile water imprinting invades the large reservoirs, the water trapped there becomes metastable and can boil at any time: this phenomenon is called cavitation, a form of cold boiling.

Also, the relative humidity of the contacting air affects the capillary water body. The Kelvin law, which depends on thermodynamic principles, explains this factor. According to this law, the capillary water body is in equilibrium with drier air than the bulk, providing the driving force for capillarization at the liquid-air interfaces and causing capillary water to be in equilibrium with this specific dry air. Then, at lower vapor pressure, even the capillary bridge starts to evaporate, while at higher vapor pressure, water condensation brings the capillary bridge at a lower tension than expected from the capillary dimensions [387, 388].

6.2. Material

6.2.1. Lab-on-a-chip (nanofluidic chipset)

The nanofluidic chipset (Figure 6.2) used in this study is a perfect example of the so-called Lab-on-a-chip experimental approach to precisely control and direct real-time visualization of flows, reactions, and transport mechanisms from the microscale down to the nanoscale. The chipset is fabricated by Niels Tas and Erwin Berenschot (University of Twente, Mesa). More details can be found in numerous references of their research team [389-391]. First, a silicon wafer with 380 µm thickness is used as the substrate. A silicon oxide layer is then developed on the substrate by dry oxidation. The thickness of this layer determines the height of the channels. It is controlled by adjusting the oxidation time. The channels are then obtained by photolithography and chemical etching with a 1% hydrofluoric acid solution. Then, a thin layer of borosilicate glass is used as a cover, and the access holes are made on it. The glass cover allows successful optical monitoring under the microscope. The wafer is first cleaned in a solution of HNO_3 and then in a second solution of H_2O_2 / H_2SO_4 (1:3) to ensure the hydrophilicity of the surface. Finally, the wafers are bonded to each other in an oven at 1100°C.

The design and geometry of a nanofluidic chipset used in this study are shown in Figure 6.2. It is characterized by two opposite macro-reservoirs (1 mm width, 2 cm length, 15-20 µm height) open to the external medium via access holes, necessary to fill in the whole inner volume in a controlled manner (content, flux). These macro-reservoirs are linked together by a series of 1D nanochannels (5, 10, or 15µm width; 3 mm length; 5 to 100 nm height), i.e., “nano” only along the vertical dimension. The channels are separated from each other by a pillar of silicon with the same width and length.

This well-defined and controlled structure, in terms of pore shapes and sizes, results in perfect ink-bottle assemblage and is adequately suited to our experimental purposes. It allows the generation of negative pressure by installing capillary bridges within nanochannels, leading to a metastable state of water simultaneously filling the macro reservoirs [392, 393]. Besides the controlled structure, this synthetic pore model provides us controlled fluxes and wall wettability. Due to the absence of a hydrophobic effect along the silica-fluid interfaces, the interfacial chemical reactivity can be neglected, meaning that any specific observables can be only related to the capillary bridging effect.

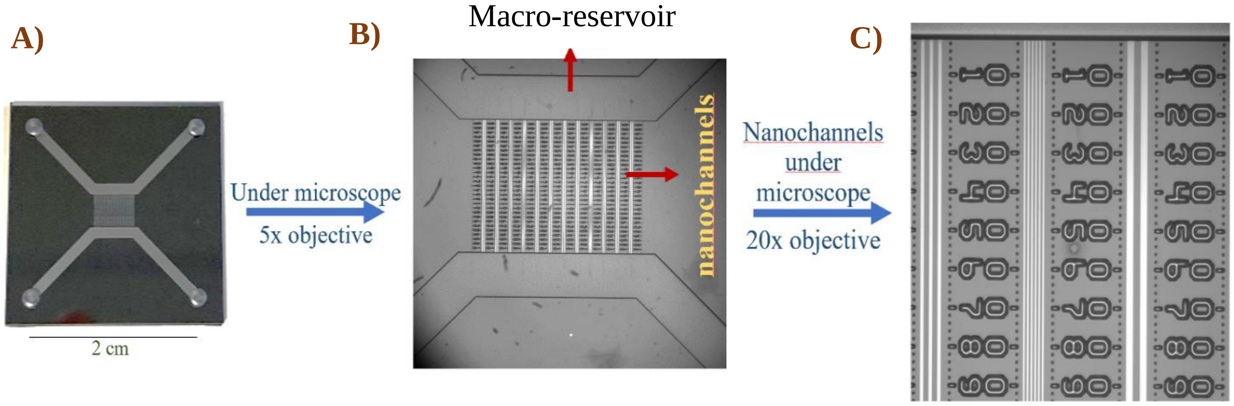

Figure 6.2. A) nanofluidic chipset. B) Micrographic images of macro-reservoirs connected by a series of nanochannels. C) Closer view of the nanochannels with the different widths.

6.3. Concept and experimental design

6.3.1. Concept

6.3.1.1. Capillary-driven imbibition

Water is omnipresent in nature, whether in soils, rocks, or the atmosphere, and its in-pores behavior is critical for soil differentiation, deep percolation towards aquifers (even or especially in the arid and semi-arid areas), plant growth (vascular flow) [394] and the formation of clouds [395]. Apart from the natural unsaturated domain, subsurface engineering (gas or nuclear waste storage, depleted aquifers, etc.) results in multiphasic porous media with the coexistence of liquids and vapors [396]. Also, the penetration of fluids through porous media (i.e., imbibition) occurs in a range of applications in technology, from printing ink on paper to oil recovery [397]. As a result, much research has been conducted on the kinetics of imbibition into the pore space in interaction with liquid, i.e., adsorption, ranging from early work by Lucas and Washburn [398, 399] to recent work on nanoporous media [80, 400, 401]. It is worth noting that the observed imbibition kinetics is efficiently fitted with the classical Lucas-Washburn (LW) equation, even when approaching the nano-scale [79]. The LW law allows to describe the liquid front position with time as follows [402]:

$$Y(t) = \sqrt{wt} \quad (6.1)$$

Where w is directly related to the permeability and pressure difference and inversely related to porosity ($w = -2k\Delta P/\phi$); and t is the time (s).

Once our chipset fills up to the top of the nanochannels, the unsaturated zone-on-a-chip can host a phase transition, following complex and unusual physical mechanisms due to the heterogeneities and pore size distribution.

6.3.1.2. Liquid-vapor (LV) phase transitions under tensile state

Herein, we focus mainly on the liquid-vapor phase transition and its mechanism in the presence of capillary bridges. Usually, evaporation/condensation arises whenever the vapor pressure is lower/higher than the pressure fixed by the saturation curve (as a function of T) (Figure 6.3B). These two processes similarly occur through the exchange of H_2O molecules from/to air to/from liquid along the surface of separation. Boiling occurs under evaporative conditions when the vapor pressure is a bit higher than the atmospheric pressure, making possible an LV bubbling transition inside the mass of the liquid.

Nevertheless, it is often forgotten that such a phase diagram (Figure 6.3A) is drawn for an infinite planar LV interface. The saturation curves of capillary water (Figure 6.3B), reveal that the vapor pressure at LV equilibrium decreases with the increasing tension of trapped water or decreasing pore radius of the host channel. But while the saturation curve moves downward for the trapped water in thin capillaries, the phase diagram stays unchanged for water inside macro-reservoirs. Consequently, this capillary "untrapped" water is in a superheating situation (Figure 6.3A), analogous to when a liquid cooled down along an isochoric trajectory. The key feature here is that such a liquid is metastable with respect to vapor and, therefore, prone to boiling at any temperature.

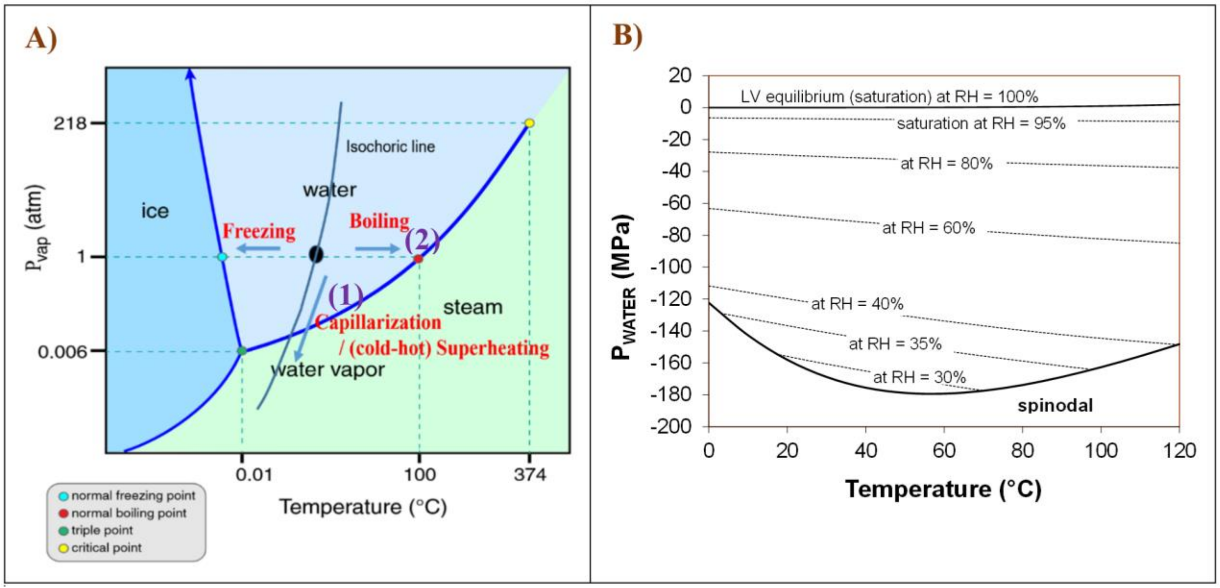

Figure 6.3. A) Schematic pressure-temperature (P−T) diagram of water (scales not respected). The black dot corresponds to the ambient conditions. Paths (1) and (2) provide the conditions of water in a superheated metastable state. The appearance of bubbles in the metastable liquid is called cavitation (path 1) and boiling (path 2). B) Saturation curves of capillary water at different relative humidity.

The liquid-vapor transition can only begin with the nucleation of a bubble, which is particularly unfavorable because of the high surface tension of water. Therefore, a kinetic barrier can keep liquid water below the liquid-vapor transition line. This explains why highly heterogeneous porous hydrosystems can last a very long time, despite the inner water being far from equilibrium. Experimental clues indicated that a liquid under as high tension as -700 bars can withstand this state for months [403]. Cavitation of metastable water is known to occur in natural or synthetic water inclusions in quartz [217, 404], in the sap of trees leading to xylems embolism [405, 406], and during the drying of porous media [407, 408].

The main concept of designing our experiments was inspired from Hulin et al., who observed that the capillary pressure imposed on the system when large pore bodies (200 µm) coexisted with a nanometric liquid-air capillary bridge. This capillary state controlled the system and induced capillary tension in the whole microvolume, changing the thermodynamic properties of the trapped water and not only towards the LV phase transitions but also towards the higher solid solubility. The metastable water is a super solvent for gas and solids, and the solubility variations are thermodynamically predictable according to a V.dP contribution (P the water tension) (Figure 6.4) [409, 410]. Complementary studies entirely supported the observations and measurements obtained in capillaries studies [411-413].

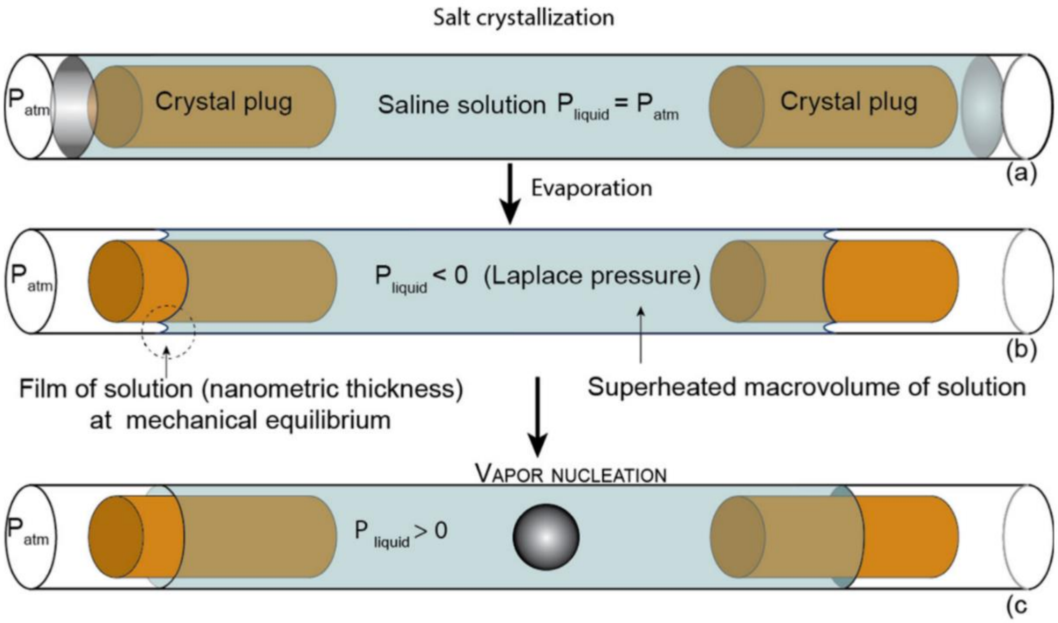

Figure 6.4. a) Salt precipitation and evaporation. b) nanometric air-water meniscus obeying the Young-Laplace law and confined metastable volume. c) Thermodynamic conditions after gas nucleation, by assuming equilibrium state between a bubble and relaxed liquid and a nonequilibrium condition at a nanometric water-air interface after gas nucleation [409].

6.3.2. Experimental design

Since most experiments rely on direct optical observations, we employ the Nikon Ni-U ECLIPSE microscope in reflected mode to track the variation inside the nanofluidic chipset over time. Nikon's NIS-Elements software makes it possible to record instantaneous or programmed image captures and to modify the contrast. In order to maintain the chipset under the objective, we designed and fabricated (ISTO workshop) a sample holder adapted to the geometry of the chipset. As shown in Figure 6.5 and Figure 6.6, the sample holder was made of transparent or opaque resin and manufactured at ISTO workshop using a 3D printer device. The VIS-transparent resin is very useful since it allows to control the water filling optically and detect any eventual liquid/gas leakage. The sample holder has four tubes (solid red square in Figure 6.5A and Figure 6.6F): two dedicated to the liquid phase (inlet and outlet) and two to the gas phase, which are directly connected to the conical connectors (yellow dash line in Figure 6.5B), where the sample holder is connected to the chipset (Figure 6.6C&D).

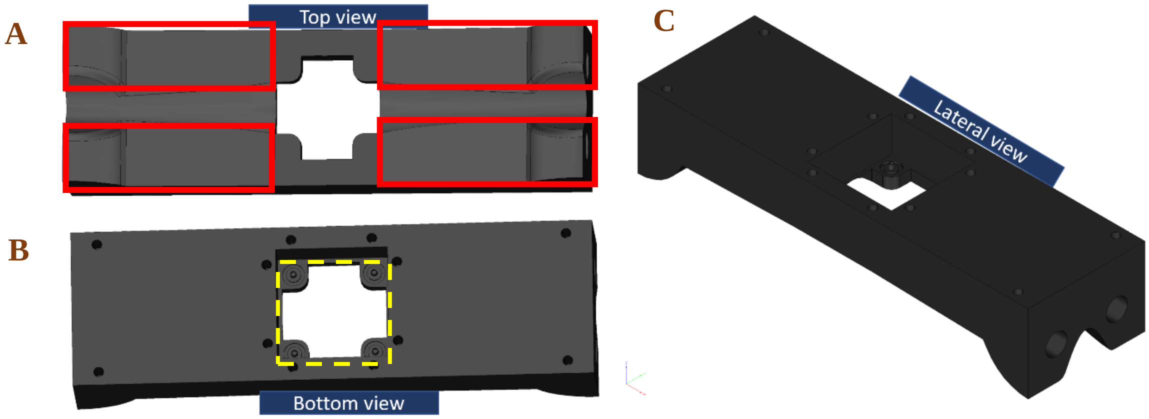

Figure 6.5. A) Top, B) Bottom, and C) Lateral view of sample holder made of opaque resin. The sample holder has four tubes (solid line square), two dedicated to the liquid phase and two to the gas phase, which are directly connected to the conical connectors (dash line square).

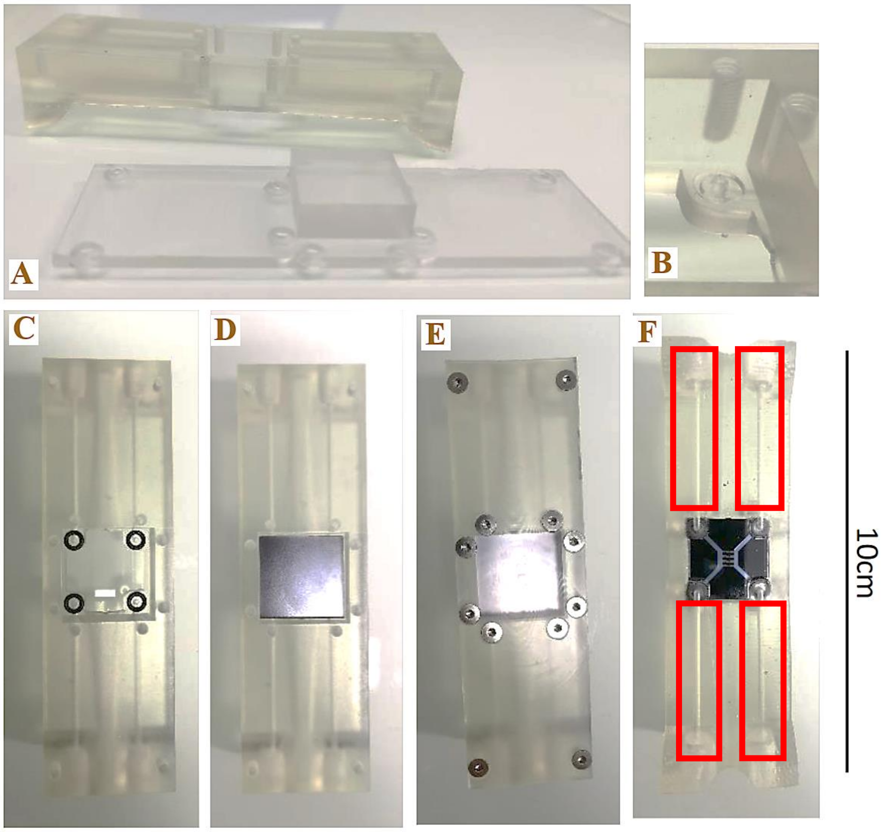

Figure 6.6. A) Transparent sample holder and its lid; B) Conical connectors for connecting the tube of the sample holder (inlet) to the chipset access holes; C) Positioning of the O-ring seals around the connectors; D) Sample installation; E) Sample holder closure; F) Top view of a system composed of chipset and holder before the installation under the microscope.

Before reaching the final experimental protocol, numerous tests and adjustments had to be carried out. Indeed, several problems encountered during the imbibition experiments, leading to the delay of experimental phases. Initially, the main difficulty was isolating the system from the surrounding condition (direct contact with the surrounding air). Leakage at the inlet of the sample holder during water injection and around the conical connection between the sample and the sample holder has been observed during the first experiments. The O-rings seals have been changed to prevent leakage at the conical location. The other leakage was limited by reducing the height of the central part of the lid and by modifying the length of the screws in the try-and-error process.

After complete isolating, various tests were conducted to observe the system behavior in response to capillary imbibition occurring through the nanochannels. During the first tests, the filling of nanochannels by the liquid was partial and heterogeneous, especially in the corners (Figure 6.7A&B). To limit the appearance of bubbles and corner effects, we decided to inject degassed liquid and put the sample under a vacuum before liquid injection, a method inspired by the work of Tamaki & al [414]. Moreover, we performed a series of heating treatments (i.e., placing the nanofluidic chipset in an oven at approximately 150°C for the 5 hr.) and plasma cleaning treatment (i.e., putting the chipset in the plasma chamber for 6 hr.). Figure 6.8 shows the successfully homogeneous filling of the nanochannels after performing the vacuum, heating, and plasma cleaning.

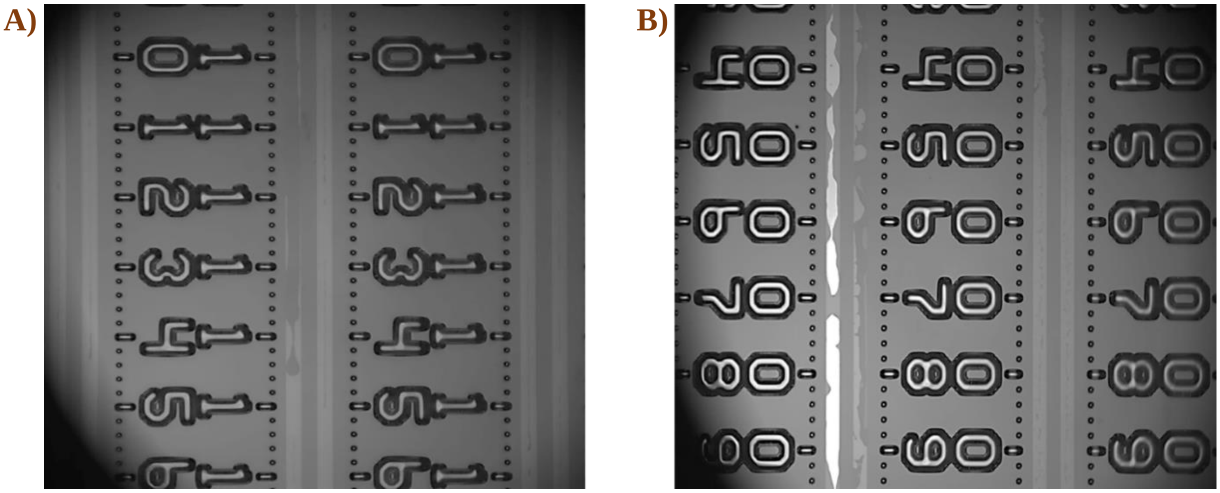

Figure 6.7. Partially filling of the 100 nm height nanochannels at two different channels (A and B), caused by some impurities inside the channels or gas trapping. The obtained images in a gray gradient, representing the liquid-gas distribution in the sample: light shade is the gaseous phase (air), and the dark shade is the liquid phase (water).

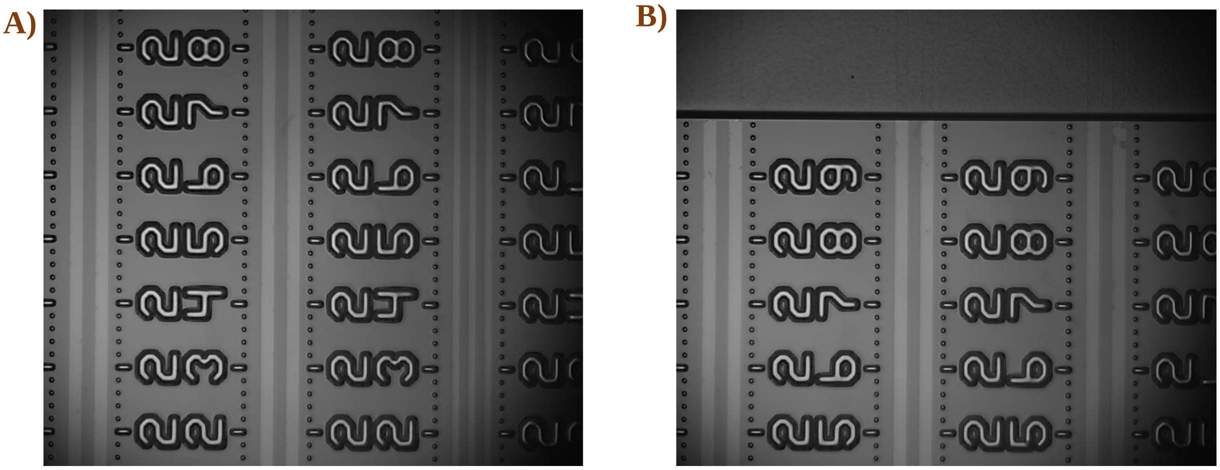

Figure 6.8. Homogeneous filling of 100 nm height nanochannels at two different channels (A and B) after heating, plasma cleaning, and vacuum treatment.

In the final experimental protocol, before each imbibition procedure, the chipset was treated by putting it in the oven and using plasma cleaner to remove any impurities inside the macro-reservoir and nanochannels. After that, O-ring seals were placed around the conical connectors to prevent leakage at the connection between the sample and the sample holder. The chipset was located on the sample holder and was tightly closed using a lid fixed by screws. Then, to prevent gas trapping in the nanochannel, the sample was treated under a vacuum for at least 12 hr. in a way that a vacuum was created by exploiting a vacuum pump connected to the gas phase outlet. Finally, the channels were filled by introducing a drop of water into the uppermost access holes using a syringe/pressure pump.

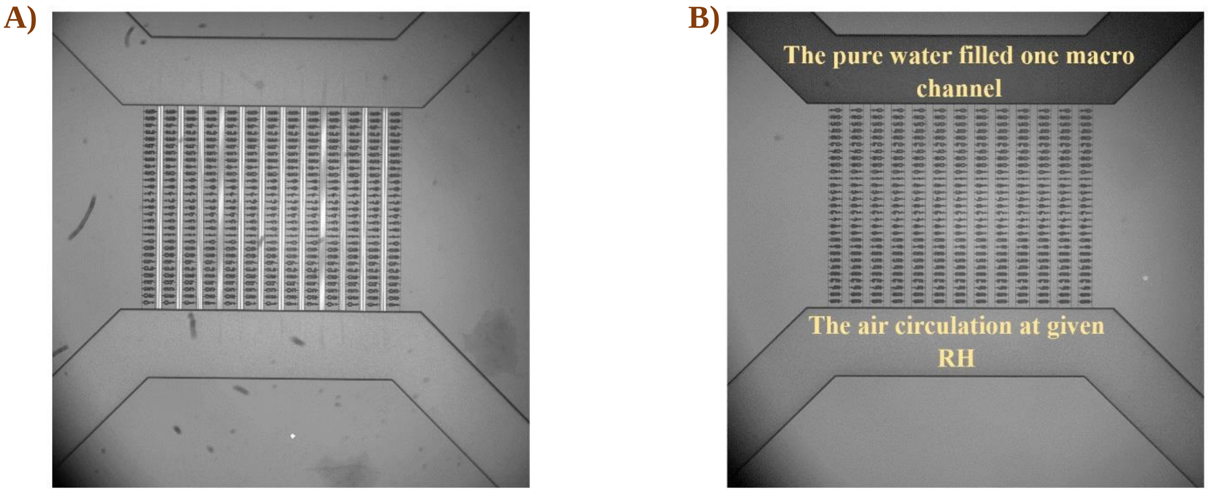

Figure 6.9. The chipset A) before and B) after imbibition with the procedure of the final experimental protocol.

To fill the nanochannels completely, it is necessary to reinject water regularly (for 30 minutes by the rate of 0.3 mL per minute). Afterward, two tubes of the sample holder, which are devoted to the water inlet and outlet, were closed by the dead-end screw. Then, the gas phase at the given RH is injected into the system by another macro-reservoir. For controlling the RH, the thermostatic bath (Julabo - FP40) is employed to adjust the temperature and water vapor pressure ($RH = \frac{p^V}{psat} \times 100$, see section 2.2.3.1). Figure 6.10 and Figure 6.11 show the experimental setup employed in this study.

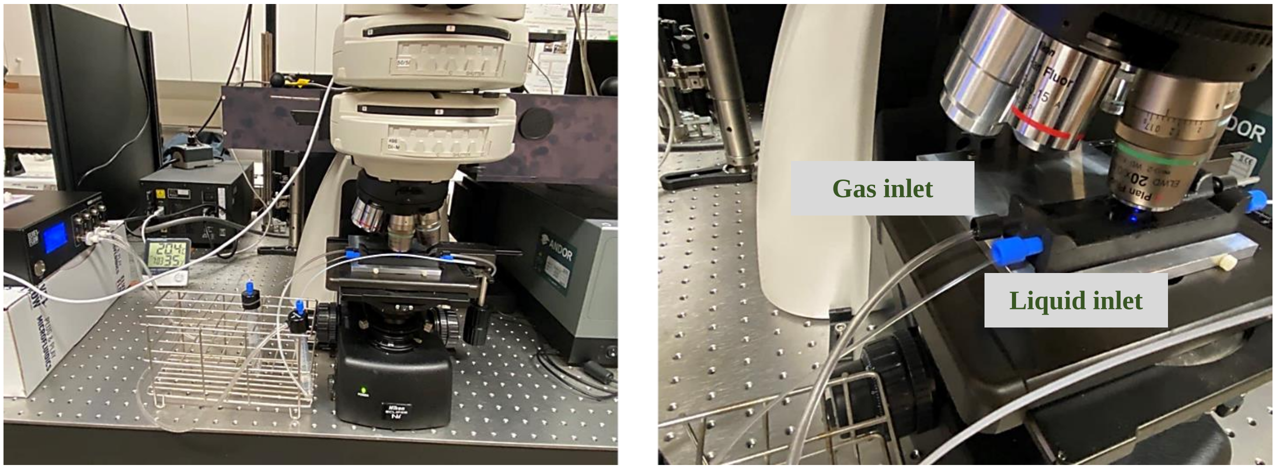

Figure 6.10. The experimental setup during the water and gas injection, including the Nikon microscope, pressure pump, sample holder, nanofluidic chipset, tubes, and screws.

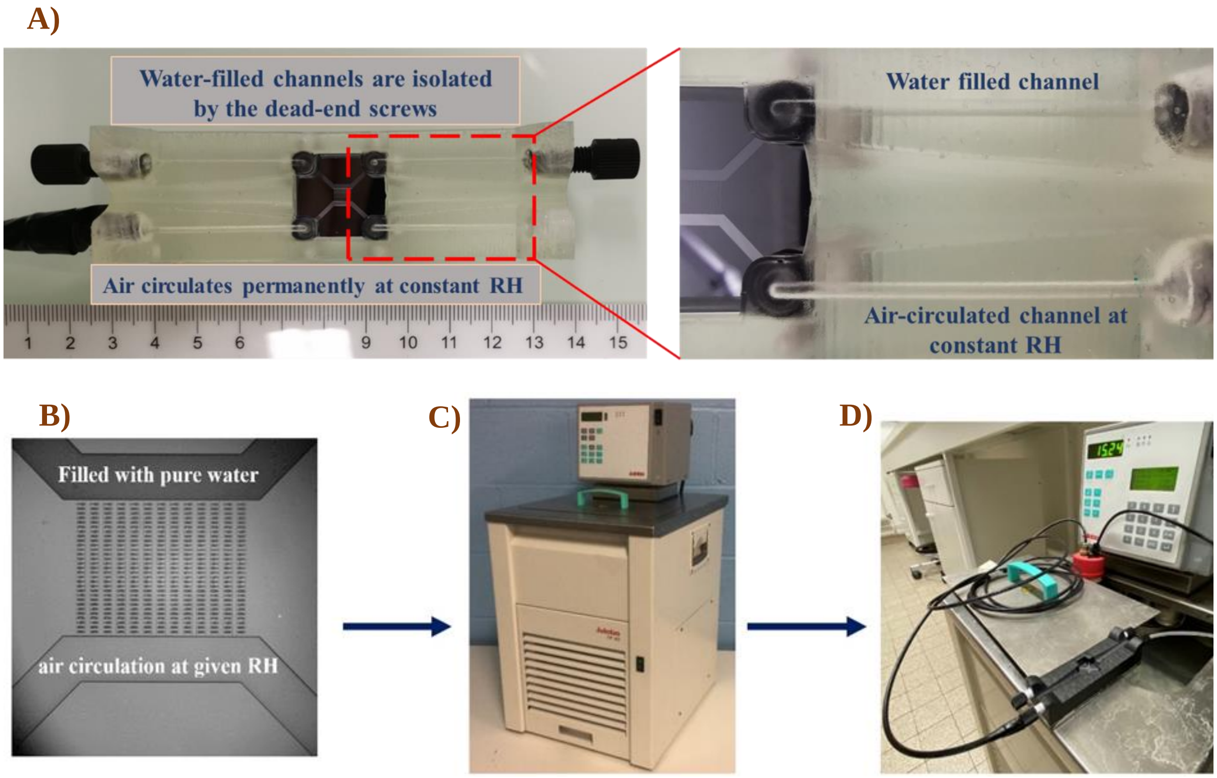

Figure 6.11. A) nanofluidic chipset with the sample holder after water injection. B) Microscopic image (10X magnification) of the nanofluidic after water injection. C) the thermostatic bath employed for controlling the RH. D) The final setup, where the sample is under permanent air circulation at the specific RH.

6.4. Result and discussion

6.4.1. Water cavitation

Before showing the water cavitation process in the nanofluidic chipset (i.e., open pore), the water cavitation phenomenon is tested in the fluid inclusion (one closed pore). In this way, we employed a synthetic fluid inclusion to monitor the water boiling (cavitation) by decreasing the pressure down to -90 MPa through the isochoric curve. Figure 6.12 shows the cavitation phenomenon in the exploited SFI. As shown in Figure 3.5, after reaching the T_h, the liquid invades all the cavity (the liquid-vapor assemblage becomes monophasic). Further cooling makes the trapped water to follow the isochoric curve down to its extreme negative pressure at which cavitation is observed. Spontaneous cavitation in the metastable liquid results in the appearance of a bubble and relaxes the tension [412, 413]. After this sudden relaxation, the previously stretched liquid contracts return to its saturation properties, while the air phase appears by water boiling and (probably) liquid degassing due to the brutally low gas solubilities in the newly saturated water.

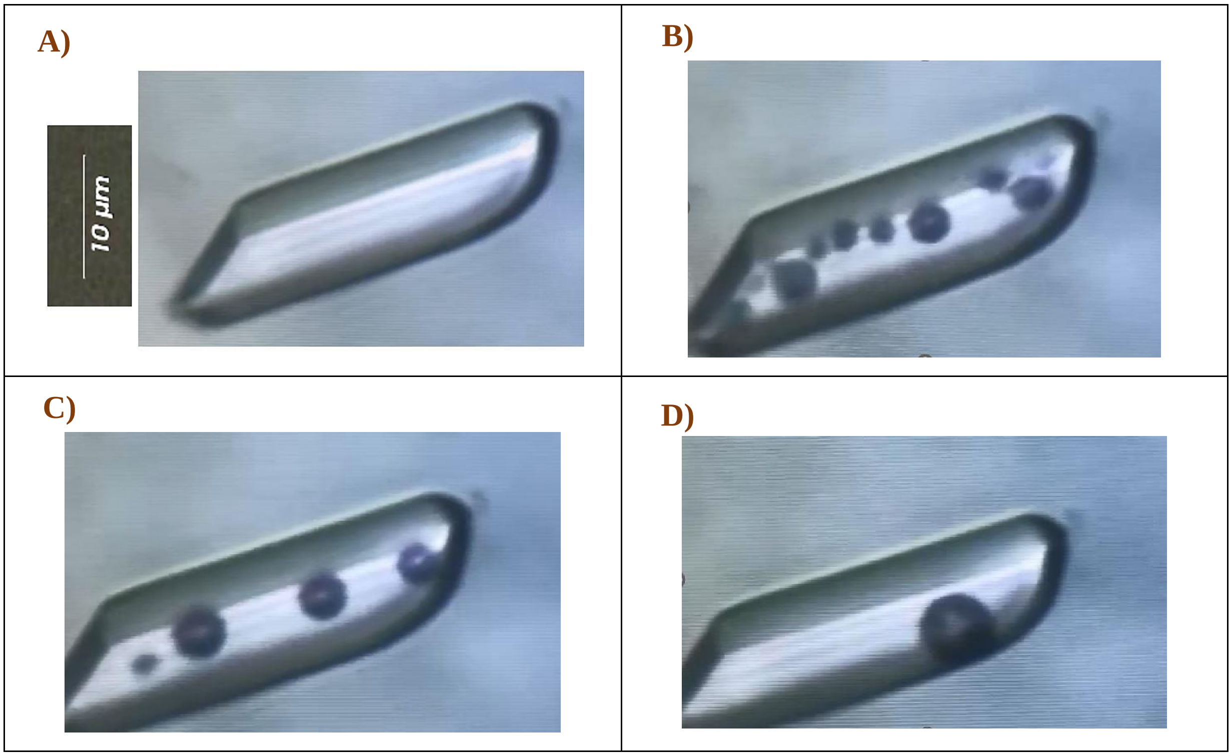

Figure 6.12. The cavitation process in SFI, starting from A to the final D state.

After introducing the cavitation in the closed pore, we move forward to study the water cavitation in a nanofluidic chipset with a capillarity state. It is worth recalling that the mechanical Young-Laplace equilibrium (equation 2.7) is allowed by the presence of liquid-gas menisci on the surface of the porous medium, which supports the pressure difference between the two phases. A growing tension is installed in water by thinning the capillary bridges in narrower and narrower capillaries. Following that procedure, Wheeler and Stroock and Vincent et al. obtained pressures up to −22 MPa using a polymer hydrogel as the porous medium [415]. With our nanofluidic devices, we can reach **-34 MPa** in the **5 nm channels** (calculated by Young–Laplace equation (equation 2.7).

Figure 6.13 illustrates our metastable experiments performed in 5 nm channels. The top reservoir is entirely water-filled, as well as the connected nanochannels. The opposite reservoir hosts air flux at constant RH, here adjusted to 80% (Kelvin law - equation 2.9, gives 78% as the equilibrium RH for 5 nm rectangular channels). As shown, the first bubble is observed after 10 days, at a distance far from any extremities, establishing that it is not hidden evaporation that produced it, but a real boiling in the middle of the liquid mass. Since the nanochannels, macro-reservoir, and sample holder tube are hydraulically connected, the capillary pressure installed at the capillary bridge can propagate inside the system, including the macro-reservoir and beyond all dimensions are at least three orders of magnitude larger than the 5 nm bridge. As a consequence, liquid water is supersaturated with respect to water vapor, meaning that the energy excess to create bubbles (creation of interfaces) is largely available according to the confinement-corrected of classical nucleation theory (CNT) [413].

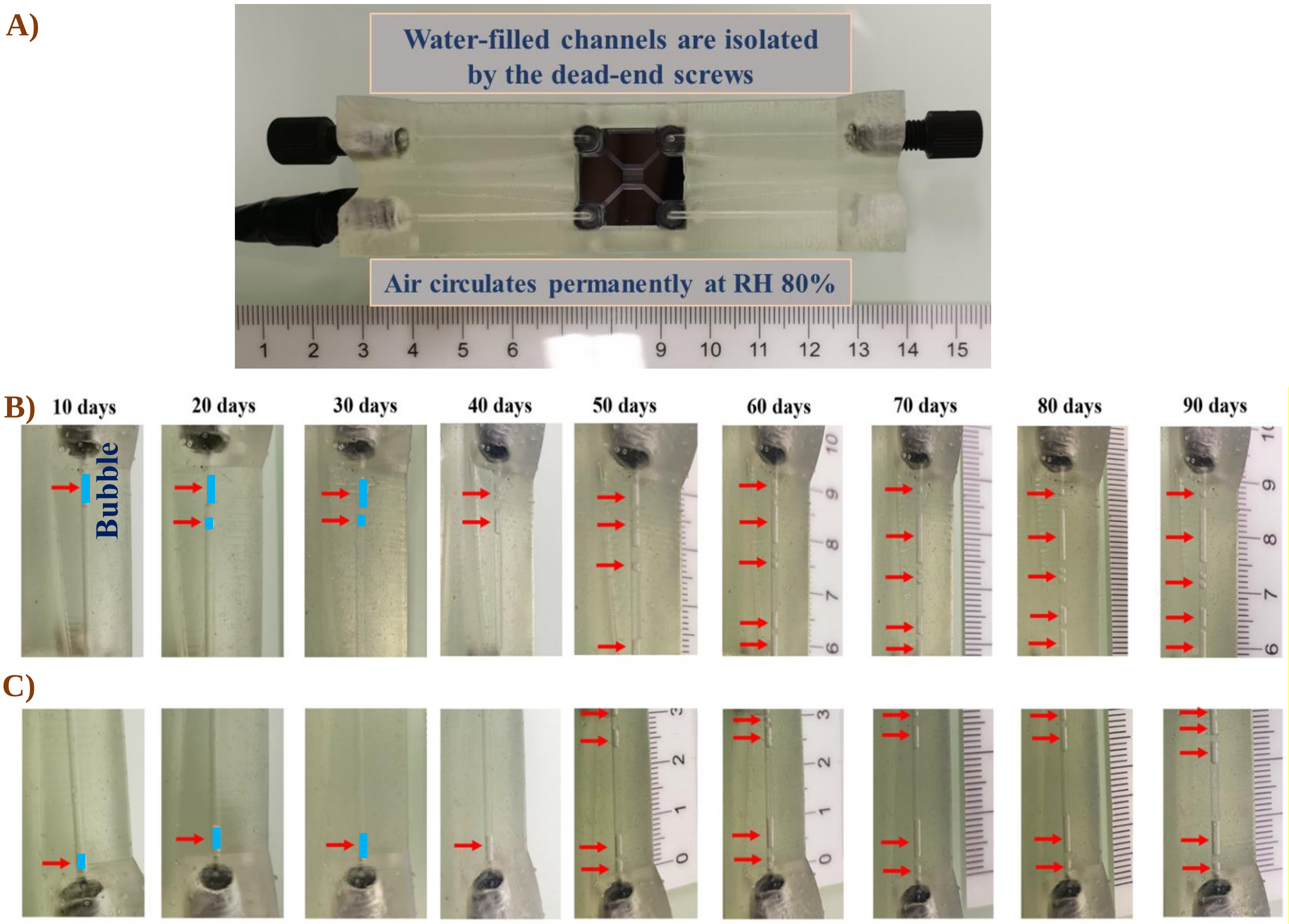

Figure 6.13. A) Filled 5 nm chipset with sample holder placed under the permanent air circulation at RH = 80%. Consecutive bubble appearance (cavitation) in the B) left and C) right sample holder tubes over 90 days. Red arrows show the air column inside the sample holder tube by time.

The main information conveyed by this experiment is that we observed real cavitation (boiling at the distance of any connectors). It occurred after ten days, not inside the chipset macro-reservoir but in the tubing inside the sample holder. As expected, the nucleation occurs through a heterogeneous process, for which any impurities, wall roughness, or crevices, lower the energy barrier. A second fact given by this experiment is that the total volume of the bubble regularly increases with time, but according to two kinetics (Figure 6.14). A first interpretation could be that we recorded a gradual cavitation process; however, it is impossible in the case of a metastability release which occurs as a rapid phase transition for thermodynamic reasons [416]. The second hypothesis is that the post-cavitation relaxation occurs along two different sequences. Herein, liquid water degassed due to the changing of solubility. This variation in solubility results in the re-increasing of the internal pressure, making the liquid undergo a self-deaeration process. To ensure clarity regarding the primary purpose of this post-cavitation kinetics, particularly in relation to water mass loss, we have made the decision to record the evaporation kinetics at various relative humidity (RH) levels. By doing so, we aim to provide a comprehensive understanding of the process and its impact on any discernible patterns or variations.

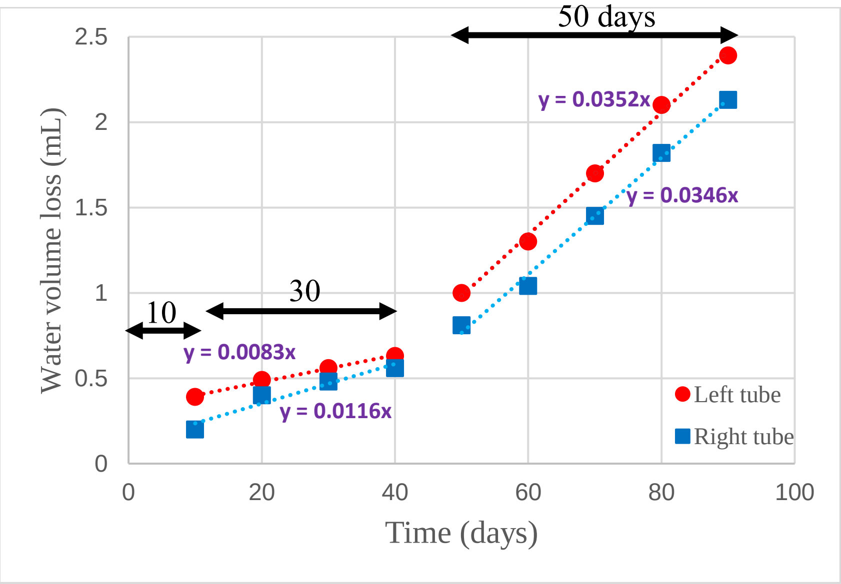

Figure 6.14. The water volume loss over 90 days in the left (Figure 6.13B) and right (Figure 6.13C) sample holder tube (total water volume in the sample holder tube and the nanofluidic chipset is equal to 5 mL).

6.4.2. Kinetics of liquid evaporation mediated by nano-channels

The experiments for evaluating the kinetics of evaporation were inspired by Vincent et al. research regarding the effect of the relative humidity on the evaporation kinetics of water located in the cylindrical nanochannels with a 2 nm radius [79]. They concluded that the evaporation mediated by cylindrical capillaries shows an unusual coherency, largely controlled by the nanoscale flow between the reservoir and water-air bridge. The thermodynamic stress between the reservoir and the bridge, implied by Kelvin equation, expresses itself as a mechanical pressure in the liquid, even in tiny pores (nanometric diameter). While this mechanical equivalence of the Kelvin stress has been shown to hold in static situations, their results provide the first demonstration in a dynamic context (permeation flows) and across an unprecedented range of stresses (down to ≈ -100 MPa).

Herein, we conducted similar drying experiments but in slit-shaped channels, where the corner flow plays a role in the drying procedure [417]. We carried out careful imbibition of one macro-reservoir and the connected slit-shaped 5 nm nanochannels with degassed water. We intentionally created a tiny bubble inside the sample holder tubing for providing the activation energy for the liquid-air meniscus to recede. Since $P_{\text{bubble}} >> P_{\text{nanobridge}}$, leads to create an advection and evaporation through nanochannels (strong ΔP). In order to prevent evaporation of the water reservoir through the inlet sample holder tubes and the conical connectors (that would compete with the water loss by capillary evaporation), they were sealed by dead-end screw and O-ring plastic, respectively. Then, the sample was placed under the permanent air circulation in the opposite macro-reservoir at three different RH, namely 25, 50, and 65%, below the equilibrium relative humidity (78%). We recorded the kinetics of evaporation (loss of water mass) at these three relative humidities (P^V/P^{sat}), following the motion of the liquid-air meniscus in the sample holder tube. Figure 6.15 shows the water mass loss (mL) over 90 days of experiments.

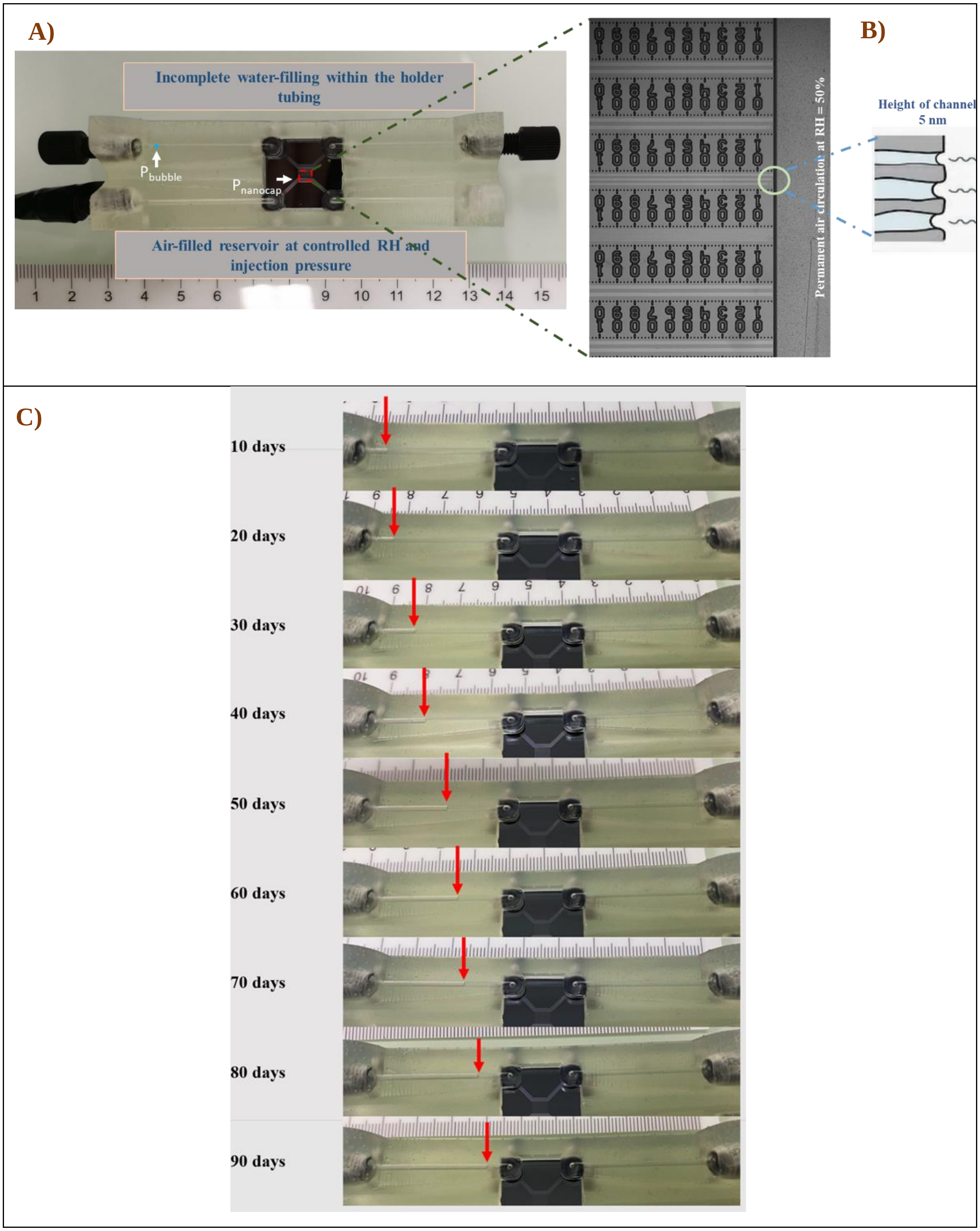

Figure 6.15. A) Water filled 5 nm chipset, on its sample holder, under the permanent air circulation at RH = 50%. B) The schematic view of the process. C) Red arrows represent the position of the air-water interface in the tube of the sample holder reservoir, X(t), reflecting the loss of water by evaporation occurring through the nanochannels.

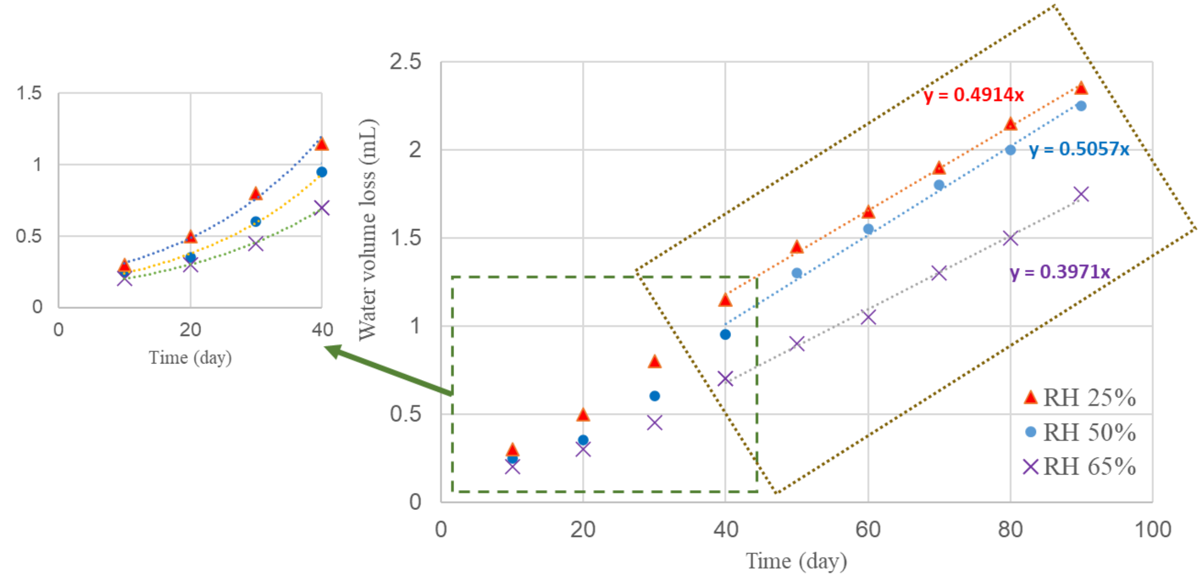

Figure 6.16. Kinetic of water evaporation (drying dynamics) at three different relative humidities, reflecting the loss of water by evaporation occurring through the nanochannels.

As shown in Figure 6.16, there are two regimes regarding the kinetics of evaporation: transient state (from 0 to 40 days) and steady-state (from 40 to 90 days). Indeed, the driving force for evaporation (drying) was provided by the water-air capillary bridge at the end of the nanochannels, where there is direct contact with the circulating air. We are dealing with the slit (rectangular) nanochannels characterized by an intrinsic capillary pressure ($\Delta P_c = -\sigma\ cos\theta/r$). One edge of the nanochannel is in contact with the macro-reservoir in which normal water pressure exists ($\Delta P_{liq} = 0$). The opposite edge is the water meniscus in contact with air and at equilibrium with the vapor pressure p^V tuned by the thermostatic bath, with: $\Delta P_{ext} = RT/v_m \ln\ (p^V/p^{sat})$. The pressure difference that drives the nanoporous flow from the reservoir to the top of the nanochannels resides in this difference between the capillary tension at the capillary menisci compared to the (higher) liquid pressure in the reservoir.

In terms of the driving force toward channel flow and evaporation, there are two situations linked to the respective value of ΔP_c and ΔP_{ext}:

If $\Delta P_{ext} \geq \Delta P_c$: the nanochannel, macro-reservoir, and sample holder tube remain entirely water-filled. The meniscus is pinned to the end of the nanochannel, and its curvature (r) is set by the external relative humidity through the Kelvin-Laplace equation. The meniscus curvature is far from being maximal, and the water tension is lower than the extreme value reachable in the capillary, which is adjusted by the value of the contact angle in the Young-Laplace equation.

If $\Delta P_{ext} < \Delta P_c$: According to Kelvin law, the evaporative demand exceeds from which the capillary meniscus can sustain. As a consequence, the meniscus starts evaporating and recedes within the nanochannel to the point that the equilibrium state is reached again due to increased vapor pressure, higher than in the "external" macro-reservoir (and up to a point that ΔP_c = ΔP_{ext}). Note that to study the kinetics of evaporation, we designed our system in that regime and explored three different RH to see the dependency of the evaporation rate on the evaporative demand.

Our experiments demonstrated that the evaporation rate is a direct function of the external RH: the lower RH, the faster the receding motion. The overall trend of our findings deviates from the results acquired by Vincent et al. [79]. By employing cylindrical (smaller) nanochannels, they showed that lowering the relative humidity led to a higher evaporation rate up to the Kelvin RH value. Beyond that, the kinetics became independent of the RH variation, and they are only controlled by the nanoporous flow, driven by the capillary pressure. In the first regime, the decreasing RH drives an increased capillary pressure in the capillary liquid (therefore, an increasing pressure drop from the reservoir to the meniscus), expressed by a growing curvature (decreasing contact angle) of the menisci. However, it stays pinned to the open edge of the nanocapillary. In that stage where the evaporation rate logically depends on the RH, the contact angle is fixed according to a canthotaxy process and not the wetting properties (Young-Dupré equation). When considering the open edge of a capillary, the contact angle can adopt a range of values depending on the true wetting contact angle θ (liquid-solid affinity) and the geometrical angle of the structure (Figure 6.17), which is called a canthotaxy effect:

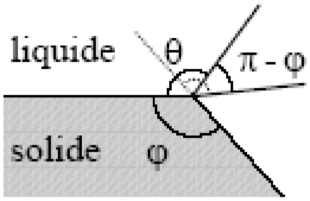

Figure 6.17. The contact angle combines the wetting contact angle and the angle of the supporting solid ([418]).

The range of the accessible angles is given in that case by π - φ, and by this effect it is possible to overfill a glass of water. When arriving at the final edge of a capillary tube, the capillary meniscus will adjust its curvature by playing with this angle to equilibrate the Young-Laplace pressure drop across the interface without flowing outside.

In the second regime observed by Vincent [17], the decreasing RH makes the capillary meniscus to evaporate; it cannot "capillarize" more than what is fixed by the pore size and the Young-Laplace mechanical equilibrium. As a result, the evaporation rate cannot increase with decreasing RH since the capillary pressure stays constant, so the driving pressure difference in the capillary flow drives the water loss.

In our results, the biggest change is related to the capillary shape. Using slit-shaped channels makes it possible to create corner flow, allowed by the water liquid film trapped in the four corners of the slit, reaching larger curvature than the main meniscus and, therefore, sensitive to a decreasing RH since able to create larger water tension. It is interesting to observe the RH dependence on the flux, even beyond the Kelvin RH value (78%) for our rectangular 5 nm height channels. However, this "screening" effect is not linear, as can be seen with the evaporative enhancement that fades when moving from 50% to 25% (Figure 6.16). Most probably, the corner flow decreases with the film thinning (due to RH decrease) as observed in square capillaries [417].

6.5. Conclusion and perspectives

We have employed the Lab-on-a-Chip nanofluidic chipset with the ink-bottle geometry to illustrate experimentally how the liquid-air capillary bridge in the ink-bottle structure porous media can modify the chemical potential of the whole hydraulically connected water body through capillary effects (tensile state). We have illustrated that air relative humidity (RH) controls the capillary pressure in the nanochannels, so this combines the water-filled nanoporous aquifer (Young-Laplace condition) with low-RH air bubbles (Kelvin condition), which makes strong capillarity to happen.

Imposing the equilibrium RH (or slightly larger) with 5 nm channels allowed us to observe water cavitation in the large reservoirs behind the nanochannels. It makes clear that the capillary pressure propagates in the whole water mass connected to the capillary bridge, making the system to obey the capillary geochemistry, as was already concluded with previous experiments [403, 409]. This illustrates that caprock-CO_2 assemblage can cause diphasic partition inside the caprock for conditions far from the breakthrough pressure.

We also studied the drying process when RH becomes lower than RH_{equib}. In that case, the nanoporous/reservoir hydrosystem evaporates with an effect driven by corner flow with a limiting parameter: the evaporative surface towards the external air decreases with the evaporative demand. Once again, this process can strongly modify our conceptualization of the mechanism, which plays a role at a caprock-CO_2 bubble interface. Our experiments viewpoint is that this is the whole water mass connected to the capillary bridges, which is impacted by the capillary properties and flux. Therefore, both the dynamic and the static behaviors are modified for the total volume of water infilling the whole caprock, or possibly also the water in the upper aquifer is equally affected.

As a consequence, the water status and reactivity in the containment barriers of underground storage can be questioned, as those made of thinly porous formations of very low permeability are the storage media itself (host rock for nuclear waste), as the impervious caprock overlying the storage aquifer (CO_2 storage, energetics vectors like H_2). The drying reservoirs come from either the ventilated tunnels (those accessible to nuclear containers), or the injected gas bubbles, and trigger the capillary-driven processes that propagate behind the liquid-air capillary bridges in the whole hydraulically connected water reservoir [419].

In terms of perspectives, it is clear that the present chapter gathers preliminary results that require further investigation and complementary measurements. The effect of the pore size on the kinetics of evaporation should be completed by new series of measurements with the 5 nm slits at intermediate RH, between 65% and 50% and from 65% to 80%, as well as under extreme RH of 10%. Also, a series of experiments with the 15, 20, and 100 nm chipset will be conducted to densify the observations and systematize the conclusions. For the cavitation experiment, having a new chipset with nanochannels at 2 nm should complement usefully our dataset, and we are discussing the corresponding fabrication with our partners.

Once controlling the drying-imbibition steps in the chipsets closely, we could design new experiments based on an aqueous solution of known composition with different concentrations (unsaturated or supersaturated) to investigate the capillary-driven effect on the phase transitions (crystallites precipitation or over-solubility) in the nanochannels or the macro-reservoir.

7. General conclusion and perspectives

7.1. Conclusion

This study concentrated on the **local chemical potential gradients** along interfaces, which controls the subsurface geological formations through the water-rock interaction. We worked at two different scales, namely the **interface scale** (nm-µm), at which phases interact together, and the **pore scale,** at which interfacial gradients combine into properties averaged over a large volume of matter throughout a pore network. Geochemists often rely on the standard model in which the macroscopic driving forces and the resulting mass balances in the water-rock interaction can be adequately described by the bulk properties of interacting phases. However, many theoretical studies and direct field observations challenged this viewpoint by demonstrating that solution properties depended on the distance from a solid surface (i.e., pore radius) or the presence of a curved liquid-air interface [30, 37]. There has been much discussion, and different conclusions regarding the length scale over which the properties change are observed with respect to the bulk and varied threshold value from 1 to 1000 nm were reported in different papers regarding this aspect [48-51].

More specifically, we tried to clarify a **local chemical potential gradient** arising along water-solid interfaces when they have got hydrophobic character. The interface scale is very often examined from the solid viewpoint trying to decipher whether or not a leached surficial layer may impact the local reactive transport coupling or still retains changing mineralogy due to the preferential weathering processes. Recent high-resolution studies (e.g., [420]) challenged this old scenario, demonstrating that the solid interface is very thin by conceptualizing the mass exchanges for water-silicates reactions through interface scale bulk-type dissolution–reprecipitation. To give another well-known but very different example, the community still questions the discrepancy between the laboratory and field-based reaction rates of silicate materials ([421]). Our contribution argues that the water viewpoint matters depending on which solid it interacts with, and so could contribute to these two debates.

In this way of reasoning, we tried to record the water properties variation as a function of distance to the solid-liquid and liquid-vapor interfaces. In light of the previous studies, we chose the vibrational spectroscopy method (FTIR) as an energetic probe to record how the vibrational energy of water changes by approaching the solid surface and water vapor boundary [56, 57]. A critical aspect is to work with well-defined materials and micro-beams, requiring a careful choice of the recording setups and giving rise to optical aberrations such as Mie scattering and interference fringes. Consequently, the experimental design and the data treatment are crucial to interpret the acquired spectra properly. Indeed, most of the time of this study was devoted to defining and performing the right acquisition in the proper mode, and conducting the correct data treatments.

The FTIR hyperspectral data were acquired on various aqueous solutions occluded in closed (and therefore isochoric and iso-concentration) well-controlled cavities at different temperatures. After the processing step, including baseline correction, smoothing, interference fringes removal, and (ideally) Mie scattering correction, we established that all water-hydrophobe interfaces displayed a distance-dependent spectral signature for water over a 1 ± 0.5 μm thickness from the solid surface and water vapor boundary (called interfacial signature). Namely, this result relates to the appearance of a specific spectral signature in the OH stretching spectral region near the solid-liquid and liquid-vapor interfaces. Near the water-solid interface, the spectral signature shows an additional peak at the end of the OH stretching band of water c.a. 3700 cm^{-1} (i.e., observing as OH broadening); however, in the water-vapor interface, this peak appears separately from the OH stretching band, which is representing of dangling OH mode (almost similar to the spectra acquired by sum frequency vibrational method [141, 142, 328]).

The OH stretching band was decomposed into the three Gaussian sub-bands to analyze the various H-bonding among water molecules. We observed the degree of water molecule connectivity decreased by approaching the solid surface in a way that the intermediate water (3 H-bonds) predominates over the network water (4 H-bonds), in agreement with previous studies but at odds with what is expected for liquid water [56]. This trend was enhanced by increasing the temperature, even much more than the usual trend expected for liquid water. It reveals that both coming closer to the interface and increasing the temperature have a chaotropic effect on the molecular network, with an interface effect ranging over a very long distance from the solid boundary.

Our third outcome was finding a way to interpret IR-based signatures in natural environments. To do so, a specific partition function previously developed was employed to convert the vibrational properties of water (microscopic scale) to its thermodynamic properties (macroscopic scale). The conversion of the spectral signature near the quartz boundary into Gibbs free energy leads to a 600 J/mol surface-imprinting at room temperature (22°C) to 1000 J/mol at high temperature (155°C). This enhancement in the Gibbs free energy increases the chemical potential and changes the reactivity of water along a solid-liquid interface. This variation along a micron-thick layer leads us to define an "interphase" domain between the interfacial region and the bulk zone, where the properties of water are different from their bulk properties. A major consequence of the interphase domain appears in interpreting water-rock interactions in pores, channels, and cavities. In general, geochemistry might be impacted by these results in nature. For example, the long-term supersaturation in large sedimentary basins [33, 34] or solubility enhancement commonly observed in small pores (smaller than 1 μm), which are justified by the "pore-sized controlled solubility" [178, 376, 377] or "confinement effect" terms [40-46], could be explained by the higher reactivity of water (or solution) in the interphase domain of the pores.

Investigating the possible origins of interfacial behavior near the solid-liquid interface, such as shape/size of the pore, the composition of occluded solution with varied salinity/pH, and different host minerals, demonstrate that only the solid surface property plays a role in controlling the interfacial behavior. In this way, we showed that the band detected c.a. 3700 cm^{-1}, visible along the quartz and fluorite boundary (water-quartz and water-fluorite interface), can be assigned to the absorption of less-connected water molecules (two to zero H-bonds) near the hydrophobic surfaces. On the contrary, the enrichment of the well-connected water molecules (near four H-bonds) has been observed along the calcite boundary, which can be assigned to the hydrophilic surface. Revealing the independency of the interphase domain to the varied geometries, occluded solutions, and host minerals was our fourth finding, representing that we are dealing with a systematic force field propagated over a micron distance far from the solid surface.

As a consequence, the perturbation among the water molecules H-bonding might be related to the long-range force fields emanating from the solid surface, such as hydrophobic interaction and electrostatic field throughout the interfacial layer. Microscopically, the lack of water-solid affinity especially compared to the high water-water affinity leads the liquid to turn to itself, as the spherical shape adopted for a droplet in the air by closing on itself. This trend at the interface gives rise to a low-density layer or a nanobubbles alignment along the water-hydrophobe domain. Once that low-density layer is in place, macroscopically, two main long-range fields can propagate the interfacial effect further, depending on conceptualization. The first possibility is a disjoining approach model, where the solid-air-liquid constitutes the three dielectrics system inside which the disjoining pressure can occur. The second option is the capillary bridging analogy, considering the nano-bubbles (bubble convex towards liquid) as alignment of nano-bridges (liquid concave towards vapor). In both models, the role of the electrification at the interface enforces the effect of adding an electrostatic contribution to either disjoining or capillary pressure.

In a second part, much reduced in the frame of this study, but no less important, we addressed the pore scale with a series of experiments conducted using nanofluidic chipsets with an ink-bottle structure (i.e., nano-throat and macro-reservoir assemblage). The primary results showed the phase transition in the macro-reservoir due to the existence of curved liquid-air capillary bridges and their capillary intensity in the nanometric pore throat, which propagates to the whole hydraulically connected water body. Herein, the capillarity was controlled by tuning the relative humidity (RH), with which we are exploring the water-rock-gases equilibria at various capillary states. The water cavitation phenomenon and kinetics of the evaporation showed that the relative humidity could control the capillary-driven effect with respect to its equilibrium value (Kelvin equation), leading to phase transitions in the deep volume of the system, namely far from the liquid-air capillary bridges. The properties determined at/by the bridges become the properties of the whole hydrosystem.

These findings illustrate that capillary pressure propagates in the whole water mass connected to the capillary bridge, leading the system to obey the capillary-controlled geochemistry. In the natural environment, this capillary-driven effect occurs in the caprock-CO_2 bubble interface when the CO_2 is injected into the deep saline formation. In this way, CO_2 bubbles approach the caprock interface due to the buoyancy of injected CO_2, which is less dense than brine. Then, the existence of the liquid-air capillary bridge modifies the water reactivity through the low-permeable caprock.

7.2. Prospective

At the end of this long-term effort, with many technical issues that have been challenging though stimulating, many questioning observables have been abandoned along the road, which require to be revised to densify and clarify our present findings.

The first intriguing result is the simple measurements of “normal” water. They were carried out within thin liquid cells, as is usually done, using hydrophobic materials over a thickness directly comparable to the present thick layer; no traces of interfacial spectral signatures were detected. This is the most questioned problem, and we do not have an alternative explanation to justify such a feature, except the geometry of the cavity but without physical reasons to support it. The CaF_2 windows, as opposed to the CaF_2 inclusion, fully illustrate the challenge to be solved. We devised a methodology to try delineating the problem. We propose to perform an ATR (attenuated total reflectance) study using a ZnSe/diamond/silicon crystal over which a water droplet would be sandwiched with a varied opposite window (quartz, possibly silanized, fluorite, etc.). Even if the optical pathway of the evanescent beam cannot be quantified, the ATR measurements prospect the very surficial layering of water deposited on the crystal. The opposite solid serves to establish the thick water layer that should superimpose on the “normal” mode at the ATR crystal-water interface. For instance, the IR spectrum would be recorded as a function of the distance between the two plates by a pressure probe or an ellipsometric measurement of the inter-crystals separation.

The second question is turned to the bulk versus. normal spectrum. We let aside the difference as of secondary importance with respect to the interface signature. This difference is characterized by a band broadening, with a very obvious question about the combination in what we call “bulk” of a contribution from the interface, which is exactly featured by high wavenumbers enrichment. Despite the confocal geometry we used throughout the study, we employ the transmission FTIR method based on exploiting the shadow zone [256]. It means that we cannot avoid a convolution of the spectral signature of the interface when the beam crosses it. However, a close examination of the bulk signature in the calcite fragment does show this band broadening, yet with much narrower spectra along the interface (Figure 4.36, p. 122). To work further on, we are designing a series of new synthetic fluid inclusions, all synthetic but with a variety of minerals host spanning from hydrophilic to hydrophobic. Also, we will infill them with various aqueous solutions to get insights into the role of kosmotropic and chaotropic dissolved solutes in organizing the interface (or not). Another aspect related to these new fabrications would be controlling the inclusions thickness. We insisted on the optical aberrations and succeeded in correcting them, but we also had many practical issues saturating the signal (many inclusions were discarded) or penalizing SNR due to bubble motion (low wall attachment).

Another crucial factor regarding the Gibbs free energy variation at the interphase domain might be related to the employed partition function, which converts the infrared-based property to the thermodynamic value. First of all, the theoretical roots of the used partition should be usefully challenged, but not by our team, of limited expertise on that topic. In particular, from the first publication of Bergonzi (2014) [57], we wonder whether the vibrational energy and the total energy of liquid water could be reconciled and put into complete continuity, at least on a reference sample.

The second aspect on the same topic is more technical, with the exclusive measurement of the OH stretching band for calculating the Gibbs free energy because of pragmatic limitations, such as the cut-off wavenumber of quartz and the spectral range limitation of emitted supercontinuum laser. However, all the modes play a role in calculating the final Gibbs free energy value. In particular, and according to our OH-stretching behavior, it can be expected that the OH-O libration mode would be shifted to lower energy than the bulk, associated with significant H-bond softening and a growing degree of disorder of H-bonds structure. This issue becomes more challenging at high temperatures (around 150°C), where the translational and rotational movements of the unbound molecules are more predominant and should be considered for the conversion, a problem already stated by Bergonzi et al. (2014) [57] and on which we made no progress.

Another innovative approach we used was to harness a silicon-based lab-on-chap wafer to quantify and observe the phase transitions under controlled conditions. It could allow us in the future to study trapped water with much more controlled dimensions than with SFIs since silicon is mostly transparent to mid-infrared and can be readily silanized to control hydrophobicity. But the challenge was to infill in a controlled manner the then-hydrophobic channels and to have enough water trapped in channels to get a signal. The first tests were discouraging. The alternative scenario may be to use porous alumina/silicon obtained by anodization and further wall-functionalized. In that case, the micro-beam would not be required, and various length scales could be tested. By the way, these types of samples, with which we are unfamiliar, could give way to a systematic study of an interface/confinement coupling. According to our reading, it seems that the weight of interfacial behavior is not considered in the interpretation of the current confinement-based studies.

The pore scale offers promising ways to better understand how geochemical gradients accumulate at certain critical interfaces, and propagate their specific and local properties to water reservoirs, orders of magnitude larger. Capillary bridges stopped at one nanoporous layer while in contact with a drying gas phase is an unknown thermodynamic player to control the reactivity and the diphasic distribution throughout a whole caprock and/or containment barriers. These encouraging preliminary results pave the way for obvious perspectives in designing water-solid equilibria inside the nanofluidic devices. Two types of experiments can be readily proposed, with saturated solutions submitted to capillary evaporation driving pore-size dependent precipitation or to use a nanoparticle flow to inseminate the nanofluidic models with supersaturated solutions and observe what will happen.

At the end of this long run, we are conscious that so much remains to be done for many conclusions inferred from our measurements to get a stronger basis and a more robust conceptualization of driving laws. The project our team developed at the nexus between interface and pore-scale opens up perspectives that we hope to see keeping lively and active in the years to come.

Bibliography

1. Prieto, M., A. Putnis, and L. Fernandez-Diaz, *Factors controlling the kinetics of crystallization: supersaturation evolution in a porous medium. Application to barite crystallization.* Geological Magazine, 1990. **127**(6): p. 485-495.
2. Seigneur, N., K.U. Mayer, and C.I. Steefel, *Reactive transport in evolving porous media.* Reviews in Mineralogy and Geochemistry, 2019. **85**(1): p. 197-238.
3. Rzig, R., N.B. Khedher, and S.B. Nasrallah, *Three-dimensional simulation of mass and heat transfer in drying unsaturated porous medium.* Heat Transfer Research, 2017. **48**(11).
4. Masmoudi, W. and M. Prat, *Heat and mass transfer between a porous medium and a parallel external flow. Application to drying of capillary porous materials.* International journal of heat and mass transfer, 1991. **34**(8): p. 1975-1989.
5. Agaoglu, B., et al., *Interphase mass transfer between fluids in subsurface formations: A review.* Advances in Water Resources, 2015. **79**: p. 162-194.
6. De Wit, A., *Chemo-hydrodynamic patterns in porous media.* Philosophical Transactions of the Royal Society A: Mathematical, Physical and Engineering Sciences, 2016. **374**(2078): p. 20150419.
7. Mitchell, A.C., et al., *Biofilm enhanced geologic sequestration of supercritical CO2.* international journal of greenhouse gas control, 2009. **3**(1): p. 90-99.
8. Tsakiroglou, C., et al., *Assessing the capacity of zero valent iron nanofluids to remediate NAPL-polluted porous media.* Science of The Total Environment, 2016. **563**: p. 866-878.
9. Tungittiplakorn, W., et al., *Engineered polymeric nanoparticles for soil remediation.* Environmental science & technology, 2004. **38**(5): p. 1605-1610.
10. Zou, A. and D. Schechter. *Investigation of the Oil Recovery Mechanism During Laboratory CO2 EOR Experiments with Unconventional Shale Cores through Compositional Simulation*. in *Carbon Management Technology Conference*. 2017. OnePetro.
11. Olorode, O., H. Amer, and H. Rashid. *The role of diffusion in primary and enhanced oil recovery from fractured unconventional reservoirs*. in *Asia Pacific Unconventional Resources Technology Conference, Virtual, 16–18 November 2021*. 2021. Unconventional Resources Technology Conference (URTeC).
12. Torcuk, M.A., et al. *Impact of chemical osmosis on brine imbibition and hydrocarbon recovery in liquid-rich shale reservoirs*. in *SPE annual technical conference and exhibition*. 2019. OnePetro.
13. Lopez, S., et al., *40 years of Dogger aquifer management in Ile-de-France, Paris Basin, France.* Geothermics, 2010. **39**(4): p. 339-356.
14. Taron, J. and D. Elsworth, *Thermal–hydrologic–mechanical–chemical processes in the evolution of engineered geothermal reservoirs.* International Journal of Rock Mechanics and Mining Sciences, 2009. **46**(5): p. 855-864.
15. Bourg, I.C., L.E. Beckingham, and D.J. DePaolo, *The nanoscale basis of CO2 trapping for geologic storage.* Environmental science & technology, 2015. **49**(17): p. 10265-10284.

16. Zuo, L., et al., *Micromodel investigations of CO2 exsolution from carbonated water in sedimentary rocks.* Advances in Water Resources, 2013. **53**: p. 188-197.
17. Bachu, S., *Review of CO2 storage efficiency in deep saline aquifers.* International Journal of Greenhouse Gas Control, 2015. **40**: p. 188-202.
18. Haddad, P., et al., *Geological storage of hydrogen in deep aquifers–an experimental multidisciplinary study.* Energy & Environmental Science, 2022. **15**(8): p. 3400-3415.
19. Aftab, A., et al., *Toward a fundamental understanding of geological hydrogen storage.* Industrial & Engineering Chemistry Research, 2022. **61**(9): p. 3233-3253.
20. Zivar, D., S. Kumar, and J. Foroozesh, *Underground hydrogen storage: A comprehensive review.* International journal of hydrogen energy, 2021. **46**(45): p. 23436-23462.
21. Oh, Y.S., et al., *A microfluidic approach to water-rock interactions using thin rock sections: Pb and U sorption onto thin shale and granite sections.* Journal of hazardous materials, 2017. **324**: p. 373-381.
22. Kurniawan, T.A., et al., *Technological solutions for long-term storage of partially used nuclear waste: A critical review.* Annals of Nuclear Energy, 2022. **166**: p. 108736.
23. Alwaeli, M. and V. Mannheim, *Investigation into the current state of nuclear energy and nuclear waste management—A state-of-the-art review.* Energies, 2022. **15**(12): p. 4275.
24. Putnis, A., J. Moore, and H. Austrheim, *Fluid-rock reaction mechanisms and the inevitable consequences for mass transport and texture formation*. 2022, Copernicus Meetings.
25. Bachu, S., W. Gunter, and E. Perkins, *Aquifer disposal of CO2: hydrodynamic and mineral trapping.* Energy Conversion and management, 1994. **35**(4): p. 269-279.
26. Zhang, Y., et al., *Ink-bottle effect and pore size distribution of cementitious materials identified by pressurization–depressurization cycling mercury intrusion porosimetry.* Materials, 2019. **12**(9): p. 1454.
27. Tuller, M., D. Or, and D. Hillel, *Retention of water in soil and the soil water characteristic curve.* Encyclopedia of Soils in the Environment, 2004. **4**: p. 278-289.
28. Anovitz, L., et al., *Diagenetic changes in macro-to nano-scale porosity in the St. Peter Sandstone: An (ultra) small angle neutron scattering and backscattered electron imaging analysis.* Geochimica et Cosmochimica Acta, 2013. **102**: p. 280-305.
29. Bear, J. and C. Braester, *On the flow of two immscible fluids in fractured porous media*, in *Developments in Soil Science*. 1972, Elsevier. p. 177-202.
30. Putnis, A. and G. Mauthe, *The effect of pore size on cementation in porous rocks.* Geofluids, 2001. **1**(1): p. 37-41.
31. Baermann, A., et al., *Anhydrite Cement in Rhaetian sandstone in Hamburg-Morphology and structures.* ZEITSCHRIFT FUR ANGEWANDTE GEOLOGIE, 2000. **46**(3): p. 138-143.
32. Abercrombie, H.J., et al., *Silica activity and the smectite-illite reaction.* Geology, 1994. **22**(6): p. 539-542.
33. Azaroual, M., C. Fouillac, and J. Matray, *Solubility of silica polymorphs in electrolyte solutions, II. Activity of aqueous silica and solid silica polymorphs in deep solutions from the sedimentary Paris Basin.* Chemical Geology, 1997. **140**(3-4): p. 167-179.
34. McBride, E.F., *Quartz cement in sandstones: a review.* Earth-Science Reviews, 1989. **26**(1-3): p. 69-112.
35. Kharaka, Y.K. and R.H. Mariner, *Chemical geothermometers and their application to formation waters from sedimentary basins*, in *Thermal history of sedimentary basins*. 1989, Springer. p. 99-117.

36. Steefel, C. and P. Lichtner, *Multicomponent reactive transport in discrete fractures: II: Infiltration of hyperalkaline groundwater at Maqarin, Jordan, a natural analogue site.* Journal of Hydrology, 1998. **209**(1-4): p. 200-224.
37. Emmanuel, S., J.J. Ague, and O. Walderhaug, *Interfacial energy effects and the evolution of pore size distributions during quartz precipitation in sandstone.* Geochimica et Cosmochimica Acta, 2010. **74**(12): p. 3539-3552.
38. Prieto, M., *Nucleation and supersaturation in porous media (revisited).* Mineralogical Magazine, 2014. **78**(6): p. 1437-1447.
39. Mürmann, M., et al., *Numerical simulation of pore size dependent anhydrite precipitation in geothermal reservoirs.* Energy Procedia, 2013. **40**: p. 107-116.
40. Brown Jr, G.E., et al., *Metal oxide surfaces and their interactions with aqueous solutions and microbial organisms.* 1999.
41. Henderson, M.A., *The interaction of water with solid surfaces: fundamental aspects revisited.* Surface Science Reports, 2002. **46**(1-8): p. 1-308.
42. Fenter, P. and N.C. Sturchio, *Mineral–water interfacial structures revealed by synchrotron X-ray scattering.* Progress in Surface Science, 2004. **77**(5-8): p. 171-258.
43. Al-Kindi, I. and T. Babadagli, *Revisiting Kelvin equation and Peng–Robinson equation of state for accurate modeling of hydrocarbon phase behavior in nano capillaries.* Scientific Reports, 2021. **11**(1): p. 1-14.
44. Tombari, E., et al., *Thermodynamic functions of water and ice confined to 2 nm radius pores.* The Journal of chemical physics, 2005. **122**(10): p. 104712.
45. Terra, J.C., et al., *Making more with less: confinement effects for more sustainable chemical transformations.* Green Chemistry, 2022. **24**(4): p. 1404-1438.
46. Meldrum, F.C. and C. O'Shaughnessy, *Crystallization in confinement.* Advanced Materials, 2020. **32**(31): p. 2001068.
47. Goral, J., et al., *Confinement effect on porosity and permeability of shales.* Scientific reports, 2020. **10**(1): p. 1-11.
48. Dai, J. and H. Zhang, *Recent Advances in Catalytic Confinement Effect within Micro/Meso-Porous Crystalline Materials.* Small, 2021. **17**(22): p. 2005334.
49. Hande, V.R. and S. Chakrabarty, *Exploration of the presence of bulk-like water in AOT reverse micelles and water-in-oil nanodroplets: the role of charged interfaces, confinement size and properties of water.* Physical Chemistry Chemical Physics, 2016. **18**(31): p. 21767-21779.
50. Dewan, S., et al., *Structure of water at charged interfaces: A molecular dynamics study.* Langmuir, 2014. **30**(27): p. 8056-8065.
51. Hande, V.R. and S. Chakrabarty, *How Far Is "Bulk Water" from Interfaces? Depends on the Nature of the Surface and What We Measure.* The Journal of Physical Chemistry B, 2022. **126**(5): p. 1125-1135.
52. Gardeniers, H.J., *Chemistry in nanochannel confinement.* Analytical and bioanalytical chemistry, 2009. **394**(2): p. 385-397.
53. Tsukahara, T., et al., *NMR study of water molecules confined in extended nanospaces.* Angewandte Chemie, 2007. **119**(7): p. 1199-1202.
54. Zheng, J.-m., et al., *Surfaces and interfacial water: evidence that hydrophilic surfaces have long-range impact.* Advances in colloid and interface science, 2006. **127**(1): p. 19-27.
55. Stack, A.G., et al., *Pore-size-dependent calcium carbonate precipitation controlled by surface chemistry.* Environmental science & technology, 2014. **48**(11): p. 6177-6183.

56. Bergonzi, I., et al., *Oversolubility in the microvicinity of solid–solution interfaces.* Physical Chemistry Chemical Physics, 2016. **18**(22): p. 14874-14885.
57. Bergonzi, I., et al., *Gibbs free energy of liquid water derived from infrared measurements.* Physical Chemistry Chemical Physics, 2014. **16**(45): p. 24830-24840.
58. Mercury, L., F. Jamme, and P. Dumas, *Infra-red imaging of bulk water and water–solid interfaces under stable and metastable conditions.* Physical Chemistry Chemical Physics, 2012. **14**(8): p. 2864-2874.
59. Guilhaumou, N. and P. Dumas, *Synchrotron FTIR Hydrocarbon fluid inclusion microanalysis applied to diagenetic history and fluid flow reconstruction in reservoir appraisal.* Oil & Gas Science and Technology, 2005. **60**(5): p. 763-779.
60. Nieuwoudt, M.K., et al., *Synchrotron FTIR microscopy of synthetic and natural CO2–H2O fluid inclusions.* Vibrational Spectroscopy, 2014. **75**: p. 136-148.
61. Brubach, J.-B., et al., *Dependence of water dynamics upon confinement size.* The Journal of Physical Chemistry B, 2001. **105**(2): p. 430-435.
62. Czarnik-Matusewicz, B., S. Pilorz, and J.P. Hawranek, *Temperature-dependent water structural transitions examined by near-IR and mid-IR spectra analyzed by multivariate curve resolution and two-dimensional correlation spectroscopy.* Analytica chimica acta, 2005. **544**(1-2): p. 15-25.
63. Deàk, J.C., et al., *Vibrational energy relaxation and spectral diffusion in water and deuterated water.* The Journal of Physical Chemistry A, 2000. **104**(21): p. 4866-4875.
64. Giguère, P.A. and K. Harvey, *On the infrared absorption of water and heavy water in condensed states.* Canadian Journal of Chemistry, 1956. **34**(6): p. 798-808.
65. Hasted, J., et al., *Far-infrared absorption in liquid water.* Chemical physics letters, 1985. **118**(6): p. 622-625.
66. Larouche, P., J.-J. Max, and C. Chapados, *Isotope effects in liquid water by infrared spectroscopy. II. Factor analysis of the temperature effect on H 2 O and D 2 O.* The Journal of chemical physics, 2008. **129**(6): p. 064503.
67. Lawrence, C. and J. Skinner, *Vibrational spectroscopy of HOD in liquid D 2 O. III. Spectral diffusion, and hydrogen-bonding and rotational dynamics.* The Journal of chemical physics, 2003. **118**(1): p. 264-272.
68. Marechal, Y., *IR spectroscopy of an exceptional H-bonded liquid: water.* Journal of molecular structure, 1994. **322**: p. 105-111.
69. Marechal, Y., *The hydrogen bond and the water molecule: The physics and chemistry of water, aqueous and bio-media*. 2006: Elsevier.
70. Akiyama, R. and F. Hirata, *Theoretical study for water structure at highly ordered surface: effect of surface structure.* The Journal of chemical physics, 1998. **108**(12): p. 4904-4911.
71. Boissiere, C., et al., *Water confined in lamellar structures of AOT surfactants: an infrared investigation.* The Journal of Physical Chemistry B, 2002. **106**(5): p. 1032-1035.
72. Crupi, V., et al., *Dynamical response and H-bond effects in confined liquid water.* Journal of molecular liquids, 1999. **80**(2-3): p. 133-147.
73. Crupi, V., et al., *T dependence of vibrational dynamics of water in ion-exchanged zeolites A: a detailed Fourier transform infrared attenuated total reflection study.* The Journal of chemical physics, 2005. **123**(15): p. 154702.
74. MacDonald, H., B. Bedwell, and E. Gulari, *FTIR spectroscopy of microemulsion structure.* Langmuir, 1986. **2**(6): p. 704-708.

75. Anbari, A., et al., *Microfluidic model porous media: Fabrication and applications.* Small, 2018. **14**(18): p. 1703575.
76. Hasham, A.A., et al., *Visualization of fracturing fluid dynamics in a nanofluidic chip.* Journal of Petroleum Science and Engineering, 2018. **165**: p. 181-186.
77. Porter, M.L., et al., *Geo-material microfluidics at reservoir conditions for subsurface energy resource applications.* Lab on a Chip, 2015. **15**(20): p. 4044-4053.
78. Song, W., et al., *Chip-off-the-old-rock: the study of reservoir-relevant geological processes with real-rock micromodels.* Lab on a Chip, 2014. **14**(22): p. 4382-4390.
79. Vincent, O., A. Szenicer, and A.D. Stroock, *Capillarity-driven flows at the continuum limit.* Soft Matter, 2016. **12**(31): p. 6656-6661.
80. Vincent, O., B. Marguet, and A.D. Stroock, *Imbibition triggered by capillary condensation in nanopores.* Langmuir, 2017. **33**(7): p. 1655-1661.
81. Yun, W., et al., *Creation of a dual-porosity and dual-depth micromodel for the study of multiphase flow in complex porous media.* Lab on a Chip, 2017. **17**(8): p. 1462-1474.
82. Pauling, L., *The Nature of the Chemical Bond 2nd edn, 145*. 1940, Cornell University Press: Ithaca, NY.
83. Isaacs, E., et al., *Compton scattering evidence for covalency of the hydrogen bond in ice.* Journal of Physics and Chemistry of Solids, 2000. **61**(3): p. 403-406.
84. Pettersson, L.G.M., R.H. Henchman, and A. Nilsson, *Water・The Most Anomalous Liquid.* Chemical reviews, 2016. **116**(13): p. 7459-7462.
85. Franks, F., *The physics and physical chemistry of water*. Vol. 1. 2012: Springer Science & Business Media.
86. Cabane, B. and S. Hénon, *Liquides. Solutions, dispersions, émulsions, gels: Solutions, dispersions, émulsions, gels*. 2015: Belin Éducation.
87. Rao, C., *Theory of hydrogen bonding in water*, in *The Physics and Physical Chemistry of Water*. 1972, Springer. p. 93-114.
88. Jedlovszky, P., I. Bakó, and G. Pálinkás, *Reverse monte carlo simulation of liquid water.* Chemical physics letters, 1994. **221**(1-2): p. 183-187.
89. Kumar, R., J. Schmidt, and J. Skinner, *Hydrogen bonding definitions and dynamics in liquid water.* The Journal of chemical physics, 2007. **126**(20): p. 05B611.
90. Cabane, B. and R. Vuilleumier, *The physics of liquid water.* Comptes Rendus Geoscience, 2005. **337**(1-2): p. 159-171.
91. Bergonzi, I. and L. Mercury, *Infrared-Thermodynamics conversion as a function of temperature: towards confined water*, in *Transport and Reactivity of Solutions in Confined Hydrosystems*. 2014, Springer. p. 43-53.
92. Lagodzinskaya, G., N. Yunda, and G. Manelis, *H+-catalyzed symmetric proton exchange in neat liquids with a network of N–H⋯N and O–H⋯O hydrogen bonds and molecular mechanism of Grotthuss proton migration.* chemical physics, 2002. **282**(1): p. 51-61.
93. Sulpizi, M., M.-P. Gaigeot, and M. Sprik, *The silica–water interface: how the silanols determine the surface acidity and modulate the water properties.* Journal of chemical theory and computation, 2012. **8**(3): p. 1037-1047.
94. Levin, Y. and A.P. dos Santos, *Ions at hydrophobic interfaces.* Journal of Physics: Condensed Matter, 2014. **26**(20): p. 203101.
95. Nir, S., S. Adams, and R. Rein, *Polarizability calculations on water, hydrogen, oxygen, and carbon dioxide.* The Journal of Chemical Physics, 1973. **59**(6): p. 3341-3355.
96. Griffiths, P.R., *Fourier transform infrared spectrometry.* Science, 1983. **222**(4621): p. 297-302.

97. McQuarrie, D.A., *Quantum chemistry*. 2008: University Science Books.
98. Harris, D.C. and M.D. Bertolucci, *Symmetry and spectroscopy: an introduction to vibrational and electronic spectroscopy*. 1989: Courier Corporation.
99. Long, D.A., *Raman spectroscopy.* New York, 1977. **1**.
100. Larkin, P., *Infrared and Raman spectroscopy: principles and spectral interpretation*. 2017: Elsevier.
101. Schrader, B., *Infrared and Raman spectroscopy: methods and applications*. 2008: John Wiley & Sons.
102. Gauglitz, G., *Hand book of spectroscopy, Edited by Günter Gauglitz and Tuan Vo-Dinh, 2003 WILEY*. VCH Verlag GmbH & Co. KGaA, Weinheim ISBN.
103. Brubach, J.-B., et al., *Signatures of the hydrogen bonding in the infrared bands of water.* The Journal of chemical physics, 2005. **122**(18): p. 184509.
104. Freda, M., et al., *Transmittance Fourier transform infrared spectra of liquid water in the whole mid-infrared region: temperature dependence and structural analysis.* Applied spectroscopy, 2005. **59**(9): p. 1155-1159.
105. Walrafen, G., *Raman spectral studies of the effects of temperature on water structure.* The Journal of Chemical Physics, 1967. **47**(1): p. 114-126.
106. Bratos, S., et al., *Infra-red spectra of hydrogen bonded systems: theory and experiment*, in *Ultrafast Hydrogen Bonding Dynamics and Proton Transfer Prosesses in the Condensed Phase*. 2002, Springer. p. 5-30.
107. Le Caër, S., et al., *A trapped water network in nanoporous material: the role of interfaces.* Physical Chemistry Chemical Physics, 2011. **13**(39): p. 17658-17666.
108. Masuda, K., et al., *Structural change of water with solutes and temperature up to 100 C in aqueous solutions as revealed by attenuated total reflectance infrared spectroscopy.* Applied spectroscopy, 2003. **57**(3): p. 274-281.
109. Rundle, R. and M. Parasol, *O–H stretching Frequencies in Very Short and Possibly Symmetrical Hydrogen Bonds.* The Journal of Chemical Physics, 1952. **20**(9): p. 1487-1488.
110. Nakamoto, K., M. Margoshes, and R. Rundle, *Stretching frequencies as a function of distances in hydrogen bonds.* Journal of the American Chemical Society, 1955. **77**(24): p. 6480-6486.
111. Mikenda, W., *Stretching frequency versus bond distance correlation of O ・ D (H)⋯ Y (Y ・ N, O, S, Se, Cl, Br, I) hydrogen bonds in solid hydrates.* Journal of Molecular Structure, 1986. **147**(1-2): p. 1-15.
112. Gaweł, B.A., et al., *Structural evolution of water and hydroxyl groups during thermal, mechanical and chemical treatment of high purity natural quartz.* RSC Advances, 2020. **10**(48): p. 29018-29030.
113. Schmidt, D.A. and K. Miki, *Structural correlations in liquid water: A new interpretation of IR spectroscopy.* The journal of physical chemistry A, 2007. **111**(40): p. 10119-10122.
114. Max, J.-J. and C. Chapados, *Isotope effects in liquid water by infrared spectroscopy. III. H 2 O and D 2 O spectra from 6000 to 0 cm− 1.* The Journal of chemical physics, 2009. **131**(18): p. 184505.
115. Chapados, C. and J. Max, *Isotope effects in liquid water by infrared spectroscopy. III. H2O and D2O spectra from 6000to0 cm-1.* The journal of Chemical Physics, 2009. **131**(184505): p. 1-184505.

116. Auer, B. and J. Skinner, *IR and Raman spectra of liquid water: Theory and interpretation.* The Journal of chemical physics, 2008. **128**(22): p. 224511.
117. Niu, F., et al., *Electrode potential dependent desolvation and resolvation of germanium (100) in contact with aqueous perchlorate electrolytes.* Physical Chemistry Chemical Physics, 2017. **19**(21): p. 13585-13595.
118. Niu, F., et al., *Vibrational spectroscopic study of pH dependent solvation at a Ge (100)-water interface during an electrode potential triggered surface termination transition.* The Journal of chemical physics, 2018. **148**(22): p. 222824.
119. Onori, G. and A. Santucci, *IR investigations of water structure in aerosol OT reverse micellar aggregates.* The Journal of Physical Chemistry, 1993. **97**(20): p. 5430-5434.
120. Bey Temsamani, M., et al., *Fourier transform infrared investigation of water states in aerosol-OT reverse micelles as a function of counterionic nature.* The Journal of Physical Chemistry B, 1998. **102**(18): p. 3335-3340.
121. Young, T., *III. An essay on the cohesion of fluids.* Philosophical transactions of the royal society of London, 1805(95): p. 65-87.
122. Pockels, A., *Surface tension.* Nature, 1891. **43**(1115): p. 437-439.
123. Gibbs, J.W., *On the equilibrium of heterogeneous substances.* 1879.
124. Thomson, W., *4. On the equilibrium of vapour at a curved surface of liquid.* Proceedings of the Royal Society of Edinburgh, 1872. **7**: p. 63-68.
125. Elliott, J.A., *On the complete Kelvin equation.* Chemical Engineering Education, 2001. **35**(4): p. 274-279.
126. Brovchenko, I. and A. Oleinikova, *Interfacial and confined water*. 2008: Elsevier.
127. Argyris, D., et al., *Molecular structure and dynamics in thin water films at the silica and graphite surfaces.* The Journal of Physical Chemistry C, 2008. **112**(35): p. 13587-13599.
128. Argyris, D., D.R. Cole, and A. Striolo, *Hydration structure on crystalline silica substrates.* Langmuir, 2009. **25**(14): p. 8025-8035.
129. Romero-Vargas Castrillón, S., et al., *Evolution from surface-influenced to bulk-like dynamics in nanoscopically confined water.* The Journal of Physical Chemistry B, 2009. **113**(23): p. 7973-7976.
130. Liu, P., E. Harder, and B. Berne, *Hydrogen-bond dynamics in the air− water interface.* The Journal of Physical Chemistry B, 2005. **109**(7): p. 2949-2955.
131. Smits, M., et al., *Ultrafast vibrational energy transfer between surface and bulk water at the air-water interface.* Physical review letters, 2007. **98**(9): p. 098302.
132. Zhang, Z., et al., *Ultrafast vibrational energy transfer at the water/air interface revealed by two-dimensional surface vibrational spectroscopy.* Nature Chemistry, 2011. **3**(11): p. 888-893.
133. Thiel, P.A. and T.E. Madey, *The interaction of water with solid surfaces: Fundamental aspects.* Surface Science Reports, 1987. **7**(6-8): p. 211-385.
134. Bridgeman, C., *Ab-initio total energy study of uncharged 2: 1 clays and their interaction with water.* Molecular Physics, 1996. **89**(3): p. 879-888.
135. Bridgeman, C. and N. Skipper, *A Monte Carlo study of water at an uncharged clay surface.* Journal of Physics: Condensed Matter, 1997. **9**(20): p. 4081.
136. Lee, S.H. and P.J. Rossky, *A comparison of the structure and dynamics of liquid water at hydrophobic and hydrophilic surfaces—a molecular dynamics simulation study.* The Journal of chemical physics, 1994. **100**(4): p. 3334-3345.
137. Spohr, E., et al., *Water in porous glasses. A computer simulation study.* Journal of Molecular Liquids, 1999. **80**(2-3): p. 165-178.

138. Toney, M.F., et al., *Distribution of water molecules at Ag (111)/electrolyte interface as studied with surface X-ray scattering.* Surface science, 1995. **335**: p. 326-332.
139. Du, Q., et al., *Vibrational spectroscopy of water at the vapor/water interface.* Physical Review Letters, 1993. **70**(15): p. 2313.
140. Du, Q., E. Freysz, and Y.R. Shen, *Vibrational spectra of water molecules at quartz/water interfaces.* Physical Review Letters, 1994. **72**(2): p. 238.
141. Du, Q., E. Freysz, and Y.R. Shen, *Surface vibrational spectroscopic studies of hydrogen bonding and hydrophobicity.* Science, 1994. **264**(5160): p. 826-828.
142. Shen, Y.R. and V. Ostroverkhov, *Sum-frequency vibrational spectroscopy on water interfaces: polar orientation of water molecules at interfaces.* Chemical reviews, 2006. **106**(4): p. 1140-1154.
143. Maccarini, M., *Water at solid surfaces: A review of selected theoretical aspects and experiments on the subject.* Biointerphases, 2007. **2**(3): p. MR1-MR15.
144. Richmond, G., *Structure and bonding of molecules at aqueous surfaces.* Annual review of physical chemistry, 2001. **52**(1): p. 357-389.
145. Kataoka, S., et al., *Investigation of water structure at the TiO2/aqueous interface.* Langmuir, 2004. **20**(5): p. 1662-1666.
146. Hopkins, A.J. and G.L. Richmond, *The water-hydrophobic interface: neutral and charged solute adsorption at fluorocarbon and hydrocarbon self-assembled monolayers (SAMs).* Applied spectroscopy, 2013. **67**(3): p. 261-273.
147. Butt, H., K. Graf, and M. Kappl, *Physics and chemistry of interfaces John Wiley & Sons.* 2013: p. 144–147.
148. Eslami, F. and J.A. Elliott, *Thermodynamic investigation of the barrier for heterogeneous nucleation on a fluid surface in comparison with a rigid surface.* The Journal of Physical Chemistry B, 2011. **115**(36): p. 10646-10653.
149. Sanfeld, A. and A. Steinchen, *Surface energy, stress, capillary-elastic pressure and chemical equilibrium constant in nanoparticles.* Surface science, 2000. **463**(3): p. 157-173.
150. Defay, R., I. Prigogine, and A. Bellemans, *Surface tension and adsorption*. 1966: Wiley.
151. Allen, S.M., R.W. Balluffi, and W.C. Carter, *Kinetics of materials*. 2005: John Wiley & Sons.
152. Roosen, A.R., R.P. McCormack, and W.C. Carter, *Wulffman: A tool for the calculation and display of crystal shapes.* Computational materials science, 1998. **11**(1): p. 16-26.
153. Mercury, L. and Y. Tardy, *Physicochemical features of water in capillaries and fog water droplets.* COMPTES RENDUS DE L ACADEMIE DES SCIENCES SERIE II FASCICULE A-SCIENCES DE LA TERRE ET DES PLANETES, 1997. **325**(12): p. 947-954.
154. Mercury, L. and Y. Tardy, *Negative pressure of stretched liquid water. Geochemistry of soil capillaries.* Geochimica et Cosmochimica Acta, 2001. **65**(20): p. 3391-3408.
155. Mercury, L., et al., *Thermodynamic properties of solutions in metastable systems under negative or positive pressures.* Geochimica et Cosmochimica Acta, 2003. **67**(10): p. 1769-1785.
156. Churaev, N.V., G. Starke, and J. Adolphs, *Isotherms of capillary condensation influenced by formation of adsorption films: 1. Calculation for model cylindrical and slit pores.* Journal of colloid and interface science, 2000. **221**(2): p. 246-253.

157. Derjaguin, B., *Definition of the concept of and magnitude of the disjoining pressure and its role in the statics and kinetics of thin layers of liquid.* Colloid J. USSR, 1955. **17**: p. 191-197.
158. Deryagin, B., *Modern state of the investigation of long-range surface forces.* Langmuir, 1987. **3**(5): p. 601-606.
159. Dzyaloshinskii, I.E., E.M. Lifshitz, and L.P. Pitaevskii, *The general theory of van der Waals forces.* Advances in Physics, 1961. **10**(38): p. 165-209.
160. Nerpin, S. and B. Derjaguin, *Role of capillary and surface forces in moisture transfer in porous bodies.* Bulletin Rilem (II), 1965(27): p. 55-60.
161. Derjaguin, B. and N. Churaev, *On the question of determining the concept of disjoining pressure and its role in the equilibrium and flow of thin films.* Journal of Colloid and Interface Science, 1978. **66**(3): p. 389-398.
162. Derjaguin, B. and N. Churaev, *Polymolecular adsorption and capillary condensation in narrow slit pores.* Journal of Colloid and Interface Science, 1976. **54**(2): p. 157-175.
163. Iwamatsu, M. and K. Horii, *Capillary condensation and adhesion of two wetter surfaces.* Journal of colloid and interface science, 1996. **182**(2): p. 400-406.
164. Tuller, M., D. Or, and L.M. Dudley, *Adsorption and capillary condensation in porous media: Liquid retention and interfacial configurations in angular pores.* Water resources research, 1999. **35**(7): p. 1949-1964.
165. Derjaguin, B. and N. Churaev, *Structural component of disjoining pressure.* Journal of Colloid and Interface Science, 1974. **49**(2): p. 249-255.
166. Churaev, N., *Surface forces in wetting films.* Advances in colloid and interface science, 2003. **103**(3): p. 197-218.
167. Pashley, R. and J. Kitchener, *Surface forces in adsorbed multilayers of water on quartz.* Journal of Colloid and Interface Science, 1979. **71**(3): p. 491-500.
168. Israelachvili, J.N. and R.M. Pashley, *Molecular layering of water at surfaces and origin of repulsive hydration forces.* Nature, 1983. **306**: p. 249-250.
169. Churaev, N., *Contact angles and surface forces.* Advances in colloid and interface science, 1995. **58**(2-3): p. 87-118.
170. Churaev, N. and V. Sobolev, *Prediction of contact angles on the basis of the Frumkin-Derjaguin approach.* Advances in colloid and interface science, 1995. **61**: p. 1-16.
171. Stumm, W., *Chemistry of the solid-water interface: processes at the mineral-water and particle-water interface in natural systems*. 1992: John Wiley & Son Inc.
172. Derjaguin, B.V., et al., *Surface forces*. 1987: Springer.
173. Karthika, S., T. Radhakrishnan, and P. Kalaichelvi, *A review of classical and nonclassical nucleation theories.* Crystal Growth & Design, 2016. **16**(11): p. 6663-6681.
174. Coquerel, G., *Crystallization of molecular systems from solution: phase diagrams, supersaturation and other basic concepts.* Chemical Society Reviews, 2014. **43**(7): p. 2286-2300.
175. Jones, S., G. Evans, and K. Galvin, *Bubble nucleation from gas cavities—a review.* Advances in colloid and interface science, 1999. **80**(1): p. 27-50.
176. Pruppacher, H.R., J.D. Klett, and P.K. Wang, *Microphysics of clouds and precipitation*. 1998, Taylor & Francis.
177. Martin, S.T., *Phase transitions of aqueous atmospheric particles.* Chemical Reviews, 2000. **100**(9): p. 3403-3454.
178. Putnis, A., *Transient porosity resulting from fluid–mineral interaction and its consequences.* Reviews in Mineralogy and Geochemistry, 2015. **80**(1): p. 1-23.

179. KUBOTA, N., H. KARASAWA, and T. KAWAKAMI, *ON ESTIMATION OF CRITICAL SUPERCOOLING FROM WAITING TIMES MEASURED AT CONSTANT SUPERCOOLING A SECONDARY NUCLEATION FROM A SINGLE SEED CRYSTAL OF POTASH ALUM SUSPENDED IN AGITATED SOLUTION.* Journal of Chemical Engineering of Japan, 1978. **11**(4): p. 290-295.
180. Jin, B., Z. Liu, and R. Tang, *Recent experimental explorations of non-classical nucleation.* CrystEngComm, 2020. **22**(24): p. 4057-4073.
181. Reguera, D., et al., *Phase transitions in systems small enough to be clusters.* The Journal of chemical physics, 2003. **118**(1): p. 340-353.
182. Reguera, D. and H. Reiss, *Extended Modified Liquid Drop− Dynamical Nucleation Theory (EMLD− DNT) Approach to Nucleation: A New Theory.* The Journal of Physical Chemistry B, 2004. **108**(51): p. 19831-19842.
183. Nyquist, R.M., V. Talanquer, and D.W. Oxtoby, *Density functional theory of nucleation: A semiempirical approach.* The Journal of chemical physics, 1995. **103**(3): p. 1175-1179.
184. Zeng, X. and D.W. Oxtoby, *Gas–liquid nucleation in Lennard-Jones fluids.* The Journal of chemical physics, 1991. **94**(6): p. 4472-4478.
185. Oxtoby, D.W. and R. Evans, *Nonclassical nucleation theory for the gas–liquid transition.* The Journal of chemical physics, 1988. **89**(12): p. 7521-7530.
186. Zeng, X. and D. Oxtoby, *Binary homogeneous nucleation theory for the gas–liquid transition: A nonclassical approach.* The Journal of chemical physics, 1991. **95**(8): p. 5940-5947.
187. Gránásy, L., *Diffuse interface theory of nucleation.* Journal of non-crystalline solids, 1993. **162**(3): p. 301-303.
188. Ostwald, W., *Studies on formation and transformation of solid materials.* Z. Phys. Chem, 1897. **22**: p. 289-330.
189. Stranski, I. and D. Totomanow, *Rate of formation of (crystal) nuclei and the Ostwald step rule.* Z. Phys. Chem, 1933. **163**: p. 399-408.
190. Wolde, P.R.t. and D. Frenkel, *Enhancement of protein crystal nucleation by critical density fluctuations.* Science, 1997. **277**(5334): p. 1975-1978.
191. Gliko, O., et al., *A metastable prerequisite for the growth of lumazine synthase crystals.* Journal of the American Chemical Society, 2005. **127**(10): p. 3433-3438.
192. Soga, K.G., J.R. Melrose, and R.C. Ball, *Metastable states and the kinetics of colloid phase separation.* The Journal of chemical physics, 1999. **110**(4): p. 2280-2288.
193. Zhang, T.H. and X.Y. Liu, *How does a transient amorphous precursor template crystallization.* Journal of the American Chemical Society, 2007. **129**(44): p. 13520-13526.
194. Savage, J. and A. Dinsmore, *Experimental evidence for two-step nucleation in colloidal crystallization.* Physical review letters, 2009. **102**(19): p. 198302.
195. Deubener, J., R. Brückner, and M. Sternitzke, *Induction time analysis of nucleation and crystal growth in di-and metasilicate glasses.* Journal of non-crystalline solids, 1993. **163**(1): p. 1-12.
196. Martineau, C., et al., *Liquid− liquid phase separation in model nuclear waste glasses: a solid-state double-resonance NMR study.* Chemistry of Materials, 2010. **22**(17): p. 4896-4903.
197. Gebauer, D., et al., *Pre-nucleation clusters as solute precursors in crystallisation.* Chemical Society Reviews, 2014. **43**(7): p. 2348-2371.

198. Sommerdijk, N.A. and H. Cölfen, *Lessons from nature—biomimetic approaches to minerals with complex structures.* MRS bulletin, 2010. **35**(2): p. 116-121.
199. De Yoreo, J.J., et al., *Crystallization by particle attachment in synthetic, biogenic, and geologic environments.* Science, 2015. **349**(6247): p. aaa6760.
200. Chakraborty, D. and G. Patey, *How crystals nucleate and grow in aqueous NaCl solution.* The journal of physical chemistry letters, 2013. **4**(4): p. 573-578.
201. Cundy, C.S. and P.A. Cox, *The hydrothermal synthesis of zeolites: Precursors, intermediates and reaction mechanism.* Microporous and mesoporous materials, 2005. **82**(1-2): p. 1-78.
202. Tosheva, L. and V.P. Valtchev, *Nanozeolites: synthesis, crystallization mechanism, and applications.* Chemistry of materials, 2005. **17**(10): p. 2494-2513.
203. Rimer, J.D. and M. Tsapatsis, *Nucleation of open framework materials: Navigating the voids.* MRS Bulletin, 2016. **41**(5): p. 393-398.
204. Li, M. and M. Dincă, *On the mechanism of MOF-5 formation under cathodic bias.* Chemistry of Materials, 2015. **27**(9): p. 3203-3206.
205. Qi, W., et al., *Nonclassical nucleation in a solid-solid transition of confined hard spheres.* Physical review letters, 2015. **115**(18): p. 185701.
206. Vekilov, P.G., *Dense liquid precursor for the nucleation of ordered solid phases from solution.* Crystal Growth & Design, 2004. **4**(4): p. 671-685.
207. Vekilov, P.G., *Nucleation.* Crystal growth & design, 2010. **10**(12): p. 5007-5019.
208. Gebauer, D., A. Volkel, and H. Colfen, *Stable prenucleation calcium carbonate clusters.* Science, 2008. **322**(5909): p. 1819-1822.
209. Pouget, E.M., et al., *The initial stages of template-controlled CaCO3 formation revealed by cryo-TEM.* Science, 2009. **323**(5920): p. 1455-1458.
210. Demichelis, R., et al., *Stable prenucleation mineral clusters are liquid-like ionic polymers.* Nature communications, 2011. **2**(1): p. 590.
211. Rodriguez-Navarro, C., et al., *Formation of amorphous calcium carbonate and its transformation into mesostructured calcite.* CrystEngComm, 2015. **17**(1): p. 58-72.
212. Sauter, A., et al., *On the question of two-step nucleation in protein crystallization.* Faraday discussions, 2015. **179**: p. 41-58.
213. Roedder, E., *Studies of fluid inclusions;[Part] 2, Freezing data and their interpretation.* Economic geology, 1963. **58**(2): p. 167-211.
214. Roedder, E., *Metastable superheated ice in liquid-water inclusions under high negative pressure.* Science, 1967. **155**(3768): p. 1413-1417.
215. Roedder, E., *Volume 12: fluid inclusions.* Mineralogical Society of America, 1984. **12**.
216. El Mekki, M., *Etude expérimentale de l'eau et de solutions aqueuses métastables implications pour le milieu naturel*. 2010, Université d'Orléans.
217. Azouzi, M.E.M., et al., *A coherent picture of water at extreme negative pressure.* Nature Physics, 2013. **9**(1): p. 38-41.
218. Shmulovich, K.I., et al., *Experimental superheating of water and aqueous solutions.* Geochimica et Cosmochimica Acta, 2009. **73**(9): p. 2457-2470.
219. Shmulovich, K.I. and C.M. Graham, *An experimental study of phase equilibria in the systems H 2 O–CO 2–CaCl 2 and H 2 O–CO 2–NaCl at high pressures and temperatures (500 -800° C, 0.5–0.9 GPa): geological and geophysical applications.* Contributions to Mineralogy and Petrology, 2004. **146**(4): p. 450-462.

220. Mercury, L., et al., *Growing Negative Pressure in Dissolved Solutes: Raman Monitoring of Solvent-Pulling Effect.* The Journal of Physical Chemistry C, 2016. **120**(14): p. 7697-7704.
221. Hurai, V., et al., *Geofluids: developments in microthermometry, spectroscopy, thermodynamics, and stable isotopes*. 2015: Elsevier.
222. Fall, A., J.D. Rimstidt, and R.J. Bodnar, *The effect of fluid inclusion size on determination of homogenization temperature and density of liquid-rich aqueous inclusions.* American Mineralogist, 2009. **94**(11-12): p. 1569-1579.
223. Katok, J., A. Sommer, and P.L. Lang, *Infrared microspectroscopy.* Applied Spectroscopy Reviews, 1989. **25**(3-4): p. 173-211.
224. Sandt, C., J. Frederick, and P. Dumas, *Profiling pluripotent stem cells and organelles using synchrotron radiation infrared microspectroscopy.* Journal of biophotonics, 2013. **6**(1): p. 60-72.
225. Clède, S., C. Policar, and C. Sandt, *Fourier transform infrared (FT-IR) spectromicroscopy to identify cell organelles: correlation with fluorescence staining in MCF-7 breast cancer cells.* Applied Spectroscopy, 2014. **68**(1): p. 113-117.
226. Klementieva, O., et al., *Pre-plaque conformational changes in Alzheimer's disease-linked Aβ and APP.* Nature communications, 2017. **8**(1): p. 1-9.
227. Sandt, C., et al., *Use of infrared microspectroscopy to elucidate a specific chemical signature associated with hypoxia levels found in glioblastoma.* Analyst, 2016. **141**(3): p. 870-883.
228. André, W., et al., *Structure of inclusions of Huntington's disease brain revealed by synchrotron infrared microspectroscopy: polymorphism and relevance to cytotoxicity.* Analytical Chemistry, 2013. **85**(7): p. 3765-3773.
229. Paulus, A., et al., *Amyloid Structural Changes Studied by Infrared Microspectroscopy in Bigenic Cellular Models of Alzheimer's Disease.* International journal of molecular sciences, 2021. **22**(7): p. 3430.
230. Pereira, T.M., et al., *The characterization of normal thyroid tissue by micro-FTIR spectroscopy.* Analyst, 2013. **138**(23): p. 7094-7100.
231. Meneghel, J., et al., *FTIR micro-spectroscopy using synchrotron-based and thermal source-based radiation for probing live bacteria.* Analytical and Bioanalytical Chemistry, 2020. **412**(26): p. 7049-7061.
232. Modugno, C., et al., *Understanding the effects of high pressure on bacterial spores using synchrotron infrared spectroscopy.* Frontiers in Microbiology, 2020. **10**: p. 3122.
233. Igisu, M., et al., *Micro-FTIR spectroscopic signatures of bacterial lipids in Proterozoic microfossils.* Precambrian Research, 2009. **173**(1-4): p. 19-26.
234. Hazen, T.C., et al., *Deep-sea oil plume enriches indigenous oil-degrading bacteria.* Science, 2010. **330**(6001): p. 204-208.
235. de Anchieta Câmara Jr, A., et al., *Dehydration stress responses of yeasts Torulaspora delbrueckii, Metschnikowia pulcherrima and Lachancea thermotolerans: Effects of glutathione and trehalose biosynthesis.* Food microbiology, 2019. **79**: p. 137-146.
236. Skoczen, A., et al., *The influence of high fat diets with different ketogenic ratios on the hippocampal accumulation of creatine–FTIR microspectroscopy study.* Spectrochimica Acta Part A: Molecular and Biomolecular Spectroscopy, 2017. **184**: p. 13-22.
237. Saulou, C., et al., *Synchrotron FTIR microspectroscopy of Escherichia coli at single-cell scale under silver-induced stress conditions.* Analytical and bioanalytical chemistry, 2013. **405**(8): p. 2685-2697.

238. Câmara Jr, A.A., et al., *Biophysical stress responses of the yeast Lachancea thermotolerans during dehydration using synchrotron-FTIR microspectroscopy.* Frontiers in Microbiology, 2020. **11**: p. 899.
239. Nguyen, T.D., et al., *Highlighting protective effect of encapsulation on yeast cell response to dehydration using synchrotron infrared microspectroscopy at the single-cell level.* Frontiers in Microbiology, 2020. **11**: p. 1887.
240. Passot, S., et al., *Understanding the cryotolerance of lactic acid bacteria using combined synchrotron infrared and fluorescence microscopies.* Analyst, 2015. **140**(17): p. 5920-5928.
241. Nguyen, T., et al., *Understanding the responses of Saccharomyces cerevisiae yeast strain during dehydration processes using synchrotron infrared spectroscopy.* Analyst, 2017. **142**(19): p. 3620-3628.
242. Cain, J.P., et al., *Micro-FTIR study of soot chemical composition—evidence of aliphatic hydrocarbons on nascent soot surfaces.* Physical Chemistry Chemical Physics, 2010. **12**(20): p. 5206-5218.
243. Gasaway, C., et al., *Applicability of micro-FTIR in detecting shale heterogeneity.* Journal of Microscopy, 2017. **265**(1): p. 60-72.
244. Chen, Y., et al., *Mapping the chemistry of resinite, funginite and associated vitrinite in coal with micro-FTIR.* Journal of microscopy, 2013. **249**(1): p. 69-81.
245. Bertarione, S., et al., *Micro-FTIR and micro-raman studies of a carbon film prepared from furfuryl alcohol polymerization.* The Journal of Physical Chemistry B, 2009. **113**(31): p. 10571-10574.
246. Li, Z., et al., *Dirac charge dynamics in graphene by infrared spectroscopy.* Nature physics, 2008. **4**(7): p. 532-535.
247. Zhang, Y., et al., *Direct observation of a widely tunable bandgap in bilayer graphene.* Nature, 2009. **459**(7248): p. 820-823.
248. Astruc, T., et al., *In situ thermal denaturation of myofibre sub-type proteins studied by immunohistofluorescence and synchrotron radiation FT-IR microspectroscopy.* Food chemistry, 2012. **134**(2): p. 1044-1051.
249. Vaskoska, R., et al., *Thermal denaturation of proteins in the muscle fibre and connective tissue from bovine muscles composed of type I (masseter) or type II (cutaneous trunci) fibres: DSC and FTIR microspectroscopy study.* Food Chemistry, 2021. **343**: p. 128544.
250. Motoyama, M., et al., *In situ characterization of acidic and thermal protein denaturation by infrared microspectroscopy.* Food chemistry, 2018. **248**: p. 322-329.
251. King, A.J., et al., *Investigating the history of volatiles in the solar system using synchrotron infrared micro-spectroscopy.* Infrared Physics & Technology, 2018. **94**: p. 244-249.
252. Chen, Y., et al., *Applications of micro-fourier transform infrared spectroscopy (FTIR) in the geological sciences—a review.* International journal of molecular sciences, 2015. **16**(12): p. 30223-30250.
253. Della Ventura, G., et al., *Application of micro-FTIR imaging in the Earth sciences.* Analytical and bioanalytical chemistry, 2010. **397**(6): p. 2039-2049.
254. Nichols, A.R. and R. Wysoczanski, *Using micro-FTIR spectroscopy to measure volatile contents in small and unexposed inclusions hosted in olivine crystals.* Chemical Geology, 2007. **242**(3-4): p. 371-384.
255. Jamme, F., et al., *Synchrotron infrared confocal microscope: Application to infrared 3D spectral imaging.* Journal of Physics: Conference Series, 2013. **425**(14): p. 142002.

256. Carr, G., *Resolution limits for infrared microspectroscopy explored with synchrotron radiation.* Review of Scientific Instruments, 2001. **72**(3): p. 1613-1619.
257. Carr, G., *High-resolution microspectroscopy and sub-nanosecond time-resolved spectroscopy with the synchrotron infrared source.* Vibrational Spectroscopy, 1999. **19**(1): p. 53-60.
258. Dumas, P., et al., *Synchrotron infrared microscopy at the French Synchrotron Facility SOLEIL.* Infrared Physics & Technology, 2006. **49**(1-2): p. 152-160.
259. Martin, M.C., et al., *Recent applications and current trends in analytical chemistry using synchrotron-based Fourier-transform infrared microspectroscopy.* TrAC Trends in Analytical Chemistry, 2010. **29**(6): p. 453-463.
260. Kilgus, J., et al., *Diffraction limited mid-infrared reflectance microspectroscopy with a supercontinuum laser.* Optics express, 2018. **26**(23): p. 30644-30654.
261. Williams, G., *Synchrotron and free electron laser sources of infrared radiation.* Handbook of Vibrational Spectroscopy, 2006.
262. Chalmers, J., N. Everall, and M. Chesters, *Fourier transform infrared microscopy: some advances in techniques for characterisation and structure–property elucidations of industrial material.* Analyst, 1998. **123**(4): p. 579-586.
263. Carr, G., L. Miller, and P. Dumas, *Synchrotron radiation as a source for infrared microspectroscopic imaging with 2D multi-element detection*, in *Biomedical Applications of Synchrotron Infrared Microspectroscopy*. 2010. p. 226-259.
264. Miller, L.M. and R.J. Smith, *Synchrotrons versus globars, point-detectors versus focal plane arrays: Selecting the best source and detector for specific infrared microspectroscopy and imaging applications.* Vibrational spectroscopy, 2005. **38**(1-2): p. 237-240.
265. Borondics, F., et al., *Supercontinuum-based Fourier transform infrared spectromicroscopy.* Optica, 2018. **5**(4): p. 378-381.
266. Lindsay, I., et al., *Towards supercontinuum-driven hyperspectral microscopy in the mid-infrared.* Optical Biopsy XIV: Toward Real-Time Spectroscopic Imaging and Diagnosis, 2016. **9703**: p. 15-23.
267. Nasse, M.J., et al., *High-resolution Fourier-transform infrared chemical imaging with multiple synchrotron beams.* Nature methods, 2011. **8**(5): p. 413-416.
268. Bassan, P., et al., *Large scale infrared imaging of tissue micro arrays (TMAs) using a tunable Quantum Cascade Laser (QCL) based microscope.* Analyst, 2014. **139**(16): p. 3856-3859.
269. Yeh, K. and R. Bhargava, *Discrete frequency infrared imaging using quantum cascade lasers for biological tissue analysis.* Biomedical Vibrational Spectroscopy 2016: Advances in Research and Industry, 2016. **9704**: p. 17-23.
270. Dudley, J.M., G. Genty, and S. Coen, *Supercontinuum generation in photonic crystal fiber.* Reviews of modern physics, 2006. **78**(4): p. 1135.
271. Lavoute, L., et al. *Mid-Infrared Spectromicroscopy with a Supercontinuum Laser Source*. in *Specialty Optical Fibers*. 2016. Optical Society of America.
272. Zorin, I., et al., *Advances in mid-infrared spectroscopy enabled by supercontinuum laser sources.* Optics Express, 2022. **30**(4): p. 5222-5254.
273. Yao, C., et al., *High-power mid-infrared supercontinuum laser source using fluorotellurite fiber.* Optica, 2018. **5**(10): p. 1264-1270.
274. Hackett, M.J., et al., *Development of single-beam wide-field infrared imaging to study sub-cellular neuron biochemistry.* Vibrational Spectroscopy, 2015. **77**: p. 51-59.

275. Wood, B.R., M. Kiupel, and D. McNaughton, *Progress in Fourier transform infrared spectroscopic imaging applied to venereal cancer diagnosis.* Veterinary pathology, 2014. **51**(1): p. 224-237.
276. Nallala, J., et al., *Infrared spectral histopathology for cancer diagnosis: a novel approach for automated pattern recognition of colon adenocarcinoma.* Analyst, 2014. **139**(16): p. 4005-4015.
277. Sandt, C., et al., *Performance comparison of aperture-less and confocal infrared microscopes.* Journal of Spectral Imaging, 2019. **8**.
278. Schiering, D., et al., *A dual confocal aperturing microscope for IR microspectrometry.* Analusis, 2000. **28**(1): p. 46-52.
279. Santoro, G., et al., *Infrared synchrotron radiation from bending magnet and edge radiation sources for the study of orientation and conformation in anisotropic materials.* Review of Scientific Instruments, 2011. **82**(3): p. 033710.
280. Faggin, M.F. and M.A. Hines, *Improved algorithm for the suppression of interference fringe in absorption spectroscopy.* Review of scientific instruments, 2004. **75**(11): p. 4547-4553.
281. Magnussen, E.A., et al., *Deep learning-enabled Inference of 3D molecular absorption distribution of biological cells from IR spectra.* Communications Chemistry, 2022. **5**(1): p. 175.
282. Esposito, F., *A review on initialization methods for nonnegative matrix factorization: towards omics data experiments.* Mathematics, 2021. **9**(9): p. 1006.
283. Feng, X.-R., et al., *Hyperspectral unmixing based on nonnegative matrix factorization: A comprehensive review.* IEEE Journal of Selected Topics in Applied Earth Observations and Remote Sensing, 2022.
284. Muto, S. and M. Shiga, *Application of machine learning techniques to electron microscopic/spectroscopic image data analysis.* Microscopy, 2020. **69**(2): p. 110-122.
285. Biémont, É., *Spectroscopie moléculaire: Structures moléculaires et analyse spectrale*. 2008: De Boeck Supérieur.
286. Poilblanc, R., *Spectroscopies infrarouge et Raman.* 2006.
287. Martin, J., J. Francois, and R. Gijbels, *First principles computation of thermochemical properties beyond the harmonic approximation. I. Method and application to the water molecule and its isotopomers.* The Journal of chemical physics, 1992. **96**(10): p. 7633-7645.
288. Griffith, J. and H. Scheraga, *Statistical thermodynamics of aqueous solutions. I. Water structure, solutions with non-polar solutes, and hydrophobic interactions.* Journal of Molecular Structure: THEOCHEM, 2004. **682**(1-3): p. 97-113.
289. Némethy, G. and H.A. Scheraga, *Structure of water and hydrophobic bonding in proteins. I. A model for the thermodynamic properties of liquid water.* The Journal of Chemical Physics, 1962. **36**(12): p. 3382-3400.
290. Eisenberg, D., *Kauzmann, The structure and properties of water*. 1969, Oxford University Press, Oxford.
291. Schuster, P., G. Zundel, and C. Sandorfy, *The Hydrogen Bond: Theory*. Vol. 1. 1976: North-Holland.
292. Luzar, A., *Resolving the hydrogen bond dynamics conundrum.* The Journal of Chemical Physics, 2000. **113**(23): p. 10663-10675.
293. Stillinger, F.H. and A. Rahman, *Improved simulation of liquid water by molecular dynamics.* The Journal of Chemical Physics, 1974. **60**(4): p. 1545-1557.

294. Swiatla-Wojcik, D., *Evaluation of the criteria of hydrogen bonding in highly associated liquids.* Chemical Physics, 2007. **342**(1-3): p. 260-266.
295. Thaomola, S., A. Tongraar, and T. Kerdcharoen, *Insights into the structure and dynamics of liquid water: A comparative study of conventional QM/MM and ONIOM-XS MD simulations.* Journal of Molecular Liquids, 2012. **174**: p. 26-33.
296. Chalmers, J.M., *Mid-infrared spectroscopy: Anomalies, artifacts and common errors.* Handbook of vibrational spectroscopy, 2006.
297. Rodig, C. and F. Siebert, *Errors and artifacts in time-resolved step-scan FT-IR spectroscopy.* Applied spectroscopy, 1999. **53**(8): p. 893-901.
298. Mohlenhoff, B., et al., *Mie-type scattering and non-Beer-Lambert absorption behavior of human cells in infrared microspectroscopy.* Biophysical journal, 2005. **88**(5): p. 3635-3640.
299. Kohler, A., et al., *Estimating and correcting Mie scattering in synchrotron-based microscopic Fourier transform infrared spectra by extended multiplicative signal correction.* Applied spectroscopy, 2008. **62**(3): p. 259-266.
300. Konevskikh, T., et al., *Fringes in FTIR spectroscopy revisited: understanding and modelling fringes in infrared spectroscopy of thin films.* Analyst, 2015. **140**(12): p. 3969-3980.
301. Azarfar, G., et al., *Estimating and correcting interference fringes in infrared spectra in infrared hyperspectral imaging.* Analyst, 2018. **143**(19): p. 4674-4683.
302. Croll, S. and A. Skaja, *Quantitative spectroscopy to determine the effects of photodegradation on a model polyester-urethane coating.* Journal of Coatings Technology, 2003. **75**(945): p. 85-94.
303. Mayerhöfer, T.G., et al., *Removing interference-based effects from infrared spectra–interference fringes re-revisited.* Analyst, 2020. **145**(9): p. 3385-3394.
304. Solheim, J.H., et al., *An automated approach for fringe frequency estimation and removal in infrared spectroscopy and hyperspectral imaging of biological samples.* Journal of Biophotonics, 2021. **14**(12): p. e202100148.
305. Mellau, G. and B. Winnewisser, *A method to remove fringing from FT-IR spectra.* Laboratory and Astronomical High Resolution Spectra, 1995. **81**: p. 138.
306. Naylor, D.A., A.A. Schultz, and T.A. Clark, *Eliminating channel spectra in Fourier transform spectroscopy.* Applied optics, 1988. **27**(12): p. 2603-2607.
307. Lipkus, A.H., *Application of Legendre polynomials to the elimination of baseline variation in biological FT-IR spectra.* Applied spectroscopy, 1988. **42**(3): p. 395-400.
308. Pistorius, A.M. and W.J. DeGrip, *Deconvolution as a tool to remove fringes from an FT-IR spectrum.* Vibrational spectroscopy, 2004. **36**(1): p. 89-95.
309. Hren, B., J. Mink, and L. Balazs, *Fourier transform infrared analysis of gas composition in low-volume light bulbs.* Analytical chemistry, 2002. **74**(24): p. 6402-6407.
310. Iwata, T. and J. Koshoubu, *New method to eliminate the background noise from a line spectrum.* Applied spectroscopy, 1994. **48**(12): p. 1453-1456.
311. Iwata, T. and J. Koshoubu, *Minimization of noise in spectral data.* Applied spectroscopy, 1996. **50**(6): p. 747-752.
312. Mie, G., *Pioneering mathematical description of scattering by spheres.* Ann. Phys, 1908. **25**(337): p. 0003-3804.
313. Van de Hulst, H., *Light Scattering by Small Particles John Wiley & Sons.* Inc., New York, 1957. **470**.

314. Walstra, P., *Approximation formulae for the light scattering coefficient of dielectric spheres.* British Journal of Applied Physics, 1964. **15**(12): p. 1545.
315. Kohler, A., et al., *EMSC as a tool for separation and characterisation of physical and chemical information in FT-IR microscopy images of cryosections of beef loin.* Appl. Spectrosc, 2005. **59**(6): p. 707-716.
316. Martens, H., J.P. Nielsen, and S.B. Engelsen, *Light scattering and light absorbance separated by extended multiplicative signal correction. Application to near-infrared transmission analysis of powder mixtures.* Analytical Chemistry, 2003. **75**(3): p. 394-404.
317. Brandsrud, M.A., et al., *The effect of deformation of absorbing scatterers on Mie-type signatures in infrared microspectroscopy.* Scientific reports, 2021. **11**(1): p. 1-14.
318. Konevskikh, T., et al., *Mie scatter corrections in single cell infrared microspectroscopy.* Faraday discussions, 2016. **187**: p. 235-257.
319. Solheim, J.H., et al., *An open-source code for Mie extinction extended multiplicative signal correction for infrared microscopy spectra of cells and tissues.* Journal of biophotonics, 2019. **12**(8): p. e201800415.
320. Bassan, P., et al., *Resonant Mie scattering (RMieS) correction of infrared spectra from highly scattering biological samples.* Analyst, 2010. **135**(2): p. 268-277.
321. Magnussen, E.A., et al., *Deep convolutional neural network recovers pure absorbance spectra from highly scatter-distorted spectra of cells.* Journal of Biophotonics, 2020. **13**(12): p. e202000204.
322. Bohren, C.F. and D.R. Huffman, *Absorption and scattering of light by small particles*. 2008: John Wiley & Sons.
323. Fukuda, J.-i. and T. Theophanides, *Water in rocks and minerals—species, distributions, and temperature dependences.* Infrared Spectroscopy-Materials Science, Engineering and Technology, 2012: p. 77-96.
324. Asanuma, H., et al., *Water structure at superhydrophobic quartz/water interfaces: a vibrational sum frequency generation spectroscopy study.* The Journal of Physical Chemistry C, 2009. **113**(50): p. 21155-21161.
325. Lewis, E.N., et al., *Fourier transform spectroscopic imaging using an infrared focal-plane array detector.* Analytical chemistry, 1995. **67**(19): p. 3377-3381.
326. Dionnet, Z., et al., *FTIR Micro-tomography of Five Itokawa Particles and one Primitive Carbonaceous Chondrite.* Microscopy and Microanalysis, 2018. **24**(S1): p. 2100-2101.
327. Mozhdehei, A., et al., *Diffraction-limited mid-infrared microspectroscopy to reveal a micron-thick interfacial water layer signature.* Analyst, 2023.
328. Moore, F. and G. Richmond, *Integration or segregation: How do molecules behave at oil/water interfaces?* Accounts of chemical research, 2008. **41**(6): p. 739-748.
329. Libnau, F.O., et al., *Spectra of water in the near-and mid-infrared region.* Vibrational spectroscopy, 1994. **7**(3): p. 243-254.
330. Maréchal, Y., *Infrared spectra of water. I. Effect of temperature and of H/D isotopic dilution.* The Journal of chemical physics, 1991. **95**(8): p. 5565-5573.
331. Gaweł, B.A., et al., *In situ high temperature spectroscopic study of liquid inclusions and hydroxyl groups in high purity natural quartz.* Minerals Engineering, 2021. **174**: p. 107238.
332. Zhou, L., T.P. Mernagh, and C. Le Losq, *Observation of the Chemical Structure of Water up to the Critical Point by Raman Spectroscopic Analysis of Fluid Inclusions.* The Journal of Physical Chemistry B, 2019. **123**(27): p. 5841-5847.

333. Yasaka, Y., et al., *Mol. Liq. Mol. Liq. 119, 119, 2005.* Bulletin of the Chemical Society of Japan, 2007. **80**(9): p. 1764-1769.
334. Frantz, J.D., J. Dubessy, and B. Mysen, *An optical cell for Raman spectroscopic studies of supercritical fluids and its application to the study of water to 500 C and 2000 bar.* Chemical Geology, 1993. **106**(1-2): p. 9-26.
335. Knight, A.W., et al., *Water properties under nano-scale confinement.* Scientific reports, 2019. **9**(1): p. 1-12.
336. Takei, T., et al., *Changes in density and surface tension of water in silica pores.* Colloid and Polymer Science, 2000. **278**(5): p. 475-480.
337. Etzler, F.M., *Enhancement of hydrogen bonding in vicinal water; heat capacity of water and deuterium oxide in silica pores.* Langmuir, 1988. **4**(4): p. 878-883.
338. Pezolet, M., et al., *Study of polymer orientation and relaxation by polarization modulation and 2D-FTIR spectroscopy.* Vibrational spectroscopy, 1998. **18**(2): p. 103-110.
339. Strazdaite, S., J. Versluis, and H.J. Bakker, *Water orientation at hydrophobic interfaces.* The Journal of chemical physics, 2015. **143**(8): p. 084708.
340. Bonn, M., Y. Nagata, and E.H. Backus, *Molecular Structure and Dynamics of Water at the Water–Air Interface Studied with Surface-Specific Vibrational Spectroscopy.* Angewandte Chemie International Edition, 2015. **54**(19): p. 5560-5576.
341. Tang, F., et al., *Molecular structure and modeling of water–air and ice–air interfaces monitored by sum-frequency generation.* Chemical reviews, 2020. **120**(8): p. 3633-3667.
342. Doshi, D.A., et al., *Reduced water density at hydrophobic surfaces: Effect of dissolved gases.* Proceedings of the National Academy of Sciences, 2005. **102**(27): p. 9458-9462.
343. Stanley, H.E. and J. Teixeira, *Interpretation of the unusual behavior of H2O and D2O at low temperatures: Tests of a percolation model.* The Journal of Chemical Physics, 1980. **73**(7): p. 3404-3422.
344. Frank, H.S. and M.W. Evans, *Free volume and entropy in condensed systems III. Entropy in binary liquid mixtures; partial molal entropy in dilute solutions; structure and thermodynamics in aqueous electrolytes.* The Journal of chemical physics, 1945. **13**(11): p. 507-532.
345. Davis, J.G., et al., *Water structural transformation at molecular hydrophobic interfaces.* Nature, 2012. **491**(7425): p. 582-585.
346. Galamba, N., *Water's structure around hydrophobic solutes and the iceberg model.* The Journal of Physical Chemistry B, 2013. **117**(7): p. 2153-2159.
347. Raschke, T.M. and M. Levitt, *Nonpolar solutes enhance water structure within hydration shells while reducing interactions between them.* Proceedings of the National Academy of Sciences, 2005. **102**(19): p. 6777-6782.
348. Rezus, Y. and H. Bakker, *Observation of immobilized water molecules around hydrophobic groups.* Physical Review Letters, 2007. **99**(14): p. 148301.
349. Turner, J., A. Soper, and J. Finney, *A neutron-diffraction study of tetramethylammonium chloride in aqueous solution.* Molecular Physics, 1990. **70**(4): p. 679-700.
350. Qvist, J. and B. Halle, *Thermal signature of hydrophobic hydration dynamics.* Journal of the American Chemical Society, 2008. **130**(31): p. 10345-10353.
351. Buchanan, P., et al., *Decreased structure on dissolving methane in water.* Chemical physics letters, 2005. **415**(1-3): p. 89-93.
352. Bakulin, A.A., et al., *Hydrophobic solvation: a 2D IR spectroscopic inquest.* Accounts of chemical research, 2009. **42**(9): p. 1229-1238.

353. Sun, Q., *The effects of dissolved hydrophobic and hydrophilic groups on water structure.* Journal of Solution Chemistry, 2020. **49**(12): p. 1473-1484.
354. Kronberg, B., *The hydrophobic effect.* Current Opinion in Colloid & Interface Science, 2016. **22**: p. 14-22.
355. Hummer, G., et al., *New perspectives on hydrophobic effects.* Chemical Physics, 2000. **258**(2-3): p. 349-370.
356. Sun, Q., *The Hydrophobic Effects: Our Current Understanding.* Molecules, 2022. **27**(20): p. 7009.
357. Hildebrand, J.H., *Is there a "hydrophobic effect"?* Proceedings of the National Academy of Sciences, 1979. **76**(1): p. 194-194.
358. Tanford, C., *Interfacial free energy and the hydrophobic effect.* Proceedings of the National Academy of Sciences, 1979. **76**(9): p. 4175-4176.
359. Djikaev, Y.S. and E. Ruckenstein, *Probabilistic approach to the length-scale dependence of the effect of water hydrogen bonding on hydrophobic hydration.* The Journal of Physical Chemistry B, 2013. **117**(23): p. 7015-7025.
360. Djikaev, Y. and E. Ruckenstein, *Recent developments in the theoretical, simulational, and experimental studies of the role of water hydrogen bonding in hydrophobic phenomena.* Advances in Colloid and Interface Science, 2016. **235**: p. 23-45.
361. Chandler, D., *Interfaces and the driving force of hydrophobic assembly.* Nature, 2005. **437**(7059): p. 640-647.
362. Stillinger, F.H. *Structure in aqueous solutions of nonpolar solutes from the standpoint of scaled-particle theory*. in *The Physical Chemistry of Aqueous System: A Symposium in Honor of Henry S. Frank on His Seventieth Birthday*. 1973. Springer.
363. Sharma, S. and P.G. Debenedetti, *Free energy barriers to evaporation of water in hydrophobic confinement.* The Journal of Physical Chemistry B, 2012. **116**(44): p. 13282-13289.
364. Lum, K., D. Chandler, and J.D. Weeks, *Hydrophobicity at small and large length scales*. 1999, The Journal of Physical Chemistry B. p. 4570-4577.
365. Hillyer, M.B. and B.C. Gibb, *Molecular shape and the hydrophobic effect.* Annual review of physical chemistry, 2016. **67**: p. 307-329.
366. Lee, C.Y., J.A. McCammon, and P. Rossky, *The structure of liquid water at an extended hydrophobic surface.* The Journal of chemical physics, 1984. **80**(9): p. 4448-4455.
367. Rego, N.B. and A.J. Patel, *Understanding hydrophobic effects: Insights from water density fluctuations.* Annual Review of Condensed Matter Physics, 2022. **13**: p. 303-324.
368. Zeng, H., et al., *Recent experimental advances on hydrophobic interactions at solid/water and fluid/water interfaces.* Biointerphases, 2016. **11**(1): p. 018903.
369. Hammer, M.U., et al., *The search for the hydrophobic force law.* Faraday discussions, 2010. **146**: p. 299-308.
370. Zhang, X., Y. Zhu, and S. Granick, *Softened hydrophobic attraction between macroscopic surfaces in relative motion.* Journal of the American Chemical Society, 2001. **123**(27): p. 6736-6737.
371. Sedlmeier, F., et al., *Water at polar and nonpolar solid walls.* Biointerphases, 2008. **3**(3): p. FC23-FC39.
372. Vinogradova, O.I., *Slippage of water over hydrophobic surfaces.* International journal of mineral processing, 1999. **56**(1-4): p. 31-60.
373. Zhang, X., et al., *Probing boundary conditions at hydrophobic solid–water interfaces by dynamic film drainage measurement.* Langmuir, 2018. **34**(40): p. 12025-12035.

374. Dalla Bernardina, S., et al., *Water in carbon nanotubes: the peculiar hydrogen bond network revealed by infrared spectroscopy.* Journal of the American Chemical Society, 2016. **138**(33): p. 10437-10443.
375. Dorsey, N.E., *Properties of ordinary water-substance in all its phases.* 1940.
376. Emmanuel, S. and B. Berkowitz, *Effects of pore-size controlled solubility on reactive transport in heterogeneous rock.* Geophysical Research Letters, 2007. **34**(6).
377. Ehrenberg, S.N. and O. Walderhaug, *Preferential calcite cementation of macropores in microporous limestones.* Journal of Sedimentary Research, 2015. **85**(7): p. 780-793.
378. Nauruzbayeva, J., et al., *Electrification at water–hydrophobe interfaces.* Nature Communications, 2020. **11**(1): p. 5285.
379. Björneholm, O., et al., *Water at interfaces.* Chemical reviews, 2016. **116**(13): p. 7698-7726.
380. Leung, K., I.M. Nielsen, and L.J. Criscenti, *Elucidating the bimodal acid− base behavior of the water− silica interface from first principles.* Journal of the American Chemical Society, 2009. **131**(51): p. 18358-18365.
381. Creux, P., et al., *Specific cation effects at the hydroxide-charged air/water interface.* The Journal of Physical Chemistry C, 2007. **111**(9): p. 3753-3755.
382. Lützenkirchen, J., T. Preočanin, and N. Kallay, *A macroscopic water structure based model for describing charging phenomena at inert hydrophobic surfaces in aqueous electrolyte solutions.* Physical Chemistry Chemical Physics, 2008. **10**(32): p. 4946-4955.
383. Gonella, G., et al., *Water at charged interfaces.* Nature Reviews Chemistry, 2021. **5**(7): p. 466-485.
384. Smith, A.M., A.A. Lee, and S. Perkin, *The electrostatic screening length in concentrated electrolytes increases with concentration.* The journal of physical chemistry letters, 2016. **7**(12): p. 2157-2163.
385. Ojha, K., et al., *Double layer at the Pt (111)–aqueous electrolyte interface: potential of zero charge and anomalous Gouy–Chapman screening.* Angewandte Chemie, 2020. **132**(2): p. 721-725.
386. Govrin, R., et al., *Regulation of surface charge by biological osmolytes.* Journal of the American Chemical Society, 2017. **139**(42): p. 15013-15021.
387. Mercury, L. and K.I. Shmulovich, *Experimental superheating and cavitation of water and solutions at spinodal-like negative pressures*, in *Transport and Reactivity of Solutions in Confined Hydrosystems*. 2014, Springer. p. 159-171.
388. Morishige, K. and H. Yasunaga, *Tensile effect on a confined phase.* The Journal of Physical Chemistry B, 2006. **110**(9): p. 3864-3866.
389. Tas, N.R., et al., *Capillary negative pressure measured by nanochannel collapse.* Langmuir, 2010. **26**(3): p. 1473-1476.
390. Tas, N.R., et al., *Capillary filling speed of water in nanochannels.* Applied Physics Letters, 2004. **85**(15): p. 3274-3276.
391. Tas, N.R., et al., *Capillarity induced negative pressure of water plugs in nanochannels.* Nano letters, 2003. **3**(11): p. 1537-1540.
392. Ravikovitch, P.I. and A.V. Neimark, *Experimental confirmation of different mechanisms of evaporation from ink-bottle type pores: equilibrium, pore blocking, and cavitation.* Langmuir, 2002. **18**(25): p. 9830-9837.
393. Grosman, A. and C. Ortega, *Cavitation in metastable fluids confined to linear mesopores.* Langmuir, 2011. **27**(6): p. 2364-2374.

394. Stroock, A.D., et al., *The physicochemical hydrodynamics of vascular plants.* Annual review of fluid mechanics, 2014. **46**: p. 615-642.
395. Marcolli, C., *Deposition nucleation viewed as homogeneous or immersion freezing in pores and cavities.* Atmospheric Chemistry and Physics, 2014. **14**(4): p. 2071-2104.
396. Kumar, S., et al., *A comprehensive review of value-added CO2 sequestration in subsurface saline aquifers.* Journal of Natural Gas Science and Engineering, 2020. **81**: p. 103437.
397. Alava, M., M. Dubé, and M. Rost, *Imbibition in disordered media.* Advances in Physics, 2004. **53**(2): p. 83-175.
398. Lucas, R., *Ueber das Zeitgesetz des kapillaren Aufstiegs von Flüssigkeiten.* Kolloid-Zeitschrift, 1918. **23**(1): p. 15-22.
399. Washburn, E., *Phys.* Review, 1921. **17**: p. 273.
400. Acquaroli, L.N., et al., *Capillary filling in nanostructured porous silicon.* Langmuir, 2011. **27**(5): p. 2067-2072.
401. Gruener, S., et al., *Anomalous front broadening during spontaneous imbibition in a matrix with elongated pores.* Proceedings of the National Academy of Sciences, 2012. **109**(26): p. 10245-10250.
402. Masoodi, R. and K.M. Pillai, *Wicking in porous materials: traditional and modern modeling approaches*. 2012: CRC Press.
403. Bouzid, M., et al., *In-pore tensile stress by drying-induced capillary bridges inside porous materials.* Journal of colloid and interface science, 2011. **355**(2): p. 494-502.
404. Zheng, Q., et al., *Liquids at large negative pressures: water at the homogeneous nucleation limit.* Science, 1991. **254**(5033): p. 829-832.
405. Tyree, M.T. and J.S. Sperry, *Vulnerability of xylem to cavitation and embolism.* Annual review of plant biology, 1989. **40**(1): p. 19-36.
406. Cochard, H., *Cavitation in trees.* Comptes Rendus Physique, 2006. **7**(9-10): p. 1018-1026.
407. Scherer, G.W. and D.M. Smith, *Cavitation during drying of a gel.* Journal of Non-Crystalline Solids, 1995. **189**(3): p. 197-211.
408. Or, D. and M. Tuller, *Cavitation during desaturation of porous media under tension.* Water Resources Research, 2002. **38**(5): p. 19-1-19-14.
409. Hulin, C. and L. Mercury, *Capillarity-driven supersolubility in dual-porosity systems.* Geochimica et Cosmochimica Acta, 2019. **252**: p. 144-158.
410. Hulin, C. and L. Mercury, *Regeneration of capillary water in unsaturated zones.* Geochimica et Cosmochimica Acta, 2019. **265**: p. 279-291.
411. Lassin, A., L. Mercury, and M. Azaroual. *Geochemistry of capillary hydrogeochemical systems in arid environments*. in *Transport and Reactivity of Solutions in Confined Hydrosystems*. 2014. Springer.
412. Vincent, O., et al., *Birth and growth of cavitation bubbles within water under tension confined in a simple synthetic tree.* Physical Review Letters, 2012. **108**(18): p. 184502.
413. Vincent, O., et al., *The fast dynamics of cavitation bubbles within water confined in elastic solids.* Soft Matter, 2014. **10**(10): p. 1455-1461.
414. Tamaki, E., et al., *Liquid filling method for nanofluidic channels utilizing the high solubility of CO2.* Analytical sciences, 2006. **22**(4): p. 529-532.
415. Wheeler, T.D. and A.D. Stroock, *The transpiration of water at negative pressures in a synthetic tree.* Nature, 2008. **455**(7210): p. 208-212.

416. Reid, R.C., *Rapid phase transitions from liquid to vapor*, in *Advances in Chemical Engineering*. 1983, Elsevier. p. 105-208.
417. Chauvet, F., et al., *Three periods of drying of a single square capillary tube.* Physical review letters, 2009. **103**(12): p. 124502.
418. Bico, J., U. Thiele, and D. Quéré, *Wetting of textured surfaces.* Colloids and Surfaces A: Physicochemical and Engineering Aspects, 2002. **206**(1-3): p. 41-46.
419. Huppert, H.E. and J.A. Neufeld, *The fluid mechanics of carbon dioxide sequestration.* Annual review of fluid mechanics, 2014. **46**: p. 255-272.
420. Hellmann, R., et al., *Nanometre-scale evidence for interfacial dissolution–reprecipitation control of silicate glass corrosion.* Nature materials, 2015. **14**(3): p. 307-311.
421. Zhu, C., et al., *Decoupling feldspar dissolution and precipitation rates at near-equilibrium with Si isotope tracers: Implications for modeling silicate weathering.* Geochimica et Cosmochimica Acta, 2020. **271**: p. 132-153.

Appendix

Appendix A: Interference fringe removal method

This section presents the developed code for effectively removing the interference fringe using Igor Pro 9.0. The code has been specifically designed to address and eliminate any unwanted fringe artifacts. By implementing this code, you can achieve improved data quality and enhance the accuracy of your analysis. Fig. 1 showcases the flowchart outlining the implemented algorithm.

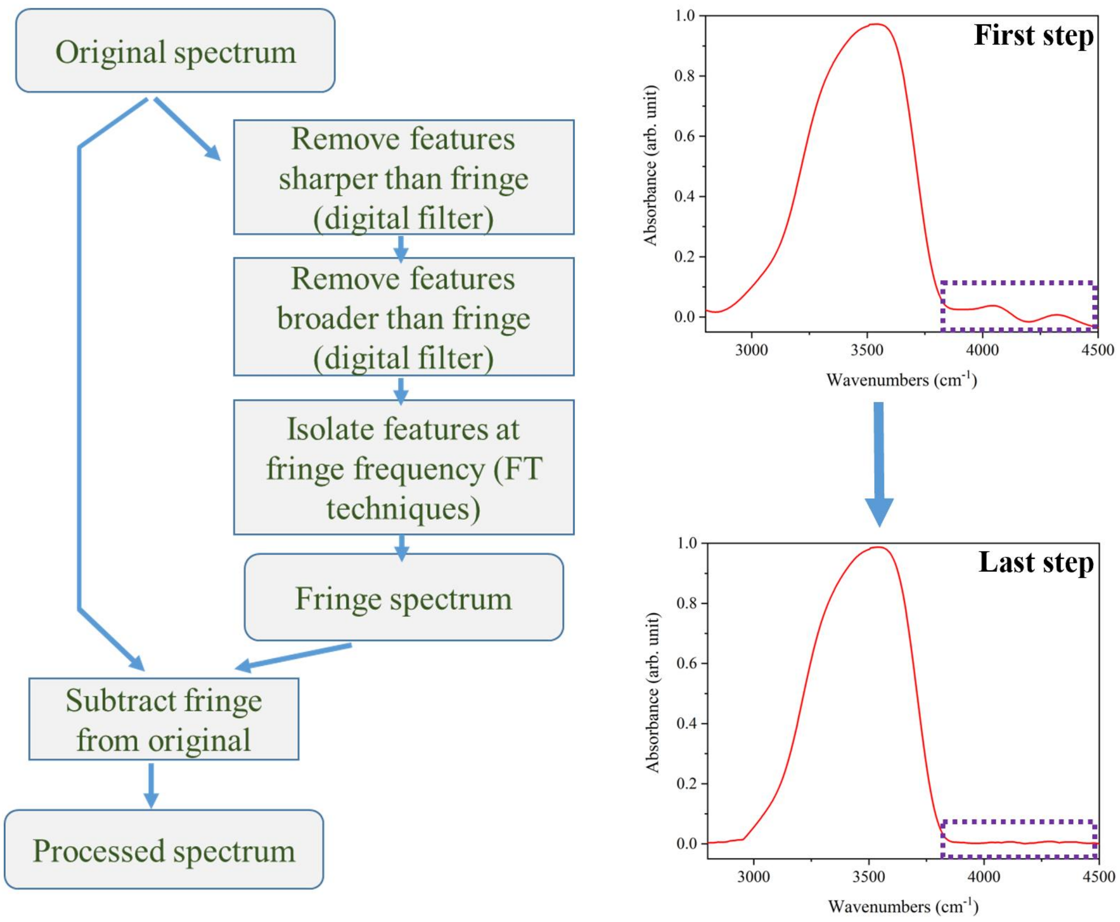

Fig. 1. The flowchart of the interference removal algorithm.

The detailed code and instructions for implementation are provided below.

```
#pragma TextEncoding = "UTF-8"
#pragma rtGlobals=3                           // Use modern global access
method and strict wave access
#pragma DefaultTab={3,20,4}           // Set default tab width in Igor Pro 9
and later
#include <FilterDialog> menus=0

Menu "Armin"
        "Process Spectra"
        "Display original spectra", DisplayFiles(0)
        "Display processed spectra", DisplayFiles(1)
end

Proc ProcessSpectra(int_wavenum, wid, smth, hiPass, ignoreLow)
variable int_wavenum = 240, wid = 0.2, smth = 10, hiPass = 3500, ignoreLow =
2
Prompt int_wavenum, "Enter the interference period (cm-1):"
Prompt wid, "Enter the relative width:"
Prompt smth, "Enter the amount of smoothing:"
Prompt hiPass, "Enter the roll-off wavenumber for the hi-pass filter:"
Prompt ignoreLow, "Use low pass filter?", popup "No; Yes"

        ProcessFolder(int_wavenum, wid, smth, hiPass, ignoreLow-1)
End
// Typical usage: ProcessFolder(240, 0.2, 10, 3500, 1)
Function ProcessFolder(int_wavenum, wid, smth, hiPass, ignoreLow)
// int_wavenum is the period of the interference in wavenumbers (e.g., 240)
// wid is the relative width of the interference (e.g., 0.1 = 10%)
// smth is the amount of smoothing. This is an integer ~ 10
// hiPass is the roll-off wavenumber for the hi-pass filter on the
interference (e.g., 3500)
// ignoreLow: If this is 1 (actually, non-zero), roll off the first half-
interference to avoid an artifact
//                         If this is 0, don't
variable int_wavenum, wid, smth, hiPass, ignoreLow

        string fileName, baseName, waveNames
        variable numItems, i

        // Find the folder of data
        NewPath/C/M="Find the folder of data"/O/Q/Z myData

        // Get a semicolon-separated list of all .csv files in the folder
        String fileList = IndexedFile(myData, -1, ".csv")

        // Process the list
        numItems = ItemsInList(fileList)
        for(i = 0; i < numItems; i += 1)
                fileName = StringFromList(i, fileList)

        LoadWave/A/J/Q/D/W/NAME={":filename:","",30}/P=myData/K=0/V={",","
$",0,0} fileName
                baseName = StringFromList(0, S_waveNames)
                baseName = baseName[0, strlen(baseName)-2]
```

```
                // The csv contains both wavenumbers and absorbance data.
Process this into one wave.
                rename $(baseName + "1"), $baseName
                wave baseName0 = $(baseName + "0")
                SetScale/P x baseName0[0],baseName0[1]-baseName0[0],"",
$baseName
                KillWaves/Z baseName0

                // The Fourier transform requires an even number of points.
If necessary, clip off last point
                wave base = $baseName
                if(mod(numpnts(base),2))
                        Redimension/N=(numpnts(base)-1) base
                endif

                Process(baseName, int_wavenum, wid, smth, hiPass,ignoreLow)
                Print "Finished processing ",baseName
        endfor


End
Function Process(wvName, int_wavenum, wid, smth,hiPass, ignoreLow)
// wvName is the name of the input wave
// int_wavenum is the period of the interference in wavenumbers (e.g., 240)
// wid is the relative width of the interference (e.g., 0.1 = 10%)
// smth is the amount of smoothing. This is an integer ~ 10
// hiPass is the roll-off wavenumber for the hi-pass filter on the
interference (e.g., 4500)
// ignoreLow: If this is 1 (actually, non-zero), roll off the first half-
interference to avoid an artifact
//                         If this is 0, don't
string wvName
variable int_wavenum, wid, smth, hiPass, ignoreLow

        // Set up some waves to work with. No science here
        string wv_outName = wvName + "_out"
        wave wv = $wvName
        duplicate/o wv, wv_smth,$wv_outName
        wave wv_out = $wv_outName

        // Take the original spectrum and smooth out the high frequency
signal (i.e., your data)
        Smooth/E=2 smth, wv_smth

        // Take the Fourier transform of the smoothed wave
        FFT/OUT=1/DEST=W_FFT wv_smth
        wave/C W_FFT

        // Isolate the part of the transformed wave that corresponds to the
interference
        W_FFT *= exp(-(x-1/int_wavenum)^2/(wid/int_wavenum)^2) > 0.01

        // Take the inverse Fourier transform of the isolated resonance.
Correct the scaling (due to FT).
        IFFT/DEST=W_FFT_IFFT  W_FFT
        SetScale/P x DimOffset(wv,0),DimDelta(wv,0),"", W_FFT_IFFT
```

```
	// Discrete Fourier transforms assume your data is periodic, which it is not. Instead, your
	//	interference occurs primarily in the low wavenumber region. I just roll off the reconstructed
	//	resonance above 3500 cm-1. This removes the high frequency artifact due to the assumed periodicity.
	W_FFT_IFFT /= (1 + (x/hiPass)^8)
	if(ignoreLow)
		variable ptsToIgnore = 0.5 * int_wavenum/DimDelta(wv,0) // Ignore first half-period of interference
		W_FFT_IFFT[0,ptsToIgnore-1] *= exp(-(4*(p-ptsToIgnore)/ptsToIgnore)^2)
	endif

	// At this point, the wave W_FFT_IFFT contains my best guess at your interference, so subtract that off.
	wv_out = wv - W_FFT_IFFT

	// Get rid of all of the scratch waves used in the calculation
	KillWaves wv_smth, W_FFT,W_FFT_IFFT
End

Function DisplayFiles(processed)
variable processed

	string allFiles, nextFile
	variable num, cnt = 0

	if(processed)
		allFiles = WaveList("*_out",";","")
	else
		allFiles = WaveList("!*_out",";","")
	endif

	num = ItemsInList(allFiles)
	if(num < 1)
		print "No files found"
		return 1
	endif
	do
		wave nextWave = $StringFromList(cnt, allFiles)
		if(cnt == 0)
			display nextWave
		else
			appendToGraph nextWave
		endif
		cnt += 1
	while(cnt < num)
End
```

After successfully implementing the algorithm in Igor Pro 9.0 software, the spectra were corrected by isolating the wavenumbers associated with the interference contribution. The correction process is depicted in the following figures, providing a comprehensive visual representation. Fig. 2 displays the Igor Pro 9.0 software interface, where we employ this algorithm for the correction procedure. These figures serve as valuable references, illustrating the steps taken to effectively eliminate interference and enhance the accuracy of the spectra.

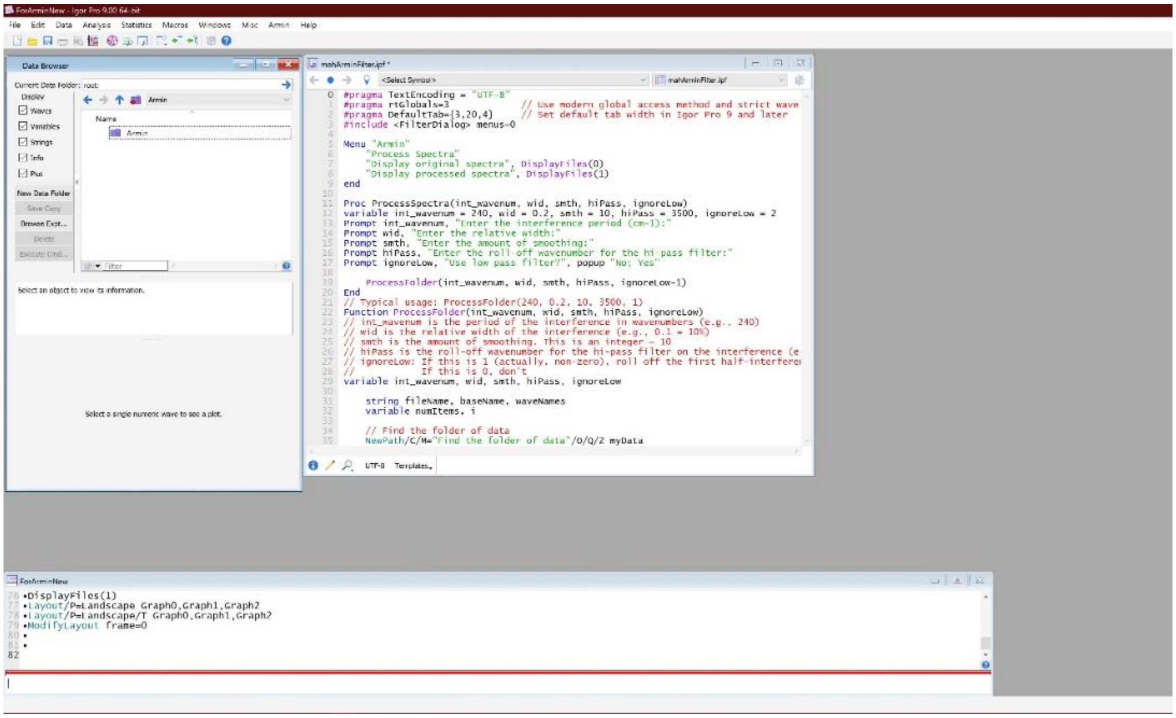

```
#pragma TextEncoding = "UTF-8"
#pragma rtGlobals=3          // Use modern global access method and strict wave
#pragma DefaultTab={3,20,4}  // Set default tab width in Igor Pro 9 and later
#include <FilterDialog> menus=0

Menu "Armin"
    "Process Spectra"
    "Display original spectra", DisplayFiles(0)
    "Display processed spectra", DisplayFiles(1)
end

Proc ProcessSpectra(int_wavenum, wid, smth, hiPass, ignoreLow)
variable int_wavenum = 240, wid = 0.2, smth = 10, hiPass = 3500, ignoreLow = 2
Prompt int_wavenum, "Enter the interference period (cm-1):"
Prompt wid, "Enter the relative width:"
Prompt smth, "Enter the amount of smoothing:"
Prompt hiPass, "Enter the roll-off wavenumber for the hi-pass filter:"
Prompt ignoreLow, "Use low pass filter?", popup "No; Yes"

    ProcessFolder(int_wavenum, wid, smth, hiPass, ignoreLow-1)
End
// Typical usage: ProcessFolder(240, 0.2, 10, 3500, 1)
Function ProcessFolder(int_wavenum, wid, smth, hiPass, ignoreLow)
// int_wavenum is the period of the interference in wavenumbers (e.g., 240)
// wid is the relative width of the interference (e.g., 0.1 = 10%)
// smth is the amount of smoothing. This is an integer ~ 10
// hiPass is the roll-off wavenumber for the hi-pass filter on the interference (e
// ignoreLow: If this is 1 (actually, non-zero), roll off the first half-interfere
//            If this is 0, don't
variable int_wavenum, wid, smth, hiPass, ignoreLow

    string fileName, baseName, waveNames
    variable numItems, i

    // Find the folder of data
    NewPath/C/M="Find the folder of data"/O/Q/Z myData
```

```
•DisplayFiles(1)
•Layout/P=Landscape Graph0,Graph1,Graph2
•Layout/P=Landscape/T Graph0,Graph1,Graph2
•ModifyLayout frame=0
•
•
```

Fig. 2. The Igor Pro 9.0 software interfaces.

To add your desired spectra, simply enter the "DisplayFiles" command in the software's command box. Fig. 3 displays the added spectrum, highlighting the interference fringe contribution in the baseline. To initiate the correction process, navigate to the "ProcessSpectra" tab within the software. Here, you can define four parameters, as illustrated in Fig. 4, which pertain to the period, width, roll-off wavenumber, and smoothing factor of the sinusoidal/harmonic trend. Fig. 5 demonstrates the corrected spectra, where the interference trend in the baseline has been eliminated.

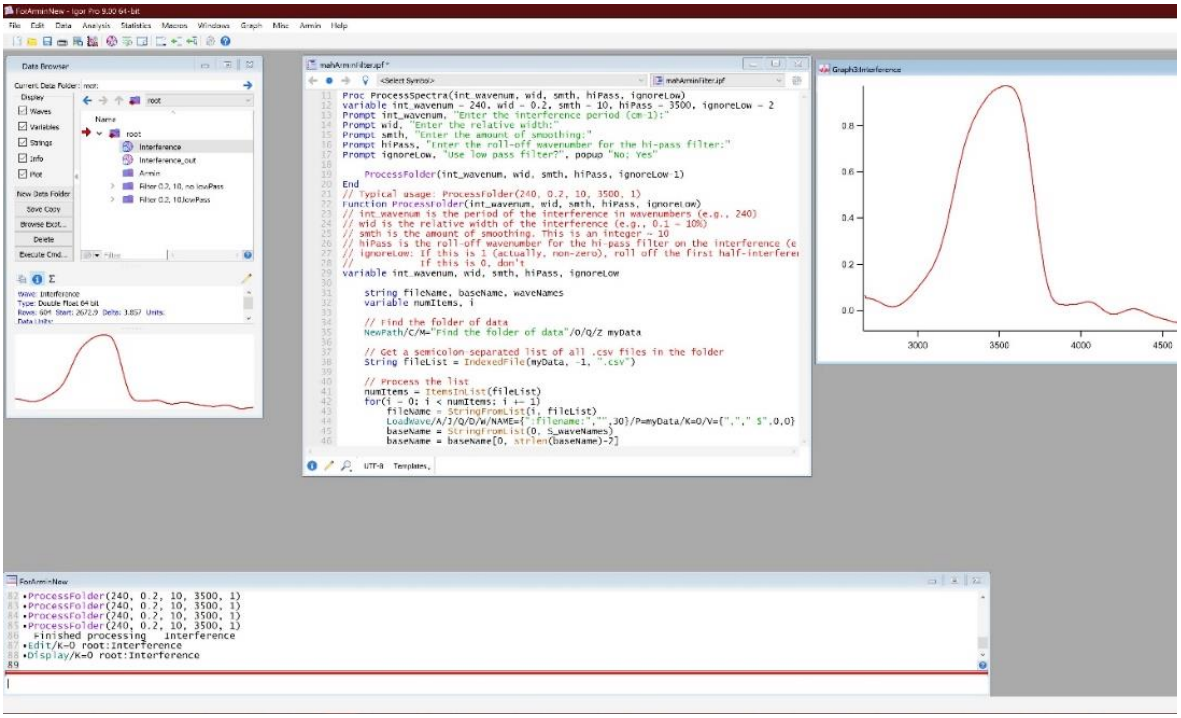

```
Proc ProcessSpectra(int_wavenum, wid, smth, hiPass, ignoreLow)
variable int_wavenum = 240, wid = 0.2, smth = 10, hiPass = 3500, ignoreLow = 2
Prompt int_wavenum, "Enter the interference period (cm-1):"
Prompt wid, "Enter the relative width:"
Prompt smth, "Enter the amount of smoothing:"
Prompt hiPass, "Enter the roll-off wavenumber for the hi-pass filter:"
Prompt ignoreLow, "Use low pass filter?", popup "No; Yes"

    ProcessFolder(int_wavenum, wid, smth, hiPass, ignoreLow-1)
End
// Typical usage: ProcessFolder(240, 0.2, 10, 3500, 1)
Function ProcessFolder(int_wavenum, wid, smth, hiPass, ignoreLow)
// int_wavenum is the period of the interference in wavenumbers (e.g., 240)
// wid is the relative width of the interference (e.g., 0.1 = 10%)
// smth is the amount of smoothing. This is an integer ~ 10
// hiPass is the roll-off wavenumber for the hi-pass filter on the interference (e
// ignoreLow: If this is 1 (actually, non-zero), roll off the first half-interfere
//             If this is 0, don't
variable int_wavenum, wid, smth, hiPass, ignoreLow

    string fileName, baseName, waveNames
    variable numItems, i

    // Find the folder of data
    NewPath/C/M="Find the folder of data"/O/Q/Z myData

    // Get a semicolon-separated list of all .csv files in the folder
    String fileList = IndexedFile(myData, -1, ".csv")

    // Process the list
    numItems = ItemsInList(fileList)
    for(i = 0; i < numItems; i += 1)
        fileName = StringFromList(i, fileList)
        LoadWave/A/J/Q/D/W/NAME={":filename:","",30}/P=myData/K=0/V={","," $",0,0}
        baseName = StringFromList(0, S_waveNames)
        baseName = baseName[0, strlen(baseName)-2]
```

```
•ProcessFolder(240, 0.2, 10, 3500, 1)
•ProcessFolder(240, 0.2, 10, 3500, 1)
•ProcessFolder(240, 0.2, 10, 3500, 1)
•ProcessFolder(240, 0.2, 10, 3500, 1)
  Finished processing   Interference
•Edit/K=0 root:Interference
•Display/K=0 root:Interference
```

Fig. 3. Added spectrum with the interference fringe.

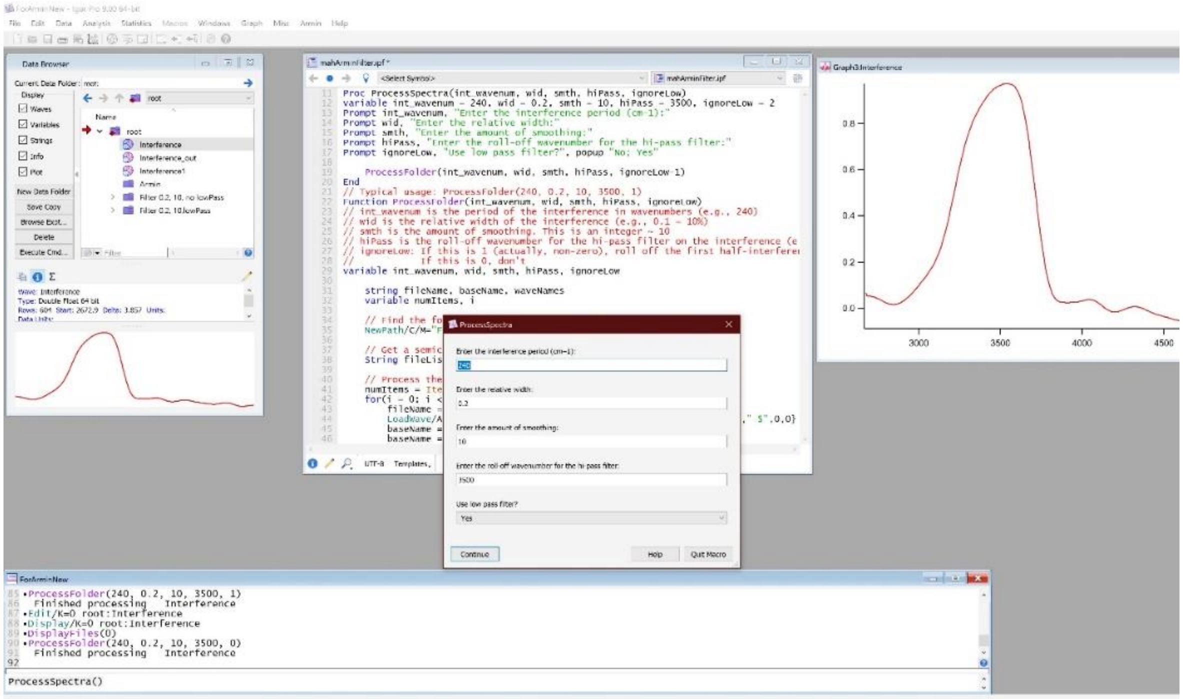

```
Proc ProcessSpectra(int_wavenum, wid, smth, hiPass, ignoreLow)
variable int_wavenum = 240, wid = 0.2, smth = 10, hiPass = 3500, ignoreLow = 2
Prompt int_wavenum, "Enter the interference period (cm-1):"
Prompt wid, "Enter the relative width:"
Prompt smth, "Enter the amount of smoothing:"
Prompt hiPass, "Enter the roll-off wavenumber for the hi-pass filter:"
Prompt ignoreLow, "Use low pass filter?", popup "No; Yes"

    ProcessFolder(int_wavenum, wid, smth, hiPass, ignoreLow-1)
End
// Typical usage: ProcessFolder(240, 0.2, 10, 3500, 1)
Function ProcessFolder(int_wavenum, wid, smth, hiPass, ignoreLow)
// int_wavenum is the period of the interference in wavenumbers (e.g., 240)
// wid is the relative width of the interference (e.g., 0.1 = 10%)
// smth is the amount of smoothing. This is an integer ~ 10
// hiPass is the roll-off wavenumber for the hi-pass filter on the interference (e
// ignoreLow: If this is 1 (actually, non-zero), roll off the first half-interfere
//             If this is 0, don't
variable int_wavenum, wid, smth, hiPass, ignoreLow

    string fileName, baseName, waveNames
    variable numItems, i
```

Enter the interference period (cm-1): 240

Enter the relative width: 0.2

Enter the amount of smoothing: 10

Enter the roll-off wavenumber for the hi-pass filter: 3500

Use low pass filter? Yes

```
•ProcessFolder(240, 0.2, 10, 3500, 1)
  Finished processing   Interference
•Edit/K=0 root:Interference
•Display/K=0 root:Interference
•DisplayFiles(0)
•ProcessFolder(240, 0.2, 10, 3500, 0)
  Finished processing   Interference

ProcessSpectra()
```

Fig. 4. ProcessSpectra window, where one can adjust the interference period, relative width, roll-off wavenumber, and smoothing factor of the harmonic trend.

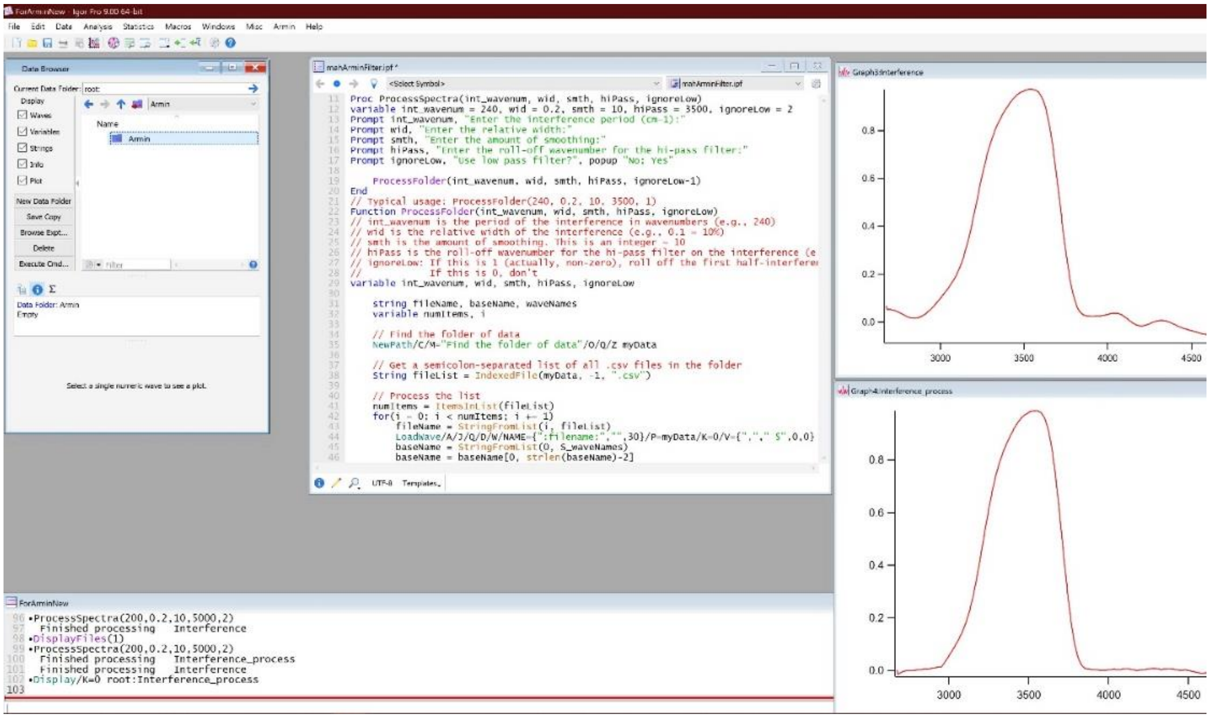

```
Proc ProcessSpectra(int_wavenum, wid, smth, hiPass, ignoreLow)
variable int_wavenum = 240, wid = 0.2, smth = 10, hiPass = 3500, ignoreLow = 2
Prompt int_wavenum, "Enter the interference period (cm-1):"
Prompt wid, "Enter the relative width:"
Prompt smth, "Enter the amount of smoothing:"
Prompt hiPass, "Enter the roll-off wavenumber for the hi-pass filter:"
Prompt ignoreLow, "Use low pass filter?", popup "No; Yes"

    ProcessFolder(int_wavenum, wid, smth, hiPass, ignoreLow-1)
End
// Typical usage: ProcessFolder(240, 0.2, 10, 3500, 1)
Function ProcessFolder(int_wavenum, wid, smth, hiPass, ignoreLow)
// int_wavenum is the period of the interference in wavenumbers (e.g., 240)
// wid is the relative width of the interference (e.g., 0.1 = 10%)
// smth is the amount of smoothing. This is an integer ~ 10
// hiPass is the roll-off wavenumber for the hi-pass filter on the interference (e
// ignoreLow: If this is 1 (actually, non-zero), roll off the first half-interfere
//              If this is 0, don't
variable int_wavenum, wid, smth, hiPass, ignoreLow

    string fileName, baseName, waveNames
    variable numItems, i

    // Find the folder of data
    NewPath/C/M="Find the folder of data"/O/Q/Z myData

    // Get a semicolon-separated list of all .csv files in the folder
    String fileList = IndexedFile(myData, -1, ".csv")

    // Process the list
    numItems = ItemsInList(fileList)
    for(i = 0; i < numItems; i += 1)
        fileName = StringFromList(i, fileList)
        LoadWave/A/J/Q/D/W/NAME={":filename:","",30}/P=myData/K=0/V={","," $",0,0}
        baseName = StringFromList(0, S_waveNames)
        baseName = baseName[0, strlen(baseName)-2]
```

```
•ProcessSpectra(200,0.2,10,5000,2)
  Finished processing   Interference
•DisplayFiles(1)
•ProcessSpectra(200,0.2,10,5000,2)
  Finished processing   Interference_process
  Finished processing   Interference
•Display/K=0 root:Interference_process
```

Fig. 5. Corrected spectrum with the implemented algorithm in the Igor Pro software.

Appendix B: Smoothing procedure in OriginPro

We utilized OriginPro v.2021 for conducting the smoothing process in our study. In this way, the FFT filter method with 15-20 points within the window was employed. Figs. 6-8 illustrate the step-by-step approach we followed to select the appropriate model for smoothing the bulk water spectrum.

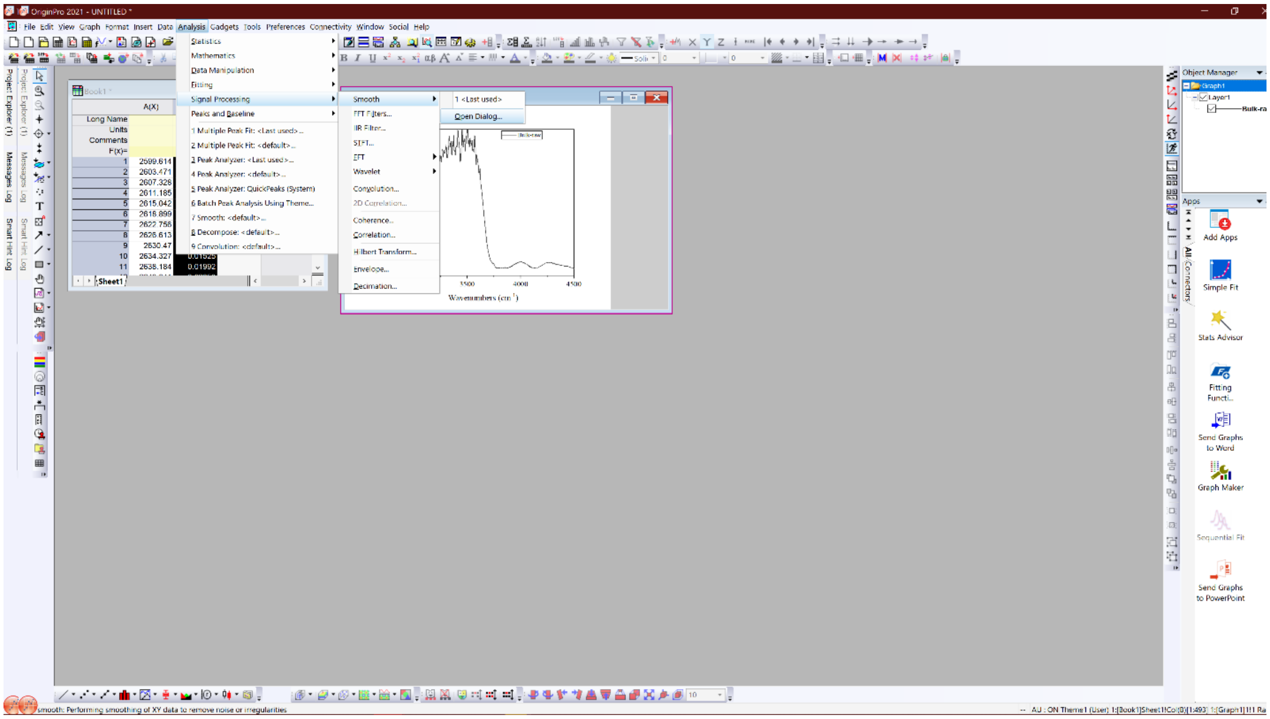

smooth: Performing smoothing of XY data to remove noise or irregularities

Fig. 6. Signal processing module, which we used for starting the smoothing process.

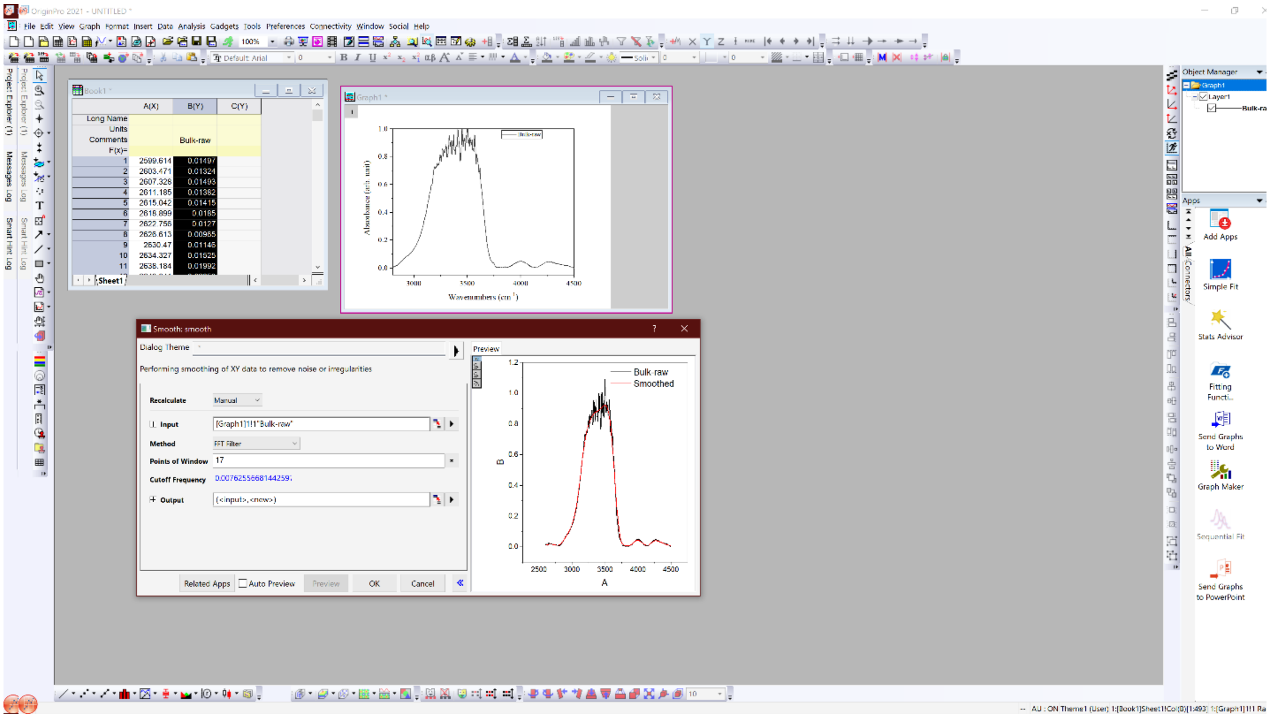

	A(X)	B(Y)	C(Y)
Long Name			
Units			
Comments		Bulk-raw	
F(x)=			
1	2599.614	0.01497	
2	2603.471	0.01324	
3	2607.328	0.01493	
4	2611.185	0.01382	
5	2615.042	0.01415	
6	2618.899	0.0185	
7	2622.756	0.0127	
8	2626.613	0.00965	
9	2630.47	0.01146	
10	2634.327	0.01525	
11	2638.184	0.01992	

Smooth: smooth

Performing smoothing of XY data to remove noise or irregularities

Recalculate: Manual

Input: [Graph1]1!1"Bulk-raw"

Method: FFT Filter

Points of Window: 17

Cutoff Frequency: 0.0076255668144259?

Output: (<input>,<new>)

Fig. 7. FFT filter method with 17 points of window for creating the smoothed spectra.

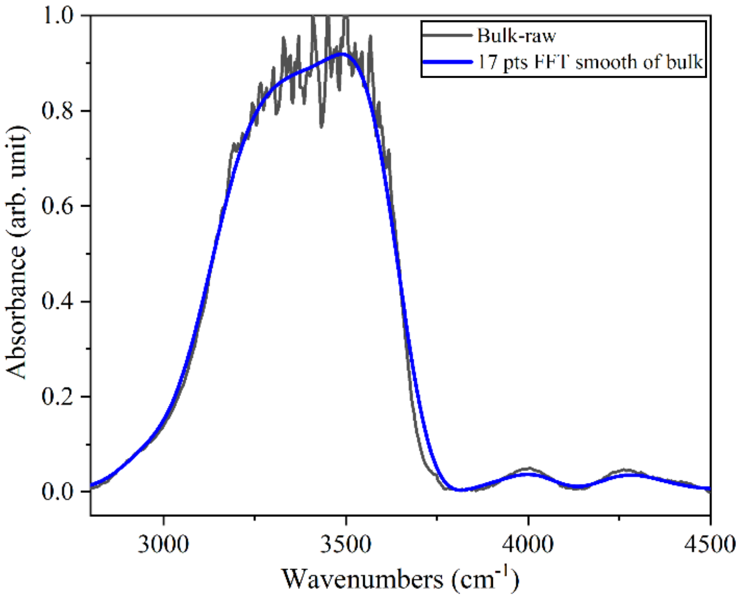

Fig. 8. The final smoothed spectrum (solid blue line) vs. raw bulk water spectrum (solid black line).

Appendix C: Fitting procedure in OriginPro

We utilized OriginPro v.2021 for conducting the fitting and decomposing processes in our study. Figs. 9-13 present the step-by-step approach we followed to select the appropriate model for decomposing the bulk water spectrum into three distinct sub-bands. After careful consideration, we opted for the Gaussian model, employing the provided formula to fit each sub-band accurately (Fig. 14). As shown in Fig. 15, we imposed specific limitations on key parameters including the main peak position, peak area, and full width at half maximum (FWHM) to ensure the validity of our results. The peak positions for each segment were fixed within the ranges of 3150-3350, 3350-3550, and 3550-3750, respectively. Moreover, we set the limitations for the peak area and FWHM between 0 and 1000, as these values align with physical expectations and provide meaningful fitting results. At the end, Fig. 16 presents the final decomposition model of the bulk water spectrum.

In the subsequent step, we applied the selected model to all the spectra recorded all around the fluid inclusion. To streamline this process, we leveraged the batch processing feature in OriginPro. To provide a detailed explanation of this procedure, I invite you to follow the link below, which provided by the OriginPro company©. This video outlines the steps involved in this meticulous approach of batch processing module: https://www.youtube.com/watch?v=avQm0WINfLs

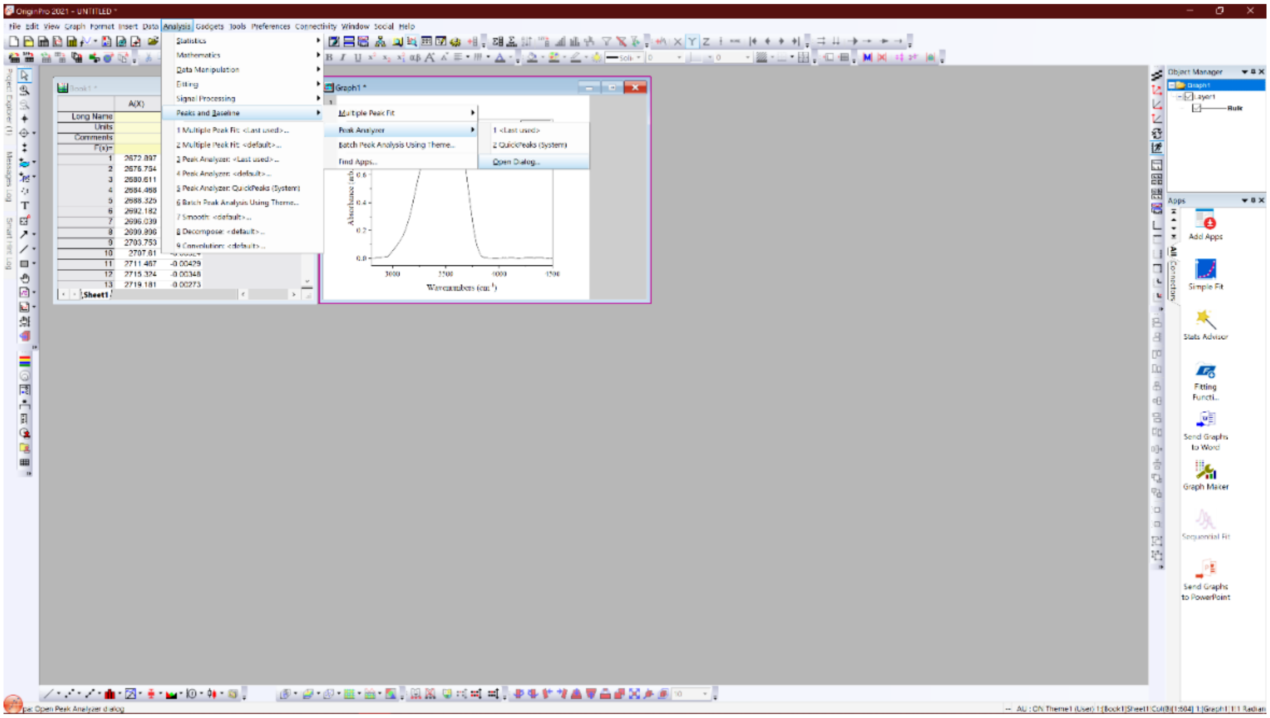

Fig. 9. The software interfaces and the peak Analyzer module, which we used for starting the fitting process.

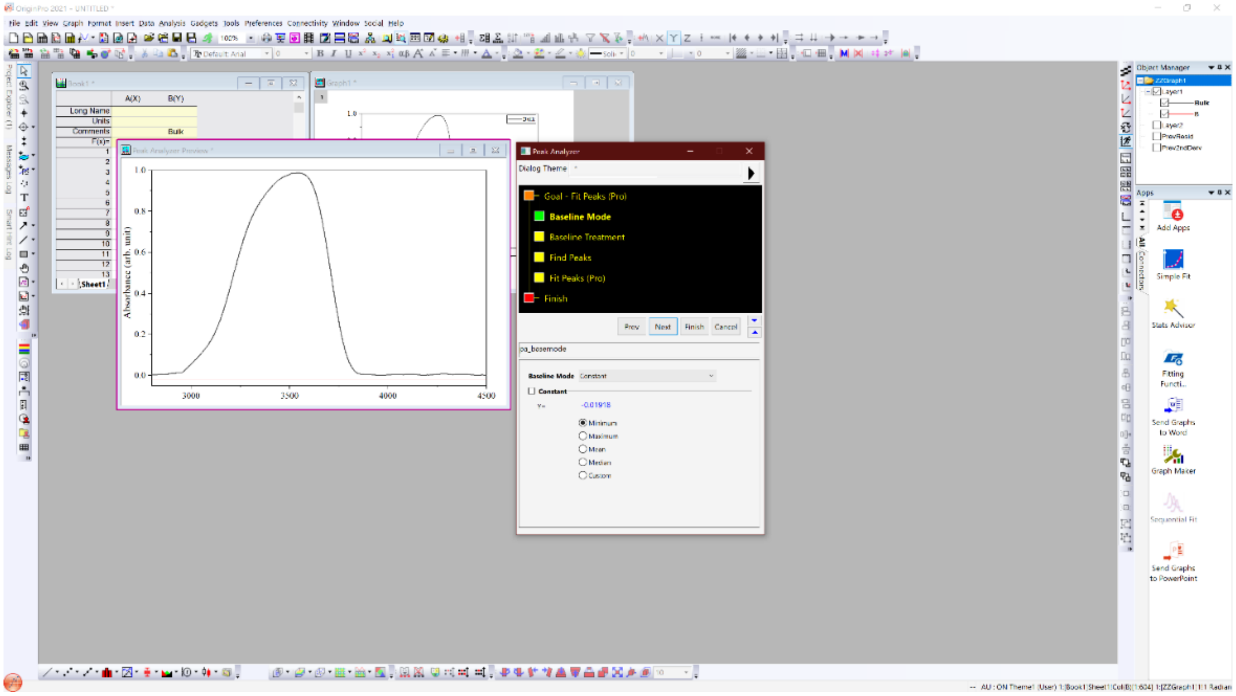

pa_basemode

Baseline Mode Constant

☐ Constant

Y= -0.01918

● Minimum
○ Maximum
○ Mean
○ Median
○ Custom

Fig. 10. Defining the minimum constant baseline for baseline correction method.

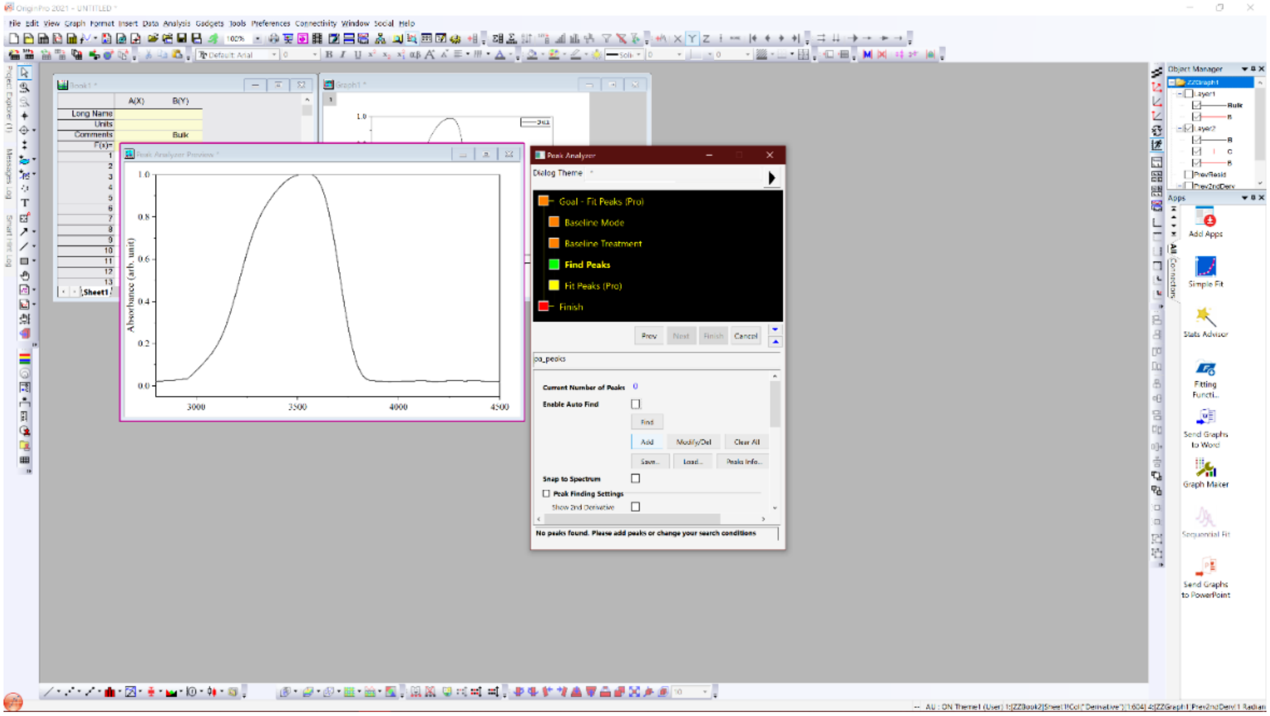

Current Number of Peaks 0

Enable Auto Find ☐

Snap to Spectrum ☐

☐ Peak Finding Settings

Show 2nd Derivative ☐

No peaks found. Please add peaks or change your search conditions

Fig. 11. Defining manually the peak location for each of three desired sub-bands.

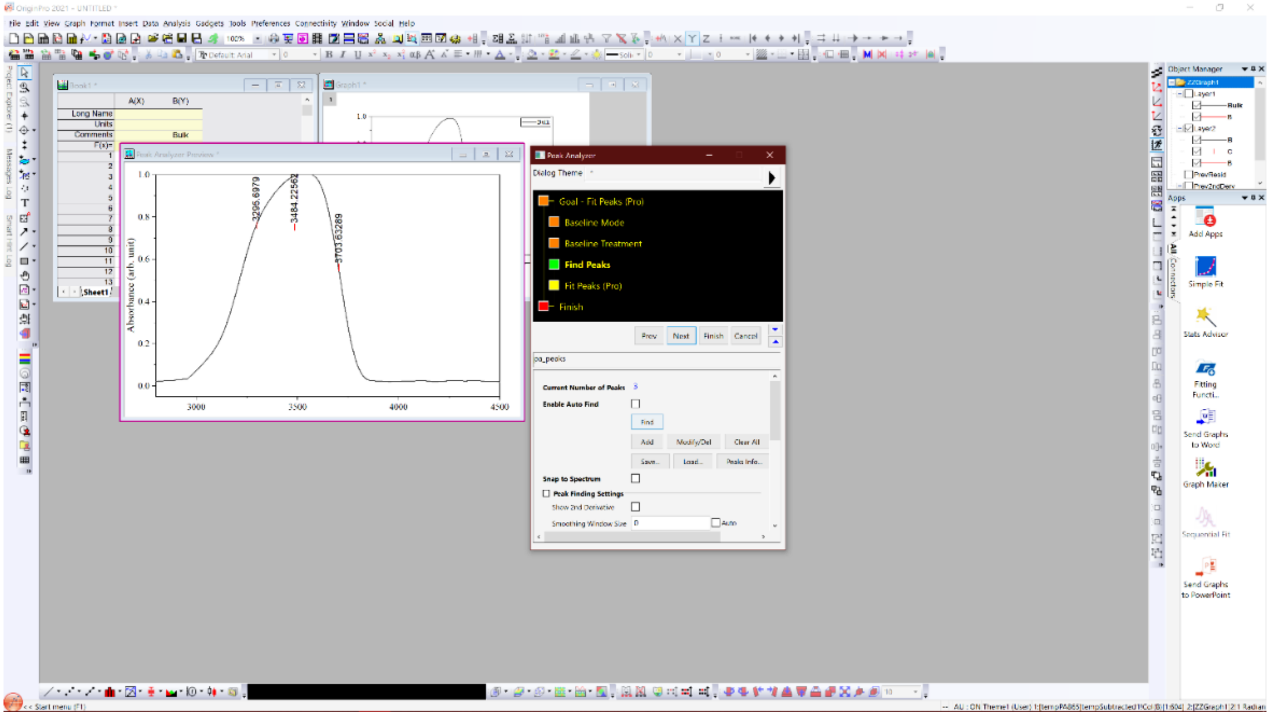

Current Number of Peaks 3

Enable Auto Find ☐

Snap to Spectrum ☐

☐ Peak Finding Settings

Show 2nd Derivative ☐

Smoothing Window Size 0 ☐ Auto

Fig. 12. The main peak location of three sub-bands.

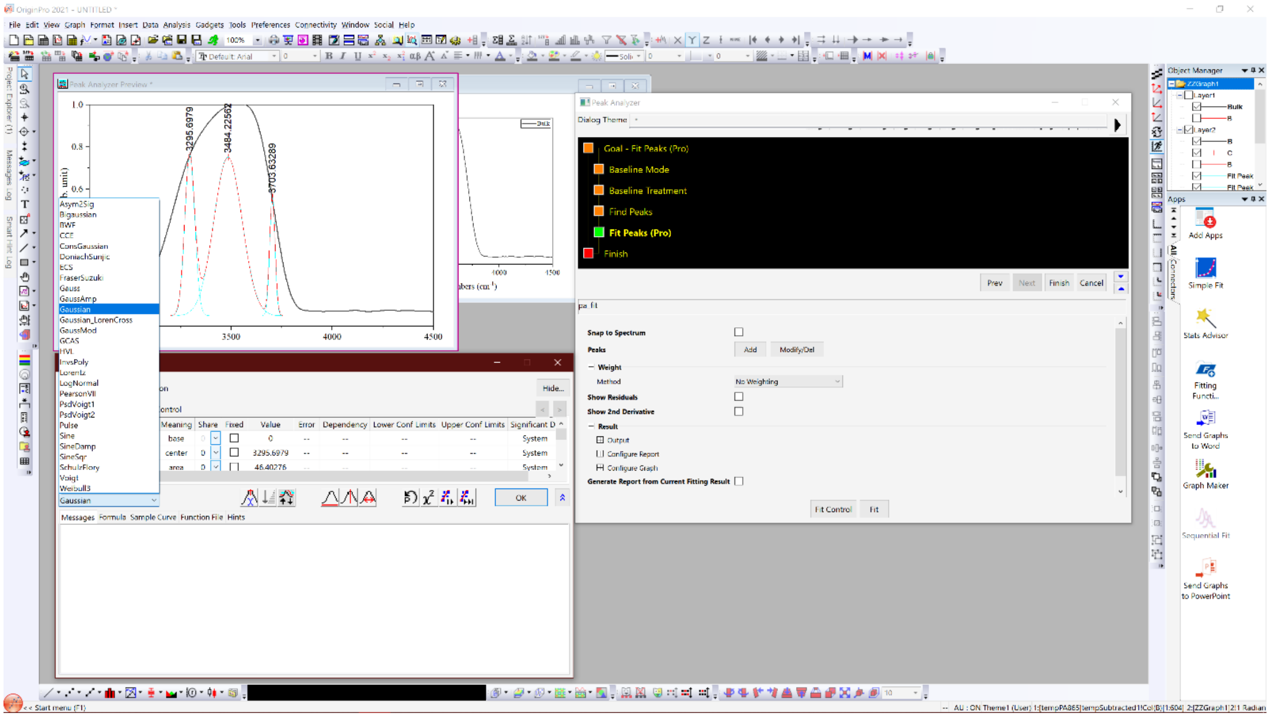

Fig. 13. Choosing the Gaussian model to fit with our recorded bulk water spectrum.

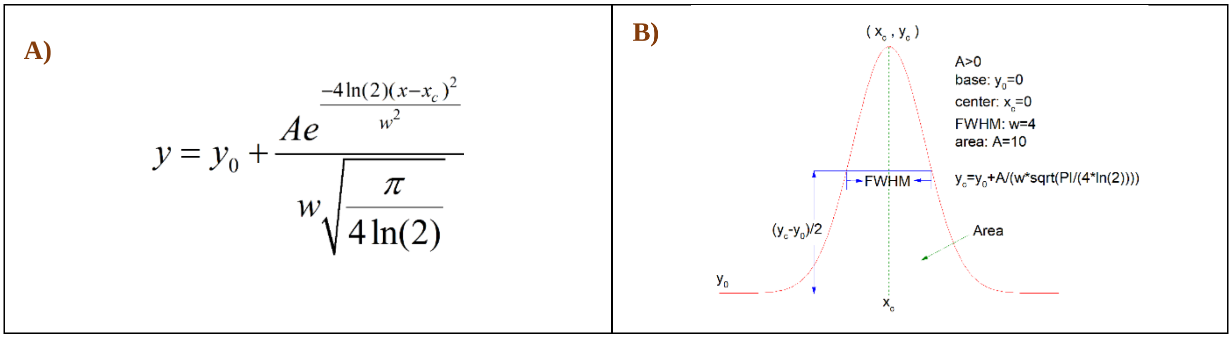

A)

$$y = y_0 + \frac{Ae^{\frac{-4\ln(2)(x-x_c)^2}{w^2}}}{w\sqrt{\frac{\pi}{4\ln(2)}}}$$

Fig. 14. A) The Gaussian formula and B) visual meaning of each parameter.

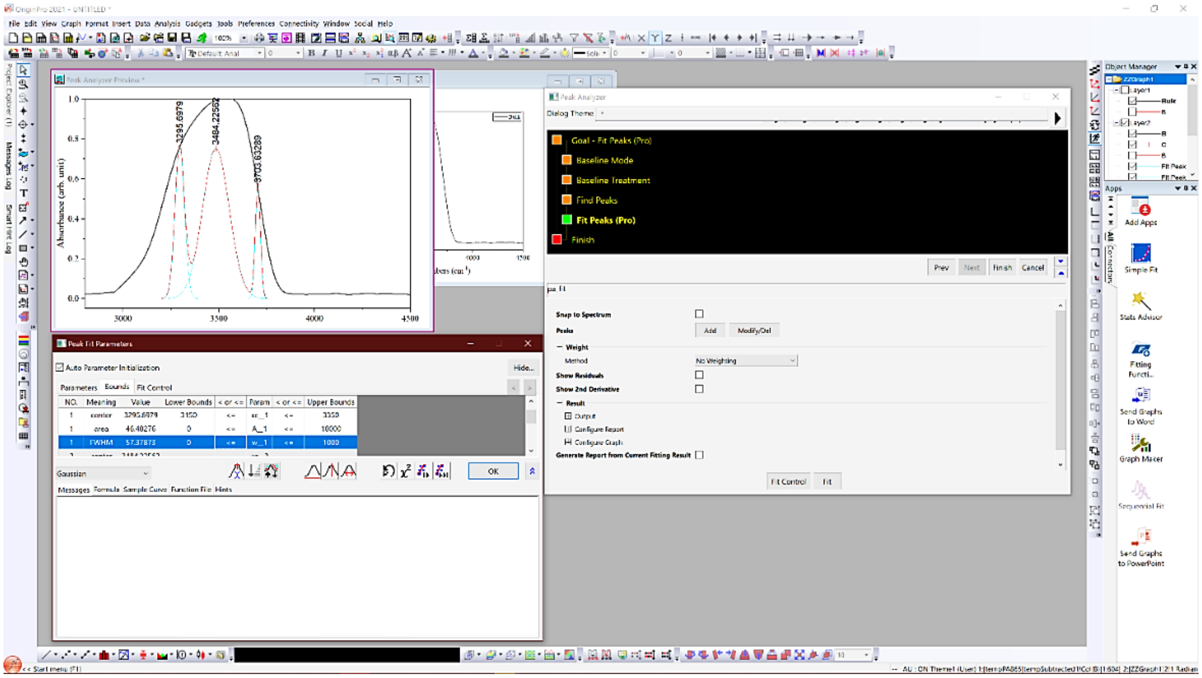

Snap to Spectrum ☐

Weight — Method: No Weighting

Show Residuals ☐

Show 2nd Derivative ☐

Generate Report from Current Fitting Result ☐

☑ Auto Parameter Initialization

NO.	Meaning	Value	Lower Bounds	< or <=	Param	< or <=	Upper Bounds
1	center	3295.6979	3150	<=	xc_1	<=	3350
1	area	46.40276	0	<=	A_1	<=	10000
1	FWHM	57.37873	0	<=	w_1	<=	1000

Gaussian

Fig. 15. Defining the specific limitations on key parameters including the main peak position, peak area, and full width at half maximum (FWHM).

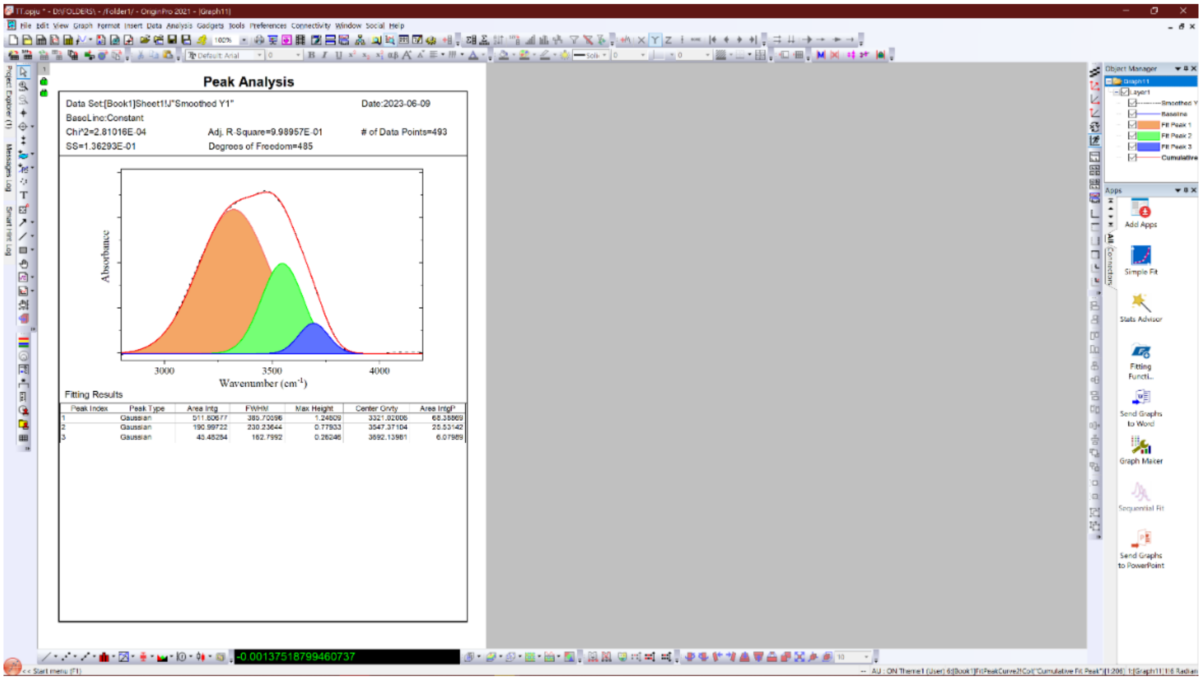

Peak Analysis

Data Set:[Book1]Sheet1!J"Smoothed Y1" Date:2023-06-09

BaseLine:Constant

Chi^2=2.81016E-04 Adj. R-Square=9.98957E-01 # of Data Points=493

SS=1.36293E-01 Degrees of Freedom=485

Fitting Results

Peak Index	Peak Type	Area Intg	FWHM	Max Height	Center Grvty	Area IntgP
1	Gaussian	511.80677	385.70096	1.24809	3321.02006	68.38869
2	Gaussian	190.99722	230.23644	0.77933	3547.37104	25.53142
3	Gaussian	45.48284	162.7992	0.26246	3692.13981	6.07989

Fig. 16. The final fitting model with three Gaussian sub-bands corresponding to water molecules with different H-bonds connectivity.

Appendix D: NMF and PCA analysis

In this study, we utilized a statistical technique known as non-negative matrix factorization (NMF) and principal component analysis (PCA) to effectively reduce the dimensionality of the dataset. By employing multivariate analysis, we aimed to investigate and identify different components present within the FTIR and Raman scattering hyperspectral data, while ensuring the preservation of maximum information.

To perform the NMF and PCA analysis, we implemented a Python v.3.11.1© script/algorithm using the Jupyter Notebook platform. This script was developed by Raoul Missodey during his Master-1 internship at CEMHTI, CNRS, Orléans. It offers a comprehensive solution for conducting the NMF and PCA analysis and enhancing the interpretability of the results. For convenient access to the Python code of this script, kindly follow the provided links: [https://github.com/CEMHTI/Raman_Analysis]
[https://github.com/CEMHTI/Raman_Analysis/blob/main/IR_data_analysis.ipynb].

This will allow you to explore and utilize the code for your own analysis or further research.

Appendix E: Mie scattering correction

In the main text (please find section 4.1.2.2), we have discussed the strong wavelength dependency of Mie scattering, which occurs when the size of the scatterer matches the magnitude of the wavelength. In the case of the bubble, both the bubble's radius and the IR radiation's wavelength are on a micrometer scale, making it reasonable to assume the presence of Mie scattering. Mie scattering is commonly used to describe scattering in perfectly spherical objects, as well as in highly symmetric systems like infinite cylinders. Therefore, it is also possible to observe Mie scattering around the cylindrical edges of the quartz in SFI-1.

It is important to note that scattering and absorption are interconnected through a Kramers-Kronig relation. This implies that molecular absorption affects how light scatters on the sample. To model this behavior, the complex refractive index is typically employed, with its imaginary part representing the absorption properties and its real part describing the optical properties of the sample. The scattering process depends on the complete complex index of refraction, revealing an intimate relationship between the absorptive and optical properties of the sample.

To address the issue of Mie scattering, we made the simplifying assumption that water spectra can be decomposed into several Gaussian curves, representing their molecular absorption spectra. In general, the OH stretch band can be attributed to the average number of hydrogen bonds in the local environment of the molecules and their connectivity. Hence, it is common to describe the stretching band using multiple Gaussian components, each associated with molecules having a specific coordination number [Brubach, J.-B., et al., The Journal of Chemical Physics, 2005. 122(18): p. 184509.]. Specifically, the OH stretching band is often decomposed into three Gaussian components [Le Caër, S., et al., Physical Chemistry Chemical Physics, 2011. 13(39): p. 17658-17666; Bergonzi, I., Mercury, L., Brubach, J. B., & Roy, P. (2014). Physical Chemistry Chemical Physics, 16(45), 24830-24840.]. Moreover, assuming a spherical sample, we solve Maxwell's equations to estimate the loss of intensity as infrared radiation transmits through the sample. This loss of intensity is a result of both molecular absorption and scattering, which are influenced by the complex refractive index.

By solving Maxwell's equations and obtaining the magnetic and electric fields, we can determine the measured loss of intensity by integrating the Poynting vector over all angles except those pointing towards the detector. This integral covers all solid angles except for those included in the numerical aperture, allowing us to calculate the extinction. Taking the logarithm of the extinction yields the absorbance. Further details regarding these calculations can be found in textbooks on electrodynamics such as Bohren and Huffman's "Absorption and Scattering of Light by Small Particles" [C. F. Bohren and D. R. Huffman, Absorption and Scattering of Light by Small Particles, John Wiley & Sons, 2008].

Additionally, we employed a neural network with a structure similar to the one used in [Magnussen et al., Commun. Chem., 2022, 5, 175.]. The neural network in our study differs only in that it has a single spectral output channel and considers samples that are single spheres rather than concentric spheres. We trained the model on simulated spectral data, following the aforementioned simulation procedure. Briefly, we solve the forward problem through exact simulation and subsequently train a deep convolutional neural network (DCCN) to solve the inverse problem. This process is shown schematically in the Magnussen et al. paper.

The BioSpec team is currently developing a package for working with spectral data and scattering. For convenient access to the code of this script, please refer to the provided links: [https://github.com/BioSpecNorway/biospectools].

They are actively working towards implementing a correction method for Mie-scattered spectra using the Quasar software©.

Appendix F: Phyton code for converting the IR-based information to the thermodynamic properties

To convert the IR-based information into thermodynamic properties, we typically follow a series of processing steps. The first step involves preparing the raw IR data for analysis. This includes several procedures such as smoothing the data to remove noise, normalizing the spectra, performing baseline correction, removing interference fringes, and applying Mie scattering correction if necessary. These steps ensure that the data is clean and ready for further analysis.

Once the data is processed, we can focus on specific features within the IR spectra. For example, in the case of water spectra, we are interested in the OH stretching band. To analyze this band, we decompose it into three sub-bands, allowing us to extract valuable information about the molecular fraction and the main peak position (expressed in wavenumber, cm^{-1}). These parameters are crucial for calculating the Gibbs free energy changes associated with the system under study. For other bands in the FTIR water spectrum that are not directly measured in this study, we utilize reference values from previously published work [Bergonzi, I., et al., Physical Chemistry Chemical Physics, 2014. 16(45): p. 24830-24840]. This reference values provide us with a basis for comparison and enable us to determine the thermodynamic properties associated with those specific bands. By combining the processed data, the analysis of the OH stretching band, and the reference values for other bands, we can proceed to calculate thermodynamic property such as Gibbs free energy changes. Fig 17. shows the flowchart of the algorithm, which we employed for converting the infrared-based information to thermodynamic properties.

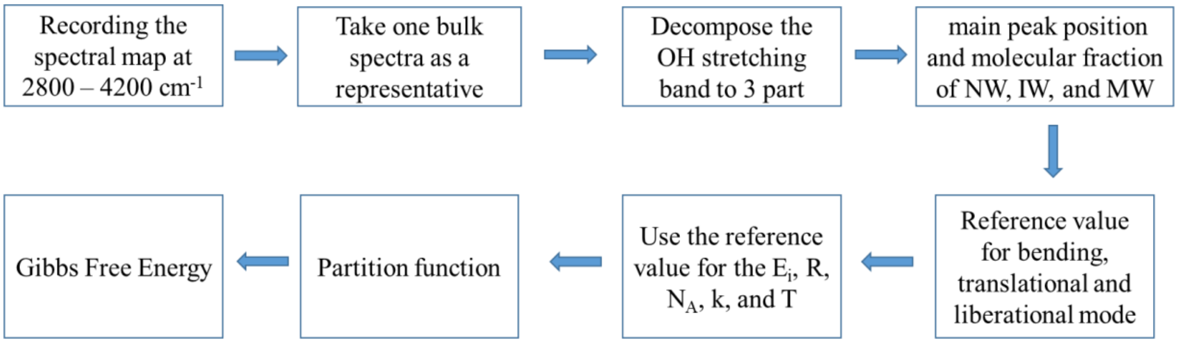

Fig. 17. The flowchart of the Python script for calculating the Gibbs free energy from the infrared-based information.

Now, we have a better understanding of the overall process, we can move on to the Python code implementation for converting the IR-based information to thermodynamic properties:

```
import numpy as np
import pandas as pd
import scipy.constants as spc

vi_b= pd.read_excel (r'C:\Users\R min\Desktop\PYCode\\vi_bending.xlsx')
vi_s= pd.read_excel (r'C:\Users\R min\Desktop\PYCode\\vi_stretching.xlsx')
vi_t= pd.read_excel (r'C:\Users\R min\Desktop\PYCode\\vi_translational.xlsx')
vi_l= pd.read_excel (r'C:\Users\R min\Desktop\PYCode\\vi_libration.xlsx')
x_frac=pd.read_excel (r'C:\Users\R min\Desktop\PYCode\\molFraction.xlsx')

h=spc.h
k=spc.Boltzmann
c=2.99792458*(10**10)
planck=h*3*(10**10)
Vi_b=np.array(vi_b['Vi_b'])
Vi_t=np.array(vi_t['gauss_1'])
Vi_l=vi_l['gauss_2']
T=np.array(vi_b['T'])
Vi_s=vi_s.iloc[:,1:4]
molfrac=x_frac.iloc[:,1:4]
E=[0,23.3,46.6]
fi_inter=((1-np.exp(-(planck*Vi_t)/(k*T)))**(-3))*((1-np.exp(-(planck*Vi_l)/(k*T)))**(-3))

fi_intra=[]
for i in range(0,3):
    fi=((1-np.exp(-(planck*Vi_b)/(k*T)))**(-3))*((1-np.exp(-(planck*Vi_s.iloc[:,i])/(k*T)))**(-3))
    fi_intra.append(fi)
```

```
Pi_inter=[]
for i in range(0,3):
    ss=(molfrac.iloc[:,i]*spc.Avogadro)*np.log(fi_inter*np.exp(-E[i]/spc.R/T))
    Pi_inter.append(ss)

Pi_inter_final=Pi_inter[:][0]+Pi_inter[:][1]+Pi_inter[:][2]

Pi_intra=[]
for i in range(0,3):
    sss=(molfrac.iloc[:,i]*spc.Avogadro)*np.log(fi_intra[:][i]*np.exp(-E[i]/spc.R/T))
    Pi_intra.append(sss)

Pi_intra_final=Pi_intra[:][0]+Pi_intra[:][1]+Pi_intra[:][2]

Pi_tot=Pi_intra_final+Pi_inter_final

g=(spc.Avogadro*((molfrac.iloc[:,0]*np.log(1/molfrac.iloc[:,0]))+(molfrac.iloc[:,1]*np.log(1/
molfrac.iloc[:,1]))+(molfrac.iloc[:,2]*np.log(1/molfrac.iloc[:,2]))))
Z=g+Pi_tot
G=-k*T*Z

test=np.array([1,2,3,4,5])
import matplotlib.pyplot as plt
plt.plot(T,G,'bo')
plt.xlabel('Temperature(Kelvin)')
plt.ylabel('Gibbs free Energy(Kj/mole)')

#Exporting Data
```

```
#to export temperature-based data
dt={'Temperature':T,'G':G}
df=pd.DataFrame(data=dt)
df.to_excel('22-55-85Python-My Int Data.xlsx')

#to export position-based data
#dt={'Position':test,'G':G}
#df=pd.DataFrame(data=dt)
#df.to_excel('Out_put.xlsx')
```

<u>You can utilize the following code to visualize the values with respect to the X and Y coordinates:</u>

```
import numpy as np
import matplotlib.pyplot as plt
import pandas as pd
import cv2 as cv
r=input('Enter r')
c=input('Enter c')
r=int(r)
c=int(c)
#r=11
#c=21
a = pd.read_excel('a-3700.xlsx')
aa = a.values
xx = aa[:,0]
yy = aa[:,1]
zz = aa[:,2]
max_x=xx.max()
min_x=xx.min()
max_y=yy.max()
min_y=yy.min()
```

```
k = zz.reshape(r,c)
y=np.zeros([int((r-1)/2),c])
for i in range(int((r-1)/2)):
    for j in range(c):
        y[i,j]=k[(r-1)-i,j]
        k[(r-1)-i,j]=k[i,j]
        k[i,j]=y[i,j]
img = cv.resize(k,None,fx=50,fy=50,interpolation=cv.INTER_CUBIC)
plt.imshow(img,cmap='jet',extent=[min_x,max_x,min_y,max_y])
plt.title('Inc. A157a')
plt.xlabel(' X Location')
plt.ylabel(' Y Location')
clb = plt.colorbar(shrink=0.65)
clb.set_label('Gibbs free energy',labelpad=10, y=0.5,rotation=-90)
plt.show()
```

Appendix G: Published Paper

(Mozhdehei A., Slodczyk A., Magnussen, E.A., Kohler A., Sandt C., Borondics F., Mercury L. (2023) Analyst 148(13), 2941-2955. https://doi.org/10.1039/d3an00138e.)

Diffraction-limited mid-infrared microspectroscopy to reveal a micron-thick interfacial water layer signature

Armin Mozhdehei[1]

Aneta Slodczyk[1,2]

Eirik Almklov Magnussen[3]

Achim Kohler[3]

Christophe Sandt[4]

Ferenc Borondics[4]

Lionel Mercury[1]

1. Institut des Sciences de la Terre d’Orléans - UMR 7327 Université d’Orléans, CNRS, BRGM - 45071 Orléans Cedex, France.

2. CEMHTI, UPR 3079 CNRS- Université d’Orléans, F-45071, Orléans, France.

3. Faculty of Science and Technology, Norwegian University of Life Sciences, Ås, Norway

4. Synchrotron Soleil, L’Orme des Merisiers Route départementale 128 – 91190 SAINT AUBIN, France

Abstract

Mid-infrared microspectroscopy is a non-invasive tool for identifying the molecular structure and chemical composition at the scale of the probe, i.e., at the scale of the beam. Consequently, investigating small objects or domains (commensurable to the wavelength) requires high-resolution measurements, even down to the diffraction limit. Herein, different protocols and machines allowing high-resolution measurements in transmission mode (aperture size (i.e., beam size) from 15×15 μm to 3×3 μm are tested using the same sample. The model sample is a closed cavity containing a water-air assemblage buried in a quartz fragment (fluid inclusion). The spectral range covers the water stretching band (3000 - 3800 cm^{-1}), whose variations are followed as a function of the distance to the cavity wall. The experiments compare the performance of one focal plane array (FPA) detector associated with a Globar source with respect to a single-element mercury cadmium telluride (MCT) detector associated with a supercontinuum laser (SCL) or a synchrotron radiation source (SRS). This work also outlines the importance of post-experiments data processing, including interference fringes removal and Mie scattering correction, to ensure that the observed spectral signatures are not related to optical aberrations. We show that the SCL and the SRS-based setups detect specific spectral features along the quartz boundary (solid surface), invisible to the FPA imaging microscope. Additionally, the broadband SCL has thus the potential to substitute at the laboratory scale the SRS for conducting diffraction-limited high-resolution measurements.

1. Introduction

Mid-infrared microspectroscopy is a well-established, non-destructive method for high-resolution measurements, which enables chemical analysis of samples, qualitatively in general or quantitatively, up to diffraction-limited spatial resolution.[1] According to Abbe equation ($d = 1.22\ \lambda / (2\ NA)$), the diffraction-limited resolution is commensurable with the wavelength (λ) of the spectral region of interest and with the numerical aperture (NA) of the applied objective. Infrared microspectroscopy down to the diffraction limit has been widely applied to study biological samples in the past 40 years. It allowed exploring the individual cells for revealing the damage mechanisms and modification of protein structure,[2, 3] diagnosing diseases,[4-8] studying microbiology and bacteria,[9-13] biochemical and biophysical modification processes,[14-19] and variation of chemical composition.[20-23] In all that, working at the diffraction limit was turned to downscale at the size of the individual biological object. Furthermore, this technique has been used in material science to investigate the charge dynamics in a single atomic layer of graphite,[24, 25] in food industry for exploring the modification of protein structure,[26-28] in astrophysics to probe the local geochemical conditions during aqueous alteration on the asteroid,[29] and in geoscience to map the distributions of organic matter, chemicals and minerals on a micrometer scale in geological samples surface.[30-34] In these studies, the objective was to reach an spatial resolution commensurable to the chemical distribution or to the heterogeneity in a material. More recently, in earth science and porous media, our group started using the high-resolution infrared transmission microspectroscopy to explore the water behavior at a solid-liquid interface.[35] Probing interfaces is usually done through nonlinear techniques such as second-harmonic generation (SHG) or sum frequency generation spectroscopy (SFG),[36-45] but we decided to apply the FTIR transmission microscopy according to classic linear spectroscopy. To increase the chance of getting specific spectral signatures near the interface, we targeted to use small beam, with size close to or at the diffraction limit.

In the mid-infrared microspectroscopy setups, optical arrangement of microscopes might have different modes, such as confocal, semi-confocal, and aperture-less. The standard confocal mode consists in positioning an aperture (mask) in front of the detector in the focal plane of the objective. The aperture defines the beam size, creating a diffraction pattern that limits the actual spatial resolution. Some studies have shown that the higher-order diffraction was limited by utilizing two apertures, the first between the sample and the detector and the second between the IR source and the sample, called dual confocal mode.[46, 47] The dual confocal configuration allows the beam to be focused on the sample while eliminating most of the diffraction pattern, but it incurs tremendous photon losses degrading the signal-to-noise ratio (SNR).[47-50] There is a strong dependency between spatial resolution, aperture size (field of view), NA of the objective, SNR, and acquisition time (number of scans). The final beam size and then the best spatial resolution achievable by a given equipment result from combining all these factors.[51] In this way, a bigger aperture size is suggested for acquiring the hyperspectral data with high SNR at a shorter acquisition time. However, spatial resolution moves away from the diffraction limit.

In order to record high-resolution measurements down to the diffraction limit, an IR source with high brilliance and collimation is required. Generally, the classical mid-infrared microspectroscopy setup exploits thermal emitters (silicon carbide—Globar). In many studies, a Globar source works properly down to an aperture of around 15×15 µm; below this value, the SNR of the recorded spectrum decreases because of the low photon count.[52-55] Since the Globar emission is not directional, most radiation is lost in all directions, and only a small fraction is collected efficiently in the microscope optics. Using a collimated infrared source such as an infrared laser or a synchrotron radiation source (SRS) allows for easier and more efficient collimation in the microscope optics and reduces photon losses.[53-55]

SRS use the property of charged particles that lose kinetic energy by emitting highly directional photon beams (emission of 'Bremsstrahlung' or 'braking radiation') when the particles are first accelerated at relativistic speeds and deviated in a magnetic field. Though a SRS can emit from the microwave to X-ray spectral regions, the Bremsstrahlung emission has several interesting properties, specifically for infrared microscopy: it covers an ultra-broadband spectral range from the Terahertz (mm wavelengths) to the near-infrared (1 µm wavelength), and it can be efficiently collected and focused in microscope optics thanks to its small emission angle. This last feature makes the SRS a tool of choice to perform high-resolution mid-infrared microspectroscopy measurements. They allow to achieve the diffraction-limited spatial resolution (aperture size 3×3 µm) over the 3.33-2.63 µm range related to the OH stretching band of water (following the Abbe equation, the diffraction limit is 2.53 µm in the case of the 2.7 µm wavelength).[35, 56-58] Meanwhile, owing to the recent development of infrared laser technology, the quantum cascade lasers (QCL) and supercontinuum generation of lasers (SCL) have been employed as an alternative high-brilliance infrared radiation source.[51, 56, 59-64] QCL has enough power and brilliance to exploit an aperture size smaller than the wavelength of radiation and therefore perform high spatial resolution measurements.[65, 66] However, QCL are discrete bandwidth sources, and so were not adapted to our study. SCL combines the primary benefits of a synchrotron light source, namely a high brilliance, high collimation, and diffraction-limited spatial resolution with broader bandwidth than the QCL in a compact structure. Obviously, the SCL spectral bandwidth is still limited compared to the ultra-broadband synchrotron sources.

Most mid-infrared microspectroscopy setups employ confocal microscopes and single-element mercury cadmium telluride (MCT) detectors. In this configuration, the hyperspectral maps are acquired via point-by-point measurements. However, another type of detector called focal plane array (FPA) comprises multiple small detector components organized in a two-dimensional grid on a focal plane. FPA-based systems produce high-definition spectral images (definition being the number of pixels in the image). Each pixel corresponds to the projected region of the sample and represents a distinct, full infrared spectrum.[67-70]

This paper aims to compare the efficiency of the mid-infrared microspectroscopy setups to deal with the interfacial water layer signatures in the light of previous synchrotron-based measurements revealing that liquid water can adopt specific infrared signatures along the water-quartz interfaces within a micron-thick layer.[35] The test sample is an intra-mineral cavity, buried inside a quartz crystal with sharp solid walls, and containing a liquid-air mixture in a totally closed environment. The quartz fragment was double-side polished down to a 19±1 µm thickness, and the cavity is located 4 µm beneath the top surface. This object is commonly called a fluid inclusion in Earth sciences, and offers optically sharp liquid-solid and liquid-air interfaces. Characterizing and quantifying the interfacial behavior requires recording mid-infrared transmission spectra at micron-scale in the OH stretching range of water (from 3000 to 3800 cm^{-1}) along precise and reproducible locations. The OH stretching band is very sensitive to changes in the network of hydrogen bonds among the water molecules.[71] The frequency of vibration of the stretching mode is commonly linked to the distance between the two oxygen atoms of the O-H···O bond.[72, 73] As a result, it is possible to attribute an average length of the hydrogen bond to each vibration frequency.

To explore the particular behavior of liquid water near the interfaces, three terms will be used in this study: “normal water,” “bulk water,” and “interfacial water.” Normal water corresponds to water not located inside any closed media. Bulk water refers to the water located in the middle of a synthetic fluid inclusion, far away from any solid-liquid interface. Interfacial water is defined as water within a thick layer along a solid wall.

Since the interfacial signature may be modified over a sub-micron layer from the solid surface,[74, 75] we need to perform the high-resolution measurements at the diffraction limit with as small as possible beam size regarding the SNR. In this way, four different experimental setups, based on three different infrared sources (Globar, SCL, and SRS), two optical arrangements (confocal and apertureless), and two detectors (MCT and FPA), are employed. Then, the hyperspectral data recorded with each experimental setup are compared in terms of SNR and spectral profiles (peak shape and position).

2. Material and Methods

2.1. Synthetic fluid inclusion as the case study

A series of microcavities in various crystalline hosts, the so-called fluid inclusions, are studied in our group. Their major advantages are: (i) their total closeness, (ii) the smoothness of the inner walls, (iii) often, the mineralogical equilibrium shape, evidenced by the negative crystal shape. Along the P-T conditions, liquid (water or solution) of known composition has a constant total volume, and follows either the monovariant saturation curve or the isochoric curve. The presence of the bubble is a chance to study the liquid-vapor interface, which is known to be hydrophobic.

For the present study, we used synthetic fluid inclusion (SFI), which was produced in a solid quartz crystal by hydrothermal synthesis.[35, 76] The quartz was chosen as a hosting mineral since it is poorly twinned, poorly soluble in saline solutions, and transparent in a wide range of electromagnetic radiation. The transparency is a crucial property for micro-FTIR measurements performed in the transmission mode.

Figure 1 illustrates the shape of the chosen SFI, which is a closed pore with constant composition and well-defined solid-liquid and liquid-gas interfaces. This geometry provides an opportunity to record the absorption signature of water and quartz at accurate positioning and capture any underlying mechanism existing at the frontiers between the two phases (interphase domain). As shown in Figure 1A, there are three different phases in the fluid inclusion: solid (quartz), liquid (water), and gas (bubble of saturated water vapor). The length, width, and depth of the SFI are 60, 20, and 5 µm, respectively. The diameter of the bubble is equal to 10µm, and its depth is 5µm. X-ray tomography measurements with sub-micron accuracy confirm the planar shape of the fluid inclusion and its dimension (Figure 1B).[35] It should be noted that all the mid-infrared microspectroscopy experiments are conducted with particular attention to the interfacial behavior of water located near the quartz boundary.

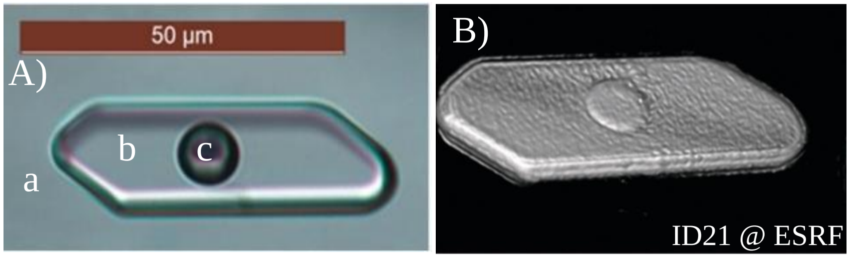

Figure 1. A) Micrographic image of the synthetic fluid inclusion including three different phases: a) solid (quartz), b) bulk water, and c) gas (bubble of saturated water vapor). B) X-ray tomography image of SFI at 0.5 µm spatial resolution (ID21 beamline, ESRF).[35]

2.2. Experimental setups and conditions

Table 1 shows four different FTIR setups employed to explore the interfacial signature of water near the quartz boundary (water-solid interface) in the transmission mode. In setup I, the Globar source was used with an FPA detector and an apertureless microscope. In setups II, III, and IV, we compared three infrared sources: Globar, SCL, and the SRS, respectively, with the same MCT detector and confocal microscope. The confocal geometry was obtained using the same Continuµm microscope which takes advantage of the catoptric design of the Schwarzschild objectives. They create a central obscuring of the incident beam below the primary mirror, a shadow, which prevents the radiation to collect most of the information outside the focal plane. The confocal arrangement is obtained by coupling that shadow with a special optical configuration called 'single aperture dual path mode.' [46, 77] This mode uses a single aperture, and confocality is obtained by passing the IR beam twice through it, once before the sample and once after crossing it. Actually, in transmission geometry, the shadow is present above and below the specimen placed at the confocal plan. This configuration allows confocal measurement, reduces diffraction, and improves X, Y, and Z spatial resolutions.[46, 77] However, as the radiation crosses all the sample, we cannot exclude a contribution of the whole volume of water into the recorded signal in various, but likely small, proportions.

The main differences between the sources were their brilliance and collimation, which allowed us to obtain a high SNR (Table 1) at various beam sizes (from 15×15 to 3×3 µm). Experiments using setups I and IV were conducted at the SMIS beamline at the SOLEIL Synchrotron facility (Gif sur Yvette, France), whereas those based on setups II and III were performed at the Earth Sciences Institute of Orléans, ISTO (Orléans, France).

During all the mid-infrared microspectroscopy experiments (Table 1), the spectrum of water in the fluid inclusion was recorded in the OH stretching range. This is because the quartz cut-off occurred at the wavenumbers below 2000 cm^{-1}; consequently, all low-wavenumber features were masked by the quartz absorption. The background spectrum was recorded through the surrounding quartz matrix before each set of spectra, to remove the effects of any changes in atmospheric CO2 and water vapor. All spectra were recorded in transmission mode at 8 cm^{-1} spectral resolution with 256 scans. All spectra of bulk and near the interface, acquired with the four setups, are shown after processing, including baseline correction (by subtracting a linear baseline in the 2800 - 4200 cm^{-1}) and normalization using OriginPro v.2021 software. Moreover, the FFT filter method with 15-20 points of window was employed by using OriginPro v.2021 software for smoothing the bulk water spectra. In the case of the spectra recorded by setups III and IV, additional processing methods, such as interference fringe removal and Mie-scattering correction, were done by implementing an algorithm in Igor Pro 9.0 software and deep learning-based modelling, respectively. For the interference fringe removal, the method illustrated in Ref.[78], and for Mie-scattering correction, the method presented in Ref.[79] were applied to the raw spectra as described below. The SNR was calculated similarly to the method applied in [Ref. [56, 80]] using the following equations:

$$\mathrm{SNR}=\sqrt{n}\times\frac{S_{average}}{\sigma}=\sqrt{n}\times\frac{1}{\mathrm{RMS}}$$

Where n is the number of scans, S_average is average absorbance value in the chosen spectral range, σ is standard deviation, corresponding to the differences between the highest and lowest absorbance value in the chosen spectral range, and RMS is root mean square of noise level.

In the case of setups II, III and IV, the 4000-4200 cm^{-1} spectral range, where no specific absorption peaks are present, was consider in the calculations. Exceptionally, for setup I, because of reduced spectral range available, the 2400-2600 cm^{-1} range was chosen.

Table 1. The detailed information of four FTIR experimental setups employed for recording the interfacial signature of water near the quartz boundary (water-solid interface) in transmission mode.

Setup	**IR source**	**Spectrometer**	**Microscope**	**Microscope optical arrangement**	**Detector**	**The smallest beam size**	**Spectral range (cm^{-1})**	**Signal -to- noise ratio**
I	Globar	Cary 670	Cary 620 (Agilent)	Apertureless	Focal Plane Array (FPA)	0.65×0.65 (projected pixel size)	900-3950	241
II		Nicolet 6700	Nicolet Continuμm	Confocal (single aperture dual path mode)	Single element mercury cadmium telluride (MCT)	15×15 μm	2800-4200	358
III	Supercontinuum laser (SCL)					5×5 μm		196
IV	Synchrotron (SRS)	Nicolet 8700				3×3 μm		148

2.2.1. Setup I

The set of infrared transmission spectral images was taken on a Cary 620 series FTIR apertureless microscope (Agilent, Courtaboeuf, France) equipped with a liquid-nitrogen cooled 128×128 pixels Lancer FPA detector and coupled to a Cary 670 FTIR spectrometer using a KBr beamsplitter and a Michelson interferometer with an internal source (Globar). The microscope was equipped with a 25X objective (NA = 0.81) and matching condenser amplified by high magnification optics giving a final magnification of 62.5X. The FPA detector and the high magnification optics provide the theoretical projected pixel size of 0.65×0.65 μm and a field of vision of 84×84 μm.

2.2.2. Setup II

Setups II was based on a Continuμm microscope coupled to a Nicolet 6700 FTIR spectrometer (Thermo Fisher Scientific, USA) with an internal source (Globar). The microscope was equipped with liquid-nitrogen cooled 50 μm MCT detector, a 32X infinity-corrected Schwarzschild type objective (NA = 0.65, WD = 7 mm, allowing a maximum beam size of 50×50 μm), and a matching 32X condenser that worked in the confocal mode. Herein, the Continuμm microscope uses the 'single aperture dual path mode' to obtain a confocal geometry. The minimum beam size acquired by this setup, is limited by the achievable SNR and the light transmittance value, is equal to 15×15 μm.

2.2.3. Setup III

Setup III was based on setup II and had the same configuration except for the IR source. In this setup, the unpolarized supercontinuum laser (Coverage®, Novae, Limoges, France) was employed as an infrared source.[64, 81] Coverage® is a turn-key supercontinuum source that emits a continuous spectrum from 1.9 μm up to 4.0 μm (5260 to 2560 cm^{-1}) in the LP01 emission mode. The very high brilliance associated with the collimated laser, high output power (>1.5W), and average spectral power density (up to 0.5 mW/nm) make this all-fiber integrated laser a suitable device for a wide range of micro-beam applications. Although this high-power level is needed to enable and fully use the non-linear processes in the optical fiber, it could damage optical parts, especially the aperture blades, the detector, and the sample. To avoid the potential damage, we used a reflective IR neutral density filter (ND=0.3, NDIR03A, Thorlabs) to decrease the intensity of the source. The Coverage® laser source had been coupled to the Nicolet spectrometer in the Earth Sciences Institute of Orléans, ISTO (Orléans, France) by an in-house designed optical configuration. Due to the high brilliance and collimation of this laser source, an aperture size of 5×5 μm2 has been reached with a high SNR. The hyperspectral data (rectangular and linear maps) of the SFI were recorded with 2 μm and 1 μm step sizes (smaller than the beam size), respectively.

2.2.4. Setup IV

The mid-infrared microspectroscopy setup in the SMIS beamline was equipped with the same Continuμm microscope as the setup II and III coupled to a Nicolet 8700 FTIR spectrometer (Thermo Fisher Scientific, USA). For the infrared source, synchrotron edge radiation from a bending magnet at the SMIS beamline of the SOLEIL Synchrotron Facility was used at the SMIS 2 branch. During the beamtime, the synchrotron emitted at a constant current of 500 mA.[49, 82] The edge radiation is mainly circularly polarized, but the beam also contains an undefined proportion of bending radiation, which is linearly polarized. The synchrotron radiation is emitted with an angular dependence; longer wavelengths are emitted at higher angles. This may result in chromatic aberrations, especially through high refractive index or birefringent materials. Quartz is a slightly birefringent crystal but the fragment was cut perpendicular to the c axis, so that no effect is expected. Also, the change in the refractive index from quartz to water (and back) is quite limited. Consequently, we expect no chromatic aberrations for the synchrotron measurements.

Due to the high quality (in terms of brilliance and collimation) of the radiation source, an aperture size of 3×3 μm was achieved. This IR beam approached the diffraction limit, which is 2.53 μm at 2.7 μm wavelength (using Abbe equation). For recording the spectral rectangular and linear maps of SFI, the step size was defined as 2 μm and 1 μm, respectively.

3. Results

3.1. Normal, bulk, and interfacial behavior of water

Figure 2 compares the absorption spectra of the normal and bulk water. The spectrum of normal water was recorded on a water film with a thickness of about 1 μm deposited between two CaF2 windows (13 mm x 2 mm) to avoid any signal saturation. Figure 2 shows the differences between the OH stretching band profile characteristics of normal and bulk water after normalization. As shown, the normal water has a narrower peak (centered around 3400 cm^{-1}) than the bulk water. It is worth noting that the spectra are not saturated, i.e., the raw absorbance values never exceed 1.3 (arb. units), and the transmittance value is 5% at minimum. However, even if this positive value guarantees that the spectrum expresses the IR absorbance dynamics of liquid water, it is small enough to give birth to the small parasitic peaks observed at the top of the OH-stretching band. To avoid altering the spectra with this artefact, while keeping the full meaning of the spectra shapes, the FFT filter method (OriginPro v.2021 software) with 15-20 points within the window was employed to smooth all the spectra affected, namely bulk and normal water.

The spectrum of bulk water recorded in the middle of fluid inclusion is considered as the reference spectral signature of water in this study. Namely, its spectral profile (peak shape and position) will be carefully compared to other spectra recorded along the solid-liquid interface as a function of distance from the quartz boundary. The setup configurations (Table 1) will be evaluated based on their potential to capture the interface signature, which is defined as an additional band appearing in the OH stretching region between 3650 and 3750 cm^{-1}.

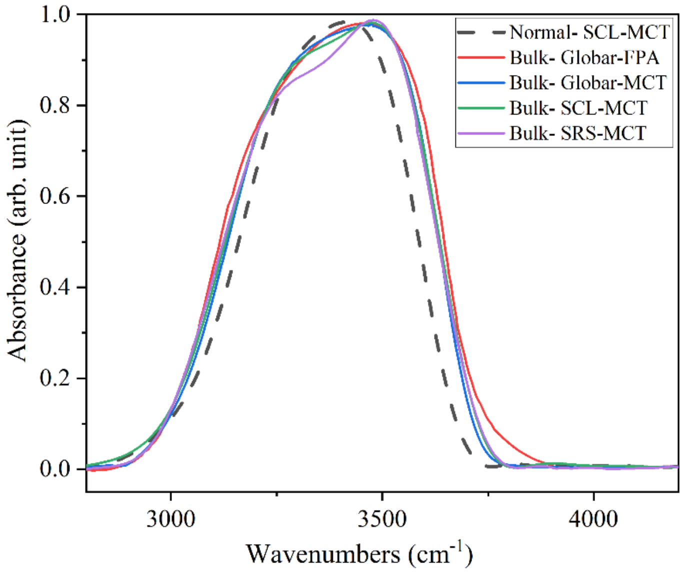

Figure 2. The comparison of the mid-infrared absorption spectra characteristic of normal water (not located inside the fluid inclusion or any closed media) and of bulk water (water located in the center of SFI (micrometric closed media).

Figure 3 compares the average/representative spectra of the OH stretching band recorded in the middle of SFI (bulk) and near the quartz-water interface using four different experimental setups. Further on, Figure 4 demonstrates that the band shapes and the absorbance values change as a function of the beam location in the SFI, i.e., from the middle (bulk) to the edge (interface). In Figure 4, by showing the series of vertical linear maps across the SFI, the characteristic spectra of quartz, quartz-water interface, and bulk water can be well distinguished.

Setups III and IV, with aperture sizes of 5×5 µm and 3×3 µm, respectively, revealed the presence of the sharp deformation of the water spectrum at ca. 3700 cm^{-1} when approaching the interface. This spectral feature is similar to that previously detected in a water layer within one micrometer of a siloxane-dominated quartz wall.[35] On the contrary, this interface signature of water cannot be recorded with setup I or with setup II. Consequently, the SCL and SRS-based setups (Figures 3C and D) allowed us to record the interfacial behavior up to 1 µm far from the quartz surface on both sides (symmetric condition). This result proved that exploiting the beam down to the diffraction limit is crucial for recording the interfacial behavior of water molecules.

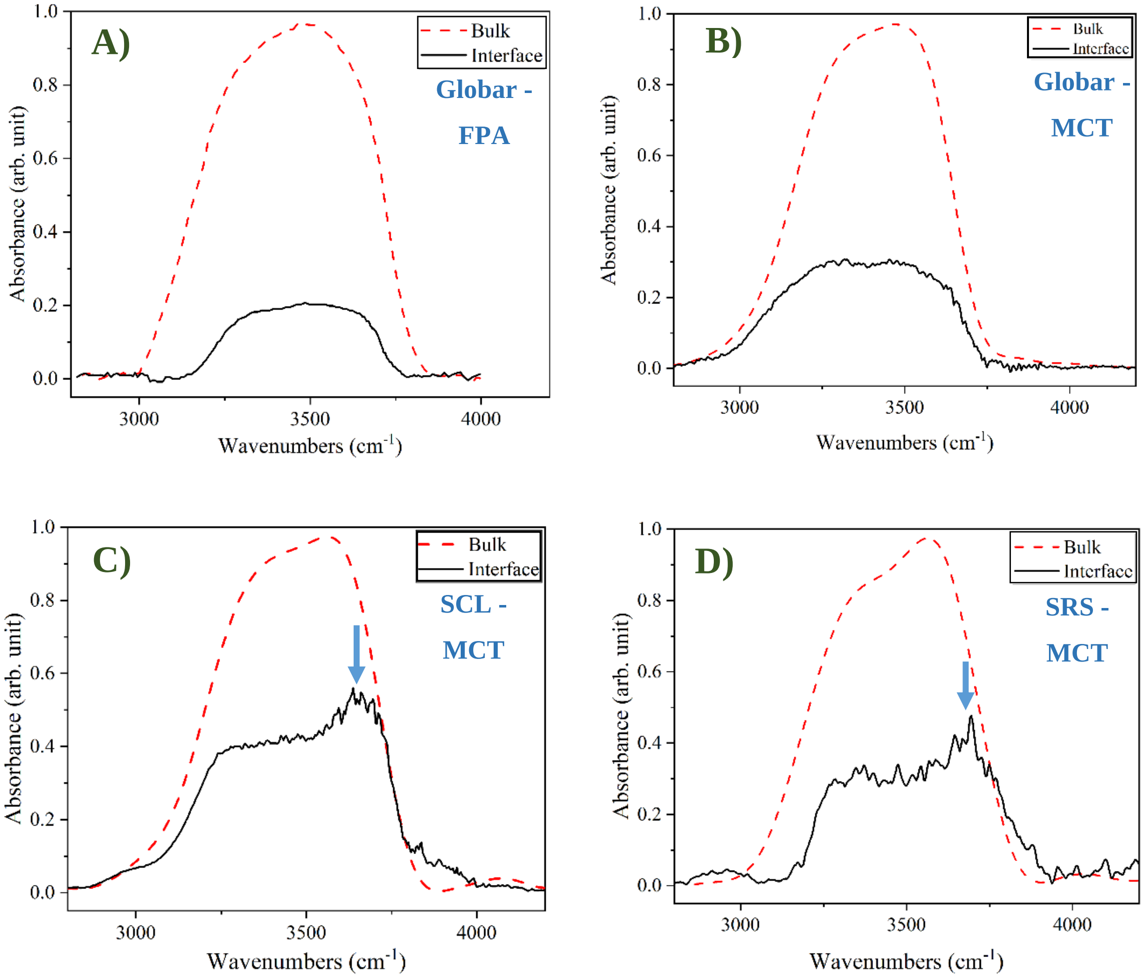

Figure 3. The representative mid-infrared spectra of bulk and interface water (at the quartz boundary) using A) setup I, B) setup II, C) setup III, and D) setup IV. The spectra were normalized and baseline corrected. The arrows show the interfacial signature of water recording with setups III and IV.

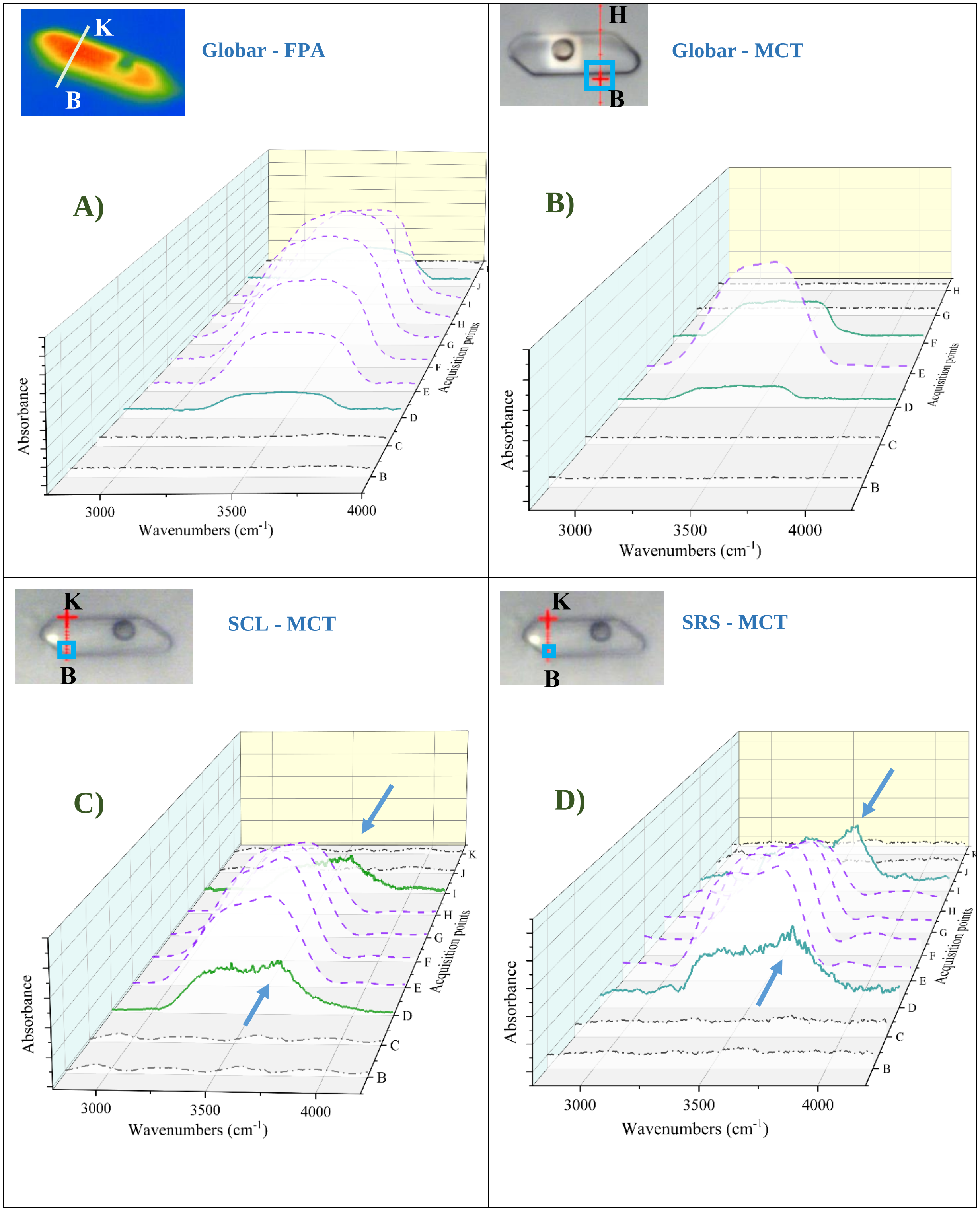

Figure 4. The variation of OH stretching band recorded across the SFI (from point B to point H or K) with A) setup I (aperture-less), B) setup II, C) setup III, and D) setup IV. Black lines (dash-dot line) correspond to quartz, green (solid line) to the near liquid-solid interface, and purple (dash line) to bulk behavior. The blue squares in panels B, C, and D correspond to the aperture size.

3.2. Data processing

The collimation of infrared radiation emerging from a synchrotron and supercontinuum laser offers many significant benefits. However, from a physical point of view, the interaction between a small beam and micrometric objects can create artefacts such as interference fringes, called also sinusoidal waveform or oscillations. Their presence is detrimental since they can be at the origin of incorrect features such as peak shifts, baseline drifts, shoulders, noise, and dispersion in the final spectrum.[83] This can be more prominent when one deals with samples such as spheres or rods with sizes similar to the beam size, where Mie-type scattering may occur.[84, 85] This can significantly affect the SNR of diffraction-limited spatial resolution measurements since scattering may direct the main intensity of the beam out of the confocal aperture.

Probing samples with plane-parallel sides, such as the upper and lower quartz surface in a distance of micrometers in mid-infrared spectroscopy transmission measurements, may lead to multiple reflections of the beam and broad sinusoidal trends in baselines called interference fringes that overlay with chemical spectral features.[86, 87]

Interference fringes and Mie scattering effect are the two main features observed in the raw spectra, making them challenging to use for their analytical function.[84, 85, 88-91] Figure 5A shows a sinusoidal baseline with an almost constant period recorded in all our spectra, whereas Figure 6A shows the Mie scattering effect (large and broad undulation of the baseline c.a. 3700 cm^{-1}). The following part will discuss how these two main artifacts can be corrected.

3.2.1. Interference fringes (side-band effect)

As shown in figure 5A, the oscillations are the common physical feature in our mid-infrared microspectroscopy measurements, especially well seen in the case of setups III and IV. The period of the sinusoid can be used to compute the distance between the two semi-reflective surfaces using the following equation: $\Delta\upsilon = 1 / (2dn)$, where $\Delta\upsilon$ = the increment in wavenumber between successive interference fringes, d = thickness of the fragment, and n = refractive index of the material.[92] According to this equation, the thickness of the quartz fragment hosting the SFI can be estimated to 18 ± 1 µm, which is in good agreement with its actual thickness according to CT tomography (19 ± 1 µm).

Processing the acquired data is necessary to define and quantify the various absorbance spectrum contributions individually in the hyperspectral data. Some models allow suppressing the interference fringes in FTIR data.[86, 87, 93, 94] A modified interferogram can suppress interference fringes in the absorption/transmission spectrum by replacing the sinusoidal trend in the interferogram with a horizontal line.[95] Using the central burst to model and eliminate the side bursts is another approach to directly edit the interferogram for rectification.[96] There are other correcting methods, which take advantage of the fact that interference fringes have much lower intensity than desired spectral features; therefore, exploiting the filtering techniques either in the spectral domain, such as a series expansion of the spectrum to eliminate low-frequency terms[97] or in the Fourier domain[90] can remove the fringes. Other methods employ a partial least-squares method to eliminate interference fringes and noises.[78, 98-100]

In this study, the same procedure as Faggin and Hines was applied, which determines the amplitude and period for every fringe in the absorption spectrum.[78] This procedure first defines sharp and broad absorption features relative to the frequency of the interference fringes. Following this step, we worked on the interferogram, and the frequency of the components related to the interference fringes was identified. After isolating the remaining components with respect to their wavenumber by applying the filtering method, the interferogram was Fourier-transformed to create the pure spectrum of the interference fringes. Finally, the isolated pure interference fringes were subtracted from the original spectrum (Figure 5A). Figure 5B shows the corrected spectra after the data treatment with the software Igor 9.0 for removing the interference fringes and baseline correction with the OriginPro v.2021 (peak analyzer function).

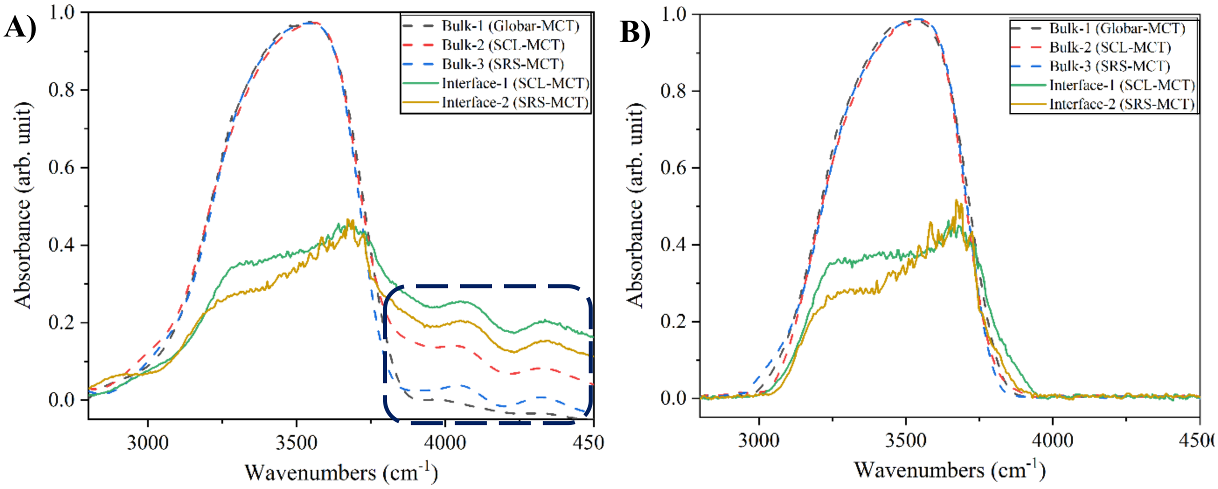

Figure 5. A) Bulk and interface mid-infrared spectra of water recorded with setups II, III, and IV showed the oscillating interference fringes. B) The corrected spectra of bulk and interface water after interference fringes removal processing according to Faggin and Hines's method.[78]

3.2.2. Mie Scattering effect

The phenomenon called Mie scattering was first studied analytically by Gustav Mie, as he presented the mathematical description of light scattering of an electromagnetic plane wave by a homogeneous sphere of arbitrary size.[101] Mohlenhoff and Romeo et al. were the first to report on Mie scattering in mid-infrared microspectroscopy of biological cells.[84, 85] Mie scattering is seen mostly as large and highly non-linear baseline fluctuations in the absorbance spectra. In addition, strong peak distortions are observed since absorption and scattering are highly entangled in Mie-type scattering, where the scattering depends on the complex refractive index whose real part determines the optical properties and the imaginary part to the absorption properties. The real and imaginary part of the refractive index are related through a Kramers-Kronig relation. Mie scattering is particularly pronounced where the surface of an object has a local curvature with a radius that is on the same order of magnitude as the wavelength of the radiation. Practical approximation theories have been established for the intricate Mie formalism, which captures many important scattering aspects.[102, 103] Generally, it is necessary to disentangle Mie scattering and other physical effects from the molecular absorption in FTIR absorbance spectra to make conclusions about the chemistry of the samples.

There are several correction methods for handling physical effects in FTIR spectroscopy. The most used is the Extended Multiplicative Signal Correction (EMSC), a flexible approach for correcting FTIR spectra, and in particular, the Mie Extinction EMSC has been used for several cases to remove Mie scattering efficiently.[104-109] Recently, deep learning-based approaches for Mie scattering correction have also been employed to successfully disentangle absorption and scattering contributions in the hyperspectral FTIR data and, in some cases, even outperform the EMSC-based algorithms.[79, 110]

As seen in Figure 6A, there is a large baseline undulation in the spectra taken in/around the bubble. To correct these spectra, we trained a scatter correction model on simulated spectral data similar manner to Ref.[79], where a deep learning model is trained to solve the IR spectroscopic inverse scattering problem. We built a deep convolutional neural network (DCNN) to infer the pure absorbance spectra as well as give an estimate of the refractive index and the radius of the curvature on which the light scatters. Then, Figure 6B shows the water spectra in/around the bubble after Mie scattering correction.

The model was trained on data created by simulating IR spectroscopic measurements. Due to the relative simplicity of the IR spectra of water, we trained our model on completely simulated absorbance spectra, where we simulated the water spectra as superpositions of three Gaussian curves. Indeed, decomposing the OH stretching region with three Gaussian components is a very classic scheme,[111, 112] providing excellent fits of the data with a minimum number of parameters (Okham's razor principle). We created the training data for our DCNN by simulating the bulk water spectra as three Gaussian sub-bands with randomly varying widths and heights and then calculating the scatter-distorted spectra for different spherical scatterers with radii between 2 and 13 microns and refractive index ratios between 0.2 and 1.3 by solving Maxwell's equations and calculating the loss of radiation as the light travels through the sample.[103, 113] Thereafter, we trained the model to solve the inverse problem and infer the absorbance spectra from the scatter-distorted spectra and the physical properties of the sample. The architecture of the DCNN is essentially the same as in Ref.[79], apart from the fact that we only have one spectral output channel since we need consider only a single sphere.

After completing training, we have a model that corrects the measured spectra, gives us the absorbance spectra, as well as predicting the radius and refractive index ratio. Thus, it can correct the scattering in the measured spectra in/around the bubble. We also used the corrected spectra and predicted physical parameters and simulate the scatter-distorted spectra to check that this is similar to the measured spectra and thereby demonstrate that our corrected spectra are viable and that Mie scattering can indeed explain the undulations seen in the measured spectra. It is crystal clear in Figure 6A that the simulated spectra are reasonably similar to the measured spectra in/around the bubble.

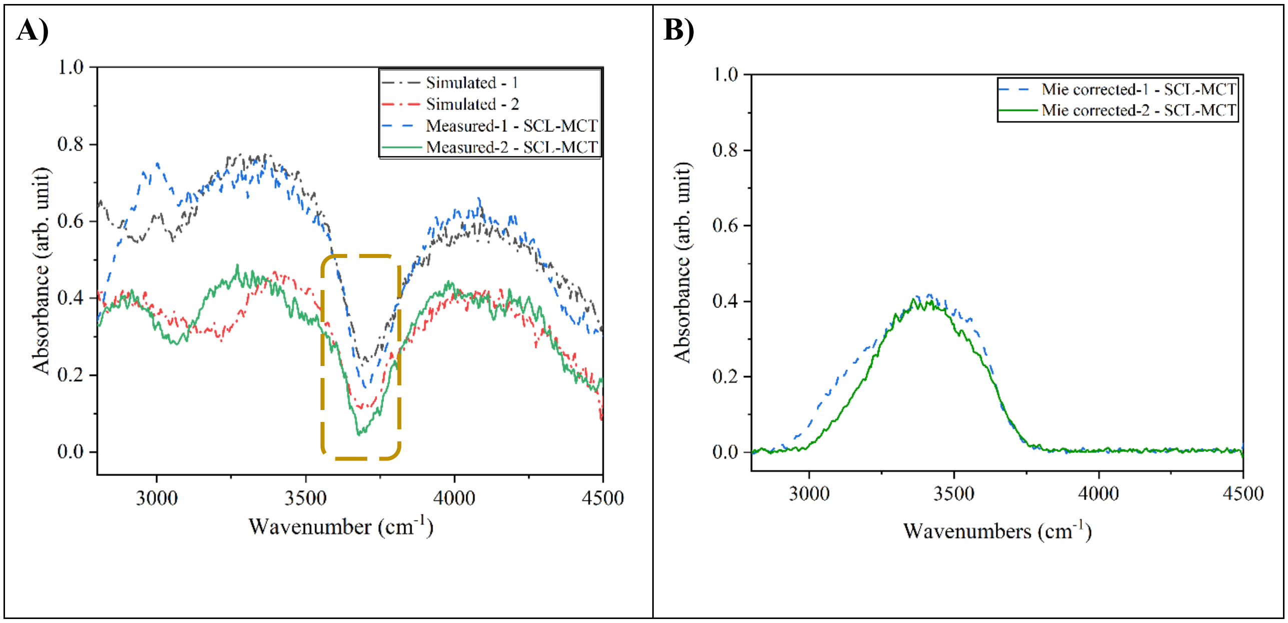

Figure 6. A) The measured and simulated mid-infrared spectra with the Mie scattering effect occurred in/around the bubble (acquired by setup III). B) The spectra after Mie-scattering correction and normalized with respect to the bulk water.

3.2.3. Final spectra after processes

Figure 7 shows the bulk and interface water spectra recorded with setups III and IV after applying the processing methods to eliminate the interference fringes and Mie scattering contributions. As can be seen, both experimental setups with diffraction-limited spatial resolution reveal evident differences between the bulk and interface as well as the presence of the particular spectral signature of water in the vicinity of the micrometric scale solid boundary. It is worth noting that the interfacial contribution is much better detectable after processing. This confirms unambiguously that the origin of the recorded interfacial signature is not related to any scattering effect.

Almost the same spectra of bulk water were recorded using setups III and IV. However, there is a slight discrepancy between the interface signatures. This difference in the spectral profile (shape) can be related to the smaller aperture size and higher spatial resolution provided by setup IV. In this setup, the integrated area of the interface spectrum and its absorption value are lower than those obtained by setup III. Also, it can be related to the geometry of the fluid inclusion, especially near the edges where the beam size is commensurate with the depth of SFI. Nevertheless, the main peak position locates in the same wavenumber (c.a. 3700 cm^{-1}) for both interface spectra (either setup III or IV).

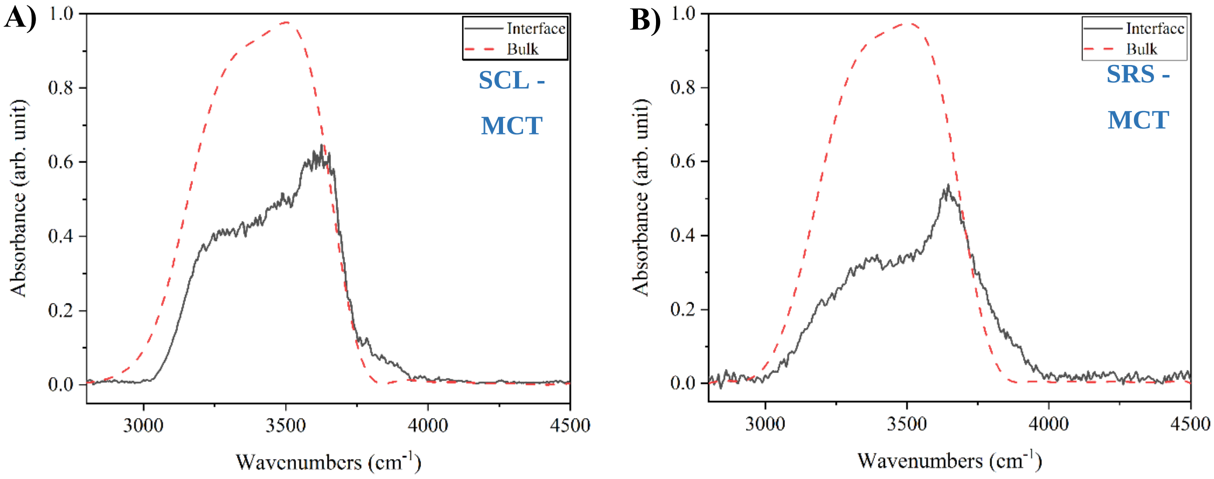

Figure 7. The average/representative mid-infrared spectra of bulk and interface water in the SFI after processing acquired by A) setup III and B) setup IV.

3.3. Hyperspectral absorption maps of SFI

3.3.1. Insight from setup III

A rastered hyperspectral map provides an opportunity to detect the interfacial effect in the SFI and compare the spectra more meticulously as a function of the beam location. Figure 8 shows the rectangular spectral map of SFI recorded with setup III in the laboratory after a few processing steps (baseline correction, normalization, and interference fringes removal). Two different absorbance distribution maps are presented with respect to the two characteristic wavenumbers: i) 3400 cm^{-1}, which corresponds to the bulk signature of water as previously shown in Figure 7A, and ii) 3700 cm^{-1} assigned to the interface signature. As shown in Figure 8, the bulk-like water spectra with maximum absorption values were observed in the middle of inclusion (far from the liquid-solid and liquid-vapor interfaces). Regarding the absorption value in bulk, this value gradually diminished toward the SFI edges, most likely because of reduced water quantity in the SFI borders.

Figure 8A shows the absorbance distribution maps before Mie scattering correction in which the interfacial behavior is observed in/around the bubble and along the quartz boundary. This is related to a large undulation detected at almost the same wavenumber as the interfacial signature (c.a. 3700 cm^{-1}) appearing in/around the bubble, which, as previously shown (Figure 6A), corresponds to the Mie scattering effect. By applying the Mie scattering correction method on all hyperspectral data, the interfacial behavior of water is observed near the quartz boundary, i.e., along the liquid-solid interface, and also around the bubble (water-air interface) (Figure 8B).

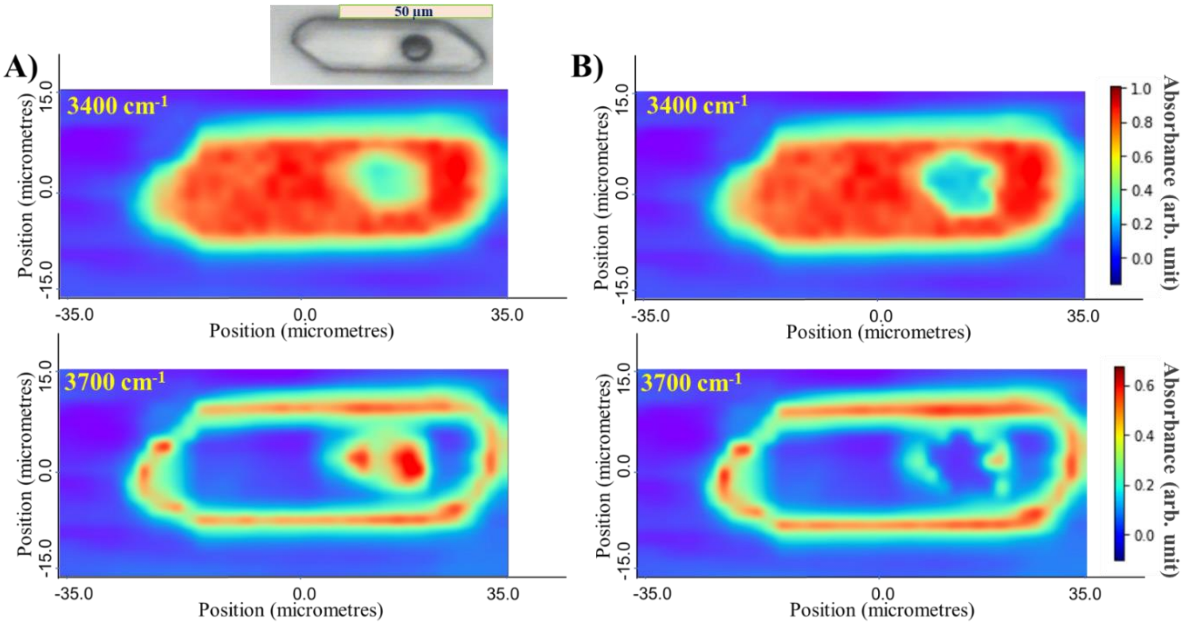

Figure 8. Hyperspectral maps of the SFI acquired by setup III showing the distribution of absorbance at two characteristic wavenumbers: 3400 cm^{-1} related to the bulk and 3700 cm^{-1} representing the interface water behavior A) before and B) after Mie scattering correction.

3.3.2. Insight from setup IV

Hyperspectral maps were also recorded using synchrotron radiation as an IR source. Because of the higher brilliance and collimation, the beam size could be reduced to 3×3 µm. With this setup, the spectral maps were taken exclusively along the half-left part of the fluid inclusion to avoid undesirable movement of the bubble. It is important to note that high energy and heat transfer of the synchrotron source caused a rapid movement of the bubble when the beam was focused on it. Since the bubble follows the beam location when getting in focus, we tried to avoid approaching too close to the bubble because such a situation significantly masks either the bulk or the interface features. Figure 9 shows the absorbance distribution maps of the half fluid inclusion after processing (baseline correction, normalization, and interference fringes removal) at the two characteristics wavenumbers representing the bulk (c.a. 3400 cm^{-1}) and interface (c.a. 3700 cm^{-1}) water behavior (as shown before in Figure 7B). The interfacial spectral signature appears very sharp due to the higher spatial resolution of this method. As can be seen, there is a good agreement between the hyperspectral maps obtained from setup IV and setup III.

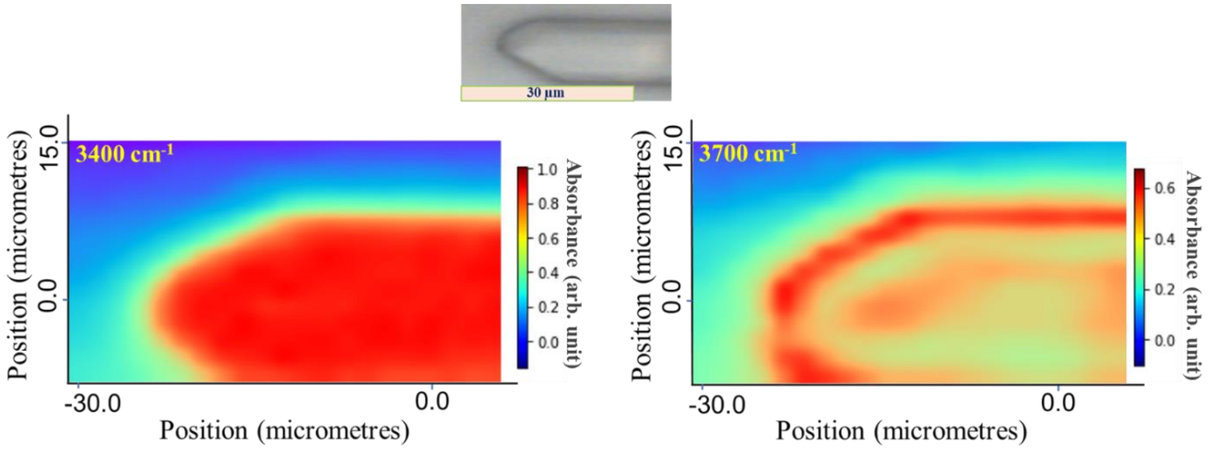

Figure 9. Hyperspectral maps of the SFI acquired by setup IV (synchrotron beam) show the absorbance distribution at two characteristic wavenumbers: 3400 cm^{-1} related to the bulk and 3700 cm^{-1} representing the interface.

4. Discussion

This study aimed to test the performance of four FTIR experimental setups (Table 1) applied to SFI (trapped water inside a quartz cavity) to detect micrometer-scale interface-imprinted spectral features. According to the presented results, setup IV employing a synchrotron radiation source allowed to record the sharpest, well-resolved band near 3700 cm^{-1}, which is unambiguous evidence of the specific behavior of water near the quartz-water interface. This is related to the high spatial resolution down to the diffraction limit (equal to 2.53 µm at 2.7 µm wavelength) offered by the synchrotron source coupled to the confocal microscope. Our results are consistent with those of Bergonzi's, which revealed for the first time the specific interfacial behavior of water molecules at the micrometric scale along a solid wall.[35]

This is worth noting that almost the same results were recorded by setup III, based on the mid-infrared fiber-based supercontinuum laser that allowed to achieve beam size of 5×5 µm in the laboratory condition. These results are coherent with previous ones,[51, 56] which revealed the ability of supercontinuum laser sources to perform high-resolution micro-FTIR measurements.

In contrast, the FPA images obtained from setup I did not allow to record the interface signature accurately because the interface domain is smaller than the actual spatial resolution of the system. Nevertheless, the aperture-less microscope with the FPA detector allows substantially faster data gathering at a spatial resolution two or three times bigger than the diffraction limit. These results confirm previous experiments, which demonstrated that the FPA detector may not always be suitable for exploring the chemical or physical features at the diffraction limit.[70] This may be counterintuitive as the area on the sample covered by each detector element has a dimension below the diffraction limit. However, because of the diffraction, each detector element receives a contribution from an area bigger than the area on the sample nominally covered by each element.

The microscope aperture of a confocal microscope employing synchrotron-based radiation or a supercontinuum laser source allows to control of the spatial resolution at the diffraction limit and consequently records the interfacial signature. In the FPA detector-equipped microscope, physical apertures do not limit the IR beam illuminating region. Instead, the projected image of the unmasked IR beam on the sample is collected using an array of IR detector components; therefore, the precision of aperture-less images is highly dependent on the optical system magnification and numerical aperture.[70, 114, 115]

The experiments performed in this study demonstrate that FTIR technique applied in the diffraction limit resolution can be used to study the water behavior in the micrometric fluid inclusion. The water behavior and corresponding spectra are highly affected as a function of beam location toward the quartz and the gas bubble; however, they are partly affected by optical issues, such as interference fringes and Mie scattering. The former corresponds to the thickness of the quartz fragment, and the latter relates to the shape of the bubble. All these phenomena can overlay with chemical spectral features and may cast doubt that such signatures are a general feature which have a systematic significance for the water-solid interphase as a whole. That is why two different methods were applied to suppress these trends. After processing the data, the variation of the overall band shape has been emphasized, making clear that an additional peak at ca. 3700 cm^{-1} takes place systematically in the vicinity of the quartz boundary. The existence of two contributions at 3400 cm^{-1} and 3700 cm^{-1} can be assigned to the difference in H-bonding due to the fact that the properties of solid surface is known to alter the H-bonding structure of water at interfaces.[116-120]

As mentioned earlier, the variation in the H-bonding near the interfaces in general is commonly investigated by nonlinear vibrational spectroscopic techniques, like SHG or SFG.[36, 37] The SFG measurement on hydrophilic surfaces revealed the presence of two peaks at 3250 cm^{-1} and 3450 cm^{-1}, leading to conclude that the water network is locally ordered close to a hydrophilic solid surface.[38-40] On the contrary, the peak between 3650 and 3750 cm^{-1} can be attributed either to isolated silanol groups41 or in the case of water near to hydrophobic surface can be corresponded to free OH groups.[39, 42, 44, 45, 121] In our case, the OH stretching bands of normal and bulk water show a strong lower wavenumber component (c.a. 3400 cm^{-1}), and they do not have a shoulder at higher wavenumbers (c.a. 3700 cm^{-1}), which is coherent with previous studies.[35, 112, 122] A band detected between 3650 and 3750 cm^{-1}, visible along the quartz boundary (water-quartz interface), can be assigned to the absorption of weakly hydrogen bonded water molecules near the hydrophobic surface.[35, 123, 124] Indeed, the silica can form either a hydrophilic or hydrophobic surface with respect to the ratio of siloxane bridge (Si-O-Si) to silanol groups (Si-O-H).[125] However, we did not record the distinct peak (i.e., separated from the OH stretching band) c.a. 3700 cm^{-1} similar to SFG measurements but we observed an additional peak as a band broadening within the stretching modes of water. As a consequence, the peak is not interpreted as detecting a pure free OH (dangling OH) mode, but assigned to an enrichment of interfacial water in the less-connected water molecules. In this way of reasoning, this interfacial behavior and the disruption between the water H-bonding might be originated from an hydrophobic character of quartz and active surface forces like the hydrophobic force emanating from the surface and causing the disorganization (chaotropic effect) of water molecules,[35] over a distance that has never been recorded up to now.

5. Conclusion

In this study, the interfacial behavior of water in synthetic fluid inclusion was investigated by high-resolution mid-infrared microspectroscopy measurements in transmission mode. The OH stretching region of water molecules (3000 to 3800 cm^{-1}) was recorded with four different setups to test the potential of beam at the diffraction limit for detecting the spectral features along the interface. We observed two undesirable trends in our raw data related to interference fringes and Mie scattering. These trends can be a common problem in the case of a micrometric-scale object like fluid inclusion. We applied the filtering algorithm and deep learning-based models for the interference fringes and Mie scattering to suppress these physical effects and correct the spectra.

According to the results, two main parameters play a major role in the high-resolution mid-infrared microspectroscopy: the optical arrangement of the microscope and the infrared source. Regarding the optical arrangement of microscopes, the confocal mode with dual path single aperture configuration connected to the single-element MCT detector has a higher efficiency in terms of spatial resolution compared to the aperture-less microscope connected to the FPA detector.

After conducting the experiments with three different infrared sources (Globar, SCL, and SRS), the hyperspectral data of the synthetic fluid inclusion proved the ability of setup III based on the supercontinuum laser (aperture size = 5×5 μm), coupled to the confocal microscope, and equipped with the MCT to record the interfacial behavior of water. The interfacial behavior of water has been observed with a vibrational signature between 3650 and 3750 cm^{-1}. These high-resolution measurements revealed that the vibrational energy of water changes over a significant thickness from the quartz boundary (solid-liquid interface). The acquired data are consistent with the synchrotron measurements, which were recorded by the aperture size equal to 3×3 μm.

Therefore, the supercontinuum laser can be considered an alternative to a synchrotron source to obtain a high brilliance and collimated broadband infrared source in the MIR with a high spatial resolution. This feature can make the laser a suitable source in the mid-infrared microspectroscopy setups for conducting high-resolution measurements down to the diffraction limit, especially in the field of geoscience and porous media, where a smaller beam size than the pore size is required to record the chemical composition or physical features of the pore.

Acknowledgments

This work has received financial support from the French Agency for Research (Agence Nationale de la Recherche) through the Labex Voltaire ANR-10-LABX-100-01 and the Equipex Planex ANR-11-EQPX-36. This study benefits from the SOLEIL Synchrotron allocation n° 20211104. The authors thank Dr. Frederic Jamme and Prof. Sophie Le Caër for the insightful discussions in processing and analyzing the data. Also, we would like to express our deep gratitude toward Prof. Melissa A. Hines's for her generous help with the interference fringe correction method. Esteban Le Moing and Frédéric Savoie from ISTO's workshop are kindly thanked for their help with the house-in coupling of supercontinuum laser to FTIR spectrometer. We are finally grateful to the Editor, Nicole Pamme, and to two anonymous reviewers, who greatly helped us to improve the initial manuscript.

Reference

1. J. Katok, A. Sommer and P. L. Lang, Applied Spectroscopy Reviews, 1989, 25, 173-211.

2. C. Sandt, J. Frederick and P. Dumas, Journal of biophotonics, 2013, 6, 60-72.

3. S. Clède, C. Policar and C. Sandt, Applied Spectroscopy, 2014, 68, 113-117.

4. O. Klementieva, K. Willén, I. Martinsson, B. Israelsson, A. Engdahl, J. Cladera, P. Uvdal and G. Gouras, Nature communications, 2017, 8, 1-9.

5. C. Sandt, C. Nadaradjane, R. Richards, P. Dumas and V. Sée, Analyst, 2016, 141, 870-883.

6. W. André, C. Sandt, P. Dumas, P. Djian and G. Hoffner, Analytical Chemistry, 2013, 85, 3765-3773.

7. A. Paulus, A. Engdahl, Y. Yang, A. Boza-Serrano, S. Bachiller, L. Torres-Garcia, A. Svanbergsson, M. G. Garcia, G. K. Gouras and J.-Y. Li, International journal of molecular sciences, 2021, 22, 3430.

8. T. M. Pereira, D. M. Zezell, B. Bird, M. Miljković and M. Diem, Analyst, 2013, 138, 7094-7100.

9. J. Meneghel, S. Passot, F. Jamme, S. Lefrançois, P. Lieben, P. Dumas and F. Fonseca, Analytical and Bioanalytical Chemistry, 2020, 412, 7049-7061.

10. C. Modugno, C. Peltier, H. Simonin, L. Dujourdy, F. Capitani, C. Sandt and J.-M. Perrier-Cornet, Frontiers in Microbiology, 2020, 10, 3122.

11. M. Igisu, Y. Ueno, M. Shimojima, S. Nakashima, S. M. Awramik, H. Ohta and S. Maruyama, Precambrian Research, 2009, 173, 19-26.

12. T. C. Hazen, E. A. Dubinsky, T. Z. DeSantis, G. L. Andersen, Y. M. Piceno, N. Singh, J. K. Jansson, A. Probst, S. E. Borglin and J. L. Fortney, Science, 2010, 330, 204-208.

13. A. de Anchieta Câmara Jr, P.-A. Maréchal, R. Tourdot-Maréchal and F. Husson, Food microbiology, 2019, 79, 137-146.

14. A. Skoczen, Z. Setkowicz, K. Janeczko, C. Sandt, F. Borondics and J. Chwiej, Spectrochimica Acta Part A: Molecular and Biomolecular Spectroscopy, 2017, 184, 13-22.

15. C. Saulou, F. Jamme, L. Girbal, C. Maranges, I. Fourquaux, M. Cocaign-Bousquet, P. Dumas and M. Mercier-Bonin, Analytical and bioanalytical chemistry, 2013, 405, 2685-2697.

16. A. A. Câmara Jr, T. D. Nguyen, R. Saurel, C. Sandt, C. Peltier, L. Dujourdy and F. Husson, Frontiers in Microbiology, 2020, 11, 899.

17. T. D. Nguyen, S. Guyot, C. Pénicaud, S. Passot, C. Sandt, F. Fonseca, R. Saurel and F. Husson, Frontiers in Microbiology, 2020, 11, 1887.

18. S. Passot, J. Gautier, F. Jamme, S. Cenard, P. Dumas and F. Fonseca, Analyst, 2015, 140, 5920-5928.

19. T. Nguyen, S. Guyot, C. Pénicaud, S. Passot, C. Sandt, F. Fonseca, R. Saurel and F. Husson, Analyst, 2017, 142, 3620-3628.

20. J. P. Cain, P. L. Gassman, H. Wang and A. Laskin, Physical Chemistry Chemical Physics, 2010, 12, 5206-5218.

21. C. Gasaway, M. Mastalerz, F. Krause, C. Clarkson and C. Debuhr, Journal of Microscopy, 2017, 265, 60-72.

22. Y. Chen, L. D. Caro, M. Mastalerz, A. Schimmelmann and A. Blandón, Journal of microscopy, 2013, 249, 69-81.

23. S. Bertarione, F. Bonino, F. Cesano, S. Jain, M. Zanetti, D. Scarano and A. Zecchina, The Journal of Physical Chemistry B, 2009, 113, 10571-10574.

24. Z. Li, E. A. Henriksen, Z. Jiang, Z. Hao, M. C. Martin, P. Kim, H. L. Stormer and D. N. Basov, Nature physics, 2008, 4, 532-535.

25. Y. Zhang, T.-T. Tang, C. Girit, Z. Hao, M. C. Martin, A. Zettl, M. F. Crommie, Y. R. Shen and F. Wang, Nature, 2009, 459, 820-823.

26. T. Astruc, F. Peyrin, A. Vénien, R. Labas, M. Abrantes, P. Dumas and F. Jamme, Food chemistry, 2012, 134, 1044-1051.

27. R. Vaskoska, A. Vénien, M. Ha, J. D. White, R. R. Unnithan, T. Astruc and R. D. Warner, Food Chemistry, 2021, 343, 128544.

28. M. Motoyama, A. Vénien, O. Loison, C. Sandt, G. Watanabe, J. Sicard, K. Sasaki and T. Astruc, Food chemistry, 2018, 248, 322-329.

29. A. J. King, P. F. Schofield, N. R. Stephen, M. D. Frogley, G. Cinque and S. S. Russell, Infrared Physics & Technology, 2018, 94, 244-249.

30. A. R. Nichols and R. Wysoczanski, Chemical Geology, 2007, 242, 371-384.

31. M. K. Nieuwoudt, M. P. Simpson, M. Tobin and L. Puskar, Vibrational Spectroscopy, 2014, 75, 136-148.

32. N. Guilhaumou and P. Dumas, Oil & Gas Science and Technology, 2005, 60, 763-779.

33. Y. Chen, C. Zou, M. Mastalerz, S. Hu, C. Gasaway and X. Tao, International journal of molecular sciences, 2015, 16, 30223-30250.

34. G. Della Ventura, F. Bellatreccia, A. Marcelli, M. Cestelli Guidi, M. Piccinini, A. Cavallo and M. Piochi, Analytical and bioanalytical chemistry, 2010, 397, 2039-2049.

35. I. Bergonzi, L. Mercury, P. Simon, F. Jamme and K. Shmulovich, Physical Chemistry Chemical Physics, 2016, 18, 14874-14885.

36. E. H. Backus, J. Schaefer and M. Bonn, Angewandte Chemie International Edition, 2021, 60, 10482-10501.

37. F. Tang, T. Ohto, S. Sun, J. r. m. R. Rouxel, S. Imoto, E. H. Backus, S. Mukamel, M. Bonn and Y. Nagata, Chemical reviews, 2020, 120, 3633-3667.

38. S. Kataoka, M. C. Gurau, F. Albertorio, M. A. Holden, S.-M. Lim, R. D. Yang and P. S. Cremer, Langmuir, 2004, 20, 1662-1666.

39. Y. R. Shen and V. Ostroverkhov, Chemical reviews, 2006, 106, 1140-1154.

40. Z. Pászti and L. Guczi, Vibrational Spectroscopy, 2009, 50, 48-56.

41. L. Dalstein, E. Potapova and E. Tyrode, Physical Chemistry Chemical Physics, 2017, 19, 10343-10349.

42. E. Tyrode and J. F. Liljeblad, The Journal of Physical Chemistry C, 2013, 117, 1780-1790.

43. S. Strazdaite, J. Versluis, E. H. Backus and H. J. Bakker, The Journal of Chemical Physics, 2014, 140, 054711.

44. S. E. Sanders and P. B. Petersen, The Journal of Chemical Physics, 2019, 150, 204708.

45. O. Isaienko and E. Borguet, Langmuir, 2013, 29, 7885-7895.

46. F. Jamme, B. Lagarde, A. Giuliani, G. Garcia and L. Mercury, Journal of Physics: Conference Series, 2013, 425, 142002.

47. G. Carr, Review of Scientific Instruments, 2001, 72, 1613-1619.

48. G. Carr, Vibrational Spectroscopy, 1999, 19, 53-60.

49. P. Dumas, F. Polack, B. Lagarde, O. Chubar, J. Giorgetta and S. Lefrançois, Infrared Physics & Technology, 2006, 49, 152-160.

50. M. C. Martin, U. Schade, P. Lerch and P. Dumas, TrAC Trends in Analytical Chemistry, 2010, 29, 453-463.

51. J. Kilgus, G. Langer, K. Duswald, R. Zimmerleiter, I. Zorin, T. Berer and M. Brandstetter, Optics express, 2018, 26, 30644-30654.

52. G. Williams, Handbook of Vibrational Spectroscopy, 2006, DOI: https://doi.org/10.1002/0470027320.s0212.

53. J. Chalmers, N. Everall and M. Chesters, Analyst, 1998, 123, 579-586.

54. G. Carr, L. Miller and P. Dumas, in Biomedical Applications of Synchrotron Infrared Microspectroscopy, 2010, DOI: https://doi.org/10.1039/9781849731997-00226 pp. 226-259.

55. L. M. Miller and R. J. Smith, Vibrational spectroscopy, 2005, 38, 237-240.

56. F. Borondics, M. Jossent, C. Sandt, L. Lavoute, D. Gaponov, A. Hideur, P. Dumas and S. Février, Optica, 2018, 5, 378-381.

57. I. Lindsay, S. Valle, J. Ward, G. Stevens, M. Farries, L. Huot, C. Brooks, P. M. Moselund, R. Vinella and M. Abdalla, Optical Biopsy XIV: Toward Real-Time Spectroscopic Imaging and Diagnosis, 2016, 9703, 15-23.

58. M. J. Nasse, M. J. Walsh, E. C. Mattson, R. Reininger, A. Kajdacsy-Balla, V. Macias, R. Bhargava and C. J. Hirschmugl, Nature methods, 2011, 8, 413-416.

59. P. Bassan, M. J. Weida, J. Rowlette and P. Gardner, Analyst, 2014, 139, 3856-3859.

60. K. Yeh and R. Bhargava, Biomedical Vibrational Spectroscopy 2016: Advances in Research and Industry, 2016, 9704, 17-23.

61. I. Zorin, P. Gattinger, A. Ebner and M. Brandstetter, Optics Express, 2022, 30, 5222-5254.

62. S. Dupont, C. Petersen, J. Thøgersen, C. Agger, O. Bang and S. R. Keiding, Optics express, 2012, 20, 4887-4892.

63. C. R. Petersen, N. Prtljaga, M. Farries, J. Ward, B. Napier, G. R. Lloyd, J. Nallala, N. Stone and O. Bang, Optics letters, 2018, 43, 999-1002.

64. L. Lavoute, C. Sandt, F. Borondics, N. Ducros and S. Février, Optica Publishing Group (specialty Optical Fibers), 2016, DOI: https://doi.org/10.1364/SOF.2016.SoTu2G.5, SoTu2G. 5.

65. M. R. Kole, R. K. Reddy, M. V. Schulmerich, M. K. Gelber and R. Bhargava, Analytical chemistry, 2012, 84, 10366-10372.

66. Y.-P. Tseng, P. Bouzy, C. Pedersen, N. Stone and P. Tidemand-Lichtenberg, Biomedical Optics Express, 2018, 9, 4979-4987.

67. M. J. Hackett, S. Caine, X. Liu, T. E. May and F. Borondics, Vibrational Spectroscopy, 2015, 77, 51-59.

68. B. R. Wood, M. Kiupel and D. McNaughton, Veterinary pathology, 2014, 51, 224-237.

69. J. Nallala, M.-D. Diebold, C. Gobinet, O. Bouché, G. D. Sockalingum, O. Piot and M. Manfait, Analyst, 2014, 139, 4005-4015.

70. C. Sandt, Z. Dionnet, M. Toplak, E. Fernandez, R. Brunetto and F. Borondics, Journal of Spectral Imaging, 2019, 8.

71. S. Bratos, J.-C. Leicknam, G. Gallot and H. Ratajczak, in Ultrafast Hydrogen Bonding Dynamics and Proton Transfer Prosesses in the Condensed Phase, Springer, 2002, pp. 5-30.

72. R. Rundle and M. Parasol, The Journal of Chemical Physics, 1952, 20, 1487-1488.

73. K. Nakamoto, M. Margoshes and R. Rundle, Journal of the American Chemical Society, 1955, 77, 6480-6486.

74. V. R. Hande and S. Chakrabarty, The Journal of Physical Chemistry B, 2022, 126, 1125-1135.

75. V. R. Hande and S. Chakrabarty, Physical Chemistry Chemical Physics, 2016, 18, 21767-21779.

76. K. I. Shmulovich and C. M. Graham, Contributions to Mineralogy and Petrology, 2004, 146, 450-462.

77. D. Schiering, T. Tague Jr, J. Reffner and S. Vogel, Analusis, 2000, 28, 46-52.

78. M. F. Faggin and M. A. Hines, Review of scientific instruments, 2004, 75, 4547-4553.

79. E. A. Magnussen, B. Zimmermann, U. Blazhko, S. Dzurendova, B. Dupuy–Galet, D. Byrtusova, F. Muthreich, V. Tafintseva, K. H. Liland and K. Tøndel, Communications Chemistry, 2022, 5, 175.

80. J. P. Blitz and D. G. Klarup, Journal of chemical education, 2002, 79, 1358.

81. J. M. Dudley, G. Genty and S. Coen, Reviews of modern physics, 2006, 78, 1135.

82. G. Santoro, I. Yousef, F. Jamme, P. Dumas and G. Ellis, Review of Scientific Instruments, 2011, 82, 033710.

83. J. M. Chalmers, Handbook of vibrational spectroscopy, 2006, DOI: https://doi.org/10.1002/0470027320.s3101.

84. B. Mohlenhoff, M. Romeo, M. Diem and B. R. Wood, Biophysical journal, 2005, 88, 3635-3640.

85. A. Kohler, J. Sule-Suso, G. Sockalingum, M. Tobin, F. Bahrami, Y. Yang, J. Pijanka, P. Dumas, M. Cotte and D. Van Pittius, Applied spectroscopy, 2008, 62, 259-266.

86. T. Konevskikh, A. Ponossov, R. Blümel, R. Lukacs and A. Kohler, Analyst, 2015, 140, 3969-3980.

87. G. Azarfar, E. Aboualizadeh, N. M. Walter, S. Ratti, C. Olivieri, A. Norici, M. Nasse, A. Kohler, M. Giordano and C. J. Hirschmugl, Analyst, 2018, 143, 4674-4683.

88. A. Ibrahim, A. Predoi-Cross and P. M. Teillet, AIP Conference Proceedings, 2010, 1214, 97-99.

89. D. L. Kingsbury and P. L. Marston, JOSA, 1981, 71, 358-361.

90. A. M. Pistorius and W. J. DeGrip, Vibrational spectroscopy, 2004, 36, 89-95.

91. Q. Fu and W. Sun, Applied Optics, 2001, 40, 1354-1361.

92. S. Croll and A. Skaja, Journal of Coatings Technology, 2003, 75, 85-94.

93. T. G. Mayerhöfer, S. Pahlow, U. Hübner and J. Popp, Analyst, 2020, 145, 3385-3394.

94. J. H. Solheim, F. Borondics, B. Zimmermann, C. Sandt, F. Muthreich and A. Kohler, Journal of Biophotonics, 2021, 14, e202100148.

95. G. Mellau and B. Winnewisser, Laboratory and Astronomical High Resolution Spectra, 1995, 81, 138.

96. D. A. Naylor, A. A. Schultz and T. A. Clark, Applied optics, 1988, 27, 2603-2607.

97. A. H. Lipkus, Applied spectroscopy, 1988, 42, 395-400.

98. B. Hren, J. Mink and L. Balazs, Analytical chemistry, 2002, 74, 6402-6407.

99. T. Iwata and J. Koshoubu, Applied spectroscopy, 1994, 48, 1453-1456.

100. T. Iwata and J. Koshoubu, Applied spectroscopy, 1996, 50, 747-752.

101. G. Mie, Ann. Phys, 1908, 25, 0003-3804.

102. H. Van de Hulst, Inc., New York, 1957, 470.

103. P. Walstra, British Journal of Applied Physics, 1964, 15, 1545.

104. A. Kohler, C. Kirschner, A. Oust and H. Martens, Appl. Spectrosc, 2005, 59, 707-716.

105. H. Martens, J. P. Nielsen and S. B. Engelsen, Analytical Chemistry, 2003, 75, 394-404.

106. M. A. Brandsrud, R. Blümel, J. H. Solheim and A. Kohler, Scientific reports, 2021, 11, 1-14.

107. T. Konevskikh, R. Lukacs, R. Blümel, A. Ponossov and A. Kohler, Faraday discussions, 2016, 187, 235-257.

108. J. H. Solheim, E. Gunko, D. Petersen, F. Großerüschkamp, K. Gerwert and A. Kohler, Journal of biophotonics, 2019, 12, e201800415.

109. P. Bassan, A. Kohler, H. Martens, J. Lee, H. J. Byrne, P. Dumas, E. Gazi, M. Brown, N. Clarke and P. Gardner, Analyst, 2010, 135, 268-277.

110. E. A. Magnussen, J. H. Solheim, U. Blazhko, V. Tafintseva, K. Tøndel, K. H. Liland, S. Dzurendova, V. Shapaval, C. Sandt and F. Borondics, Journal of Biophotonics, 2020, 13, e202000204.

111. I. Bergonzi, L. Mercury, J.-B. Brubach and P. Roy, Physical Chemistry Chemical Physics, 2014, 16, 24830-24840.

112. J.-B. Brubach, A. Mermet, A. Filabozzi, A. Gerschel and P. Roy, The Journal of chemical physics, 2005, 122, 184509.

113. C. F. Bohren and D. R. Huffman, Absorption and scattering of light by small particles, John Wiley & Sons, 2008.

114. E. N. Lewis, P. J. Treado, R. C. Reeder, G. M. Story, A. E. Dowrey, C. Marcott and I. W. Levin, Analytical chemistry, 1995, 67, 3377-3381.

115. Z. Dionnet, A. Aléon-Toppani, F. Borondics, R. Brunetto, A. Buellet, Z. Djouadi, A. King, S. Rubino and D. Troadec, Microscopy and Microanalysis, 2018, 24, 2100-2101.

116. E. Breynaert, M. Houlleberghs, S. Radhakrishnan, G. Grübel, F. Taulelle and J. A. Martens, Chemical Society Reviews, 2020, 49, 2557-2569.

117. G. Gonella, E. H. Backus, Y. Nagata, D. J. Bonthuis, P. Loche, A. Schlaich, R. R. Netz, A. Kühnle, I. T. McCrum and M. T. Koper, Nature Reviews Chemistry, 2021, 5, 466-485.

118. T. Hayashi, Chemistry Letters, 2021, 50, 1173-1180.

119. J. Monroe, M. Barry, A. DeStefano, P. Aydogan Gokturk, S. Jiao, D. Robinson-Brown, T. Webber, E. J. Crumlin, S. Han and M. S. Shell, Annual Review of Chemical and Biomolecular Engineering, 2020, 11, 523-557.

120. M. Maccarini, Biointerphases, 2007, 2, MR1-MR15.

121. S. Strazdaite, J. Versluis and H. J. Bakker, The Journal of chemical physics, 2015, 143, 084708.

122. D. A. Schmidt and K. Miki, The journal of physical chemistry A, 2007, 111, 10119-10122.

123. M. A. Henderson, Surface Science Reports, 2002, 46, 1-308.

124. A. J. Hopkins and G. L. Richmond, Applied spectroscopy, 2013, 67, 261-273.

125. J. D. Cyran, M. A. Donovan, D. Vollmer, F. Siro Brigiano, S. Pezzotti, D. R. Galimberti, M.-P. Gaigeot, M. Bonn and E. H. Backus, Proceedings of the national academy of sciences, 2019, 116, 1520-1525.

Armin Mozhdehei

Rôle Macroscopique des Interfaces Solide-Liquide et Liquide-Gaz sur l'Interaction Eau-Roche en Milieu Poreux

Dans l'étude des interactions eau-roche, l’aire de surface des interfaces est un point d’attention depuis longtemps pour les géochimistes, mais la réactivité locale le long des interfaces joue également un rôle important. Généralement, on considère que les propriétés volumiques des phases en interaction décrit bien les forces motrices macroscopiques et le transfert de masse résultant. Cependant, les observations directes sur le terrain des transitions de phase ont remis en cause ce classicisme, avec de claires indications que la taille des pores, la distance à l’interface solide, ou bien la présence d'une interface liquide-air incurvée, peuvent entraîner les transitions de phase sur des voies réactionnelles inattendues. Deux types d'expériences ont été menées, l’une à l'échelle de l'interface, principalement centrée sur l’interface eau-solide, et l’autre à l'échelle du pore, tournée vers l'influence de ponts capillaires sur la géochimie intra-porale. Tout d'abord, des mesures de micro-spectroscopie infrarouge aux interfaces, utilisant un micro-faisceau (source laser et synchrotron) et un microscope confocal, ont été réalisées sur une cavité micrométrique fermée (inclusion fluide) pour explorer la variation de l'énergie vibratoire de l'eau en fonction de la distance à l’interface solide. Les données hyperspectrales ont affiché une signature dépendant de la distance pour l'eau sur une épaisseur de 1 ± 0,5 µm en lien avec l’état de surface du solide (effet hydrophobe) et des énergies de surface résultantes. La conversion de la signature spectrale près de l’interface du quartz en énergie libre de Gibbs conduit à une signature de surface de 600 J/mol à température ambiante (22°C) et de 1000 J/mol à plus haute température (155°C). Ce potentiel chimique croissant modifie évidemment la réactivité le long d'une telle interface solide-liquide, et affecte une quantité importante d'eau. Il en ressort que les interactions eau-roche dans les pores, les canaux et les cavités doivent tenir compte de la chimie de surface des minéraux et pas seulement de leur composition, de leur forme ou de leur taille. Deuxièmement, la variation de réactivité dans un réseau de pores est étroitement liée à la présence (ou non) de ponts capillaires liquide-air et à leur intensité capillaire. Nous avons exploité des puces nanofluidiques pour y établir un état capillaire contrôlé en ajustant l'humidité relative. Le phénomène de cavitation de l'eau et la cinétique de l'évaporation capillaire tenant compte de la forme des pores montrent les relations de cause à effet entre l'humidité relative et l'effet capillaire. Ces mesures remettent en question l'utilisation systématique des données macroscopiques sur les phases volumiques pour évaluer et prédire comment les interactions eau-roche se produisent et évoluent avec le temps dans les milieux poreux, en particulier dans les aquifères non saturés en eau.

Mots clés : Variation de réactivité, Thermodynamique, Spectroscopie vibrationnelle, Interface/Interphase, Pont capillaire

Macroscopic Role of Solid-Liquid and Liquid-Gas Interfaces on the Water-Rock Interaction in Porous Media

In water-rock interaction, the surface area of interfaces has received long-term attention from geochemists, but local reactivity along interfaces also plays a significant role. The general statement is that using the bulk properties of interacting phases describes the macroscopic driving forces and the resulting mass balances. However, direct field observations challenged classicism, demonstrating that the pore radius, the distance to the solid boundary, or the presence of a curved liquid-air interface can drive the phase transitions along unexpected reactional pathways. This study has targeted two types of experiments to probe what can be the additional parameters involved in the reasoning, one at the interface-scale, mainly focused on the water-solid boundary, and one at the pore-scale, turned to the influence of capillary bridges on the in-pore geochemistry. First, the interface-based infrared micro-spectroscopy measurements, using micro-beam (laser and synchrotron source) and a confocal microscope, were performed on a micrometric closed cavity (fluid inclusion) to explore the variation of the vibrational energy of water as a function of the distance to the solid boundary. The hyperspectral data displayed a distance-dependent signature for water over a 1 ± 0.5 µm thickness (called interphase domain) because of the solid surface property (hydrophobic effect) and the resulting surface energies. The conversion of the spectral signature near the quartz boundary into Gibbs free energy leads to a 600 J/mol surface-imprinting at room temperature (22°C) to 1000 J/mol at high temperature (155°C). Consequently, this increasing chemical potential changes the reactivity along such a solid-liquid interface, which affects a significant amount of water. It comes out that the surface chemistry of minerals and not only their composition, shape, or size play a crucial role in water-rock interactions in pores, channels, and cavities. Second, the reactivity variation in a pore network is closely linked to the presence (or not) of liquid-air capillary bridges and their capillary intensity. We exploited nanofluidic chipsets to establish capillarity in a controlled way by tuning the relative humidity, with which we are exploring the water-rock-gases equilibria at various capillary states leading to a phase transition. The water cavitation phenomenon and kinetic of the evaporation concerning the pore shape show the effect of relative humidity on the capillary-driven effect. These measurements question the systematic use of the bulk phases datasets to evaluate and predict how water-rock interactions occur and evolve with time in the porous media, especially in water-unsaturated aquifers.

Keywords: Reactivity variation, Thermodynamic, Vibrational spectroscopy, Interface/Interphase, Capillary bridge

ISTO UMR 7327 Université d’Orléans/CNRS, 45071
Orléans cedex